Non-Parametric and Machine Learning Techniques for Continuous Gravitational Wave Searches

Joseph Bayley

Submitted in fulfilment of the requirements for the
Degree of Doctor of Philosophy

School of Physics and Astronomy
College of Science and Engineering
University of Glasgow

May 2020

Abstract

The field of gravitational wave astronomy is still in its early stages, with detections of compact binary coalescences numbering $\sim$ 12 and the most recent observing run (O3) providing $\sim$ 50 more candidates. Another possible source of gravitational waves is rapidly rotating neutron stars which can emit gravitational waves if they have some asymmetry around their rotation axis. These are predicted to emit long duration quasi-sinusoidal signals known as continuous gravitational waves.

All-sky and wide parameter space searches for continuous gravitational waves are generally template-matching schemes which test a bank of signal waveforms against data from a gravitational wave detector. Often these searches are highly-tuned to specific signal types and are computationally expensive. We have developed a search method (entitled SOAP) based on the Viterbi algorithm which is model-agnostic and has a computational cost several orders of magnitude lower than template methods and with a comparable sensitivity. In particular, this method can search for signals which have an unknown frequency evolution. We test the algorithm on three simulated and real data sets: gapless Gaussian noise, Gaussian noise with gaps and real data from the final run of initial LIGO (S6). We show that at 95% efficiency, with a 1% false alarm rate, the algorithm achieves a sensitivity of $\sim$ 60, 72 and 74 in the optimal coherent signal to noise ratio in each of these datasets. We discuss the use of this algorithm for detecting a wide range of quasi-monochromatic gravitational wave signals and instrumental artefacts, and demonstrate that it can also identify shorter duration signals such as compact binary coalescences.

Many continuous gravitational wave searches are affected by instrumental lines as the long duration narrowband nature of a line can appear to be very similar to a real continuous gravitational wave signal. This has led to the development of techniques to try and limit the effect of instrumental lines, which mostly involve developing a statistic to penalise signals that appear in only a single detector. Whilst these statistics limit the effect of instrumental lines, in the SOAP search described above, many lines still contaminate the statistics and have to be manually removed by investigating other search outputs. We have developed a method using convolutional neural networks to reduce the impact of instrumental artefacts on the SOAP search described above. This has the ability to identify features in each of the detectors spectrograms such that a frequency band can be

classified into a signal or noise class. This limits the amount of manual investigation of frequency bands and allowed the SOAP search to be fully automated without a reduction in the sensitivity.

Once a continuous gravitational wave is detected, we would want to extract some parameters associated with the source to help understand more about its structure and evolution. We describe a Bayesian method which extracts the sky location, frequency, frequency derivative and signal to noise ratio of a source associated with the frequency evolution returned by the SOAP algorithm. This has the aim of limiting the size of the parameter space for a more sensitive fully coherent follow up search. We tested this approach on 200 simulations in Gaussian noise, generating posterior distributions for the parameters described above. In 90% of these simulations we limit the sky area to 45 deg^2 with a 95% confidence contour. However, find that this contour contains the true parameter only 42% of the time. We present these results and describe the features and shortcomings of our approach.

As mentioned above, we limit the effect of instrumental lines on the SOAP search using machine learning, however we can also identify and mitigate these lines separately before a search is run. We demonstrate how we can use SOAP in a simple configuration to identify instrumental lines. We compare this method to existing line identification tools used in the Laser Interferometer Gravitational-wave Observatory (LIGO) collaboration, and find that using the Viterbi statistic SOAP identifies $\sim 37\%$ of the same lines as these methods, where for many of the lines which were not identified, other SOAP outputs do show evidence of a line. With further investigation, we expect to identify many more lines in common with existing methods. As well as these common lines, the SOAP algorithm returned ~ 150 more bands which potentially contain an instrumental line, which did not appear on LIGO line-lists.

Contents

List of Tables

List of Figures

Acknowledgements

*"I've had it with these motherf****g snakes on this motherf****g plane"*

— *Samuel Jackson (Neville Flynn)*, **S**nakes **O**n **A** **P**lane

There are many people to thank who have helped me throughout my PhD, who I will mention briefly here. Firstly my supervisors Graham and Chris, who have always been around to offer me consistently great advice for the last 3.5 years. Then Matt Pitkin, David Keitel and many other members of the IGR and LIGO collaboration who have helped me with various problems. I would also like to thank Stewart Boogert and others at Royal Holloway who helped get me to this point and continue to offer advice whenever I see them. Then the many friends who have kept me nice and distracted from my work: Alex, Abi, Paul, Ashlea, Simon, Joe, Martin, Andrew, Jenny and many others (you know who you are). Finally I would like to thank my family for keeping me grounded and supporting me with whatever I wanted to do.

Declaration

The material presented in this thesis is the result of my own work under the supervision of Prof. Graham Woan and Dr Chris Messenger in the Institute for Gravitational Research at the University of Glasgow. It has not been submitted for any other degree at the University of Glasgow, or at any other institution. This work was conducted as part of the LIGO, Virgo and Kagra (LVK) collaboration and therefore was made possible with the interaction of many researchers within this collaboration.

- Chapter 1 and Chapter 2 is introductory material written by myself under the advice of Prof. Graham Woan and Dr Chris Messenger.
- Chapter 3 is my own work which has been published in [**bayley2019SOAPGeneralised**], and was written in collaboration with my supervisors.
- Chapter 4 has been written into a paper which is yet to be published, but will be submitted soon. This was written in collaboration with my supervisors and was predominantly my own work.
- Chapter 5 is work which is planned to be a paper in the future when the work is complete, and is my own work done in collaboration with my supervisors.
- Chapter 6 is again work which is planned to be a paper in the future when the work is complete, and is my own work done in collaboration with my supervisors.

Acronyms

A | B | C | E | F | G | I | K | L | M | N | P | R | S | U

A

ASD amplitude spectral density. viii, 139, 140

B

BBH binary black hole. 1, 6, 7, 77, 80, 162

BNS binary neutron star. 1, 6, 7, 9, 77, 79, 162

C

CBC compact binary coalescence. 5–8, 77, 78, 83–85

CFS Chandrasekhar, Friedman and Schutz. 10

CI confidence interval. 132

CMB cosmic microwave background. 8, 10

CNN convolutional neural network. vi–viii, 84–86, 91, 92, 94, 95, 98–101, 103, 105–122, 162–164

CPU central processing unit. 113, 114

CR critical ratio. 143

CW continuous gravitational wave. v, vi, viii, ix, 2, 5, 6, 8, 9, 20, 31, 34–36, 38, 65, 71, 73, 75, 77, 81–84, 86, 87, 91, 95, 98, 101, 103, 107, 111, 113, 115–117, 119, 122–124, 126–130, 137–139, 141, 142, 144, 161–166, 171, 172, 174

E

EM electromagnetic. 85

EOS equation of state. 7, 9

ETMX end test mass X. 12, 14

ETMY end test mass Y. 12, 14

F

FFT fast Fourier transform. viii, 32, 54, 79, 85, 86, 142, 143, 161, 162, 166, 168, 171

G

GMST Greenwich mean sidereal time. 125

GPU graphics processing unit. 113, 114

GR general relativity. 1

GW gravitational-wave. 1–17, 19–22, 32, 38, 39, 42, 45, 54, 60, 77, 82, 84, 85, 101, 108, 123, 138, 139, 141–144, 156, 165, 167

I

ITMX internal test mass X. 12, 14

ITMY internal test mass Y. 12, 14

K

KDE kernel density estimate. 127, 128

L

LIGO Laser Interferometer Gravitational-wave Observatory. ii, vii, viii, 1, 5, 7, 11, 12, 14, 17, 18, 20, 32, 34, 35, 37–39, 57, 65, 75, 77, 79, 82, 84, 87, 98, 102, 103, 116, 129, 130, 139, 140, 142, 144, 148–151, 154–156, 158, 161–165

LISA laser interferometer space antenna. 7, 11

LVK LIGO, Virgo and Kagra. x

M

MCMC Markov-Chain Monte Carlo. 26, 27, 62

MDC mock data challenge. iv, viii, 34, 57, 60, 62–65, 67, 69, 71–75, 81–83, 102, 107, 111–113, 162

MSU million standard units. 35

N

NoEMi noise frequency event miner. 143

NSBH neutron star black hole. 6

P

PDF probability density function. 31

PEM physical environment monitor. 142, 143

PRM power recycling mirror. 12

PSD power spectral density. 8, 42, 54–58, 60, 85, 101, 108, 111, 139, 166, 167

R

RMS root median square. 61–64, 82

S

SFT short Fourier transform. 33, 34, 38, 42, 46, 47, 49–54, 56, 57, 59, 61–63, 65, 66, 71, 72, 74, 77, 81–83, 103, 105, 111, 113–115, 143–150, 152, 153, 156, 157, 162, 165

SGWB stochastic gravitational wave background. 139

SNR signal-to-noise-ratio. viii, 14, 20, 32, 49–52, 54, 56, 60–66, 68–71, 75, 78, 82, 101–103, 106–112, 116–118, 122, 127–132, 134, 137, 144, 151, 155, 162, 164, 166–168, 172, 173

SRM signal recycling mirror. 12

SSB solar system barycenter. 21, 22, 32, 125, 126

U

UCD up, centre or down. 41, 44, 45, 48, 49

USA United States of America. 141

Chapter 1

Introduction

Gravitational-waves (GWs) were first predicted in 1915 as a consequence of Einstein's general theory of relativity [**einstein2005GrundlageAllgemeinen**], where they were theorised as ripples in the fabric of space-time. Observations of these waves would would open up a new window into the universe which is not accessible in the electromagnetic spectrum.

The first observational evidence that GWs exist came from observations of the Hulse-Taylor binary [**weisberg1981GravitationalWaves**, **weisberg2004RelativisticBinary**], which subsequently won the Nobel prize in 1993. This observation, which was of a pulsar in a binary system, showed that the periastron was reached slightly early after each orbit, implying that the pulsars orbital radius was decreasing with time. If the separation of two orbiting objects is decreasing then the system must be losing energy. The measurement of the loss in energy matched the general relativity (GR) prediction which assumed the energy was lost to GWs, giving hope of the existence of GWs and motivating the design of instruments which could directly detect them.

The first direct detection of GWs was made in 2015 when the two Laser Interferometer Gravitational-wave Observatory (LIGO) detectors in the US [**abbott2016ObservationGravitati** identified a signal from a binary black hole (BBH) system. This was not only the first observation of a GW but gave information on an as yet unobserved type of astrophysical system. This has since been followed by many more detections of BBH signals, including those from a three detector network (the two LIGO detectors and Virgo) [**abbott2017GW170814ThreeDetector**, **theligoscientificcollaboration2020GW190425Ob** which allowed better localisation of the source on the sky. In 2017 the LIGO and Virgo detectors observed the first binary neutron star (BNS) system [**abbott2017GW170817Observation** which was shortly ($\sim 1.7s$) followed by an observation of a gamma ray burst event [**goldstein2017OrdinaryShort**]. The combination of the LIGO and Virgo observations allowed a precise localisation in sky position, which led to the identification of the host galaxy of the BNS [**coulter2017SwopeSupernova**]. This was then followed up by obser-

vations across the electromagnetic spectrum, starting the era of multi-messenger astronomy. These detections opened up the field of GW astronomy, where many more detections are expected to give more information on the universe and objects within it.

As well as searching for BBH and BNS signals, there are many efforts to detect other types of GW signals. This thesis focuses on efforts to search for a particular type of GW which are thought to originate from rapidly rotating neutron stars. In Chapters 1 and 2 we will review introductory material. This includes a general introduction to the generation of GWs in Sec. 1.1 and their sources in Sec. 1.2. We will then introduce instruments used to detect GW in Sec. 1.3. In Chapter 2 we will introduce the general model for continuous gravitational waves (CWs) and current methods used to detect them. Chapters 3, 4, 5 and 6 will go into detail about techniques developed by the author to search for CW signals and instrumental artefacts. Finally we will summarise this work and discuss future developments in Chapter 7.

1.1 Gravitational waves

In general relativity, gravity is thought of as the curvature of space-time, where matter moves according to this curvature. Matter also has an effect on the curvature itself, where larger masses will distort space-time more than smaller masses. To describe space-time, one would want to link the curvature to the matter mathematically, this was done in 1915 [**einstein2005GrundlageAllgemeinen**] where Einstein developed his field equations

$$G_{\mu\nu} = \frac{8\pi G}{c^4} T_{\mu\nu}. \tag{1.1}$$

where $G_{\mu\nu}$ is the Einstein tensor, G is the gravitational constant, c is the speed of light and $T_{\mu\nu}$ is the stress-energy tensor. The stress energy tensor contains information on the density and flux of energy and momentum at a given point in space-time. The Einstein tensor contains information on the curvature of the universe, this can be derived directly from the metric tensor $g_{\mu\nu}$ which describes the space-time geometry. Einstein's equations then explain how the curvature of space-time changes with the mass-energy within it.

In empty space, i.e $T_{\mu\nu} = 0$, one can assume that the geometry of space-time is flat, i.e. there is no curvature to space-time. The metric tensor for flat space is defined as

$$g_{\mu\nu} = \eta_{\mu\nu} = \begin{pmatrix} -1 & 0 & 0 & 0 \\ 0 & 1 & 0 & 0 \\ 0 & 0 & 1 & 0 \\ 0 & 0 & 0 & 1 \end{pmatrix}. \tag{1.2}$$

Each index of this matrix refers to a space-time dimension, i.e. $x^0 = t$, $x^1 = x$, $x^2 = y$

and $x^3 = z$. Measuring a distance dx in space-time can be different for different observers, therefore, one needs a measure which is invariant for every observer. This is the space-time interval ds, also known as the line element, between two 'events' in space-time, and is defined as

$$ds^2 = g_{\mu\nu} dx^\mu dx^\nu. \tag{1.3}$$

This equation is a sum over the indices μ and ν. Equation 1.3 can be thought to describe the space-time 'distance' between the two events. For flat space-time, $\eta_{\mu\nu}$, Eq. 1.2 and 1.3 can be combined to find the space-time interval

$$ds^2 = -c^2 dt^2 + dx^2 + dy^2 + dz^2. \tag{1.4}$$

A GW is then a wave which propagates through space-time, where the simplest way to visualise this is just a small time dependent change to the flat space-time metric $\eta_{\mu\nu}$. In the linearised theory of gravity, the space-time metric $g_{\mu\nu}$ can be defined as

$$g_{\mu\nu} = \eta_{\mu\nu} + h_{\mu\nu}, \tag{1.5}$$

where $\eta_{\mu\nu}$ is the metric for flat space-time and $h_{\mu\nu}$ is some perturbation, where $|h_{\mu\nu}| \ll 1$ [**flanagan2005BasicsGravitational**]. In the regime of small perturbations, it can be shown that the solutions are plane waves, more information on this derivation can be found in [**flanagan2005BasicsGravitational**, **letiec2016TheoryGravitational**].

By using $g_{\mu\nu}$ from Eq. 1.5, we can write the linearised Einstein equations as

$$\Box h_{\mu\nu} = -16\pi T_{\mu\nu}, \tag{1.6}$$

where $\Box$ is the d'Alembert operator defined by

$$\Box = -\frac{1}{c^2}\frac{\partial^2}{\partial t^2} + \frac{\partial^2}{\partial x^2} + \frac{\partial^2}{\partial y^2} + \frac{\partial^2}{\partial z^2} \tag{1.7}$$

In empty space there is no matter, therefore, all the components of the stress energy tensor are zero, i.e. $T_{\mu\nu} = 0$. This allows Eq. 1.6 to be reduced to

$$\Box h_{\mu\nu} = 0, \tag{1.8}$$

which is of course the wave equation. This follows the same form as in electrodynamics and the general plane-wave solutions have the form

$$h_{\mu\nu} = A_{\mu\nu} e^{ik_\alpha x^\alpha}, \tag{1.9}$$

where each component of $h_{\mu\nu}$ is a sinusoid travelling along vector $\mathbf{k}$ with amplitude $A_{\mu\nu}$

[**capano2011SearchingGravitational**].

At this point the set of equations are not simple; the symmetric tensor $A_{\mu\nu}$ has 10 independent components. This can be greatly simplified by choosing a different gauge where the metric perturbation is both transverse and traceless (TT) [**flanagan2005BasicsGravitationa**
This is just a choice of coordinate system which does not change any current assumptions. This gauge imposes two conditions: one is that $h_{\mu\nu}$ is traceless, i.e. that the sum of the diagonal elements are 0 and the other is that $h_{\mu\nu}$ is transverse. The transverse element means that the oscillations of the wave happen perpendicular to the direction of travel. At this point we can choose that the wave is travelling in the z direction which means that $k = (\omega, 0, 0, k)$. By then adopting the TT gauge there are only two unique components to the metric such that the perturbation is

$$h_{\mu\nu}^{\mathrm{TT}} = \begin{pmatrix} 0 & 0 & 0 & 0 \\ 0 & h_+ & h_\times & 0 \\ 0 & h_\times & -h_+ & 0 \\ 0 & 0 & 0 & 0 \end{pmatrix} e^{i(kt-wt)}. \tag{1.10}$$

The two unique components are then the two polarisations of gravitational waves, h_+ and $h_\times$. The effect of each of the polarisations on a ring of independent test masses can be seen in Fig. 1.1, where in this example the GW is travelling out of the page along the z axis. From Eq. 1.10 one can see that the h_+ component causes space-time to be stretched in the x axis and compressed in the y axis before returning to normal then stretching in the y axis and compressing in the x axis. This can be seen as the test masses being distorted into an ellipse with the semi-major axis along the x or y axis. The cross polarisation has a similar affect to the plus polarisation but is rotated 45 degrees.

Generating gravitational waves

To generate GWs we can follow the derivation in [**flanagan2005BasicsGravitational**] and [**letiec2016TheoryGravitational**], where one can solve Eq. 1.6 to find the GW perturbation $h_{\mu\nu}$. The result of this is that the spatial part of the metric perturbation h_{ij} is related to the second moment of the mass distribution by

$$h_{ij} = \frac{2G}{c^4 r}\frac{d^2}{dt^2}Q_{ij}(t - r/c), \tag{1.11}$$

where r is the distance from the source [**letiec2016TheoryGravitational**] and Q_{ij} is the second moment of the mass distribution defined by

$$Q_{ij}(t) = \int \rho(t, \mathbf{x}) x^i x^j d^3x, \tag{1.12}$$

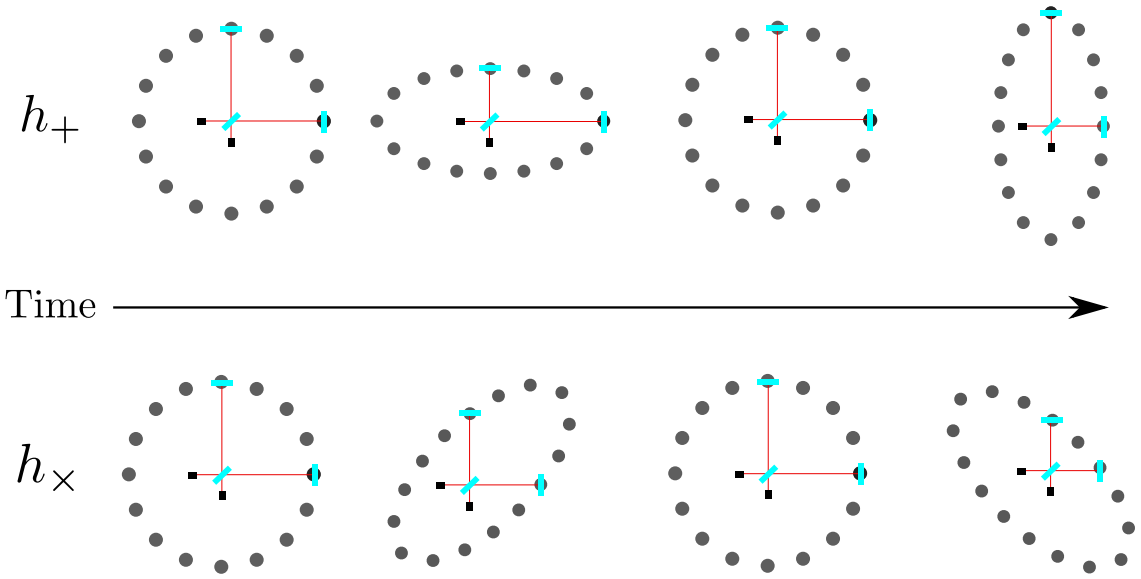

Figure 1.1: These diagrams show how the plus and cross polarisations affect a ring of test particles. This assumes the GW is travelling out of the page, where the effects have been greatly exaggerated. This also shows an example of how the polarisations affects the test masses of an interferometer. This will be described in more detail in Sec. 1.3.

where ρ is the mass density [**letiec2016TheoryGravitational**]. This second mass moment has a slight modification in the TT gauge, see [**flanagan2005BasicsGravitational**], where its trace is subtracted defining the mass quadrupole moment. However, this has the same relationship between the mass quadrupole moment (or second mass moment) and the GW amplitude. This shows that for GW to be generated, we need the the second time derivative of the mass quadrupole moment to be non zero. Gravitational monopole and dipole radiation is not possible due to the conservation of energy and momentum respectively [**misner1973Gravitation**] and radiation can be emitted from higher orders but is generally weaker than quadrupole radiation.

There are many types of system which could emit quadrupole GWs, including supernovae, colliding objects and orbiting black holes. Some of the primary sources of GWs that are currently searched for will be described in the following section.

1.2 Sources and signals

There are many potential sources for GWs, which can be split into 3 general categories based on their signal type: compact binary coalescence (CBC), Burst, Stochastic and CWs. These categories are chosen based on the length of the signal and how well modelled the signal is. Figure 1.2 shows an example of each of the signals and their category.

In the sections that follow, I will give an overview of the potential sources within each

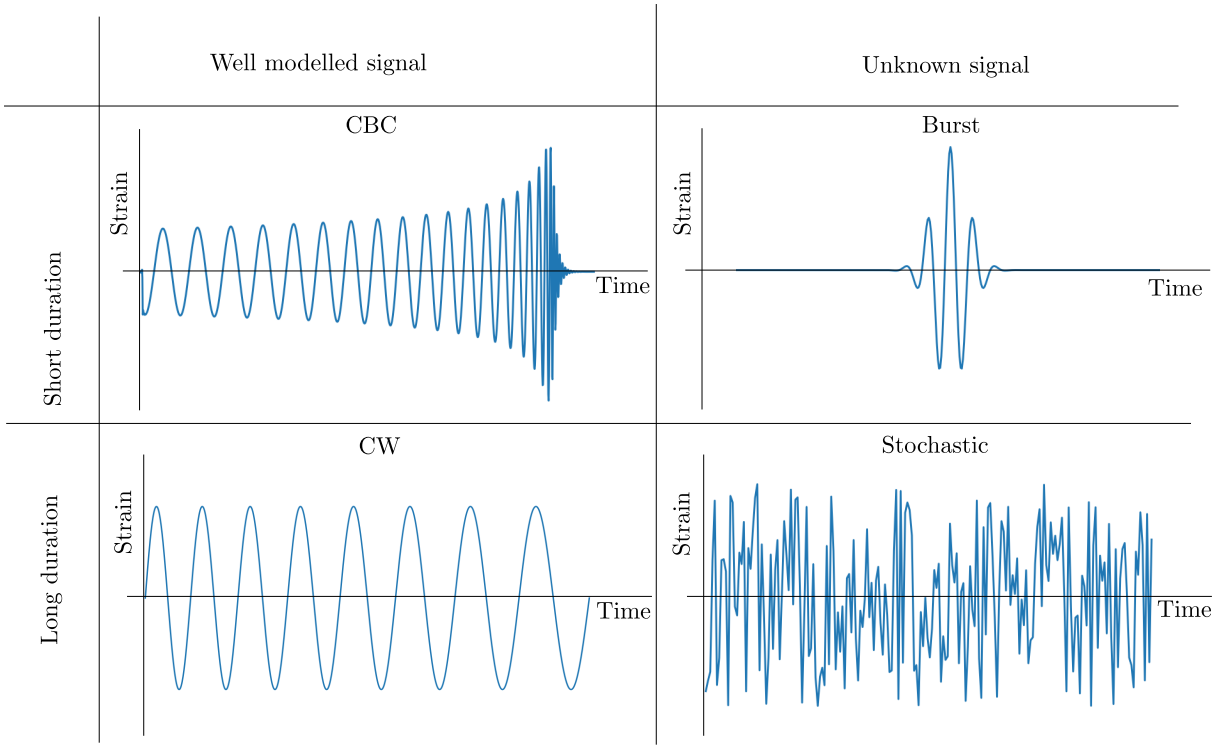

Figure 1.2: Each GW signal type can be categorised based on its signal length and how well the signal is modelled. Transient signals which are short duration in the ground based detector band, include both well modelled CBC signals and unknown Burst signals. Long duration signals include well modelled CW signals and Stochastic signals, where whilst the sources may be well modelled, the signal at the detector is unknown. Whilst there is no scale in the diagram above, shorter duration signals typically have much larger strain amplitudes than long duration signals, however, this does also depend on the distance to the source.

of these signal categories and their waveforms.

1.2.1 Compact Binary Coalescence

CBCs originate from the inspiral, merger and ring-down of two compact objects which are gravitationally bound. The objects inspiral as they lose energy through the radiation of GWs. Dependent on the masses and distances of the two objects, the GWs generated by the system can be detected by ground based detectors such as LIGO [**aasi2015AdvancedLIGO**] and Virgo [**acernese2015AdvancedVirgo**]. In fact, the only detections to date have been of this type; these are summarised in [**ligoscientificcollaborationandvirgocollaboration2019G** The first of these detections, GW150914 [**abbott2016ObservationGravitational**], not only provided evidence that BBHs exist and merge at an observable rate, but the measurements of their component masses ($\sim 29\ M_\odot$ and $\sim 36 M_\odot$) were larger than that of previous measurements of black holes in binary systems from x-ray observations [**abbott2016ASTROPHY**

The compact objects referred to here are either black holes or neutron stars, where

combinations of these make up the three general types of CBC source: BBH, BNS and neutron star black hole (NSBH). The general structure of the waveform is the same for each of these and follows a 'chirp' where the GW frequency increases until they reach the innermost stable circular orbit. After this they will merge into a single black hole which will oscillate (ring down). A simple example of the waveform is shown in Fig. 1.2. The maximum frequency of this inspiral is defined by the mass of the system, where higher mass systems will merge at lower frequencies. To find the relationship between mass and frequency, we can look at the final stable orbit of the inspiral which is at the innermost stable circular orbit, $R_{\mathrm{ISCO}} = 6GM/c^2$ [**maggioreGravitationalWaves**]. As we assume a circular orbit we can use Keplers law $T^2 \propto a^3$ where T is the period of the orbit and a is the radius, to estimate the orbital frequency f_{ISCO} at the end of the inspiral,

$$f = \frac{1}{T} \lesssim \sqrt{\frac{GM}{4\pi^2 R_{\mathrm{ISCO}}^3}} \sim 2200\,\mathrm{Hz}\frac{\mathrm{M}_\odot}{\mathrm{M}}, \tag{1.13}$$

where M is the total mass of the two objects and $M_\odot$ is the mass of the sun.

LIGO is sensitive from $\sim$ 10 Hz to $\sim 10^4$ Hz, therefore by the approximation in Eq. 1.13 can observe CBC systems with total masses of $\mathcal{O}(1)\,M_\odot$ to $\mathcal{O}(200)\,M_\odot$. Current GW detections of BBHs have component masses ranging between $\sim 7M_\odot$ to $\sim 50M_\odot$ [**ligoscientificcollaborationandvirgocollaboration2019GWTC1GravitationalWave**], where the signals are detectable by ground based detectors for $\lesssim 1\,s$. BNSs have lower masses $(1-2\,M_\odot)$, where due to their compact size, both merge at higher frequencies and lose energy to GW at a lower rate, therefore spending more time ($\mathcal{O}(100)$ s) within LIGOs frequency band. At earlier stages of the inspiral, BBH signals have frequencies below that which LIGO can detect. However, future space based detectors such as laser interferometer space antenna (LISA) [**danzmann1996LISALaser**] are expected to detect these signals, and could offer a method to predict when and where the signal will appear in the LIGO band [**sesana2016ProspectsMultiband**].

In systems which have a neutron star as one of the objects, the neutron star can deform due to tidal interactions between the objects [**flanagan2008ConstrainingNeutronstar**]. This becomes useful as it will affect the GW waveform and can help us place limits on, and determine the equation of state (EOS) for the dense matter in a neutron star [**harry2018ObservingMeasuring**]. CBCs can also be used in cosmology, where they offer a method to independently measure the Hubble constant as well as other cosmological parameters. The Hubble constant relates the distance and recession velocity of an astrophysical object via $v = H_0 d$. Given that for a GW observation the distance is a direct observable, if the redshift can be inferred, one can use these parameters to estimate the Hubble constant. In [**theligoscientificcollaborationandthevirgocollaboration2017Gravitationa**] the Hubble constant is estimated by using the BNS observation GW170817 [**abbott2017GW1708**

where the redshift is inferred from observations of the electromagnetic counterpart. One can also estimate the Hubble constant using multiple CBC signals as in [**delpozzo2012InferenceC**
As well as the EOS and Hubble constant measurements, there are many other problems which can be addressed using observations of CBC signals including, understanding the formation of BBHs [**zevin2017ConstrainingFormation**, **mandel2018MergingStellarmass**] or testing general relativity [**theligoscientificcollaborationandthevirgocollaboration2019Tes**

1.2.2 Burst

Similar to CBC signals, burst sources are also short duration, however they are unmodelled or difficult to model, in the sense that the exact waveform of the signal is unknown. There are two possible reasons for the lack in knowledge of the waveform: the physics of the system is unknown or too complicated to model, or the system itself is unknown.

There are a number of systems which could potentially emit short duration burst signals, including core collapse supernovae [**ott2008GravitationalWave**], cosmic strings [**damour2005GravitationalRadiation**] and other unknown sources. Detecting GWs from core collapse supernovae could offer more insight into the processes and parameters associated with them, this is due to the GWs being emitted from deeper inside the star than electromagnetic waves. As well as searching for core collapse supernovae, cosmic strings and well modelled CBC signals [**aasi2014SearchGravitational**], they offer a method to search for short GW signals from an unknown source.

Searching for these types of signals requires methods which do not depend on a model, therefore look for signals with a broad range of possible waveforms. For example, one of these methods takes the wavelet transform of individual detectors data to get a time-frequency representation [**klimenko2004PerformanceWaveBurst**], then identifies coincident power in these time-frequency maps between the detectors. Other searches develop this idea further to search for signals which are coherent between detectors [**cornish2015BayeswaveBayesian**, **klimenko2008CoherentMethod**], i.e. the phase information is the same in each detector.

1.2.3 Stochastic

The stochastic background differs from transient GWs (Sec. 1.2.1, 1.2.2) and continuous GW (Sec. 1.2.4) as rather than the signal originating from a specific location on the sky, it will come from all directions [**christensen2018StochasticGravitational**]. The signal is then persistent in the GW detectors output, where the statistical properties of this noise can be predicted using various different models [**christensen2018StochasticGravitational**]. There are broadly two categories to the stochastic background: the astrophysical back-

ground and the cosmological background. The astrophysical background originates from the superposition of many weak GWs from astrophysical sources such as CBCs [**regimbau2011Ast** This would provide information on the history of astrophysical processes in the universe. The cosmological background originates from the early universe with sources such as inflation or cosmic strings [**maggiore2000GravitationalWave**], and can be though of as the GW analogue of the cosmic microwave background (CMB). GWs from inflation or cosmic strings would help describe early times in the evolution of the universe [**christensen2018StochasticGravitational**].

The stochastic GW background is generally characterised by its energy density per log frequency, where different models predict the frequency dependence of the energy density and use this to filter the GW detectors power spectral density (PSD) [**allen1999DetectingStocha** As the stochastic background is noise-like it is very difficult to distinguish from noise within a single detector [**christensen2018StochasticGravitational**], therefore, search methods correlate signals between multiple detectors [**romano2019SearchesStochastic**, **christensen2018StochasticGravitational**, **allen1999DetectingStochastic**].

1.2.4 Continuous waves

CWs are long duration signals, where its duration is greater than the typical length of an observation run of ground based detectors and in general has a slowly varying and narrowband frequency.

The primary source for many CW searches is rapidly rotating neutron stars with spin periods ranging from $\sim 10^{-3} - 10$ s [**manchester2005AustraliaTelescope**], and in general have well modelled signals. Neutron stars can form when a massive star $\sim 8 - 20 M_{\odot}$ collapses [**fryer2005NeutronStar**], leaving a remnant of around $1.2 - 2\ M_{\odot}$ with a radius of ~ 10 km [**ozel2016MassesRadii**]. This gives the objects high densities of $\sim 10^{17}$ kgm^{-3} and high magnetic field strengths of $10^{8} - 10^{15}$ G [**konar2017MagneticFields**]. Despite many observations of neutron stars in the electromagnetic spectrum, these objects are not well understood. A key part of neutron stars which is not understood is the EOS, where a review of the current understanding can be found in [**lattimer2016EquationState**]. The EOS relates quantities such as the pressure and density of a neutron star and dictates how the neutron star matter behaves. Observations of GWs from neutron stars can place limits on the EOS of this type of matter. These observations have already been made in the form of BNS mergers [**abbott2017GW170817Observation**], however, independent observations of rapidly rotating neutron stars can add to this understanding by placing limits on the deformability of the star and therefore the EOS.

For a neutron star to emit a CW, Eq. 1.11 tells us that it needs to have some asymmetry in its mass distribution around its rotation axis. There are a number of different mechanisms which could cause this and emit GWs, some of these are reviewed in

[**glampedakis2017GravitationalWaves**, **riles2017RecentSearches**, **haskell2015DetectingG**
lasky2015GravitationalWaves]. Here I will summarise two main theories: Neutron star mountains and neutron star oscillations.

Mountains

One of the more likely mechanisms for detectable GW emission from neutron stars is from 'mountains' on the surface of the star. These are permanent deformations of the crust which are non axisymmetric, i.e. the deformation is not symmetric around the rotation axis.

This deformation or asymmetry can be quantified by the ellipticity ϵ of the neutron star. This is defined using the principal moments of inertia

$$\epsilon = \frac{I_{xx} - I_{yy}}{I_{zz}}, \tag{1.14}$$

where I_{zz}, I_{xx}, I_{yy} are the components of the moment of inertia in each of the spatial axes and the star is rotating around the z axis, i.e. I_{zz} is parallel with the z axis.

There are a number of theories which describe the origin of this asymmetry. If the pulsar is in a binary system and accreting material from its companion star, the material can be funnelled towards the magnetic poles by the magnetic field, thereby causing a 'hot spot' [**haskell2015DetectingGravitational**]. This 'hot spot' could cause a deformation on the surface of the star which if the rotational and magnetic axes are not aligned would not be axisymmetric. The magnetic stresses from strong magnetic fields within the star, could potentially also cause non axisymmetric deformations to the star [**cutler2002GravitationalWaves**]. Finally the spin down of the pulsar itself could cause stresses in the crust of the star until the point of breaking, after this break a distortion could remain in the crust [**becker2009NeutronStars**, **ruderman1976CrustbreakingNeutron**]. More details on the signal waveform of this type of GW and methods to search for it will be explained in Sec. 2.

Neutron star oscillations

There are a number of oscillation modes within a star such as f-modes, p-modes and r-modes [**becker2009NeutronStars**]. These are similar to oscillations in the Earth which are measured in terrestrial seismology. The difference between these modes is the restoring force bringing the perturbed state back to equilibrium. For example, gravity is the restoring force for f-modes where the oscillations happen in the crust of the star. The more promising of these for GW emission and detection is the r-mode [**owen2000GravitationalWaves**]. These are oscillations in the neutron superfluid part of the star, where the restoring force is the Coriolis effect from the rotation of the star. These oscillations would cause an

asymmetry in the mass distribution of the neutron star which is changing with time, generating GWs that would then dampen the oscillations and therefore the GW emission. However, due to the different frames of reference of the observer and rotating star, an instability known as the Chandrasekhar, Friedman and Schutz (CFS) instability [**chandrasekhar1970SolutionsTwo**] can arise such that GW emission drives the oscillation. The modes then become unstable to GW emission in rapidly rotating neutron stars [**owen2000GravitationalWaves**], making them more likely for a detection. For more details on this mechanism see [**owen2000GravitationalWaves**, **lasky2015GravitationalWaves**, **owen1998GravitationalWaves**, **jonesCFSInstability**].

1.3 Detectors

The indirect detection of GWs from the Hulse-Taylor binary pulsar system [**weisberg1981Gravita** left little doubt that GWs existed. The real challenge was to design an instrument or develop a technique which could directly detect GWs. There were a number or proposed methods, notably: resonant bar detectors, both ground based and space based interferometers, pulsar timing arrays and cosmic microwave background (CMB) detectors. The first resonant bar detector was designed and built by Joseph Weber [**weber1966ObservationThermal** this is a large cylinder of metal which resonates as a GW passes by. There are a few different designs of this type of detector, including an omni-directional design [**dewaard2003MiniGRAILF** With pulsar timing arrays, the accurate arrival time of pulses from millisecond pulsars can be used to measure GWs [**hobbs2017GravitationalWave**]. As a GW passes between the pulsar and the observer, the arrival time of the pulses will change. The change in arrival time depends on the source and its parameters, for supermassive black hole binaries emitting at nanohertz frequencies at around 1 Gpc, the change in arrival time is $\mathcal{O}(10)$ ns [**hobbs2017GravitationalWave**]. CMB detectors can be used to find evidence of GWs by investigating the B-mode polarisations of the CMB [**ade2018ConstraintsPrimordial**]. A number of detectors are used to look at the CMB however, they are yet to confirm a detection of a GW signal. The current best known design of a GW detector is the interferometer, this includes the ground based detector LIGO [**aasi2015AdvancedLIGO**] which made the first detection of GW in 2015 [**abbott2016ObservationGravitational**] and space based interferometers such as LISA [**danzmann1996LISALaser**]. These are the focus of this section as the analysis that will follow uses data from the LIGO detectors in the USA [**abbott2009LIGOLaser**, **aasi2015AdvancedLIGO**] and Virgo detector in Italy [**acernese2015AdvancedVirgo**, **acernese2008StatusVirgo**].

1.3.1 Laser Interferometers

Laser interferometers use the interference of light to measure a length change with high precision. The majority of this section will focus on ground based interferometers such as LIGO and Virgo [**aasi2015AdvancedLIGO**, **acernese2015AdvancedVirgo**]. A simple design of an interferometer is shown in Fig. 1.3a. Here a laser beam is fired at a beam splitter which splits the light equally down two perpendicular arms. Each of these beams are reflected from a mirror at the end of each arm, where the light then returns to the beam splitter and the two beams are combined and sent to a photo-detector. At the output there is an interference pattern between the two beams and if the length of one of the arms is changed then the phase of one beam will be different to the other, causing the interference pattern to change. The phase difference of the light can be related to its wavelength λ_l, and the path length of the light L_{path} by

$$\Delta\phi \sim \frac{\Delta L_{\text{path}}}{\lambda_l}, \tag{1.15}$$

where $\Delta\phi$ is the phase change and ΔL_{path} is the difference in the light path lengths along each arm. By measuring this phase difference an interferometer can then measure small changes in the mirror positions.

This can be used in GW detection as the mirrors at the end of each arm of the interferometer can be treated as 'free' test masses. Figure 1.1 shows the effect of a GW on free test masses, where this can be seen by looking at the proper distance between two test masses. If we place two test masses along the x axis ($\mu = 1$) with separation L_0 and a gravitational wave is travelling along the z axis ($\mu = 3$), the proper distance between them is given by

$$L = \int_0^{L_0} \sqrt{g_{\mu\nu} dx^\mu dx^\nu} = \int_0^{L_0} \sqrt{g_{11}} dx^1, \tag{1.16}$$

where,

$$g_{11} = g_{xx} = 1 + h_{11} = 1 + h_+(t), \tag{1.17}$$

which is the combination of Eq. 1.5 and Eq. 1.10. As $h_+(t) \ll 1$, $\sqrt{g_{11}}$ can be expanded to first order, i.e. $\sqrt{g_{11}} = \sqrt{1 + h_+(t)} \approx 1 + \frac{1}{2}h_+(t)$. The proper distance is then

$$\begin{aligned} L &\approx \int_0^{L_0} 1 + \frac{1}{2}h_+(t) dx \\ &\approx L_0 + L_0 \frac{1}{2} h_+(t), \end{aligned} \tag{1.18}$$

where we use the long wavelength approximation which assumes that the wave $h(t)$ does not change considerably whilst the photon travels along the arm. From Eq. 1.18 one can see that in this configuration the plus polarisation of the GW causes the separation between

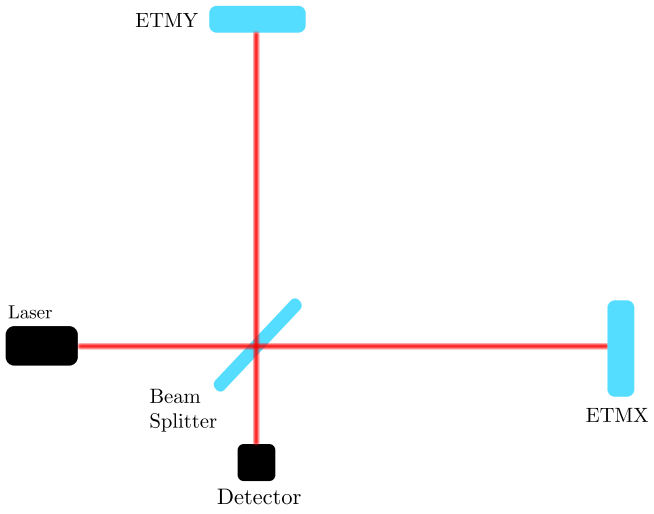

(a) Simple interferometer.

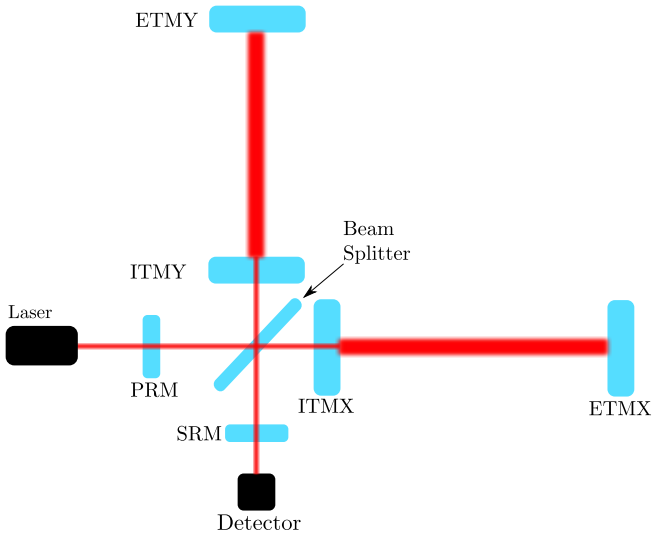

(b) Fabry-Perot interferometer.

Figure 1.3: Fig. 1.3a shows a basic interferometer. LIGO includes many additions to this interferometer to increase its sensitivity to GW, one addition known as a Fabry-Perot cavity is shown in Fig. 1.3b. End test mass Y (ETMY) and end test mass X (ETMX) refer to the mirrors at the end of the interferometer arms. Internal test mass Y (ITMY) and internal test mass X (ITMX) create a Fabry-Perot cavity in the interferometers arms causing the light to spend more time in the arm, increasing the laser power in the arm. Figure 1.3b also include the power recycling mirror (PRM) and signal recycling mirror (SRM) which increase the sensitivity of the detector.

the two test masses to oscillate [**flanagan2005BasicsGravitational**]. This oscillation can then be expressed as a fractional length change

$$\frac{\delta L}{L_0} \approx \frac{1}{2} h_+. \tag{1.19}$$

The fractional length change is then proportional to the GW.

We can generalise Eq. 1.18 slightly as in [**whelanGeometryGravitational**] by defining the proper length measured along any axis defined by the vector $\boldsymbol{v} = v^i$, where in Eq. 1.18 $v^i = (1, 0, 0)$, i.e. is along the x-axis. Using $v^i = (1, 0, 0)$, the metric perturbation component h_{11} in Eq. 1.17 can be written generally in terms Eq. 1.10

$$h_{11} = v^i h_{ij} v^j, \tag{1.20}$$

where, i, j are the spatial indices of the metric. From Eq.1.18, the length along some vector $\boldsymbol{v}$ can then be defined as

$$L_{\boldsymbol{v}} = L_0 + \frac{L_0}{2} h_{ij} v^i v^j. \tag{1.21}$$

An interferometer measures the difference in length between two arms ΔL, where we can define the arms along vector $\boldsymbol{v}$ and $\boldsymbol{u}$. We can then write the difference in arm length along these vectors as

$$\begin{aligned} \Delta L = L_{\boldsymbol{v}} - L_{\boldsymbol{u}} &= \frac{L_0}{2} \left(h_{ij} v^i v^j - h_{ij} u^i u^j \right) \\ &= L_0 \, h_{ij} \frac{v^i v^j - u^i u^j}{2} \\ &= L_0 \, h_{ij} D^{ij}, \end{aligned} \tag{1.22}$$

where D^{ij} is the detector tensor which depends on the detector's geometry [**whelanGeometryGra**
The GW strain is then the fractional difference in length of the arms

$$h(t) = \frac{\Delta L(t)}{L_0} = h_{ij}(t) D^{ij}. \tag{1.23}$$

In practice, rather than measuring the phase difference in Eq. 1.15 at the output of the detector, the two mirrors are held in position such that the two beams destructively interfere at the detector output, i.e. the interference pattern is on a dark fringe. The GW strain is then proportional to the readout of the control systems $d(f)$ which hold the mirrors at this position [**ligoscientificcollaboration2017CalibrationAdvanced**]

$$\tilde{h}(f) = T(f) \frac{d(f)}{L_0}, \tag{1.24}$$

where $T(f)$ is a transfer function which describes how the control systems affect the signal where $\Delta L = T(f)d(f)$. For more details on this see [**ligoscientificcollaboration2017Calibratio**

If one looks at Eq. 1.23 then if the mirrors at the end of the arms (ETMX and ETMY) are are placed further from the beam splitter, i.e. L_0 is increased, then in the long wavelength approximation the length change of the arms ΔL for the same GW $h(t)$ will be greater. Given that the interferometer measures ΔL, this means that increasing the length of the detectors arms increases the sensitivity of the interferometer. A method to achieve a similar affect without physically increasing the arm length is to use a Fabry-Perot cavity [**aasi2015AdvancedLIGO**], this is shown in Fig. 1.3b. This is where a semi-transparent mirror is placed between the beam splitter and end mirror in each arm (ITMX and ITMY). Light enters this cavity and reflects back and forth between the two mirrors (ITMX and ETMX) a number of times before returning to the beam splitter. This increases the time the light spends in an arm which is equivalent to increasing the arm length.

As mentioned above, the interference pattern of is held on a dark fringe, this means that when a GW is not present, the laser light will be reflected back to the input of the interferometer. By placing a mirror between the beam splitter and the input laser, this light can be reflected back into the interferometer increasing the laser power in the arms [**pitkin2011GravitationalWave**], this is known as power recycling. The increase in power improves the sensitivity of the detector by reducing the shot noise [**abbott2009LIGOLaser**] which is the statistical fluctuations associated with the discrete nature of photons. A technique which can be used to tune the detectors sensitivity to a smaller bandwidth is known as signal recycling. If a GW is incident on the detector then it will modulate the phase of the laser light causing sidebands which will be visible at the output of the detector. By placing a mirror at this output, the sideband signal is 'recycled' back into the arms increasing its signal-to-noise-ratio (SNR) [**pitkin2011GravitationalWave**]. The bandwidth over which this signal can be recycled is governed by the reflectivity of the mirror, therefore, this can improve the sensitivity of the detector to specific bandwidths.

Actual ground based GW detectors such as LIGO [**abbott2009LIGOLaser**] and Virgo [**acernese2015AdvancedVirgo**] are much more complicated than described above. They use many techniques to increase the sensitivity, some of which are outlined in [**aasi2015AdvancedLIGO**, **abbott2009LIGOLaser**]. Many of these techniques are designed to reduce non-astrophysical effects on the detector and some of these effects and solutions are listed in Sec. 1.3.1.

Detector response

The detectors are not equally sensitive to all polarisations and all locations on the sky, rather each detector has an antenna pattern which is dependent on the sky location

and the polarisation of the GW. We can find the antenna response of the detector as in [**maggioreGravitationalWaves**], by thinking about the GW in the frame of the detector. We can define the detector to be in the frame (x, y, z) with the detector arms along the x and y axes, and the source to be in the frame (x', y', z'), where the GW is travelling along $z^{'}$ and is pointing towards the detector. The axis z' then has polar coordinates θ and ϕ in the detector frame. We can determine the antenna pattern functions by first looking at the spatial components of the GW, where the h_+ and $h_\times$ polarisations are defined with respect to the (x', y', z') frame

$$h'_{ij} = \begin{pmatrix} h_+ & h_\times & 0 \\ h_\times & -h_+ & 0 \\ 0 & 0 & 0 \end{pmatrix}. \tag{1.25}$$

The frame of the source (x', y', z'), can then be transformed into the detector frame using a rotation around the z and y axes

$$\mathcal{R} = \begin{pmatrix} \cos(\phi) & \sin(\phi) & 0 \\ -\sin(\phi) & \cos(\phi) & 0 \\ 0 & 0 & 1 \end{pmatrix} \begin{pmatrix} \cos(\theta) & 0 & \sin(\theta) \\ 0 & 1 & 0 \\ -\sin(\theta) & 0 & \cos(\theta) \end{pmatrix}. \tag{1.26}$$

This rotation matrix is then applied to the GW twice as it is a tensor, i.e. $h_{ij} = \mathcal{R}_{il}\mathcal{R}_{jk}h'_{lk}$ or in matrix notation $\boldsymbol{h} = \boldsymbol{\mathcal{R}}\boldsymbol{h}'\boldsymbol{\mathcal{R}}^T$.

From Eq.1.22, we can see that the GW strain measured by the detector $h(t)$ depends on the detector tensor D_{ij}, where if we take $v^i = (1, 0, 0)$ and $u^i = (0, 1, 0)$, i.e. the detectors arms are along the x and y axes the GW strain becomes

$$h(t) = \frac{1}{2}\left(h_{11} - h_{22}\right) = \frac{1}{2}\left(h_{xx} - h_{yy}\right), \tag{1.27}$$

where we are then only interested in the h_{xx} and h_{yy} components of the GW metric [**maggioreGravitationalWaves**]. After applying the rotation tensor $\mathcal{R}$ in Eq.1.26 to the GW metric in Eq.1.25, one can look at the xx and yy component of the signal

$$\begin{aligned} h_{xx} &= \left[\cos^2(\theta)\cos^2(\phi) - \sin^2(\phi)\right] h_+ + 2\cos(\theta)\sin(\phi)\cos(\phi)h_\times \\ h_{yy} &= \left[\cos^2(\theta)\cos^2(\phi) - \cos^2(\phi)\right] h_+ - 2\cos(\theta)\sin(\phi)\cos(\phi)h_\times. \end{aligned} \tag{1.28}$$

From Eq. 1.27 we can write the GW strain as

$$\begin{aligned} h(t) &= \frac{1}{2}\left[1 + \cos^2(\theta)\right]\cos(2\phi)\, h_+(t) + \cos(\theta)\cos(2\phi)\, h_\times(t) \\ &= F_+(\theta, \phi)h_+(t) + F_\times(\theta, \phi)h_\times(t), \end{aligned} \tag{1.29}$$

where $F_+(\theta, \phi)$ and $F_\times(\theta, \phi)$ are the antenna pattern functions of the detector. This is a a measure of how sensitive the detector is to different directions and polarisations.

An example of the antenna response for a detector where the arms lie on the x and y axis is shown in Fig. 1.4. The shape of the antenna pattern is clear when thinking about

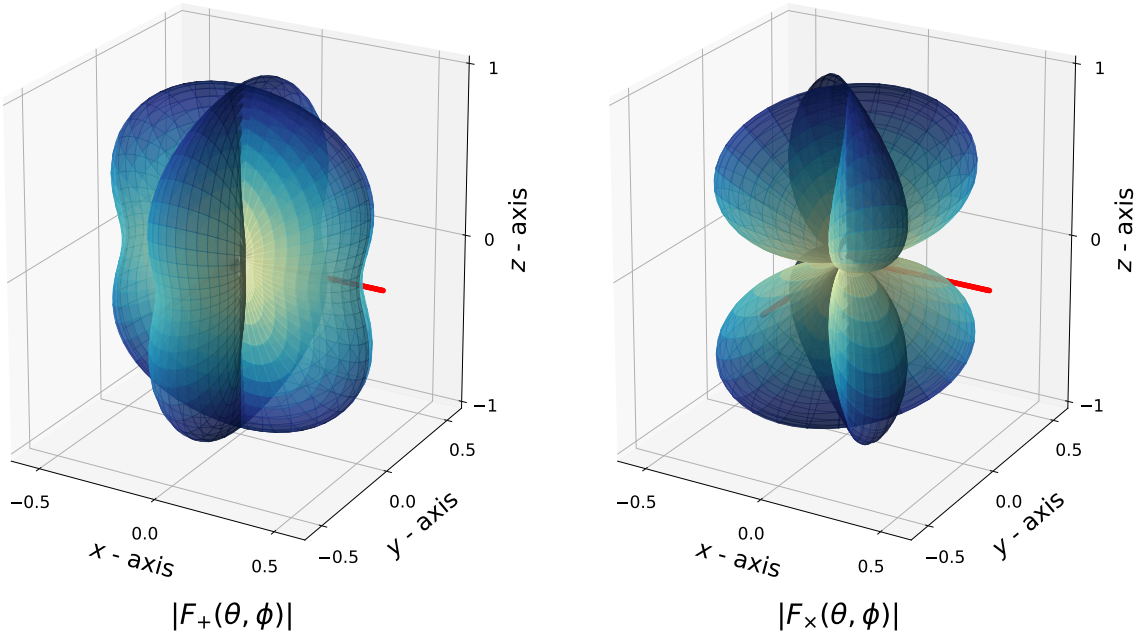

Figure 1.4: The antenna response is shown for the plus and cross polarisations $F_+(\theta, \phi, \psi = 0)$ and $F_\times(\theta, \phi, \psi = 0)$ defined in Eq. 1.29 and Eq. 1.31. The detectors arms lie on the x and y axis in the above plots.

how a gravitational wave affects the test masses as in Fig. 1.1. As the GW acts on test masses transverse to its propagation, when the detector is face on to the source, there will be a maximum change in the arm lengths and therefore a maximum sensitivity. In the same way the sensitivity will be at a minimum when edge on to the source. From some directions the GW will change the length of the arms by the same amount, in these cases $\Delta L = 0$, therefore the detector is not sensitive to any GW from that direction and this shows as the null areas in Fig. 1.4

In the above example Eq. 1.29 we have defined the detector's frame (vectors $\boldsymbol{v}$ and $\boldsymbol{u}$) orthogonal to the propagation direction of the wave where h_+ and $h_\times$ are defined. We can however, define this more arbitrarily by performing a rotation ψ, known as the polarisation angle, in the plane transverse to the direction of propagation. With respect to this rotated axes, the GW amplitudes are then defined as

$$\begin{aligned} h'_+(t) &= h_+ \cos 2\psi - h_\times \sin 2\psi \\ h'_\times(t) &= h_+ \sin 2\psi + h_\times \cos 2\psi, \end{aligned} \tag{1.30}$$

and the polarisation functions are

$$\begin{aligned} F'_+(\theta,\phi,\psi) &= \frac{1}{2}\left[1+\cos^2(\theta)\right]\cos(2\phi)\cos 2\psi + \cos(\theta)\cos(2\phi)\sin 2\psi \\ F'\times(\theta,\phi,\psi) &= \frac{1}{2}\left[1+\cos^2(\theta)\right]\cos(2\phi)\sin 2\psi + \cos(\theta)\cos(2\phi)\sin 2\psi \end{aligned} . \tag{1.31}$$

The GW strain then becomes

$$h(t) = F'_+(\theta,\phi,\psi)h'_+(t) + F'_\times(\theta,\phi,\psi)h'_\times(t), \tag{1.32}$$

which is the equivalent of Eq 1.29 where the source has been rotated around the direction of propagation by angle ψ [**maggioreGravitationalWaves**].

Noise sources

The sensitivity of the LIGO detectors is limited by the combination of noise sources within the detector, where noise sources are any effect on the output of the interferometer which is not from an astrophysical source. To increase the sensitivity of a detector, one needs to understand what causes certain noise features in the detector, and how the effect of these can be limited. There are many sources of noise which can be broadly categorised into: fundamental noise, which is what ultimately limits the design sensitivity of the detector, technical noise which originates from sources such as electronics in the control systems, and environmental noise which originates from the surrounding environment such as seismic motion [**martynov2016SensitivityAdvanced**]. Some of these noise sources and how they limit the detectors' strain sensitivity are shown in Fig. 1.5 from [**aasi2015AdvancedLIGO**], where in general, different noise sources affect different areas of the frequency spectrum.

Here I will summarise some of the limiting sources and also sources which become useful for understanding later sections.

Seismic noise This originates from vibrations in the Earth which can be from effects such as the Earth's seismic activity or anthropogenic sources, where this affects frequencies $\lesssim 20$ Hz in the LIGOs spectrum. The oscillations originate from a range of sources including earthquakes, ocean waves and traffic on nearby roads. They cause the mirrors to oscillate and induce a change in the length of the arms and therefore a change in the GW readout channel. At the LIGO sites, this causes the ground to move by about 10^{-9} m/$\sqrt{\text{Hz}}$ at 10 Hz [**martynov2016SensitivityAdvanced**], which is orders of magnitude above the detectors design sensitivity. This is reduced by having multi-stage suspensions in the detectors which both actively and passively filter out the majority of seismic oscillations [**matichard2015SeismicIsolation**].

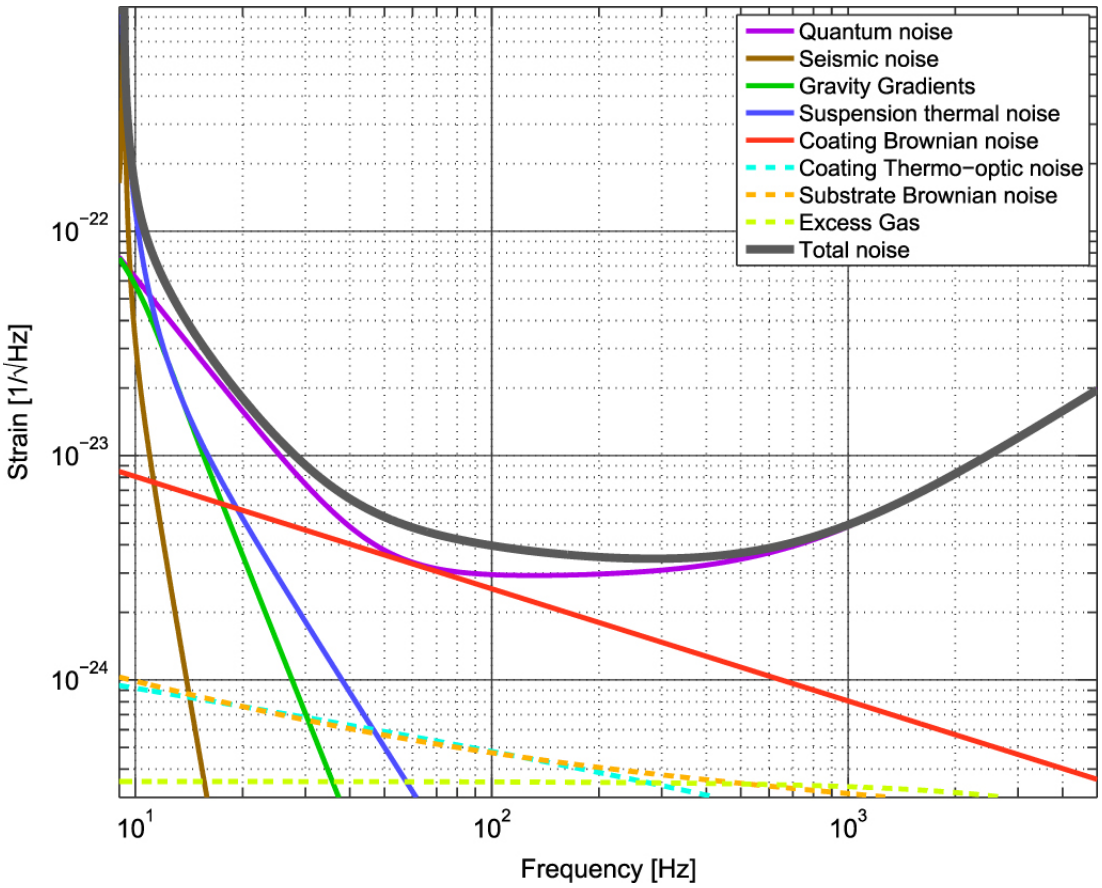

Figure 1.5: The different noise sources affect the sensitivity of the advanced LIGO detectors at different frequencies, this figure shows a subset of the noise sources and how they limit the strain sensitivity of the detector [**aasi2015AdvancedLIGO**].

Thermal noise This originates from mechanical systems where thermal motion can be transferred (coupled) into the measurement of the displacement of the test mass. There are a number of sources of this including the suspension thermal noise and the Brownian noise in the mirror coatings. The suspension thermal noise causes the test masses to move due to the thermal vibrations of the fibres suspending the test masses [**gonzalez2007HandbookApproximation**]. The spectral density of the thermal motion of the mass can be written as in [**pitkin2011GravitationalWave**]

$$x^2(\omega) = \frac{4k_{\mathrm{B}}T}{m\omega}\frac{\omega_0^2\phi(\omega)}{(\omega_0^2-\omega^2)^2+\omega_0^4\phi^2(\omega)}, \tag{1.33}$$

where k_{B} is the Boltzmann constant, T is the temperature, m is the mass and $\phi(\omega)$ is the loss angle of the oscillator. This is generally reduced by using low loss materials such that the displacement noise reduced off the resonance frequency of the suspension [**hammond2012ReducingSuspension**]. The coating Brownian noise is from thermal fluctuations in the layers of optical coatings in the test masses [**martynov2016SensitivityAdvanced**]. These effects are limited by using differ-

ent coatings on the mirrors [**abernathy0OverviewResearch**, **martin2008Measurements**

Quantum noise Quantum noise originates from two main mechanisms: the shot noise associated with the statistical uncertainty of the arrival time of photons at detector output, and the fluctuation in the radiation pressure noise associated with the momentum that photons transfer to the test masses [**aasi2013EnhancedSensitivity**]. The strain sensitivity limited by shot noise is defined in [**abbott2009LIGOLaser**] as

$$h(f) = \sqrt{\frac{\pi\hbar\lambda}{Pc}}\frac{\sqrt{1+(4\pi f\tau_s)^2}}{4\pi\tau_s}, \tag{1.34}$$

where P is the power of the laser, λ is the wavelength of the laser, f is the GW frequency, $\hbar$ is Planck's constant and τ_s is the arm cavity storage time. One can see from this that the shot noise decreases as the laser power increases, which is a reason for the power recycling cavity described in Sec. 1.3.1. In [**pitkin2011GravitationalWave**] the fluctuation in the radiation pressure noise is defined to cause a displacement

$$\delta x^2(\omega) = \frac{4Ph}{m^2\omega^4 c\lambda}, \tag{1.35}$$

where ω is the angular frequency and m is the test mass. One can see from this that by using larger test masses the radiation pressure noise is reduced. Radiation pressure noise and shot noise are then a fundamental limit of the detectors sensitivity; as shot noise decreases with laser power the radiation pressure noise increases. However, there are methods which 'cheat' this limit to reduce the noise, for example using squeezed states of light [**aasi2013EnhancedSensitivity**].

Technical noise Whilst this is not shown in Fig. 1.5, particular types of technical noise become important to searches described Chapter 3, 4 and 6. An example of this is the noise generated by the digital and analogue electronics that are used to measure the GW signal and control the complex detector system [**martynov2016SensitivityAdvanced**] Any fluctuations in the control system electronics can be transferred (coupled) into the measurement of the displacement of the test masses. If some electronics have a periodic fluctuation which affects the displacement measurement, then this will show up as a narrow peak in the frequency spectrum. These narrow spectral lines are the topic of discussion in Chapter 6.

There are also many other sources of noise including those from fluctuations in the laser frequency and amplitude, jitter noise which is caused by motion of the mirrors that steer the laser, and Newtonian noise where variations in the density of matter surrounding the test mass changes the gravitational gradient [**martynov2016SensitivityAdvanced**]. For more discussion and detail of these noise sources and others see [**martynov2016SensitivityAdvan**

aasi2015AdvancedLIGO, **aasi2015CharacterizationLIGO**]. For the majority of this thesis, noise sources which cause narrowband spectral artefacts known as instrumental lines provide the biggest challenge. In Sec. 6 I will go into more detail about these noise sources and how they can be monitored and potentially removed.

Chapter 2

Searching for continuous gravitational waves

CWs have particular challenges when it comes to their detection. CWs are long duration, this means that they would be observed for the entirety of a detector's observing run. The signals also have an intrinsically small amplitude which is below the noise floor of current ground based detectors such as LIGO. This means that for a detection, the entire observing run's data will be needed to accumulate enough SNR for a signal to be observed. Given that LIGO samples at $\sim$ 16 kHz (generally downsampled to $\sim$ 4 kHz) this leaves a huge amount of data ($\mathcal{O}(2)$ TB for one year at 16kHz) which needs to be searched through. As will be described in Sec. 2.3, this means that a large amount of computational resources is required to perform a search for CW. For some types of search the parameter space can also be very large, this only adds to the computational time and in some cases makes the search infeasible.

Whilst I have described the potential sources a CW signal and its approximate signal type in Sec. 1.2.4, to perform a search we need to understand the intrinsic waveform of the signal and the observed waveform at a detector. In Sec. 2.1 we will go into more detail on the CW signal model. In Sec. 2.2.2 we introduce Bayesian techniques which are used in many analyses. The CW signal model and Bayesian techniques are then used in various search methods for CW signals, where I will overview a subset of current searches in Sec. 2.3.

2.1 Continuous signal model

The model of a GW signal from a rapidly rotating neutron star is relatively simple, it is intrinsically a quasi-sinusoidal signal, meaning that it is a sinusoid with a slowly varying frequency. This indicates that as the neutron star's rotational frequency decreases (spins down) it is losing energy. The rate at which the star loses energy is generally characterised

by the braking index defined by

$$n = \frac{f_{\rm rot}\ddot{f}_{\rm rot}}{\dot{f}_{\rm rot}^{\,2}}, \tag{2.1}$$

where $f_{\rm rot}$ is the rotational frequency of the neutron star [**dearaujo2016GravitationalWaves**]. There are a number of potential reasons for the spin down, including: the energy loss to GWs, which should have a braking index of 5 [**dearaujo2016GravitationalWaves**] and magnetic braking which gives a braking index of 3 [**dearaujo2016GravitationalWaves**].

The parameters of each neutron star can be split into two sections: the Doppler components $(\alpha, \delta, \boldsymbol{f})$ and its amplitude components $(\psi, \phi_0, \iota, h_0, \theta)$. This ignores any orbital parameters which would be present if the star was in a binary system. The Doppler parameters are defined as follows: the sky positions α and δ refer to the right ascension and declination of the source. The frequency $\boldsymbol{f}$ refers to the GW source frequency and its spin derivatives. The parameters ψ, ϕ_0 and h_0 are the GW polarisation, initial phase and amplitude respectively. The inclination angle ι is the angle between a vector pointing towards the source and the rotation axis of the source. Finally, θ is the 'wobble angle' or the angle between the rotation axis and the symmetry axis of the neutron star.

The definition of the GW from a neutron star given here follows that in [**riles2017RecentSearc schutz1998DataAnalysis**, **dupuis2005BayesianEstimation**]. The amplitude of the GW is defined in Eq. 1.32, however I will redefine it here

$$h(t) = F_+ h_+(t) + F_\times h_\times(t), \tag{2.2}$$

where $h_+, h_\times$ are the plus and cross polarisation functions as defined in Eq.1.10, and $F_+, F_\times$ are the antenna pattern functions defined in Eq.1.4. The plus and cross polarisation functions are defined by

$$\begin{aligned} h_+(t) &= h_0 \frac{1 + \cos^2(\iota)}{2} \cos(\Phi(t)) \\ h_\times(t) &= h_0 \cos(\iota) \sin(\Phi(t)), \end{aligned} \tag{2.3}$$

where h_0 is the GW amplitude, ι is the inclination angle of the source and $\Phi(t)$ is the phase of the GW. Here we assume that the wobble angle θ is small, however this assumption is accounted for in the derivation in [**schutz1998DataAnalysis**]. The phase of the wave $\Phi(t_{\rm SSB})$ at the solar system barycenter (SSB) can be defined as

$$\Phi(t_{\rm SSB}) = \phi_0 + 2\pi \left[f_0(t_{\rm SSB} - t_0) + \frac{1}{2}\dot{f}_0(t_{\rm SSB} - t_0)^2 + ... \right]. \tag{2.4}$$

This consists of an initial phase ϕ_0 which is the phase at time t_0, the frequency of the GW signal f_0 and its derivative $\dot{f}$ measured at time t_0. The time at the SSB $t_{\rm SSB}$ can be

transformed to the time t at the detector by

$$t_{\mathrm{SSB}} = t + \frac{\mathbf{r}_d \cdot \mathbf{n}}{c} + \delta_t, \tag{2.5}$$

where c is the speed of light, $\mathbf{r}_d$ is the position of the detector with reference to the SSB, $\mathbf{n}$ is a unit vector in the direction of the source. The factor $\mathbf{r}_d \cdot \mathbf{n}/c$ takes into account the Doppler shift of the signal due to the movement of the detector, i.e. as the earth rotates on its axis and orbits the sun. The factor δ_t take into account extra corrections from the Einstein and Shapiro delay [**taylor1992PulsarTiming**]. Shapiro delay originates from the extra time a signal takes to pass through a gravitational potential, for example the Sun's. Einstein delay accounts for the time dilation of the moving observer or pulsar and the gravitational redshift due to the Sun or a companion star. The amplitude h_0 in Eq. 2.3 is defined by

$$h_0 = \frac{4\pi^2 G}{c^4}\frac{\epsilon I_{zz} f^2}{r}, \tag{2.6}$$

where G is the gravitational constant, ϵ is the ellipticity of the star, f is the GW frequency, r is the distance to the star and I_{zz} is the moment of inertia with respect to the rotation axis z. The ellipticity ϵ is a measure of the distortion of the star around its rotation axis and is defined in Eq. 1.14, however I will redefine it here

$$\epsilon = \frac{I_{xx} - I_{yy}}{I_{zz}}, \tag{2.7}$$

where I_{xx}, I_{yy} and I_{zz} are the moments of inertia for each axis.

In Eq. 2.2, $F_+(t)$ and $F_\times(t)$ are the antenna pattern functions of the detector. These describe how sensitive a detector is to a particular location on the sky and are derived in Sec. 1.3.1 where the response to sky location is shown in Fig. 1.4. In [**schutz1998DataAnalysis**] these are defined more completely

$$\begin{aligned} F_+(t) &= \sin\zeta[a(t)\cos(2\psi) + b(t)\sin(2\psi)], \\ F_\times(t) &= \sin\zeta[b(t)\cos(2\psi) - a(t)\sin(2\psi)], \end{aligned} \tag{2.8}$$

where ζ is the angle between the arms of the detectors, ψ is the polarisation angle of the GW and $a(t)$ and $b(t)$ are defined in [**schutz1998DataAnalysis**] and relate the sky location to the orientation of the detector at a given time. A full derivation of the terms $a(t)$ and $b(t)$ in Eq. 2.8 can be found in [**schutz1998DataAnalysis**]. Equations 2.2 - 2.8 then describe the amplitude and phase evolution of a signal at a given detector location and orientation.

2.2 Bayes Theorem

A key part in understanding the different methods used to search for GWs or many other data analysis problems, is understanding probability and statistics. This gives us understanding of the random processes underlying all measured quantities. Whilst there are generally two approaches to statistics: Frequentist and Bayesian, here I will focus on the Bayesian approach.

2.2.1 Basic probability

Initially I will define some basic concepts of probability. We can define the probability of some event A as $p(A)$ where probabilities lie in the range $0 \leq p(A) \leq 1$ and some other event B which has a probability $p(B)$ and which lies in the range $0 \leq p(B) \leq 1$.

Union A union is the probability of either event A happening or event B happening. This is written as, $p(A \cup B)$.

Intersection An intersection is then the probability that both an event A and an event B happens. This is written as $p(A \cap B)$.

Independent and dependent Events If the event A is dependent on event B, i.e. the event A affects event B or vice versa, then the joint probability of both events is

$$p(A \cap B) = p(A)p(B \mid A) = p(B)p(A \mid B). \tag{2.9}$$

Here $p(B \mid A)$ means the probability of event B given an event A. However, if the events A and B are independent, i.e. the event A does not affect the outcome of event B, then

$$p(A \cap B) = p(A)p(B). \tag{2.10}$$

Conditional probability Conditional probability arises from situations where one event A affects the event B. The definition of this arises from the the dependent events defined above in Eq. 2.9

$$p(A \mid B) = \frac{p(A \cap B)}{p(B)}. \tag{2.11}$$

Bayes Theorem Bayes theorem can then be defined using conditional probabilities. i.e we can use

$$p(A \mid B) = \frac{p(A \cap B)}{p(B)} \quad \text{and} \quad \mathrm{p(B \mid A)} = \frac{\mathrm{p(A \cap B)}}{\mathrm{p(A)}} \tag{2.12}$$

such that

$$p(B)p(A \mid B) = p(A)p(B \mid A) \tag{2.13}$$

and this is rearranged to Bayes theorem

$$p(A \mid B) = \frac{p(A)p(B \mid A)}{p(B)} \tag{2.14}$$

2.2.2 Bayesian Inference

We can take Bayes theorem from Sec. 2.2.1 and apply it to a problem which involves inferring the parameters from some model. Here we can relabel the events A and B with the data $\boldsymbol{d}$ and the parameters $\boldsymbol{\theta}$ of some model I. Equation 2.14 then becomes

$$p(\boldsymbol{\theta} \mid \boldsymbol{d}, I) = \frac{p(\boldsymbol{\theta}, I)p(\boldsymbol{d} \mid \boldsymbol{\theta}, I)}{p(\boldsymbol{d} \mid I)} \tag{2.15}$$

where each of the components are assigned names: $p(\boldsymbol{\theta} \mid \boldsymbol{d})$ is the posterior distribution, $p(\boldsymbol{\theta})$ is the prior distribution, $p(\boldsymbol{d} \mid \boldsymbol{\theta})$ is the likelihood, and $p(\boldsymbol{d})$ is the Bayesian Evidence.

Posterior The posterior distribution describes the probability of a parameter $\boldsymbol{\theta}$ in some model I given some data $\boldsymbol{d}$. For many problems this is the distribution which is most useful as it informs you how likely any set of parameters from your model are given some observation.

Prior The Prior distribution is a key part of Bayesian statistics which describes the distribution of the parameters $\boldsymbol{\theta}$ given the model I. This should reflect any beliefs about the parameters $\boldsymbol{\theta}$ prior to the observations.

Likelihood The likelihood is where the observation is included in the calculation. This tells you how probable it is to get the observed data $\boldsymbol{d}$ given the model I with the set of parameters $\boldsymbol{\theta}$.

Bayesian Evidence This is the probability of the data itself given the choice of model. This is found by integrating the likelihood over all possible values of $\boldsymbol{\theta}$ weighting them by our prior belief of that value of $\boldsymbol{\theta}$. This is also known as the marginal likelihood and is defined by,

$$p(\boldsymbol{d} \mid I) = \int p(\boldsymbol{\theta}, I)p(\boldsymbol{d} \mid \boldsymbol{\theta}, I)d\boldsymbol{\theta}. \tag{2.16}$$

Bayes theorem then gives a description of the probability distribution of some parameters in a model given some observation. Often when using Bayesian statistics the aim is to find the posterior distribution of parameters. There are very few cases where this can be calculated analytically, therefore, numerical methods are often used to find the posterior. This can be difficult to calculate numerically especially in problems where the parameter

space has many dimensions. The most difficult part to calculate is the Bayesian Evidence in Eq. 2.16 which involves calculating an integral over all possible parameters. However, if you are only interested in the posterior there is a way around having to calculate this. For any given model I, the Bayesian Evidence $p(\boldsymbol{d} \mid I)$ is independent of any parameters $\boldsymbol{\theta}$ in Eq. 2.15 and depends only on the model I. The Bayesian Evidence is then just a normalisation factor for the posterior distribution. When different models are not being compared, and we assume the model I to be true, we no longer need to calculate the Bayesian Evidence. The un-normalised posterior distribution

$$p(\boldsymbol{\theta} \mid \boldsymbol{d}, I) \propto p(\boldsymbol{\theta}, I)p(\boldsymbol{d} \mid \boldsymbol{\theta}, I) \tag{2.17}$$

can then be found by a method known as 'sampling'.

Sampling

Sampling a distribution, say the posterior $p(\boldsymbol{\theta} \mid \boldsymbol{d})$, means choosing a value (or sample) of the parameters $\boldsymbol{\theta}$ such that if we chose many independent samples of $\boldsymbol{\theta}$ the number within any range $\boldsymbol{\theta} \rightarrow \boldsymbol{\theta} + \delta\boldsymbol{\theta}$ is proportional to the height of the distribution $p(\boldsymbol{\theta} \mid \boldsymbol{d})$. One technique, known as rejection sampling, offers an intuitive way to understand what it means to generate samples from a distribution, where in this example I will assume a one dimensional distribution $p(\theta \mid \boldsymbol{d})$ for simplicity. One can, for example, uniformly generate random samples in a two dimensional space, where each sample has a value of θ_i and p_i as represented by the points in the first panel of Fig. 2.1. For this method the values of p_i here need to have a maximum value at least equal to the maximum of $p(\theta \mid \boldsymbol{d})$. In this example we know the exact posterior distribution $p(\theta \mid \boldsymbol{d})$ and therefore can plot it over these points. For each of these points, we can calculate the height of the distribution $p(\theta_i \mid \boldsymbol{d})$, where values of θ which give $p_i > p(\theta_i, \mid \boldsymbol{d})$ are assumed to not be part of the distribution and ignored. The values of θ where $p_i < p(\theta_i \mid \boldsymbol{d})$ are then assumed to be sampled from the distribution $p(\theta \mid \boldsymbol{d})$. One can see this is true from Fig. 2.1, in any range $\theta \rightarrow \theta + \delta\theta$ the density of accepted points (ones which fall below the $p(\theta \mid \boldsymbol{d})$ curve) is proportional to the height of $p(\theta \mid \boldsymbol{d})$. By taking the histogram of samples θ, we find the density of the samples in a given $\theta \rightarrow \theta + \delta\theta$ and therefore a distribution which is proportional to $p(\theta \mid \boldsymbol{d})$ as shown in Fig. 2.1

Whilst this method provides an easy way to understand sampling a distribution, it is computationally inefficient. For example, it is often the case that the posterior distribution $p(\theta \mid \boldsymbol{d})$ is narrow and covers a small area of parameter space, this method would then discard many more samples than it accepts, wasting computational time calculating the posterior value at these points. When there are a larger number of parameters $\{\theta^{(1)}, \theta^{(2)}, ...\}$, rejection sampling can quickly become impractical due to the computational time required

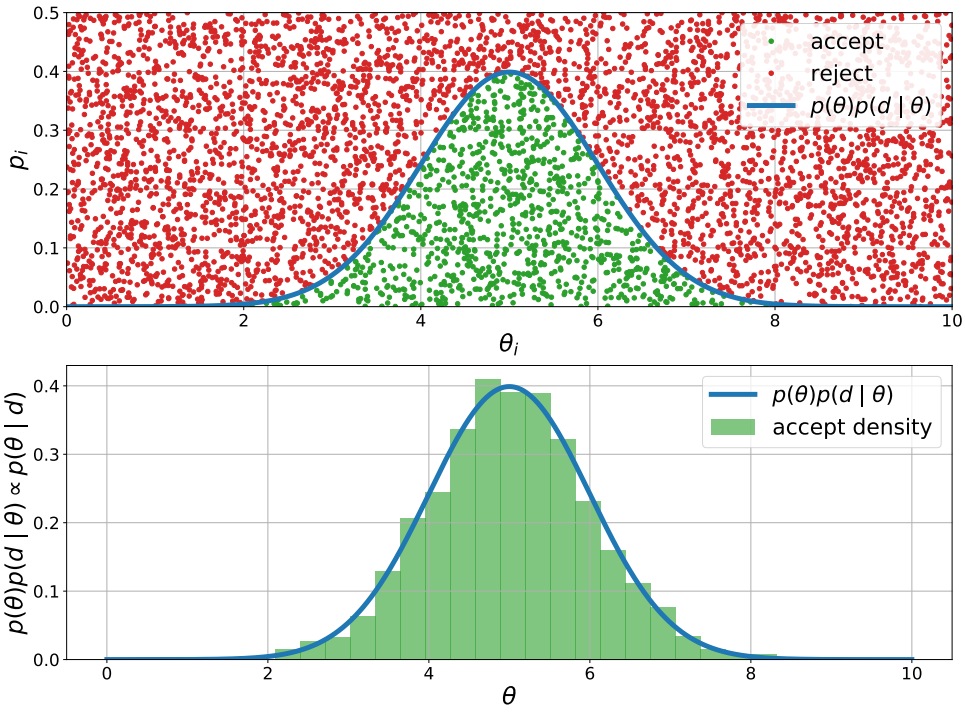

Figure 2.1: Example of rejection sampling applied to a simple one dimensional Gaussian distribution. To top panel shows a number of samples (θ_i, p_i) with the distribution $p(\theta)p(\boldsymbol{d} \mid \theta)$ which is proportional to the true posterior $p(\theta \mid \boldsymbol{d})$ overlaid. The green samples are accepted and red samples are rejected. The bottom panel shows a histogram of the accepted samples, where each bin contains the density of points in the range $\theta \to \theta + \delta\theta$.

to estimate the posterior distribution of those parameters $p(\theta^{(1)}, \theta^{(2)}, ... \mid \boldsymbol{d})$. There are however other techniques which have been developed which can sample the posterior distribution more efficiently.

MCMC

As described in Sec. 2.2.2, rejection sampling is an inefficient method to sample from a posterior distribution, especially if the posterior is located in a small region of parameter space. Therefore, another sampling method titled Markov-Chain Monte Carlo (MCMC) can be used which concentrates the samples around areas of high probability, approximating the posterior distribution more efficiently. More information on this technique can be found in [**metropolis1953EquationState**, **vanravenzwaaij2018SimpleIntroduction**, **sharma2017M**
Rather than calculating the posterior for many independent locations in parameter space, an MCMC algorithm randomly wanders around in parameter space such that the amount of time spent in any location is proportional to the height of the posterior distribution. An example of a simple MCMC algorithm can be seen in Alg. 2.1.

An MCMC algorithm builds up samples from the posterior distribution by using a Markov chain, where each step in the chain only depends on the previous step. It starts

by calculating the posterior value for a particular point in parameter space. Then it will randomly jump to another point parameter space, where a new value for the posterior can be calculated. The size of the 'jump' is defined by a proposal distribution (usually a Gaussian), which makes it difficult to jump to a value far away from the current value. If the new posterior value is higher than the previous step then the jump is 'accepted', which means that the parameter values of this point are assumed to be from the posterior distribution and are recorded. If the posterior value is lower than the previous step then the jump is accepted with a probability which is the ratio of the probabilities at the new and old locations. The probability of acceptance can be written as

$$p_{\text{accept}} = \begin{cases} \frac{p(\theta_i|\boldsymbol{d})}{p(\theta_{i-1}|\boldsymbol{d})} & \text{if } p(\theta_i \mid \boldsymbol{d}) < p(\theta_{i-1} \mid \boldsymbol{d}) \\ 1 & \text{if } p(\theta_i \mid \boldsymbol{d}) \geq p(\theta_{i-1} \mid \boldsymbol{d}) \end{cases}, \tag{2.18}$$

where $p(\theta_i \mid \boldsymbol{d})$ is the posterior value at the current parameter location and $p(\theta_{i-1} \mid \boldsymbol{d})$ is the posterior value at the previous parameter location. This means that the accepted positions are located around areas of high posterior values; the MCMC algorithm does not waste time calculating the posterior in uninteresting areas of parameter space. One can see this correctly samples the posterior distribution by thinking about the condition in Eq. 2.18. Say we only allow jumps between two locations in parameter space, one which corresponds to the maximum of the posterior and one at half of this value. If we start at the maximum, the probability of accepting the jump to the parameter with half the value of the posterior is 0.5. Repeating this many times would mean that the chain would jump to the lower value half the time, and therefore have half the samples at the parameter which is at half the maximum of the posterior. The accepted samples then have a density proportional to the posterior distribution.

Nested Sampling

In Bayesian inference it is often useful to compare different models or hypotheses to gain insight into which is more likely. One can do this by using the Odds ratio

$$O = \frac{p(I_1 \mid \boldsymbol{d})}{p(I_2 \mid \boldsymbol{d})} = \frac{p(I_1)}{p(I_2)} \frac{p(\boldsymbol{d} \mid I_1)}{p(\boldsymbol{d} \mid I_2)} = \text{prior odds} \times \text{bayes factor}, \tag{2.19}$$

where the bayes factor compares the marginal likelihood of one model $p(\boldsymbol{d} \mid I_1)$ to the marginal likelihood of another $p(\boldsymbol{d} \mid I_2)$ and describes the evidence in favour of one model over the other and the prior odds reflects the relative belief of I_1 over I_2 prior to any observation **JOE: reread this**. This requires the calculation of the Bayesian Evidence in Eq. 2.16, which traditionally is very difficult to calculate as it is an integral over the entire parameter space. To calculate this, a method known as nested sampling was developed

Input: N {Chain length}
Output: S {Samples}

Initialisation: θ_0
for Sample, $i = 1 \rightarrow N$ **do**
  $\theta_i = \theta_{i-1} + f$
  if $p(\theta_i \mid \boldsymbol{d}) > p(\theta_{i-1} \mid \boldsymbol{d})$ **then**
    $S_i = \theta_i$
  else
    if $\frac{p(\theta_i|\boldsymbol{d})}{p(\theta_{i-1}|\boldsymbol{d})} < U(0,1)$ **then**
      $S_i = \theta_i$
    else
      $S_i = \theta_{i-1}$
    end if
  end if
end for

ALGORITHM 2.1: This is a basic pseudo MCMC algorithm, where we draw samples θ_i from the posterior distribution $p(\theta_i \mid \boldsymbol{d})$. Here f is some distribution (often a Gaussian) which describes the jump to the new point in parameter space and $U(0,1)$ is a values drawn from a uniform distribution between 0 and 1. This algorithm returns a set of samples S from the posterior distribution $p(\theta_i \mid \boldsymbol{d})$.

[**skilling2006NestedSampling**, **speagle2019DynestyDynamic**]. In nested sampling, rather than directly sampling from the posterior as in MCMC, the posterior is broken into 'slices' where samples are generated from each 'slice'. The posterior is reconstructed by combining the samples using weights associated with each slice. The idea is to transform the integral for the Bayesian Evidence such that it is no longer multidimensional. This is done by using the prior mass, defined by

$$X(\lambda) = \int_{\theta:\mathcal{L}(\theta)>\lambda} \pi(\theta) d\theta, \tag{2.20}$$

where $\pi(\theta) = p(\theta \mid I)$ is the prior and $\mathcal{L}(\theta) = p(\boldsymbol{d} \mid \theta, I)$ is the likelihood. This is the amount of the prior where the likelihood $\mathcal{L}(\theta)$ is greater than some value λ. The Bayesian Evidence is then defined as

$$Z = p(\boldsymbol{d} \mid I) = \int \mathcal{L}(\theta)\pi(\theta) d\theta = \int_0^1 \mathcal{L}(X) dX, \tag{2.21}$$

where $\mathcal{L}(X)$ is the value of the likelihood where $P(\mathcal{L}(\theta) > \lambda) = X$. One can find how we can get to this integral in Appendix B. The integral for the Bayesian Evidence has then been transformed to a one dimensional integral between 0 and 1 over the prior mass rather than a potentially multidimensional integral over θ.

In Fig. 2.2 the prior mass is shown for a given value of λ as the blue shaded area in the first panel, where this area is the amount of the prior in areas of parameter space where $\mathcal{L}(\theta) > \lambda$. One can then see that when $\lambda = 0$ the prior mass must be one, and as $\lambda \to \infty$ the prior mass must approach zero. The bottom right panel of Fig. 2.2 shows the equivalent plot where as the prior mass decreases, the value of the likelihood at that prior mass increases. The two representations of the Bayesian Evidence defined in Eq. 2.21 can then be seen as the integral of the lower two panels in Fig. 2.2 respectively, where the shaded regions represent Z.

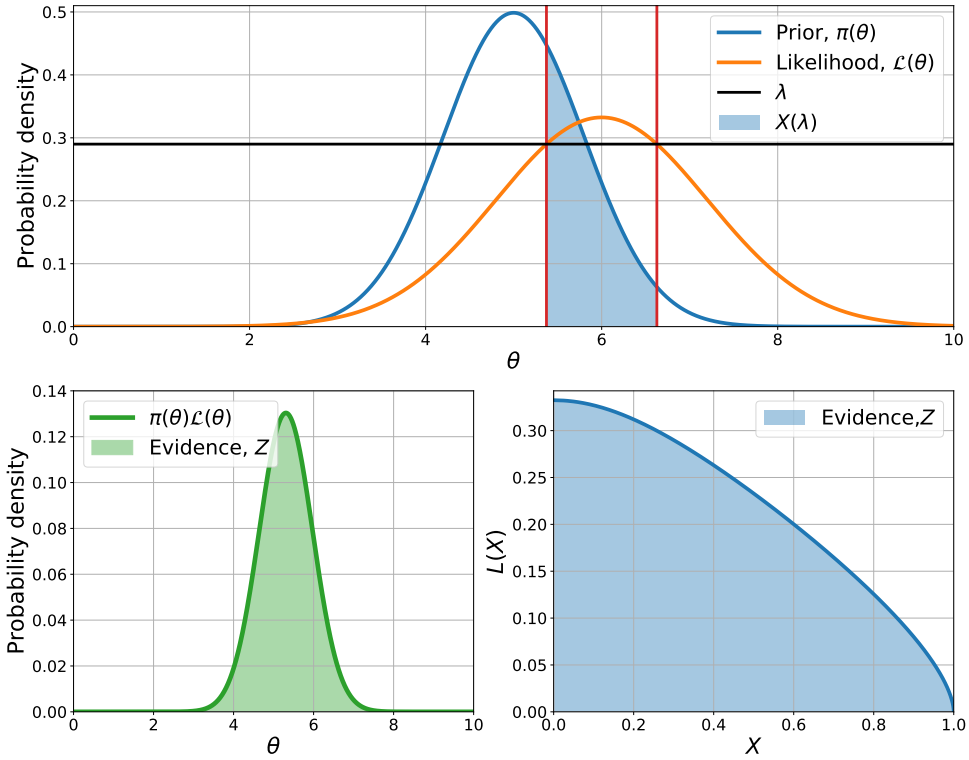

Figure 2.2: An example of a prior distribution and a likelihood are shown in the top panel for a 1D distribution, where the prior mass $X(\lambda)$ is the shaded region for a given λ defined in Eq. 2.20. The black horizontal line in the top panel represents the value of λ which increases from zero to the maximum of the likelihood, where corresponding values of the likelihood $\mathcal{L}$ and prior mass $X(\lambda)$ for each λ are used to calculate the evidence in Eq. 2.21. The bottom left panel then shows $\pi(\theta)\mathcal{L}(\theta)$, where the integral of this defined in Eq. 2.21 is the Evidence Z. The bottom right panel shows the likelihood as a function of prior mass which for any number of parameters is a 1D integral, where again the integral of this is the Evidence in Eq. 2.21.

If the form of $\mathcal{L}(X)$ is known, then the Evidence could be approximated numerically by evaluating $\mathcal{L}_i = \mathcal{L}(X_i)$ for a number of values of the prior mass $0 < X_M < ... < X_1 < X_0 = 1$ such that

$$Z \approx \hat{Z} = \sum_{i=1}^{M} \mathcal{L}_i \left[X_{i-1} - X_i\right]. \tag{2.22}$$

This would just be summing the area in columns under the curve in the bottom right panel of Fig. 2.2, however $\mathcal{L}(X)$ is typically not known.

Nested sampling algorithms instead estimate Z by drawing samples from the constrained prior mass as described in Alg. 2.2. One could take N_{live} samples (or live points) of θ from the prior distribution $\pi(\theta)$, then calculate the minimum value of the likelihood for these values $\mathcal{L}_{\text{min}}$ and save the values of the parameters θ_{min} associated with this likelihood. The sample θ_{min} can then be replaced with a new sample from the prior distribution with the constraint that $\mathcal{L}(\theta) > \mathcal{L}_{\text{min}}$. This process can then be repeated a number M times. This then records samples θ_{min} after each step such that the values of $\mathcal{L}_{\text{min}}$ are increasing, and therefore X is decreasing

$$0 < X_M < ... < X_1 < X_0 = 1. \tag{2.23}$$

The values of $\mathcal{L}_{\text{min}}$ can then be used with Eq. 2.22 to approximate the evidence, where the prior mass would be calculated for each step $X_i = P(\mathcal{L}(\theta) > \mathcal{L}_{\text{min,i}})$. However, we can notice that the value of the prior mass shrinks at each step following $X_i = t_i X_{i-1}$, where t_i follows the probability distribution of the maximum value of N_{live} samples from $U(0,1)$, i.e. $p(t) = N_{\text{live}} t^{N_{\text{live}}-1}$. Therefore, rather than calculating the prior pass at each stage, we can assume the prior mass is a random variable, where after each iteration it shrinks by the expectation value of t_i

$$E[t_i] \approx \exp\left(-\frac{i}{N_{\text{live}}}\right), \tag{2.24}$$

and then after each step we can set $X_i = E[t_i] X_{i-1}$ [**feroz2019ImportanceNested**]. This tells us that using this algorithm the log-prior mass shrinks by a factor $\sim -1/N_{\text{live}}$ after each iteration [**speagle2019DynestyDynamic**].

The integral in Eq. 2.21 can then be approximated using Eq. 2.22,

$$Z = \int_0^1 \mathcal{L}(X) dX \approx \sum_{i=1}^{M} \mathcal{L}(\theta_i) \left[X_{i-1} - X_i\right] = \sum_{i=1}^{M} p(\theta_i), \tag{2.25}$$

where M is the number of iterations in Alg. 2.2, $p(\theta_i)$ is the importance weight defined as $p(\theta_i) = \mathcal{L}(\theta_i)\left[X_{i-1} - X_i\right]$. The likelihood value $\mathcal{L}(\theta_i)$ is calculated for each dead point D_i with its associated change in prior mass $\Delta X = [X_{i-1} - X_i] \approx -1/N_{\text{live}}$. This then gives an estimate of the Bayesian Evidence, for more details on this and some simple examples see [**skilling2006NestedSampling**, **speagle2019DynestyDynamic**, **feroz2019ImportanceNested**].

Nested sampling also provides an estimate of the posterior distribution as well as the

Draw N_{live} "live" points $\{\theta_{n=1}, ...\theta_{N_{\text{live}}}\}$ from the prior $\pi(\theta)$ {Samples from the prior distribution}
initialise: D {initialise a list to store samples}
initialise: $Z = 0$ {Initialise the Evidence calculation}
initialise: $i = 0$

while stopping criterion not met **do**
    $\mathcal{L}^{\text{min}} = \min\{\mathcal{L}(\theta_1), ...\mathcal{L}(\theta_{\text{N}_{\text{live}}})\}$ {find minimum likelihood values for all live points}
    $D_i = \theta_n$ {add the nth live point θ_n associated with $\mathcal{L}^{\text{min}}$ to list of 'dead' points D.}
    draw θ_{new} from constrained prior where $\mathcal{L}(\theta_{\text{new}}) > \mathcal{L}^{\text{min}}$
    $\theta_n = \theta_{\text{new}}$
    $Z = Z + \mathcal{L}^{\text{min}}\Delta X$ {add point to the sum of the Evidence as Eq. 2.25}
    Evaluate stopping criterion
    $i = i + 1$
end while

Estimate the final part of the prior volume from remaining live points.
while $N_{\text{live}} > 0$ **do**
    $\mathcal{L}^{\text{min}} = \min\{\mathcal{L}(\theta_1), ...\mathcal{L}(\theta_{\text{N}_{\text{live}}})\}$ {compute minimum likelihood of current live points}
    $D_i = \theta_n$ {add the live point θ_n associated with $\mathcal{L}^{\text{min}}$ to list of 'dead' points D.}
    remove θ_n
    $N_{\text{live}} = N_{\text{live}} - 1$
end while

ALGORITHM 2.2: Nested sampling algorithm from [**speagle2019DynestyDynamic**]. This describes how the evidence integral in Eq. 2.21 can be approximated by sampling over increasingly smaller prior masses.

Bayesian Evidence from the set of samples (dead points)

$$p(\theta \mid \boldsymbol{d}, I) \approx \frac{\sum_{i=1}^{M} p(\theta_i)\delta(\theta - \theta_i)}{\sum_{i=1}^{M} p(\theta_i)}. \tag{2.26}$$

where $\delta(\theta - \theta_i)$ is the Dirac delta function [**speagle2019DynestyDynamic**]. This leaves us with a set of delta functions at values of θ, where the posterior probability density function (PDF) can be found by taking the histogram of these delta functions. Alternatively one can think of this as resampling the points θ_i based on their importance weight $p(\theta_i)$, which leaves a set of samples from the posterior PDF.

The methods described above then provide a way to estimate parameters of a model given some data. Also this provides a way to compare different models given some observation. In Chapters 3, 4 and 5 the methods described above are used to estimate various parameters.

2.3 Continuous wave searches

Searches for CWs can be split into three general categories: Targeted searches, Directed searches and All-sky searches, where the different categories are based on the number of source parameters for which there is an estimate of its value prior to running the search.

2.3.1 Targeted

Targeted searches are used to search for specific pulsars which have parameters known from electromagnetic observations, i.e. X-ray, radio or γ-ray. These observations can give accurate estimates of the sky position parameters α and δ, and the source frequency parameters f and its derivatives, where there could also be extra parameters if the pulsar is in a binary system. Targeted searches can then use these parameters as input such that they search over the remaining unknown parameters h_0, ι, ϕ_0, ψ. The main targeted searches are the Bayesian time-domain search [**dupuis2005BayesianEstimation**], the matched filter $\mathcal{F}$-statistic [**schutz1998DataAnalysis**] and the 5-Vector approach [**astone2010MethodDetection**].

The Bayesian time-domain search takes advantage of the narrow-band nature of the signal and reduces the size of the dataset such that Bayesian parameter estimation can be applied with a reasonable computational cost. This search uses sky position and frequency parameters of the source to perform a slowly evolving heterodyne which removes the phase evolution of the signal [**dupuis2005BayesianEstimation**]. This allows the signal to be low pass filtered and heavily downsampled without losing any of the signal information. This reduced dataset can then be used in a Bayesian approach to generate posterior

distributions on the parameters h_0, ι, ϕ_0, ψ, see [**dupuis2005BayesianEstimation**] for further information.

The matched filter $\mathcal{F}$-statistic [**schutz1998DataAnalysis**] analytically maximises the likelihood ratio of a signal model over a noise model with respect to the neutron star's amplitude parameters h_0, ι, ϕ_0, ψ such that it is then only a function of the Doppler parameters α, δ, f and $\dot{f}$. This method resamples the data over some time length T_{coh} based on the parameters α, δ, f and $\dot{f}$ using the SSB time in Eq. 2.5 [**schutz1998DataAnalysis**]. If the GW signal matches these parameters then resampling removes the Doppler modulation of the signal such that it appears at a fixed frequency. This means that the $\mathcal{F}$-statistic can be efficiently calculated using the fast Fourier transform (FFT). Once the maximum of the $\mathcal{F}$-statistic with respect to parameters α, δ, f and $\dot{f}$ is found, the amplitude parameters can be analytically calculated from these parameters. For more details on this search see [**schutz1998DataAnalysis**, **brady2000SearchingPeriodic**, **prix2007SearchContinuous**, **aasi2014GRAVITATIONALWAVES**].

The 5-Vector search is based in the frequency domain, where it makes use of the five frequency harmonics caused by the sidereal amplitude modulation which originates from the detector's antenna response as the earth rotates [**astone2010MethodDetection**, **aasi2014GRAVITATIONALWAVES**]. A summary of the application of these three searches for initial and advanced LIGO can be found in [**aasi2014GRAVITATIONALWAVES**, **abbott2019SearchesGravitationala**].

Due to the long observation times needed to accumulate the required SNR for detection, most searches use data from an entire or multiple LIGO and Virgo observing runs which can last for $\mathcal{O}(1)$ year. Given the sampling rate for the GW channel is 16 kHz (often downsampled to ~ 4 kHz), the amount of data in a year can be $\mathcal{O}(2)$ terabytes, therefore these types of search can be computationally costly. Whilst the fully coherent matched filter searches have methods to reduce the computational time for known sources, in wide parameter space searches such as all-sky and directed searches, this type of search is not feasible. This is due to the computational cost associated with running a fully coherent search over a wide parameter space. This problem led to the development of semi-coherent searches which will be introduced in the next sections.

2.3.2 Directed

In directed searches, the sky position parameters (α, δ) are known but the rotation frequency and other parameters are not. This includes searches for neutron stars in binary systems such as Sco-X1 [**abbott2017UpperLimits**, **meadors2016TuningScorpius**], for young supernovae remnants [**abadie2010FIRSTSEARCH**] and for neutron stars in the galactic center [**piccinni2019DirectedSearch**]. These searches use similar techniques as all-sky searches, which will be described in Sec. 2.3.3, they differ in that they

can limit the parameter space based on the known sky position.

2.3.3 All-sky searches

All-sky searches have no prior knowledge of the pulsar's parameters, therefore, they are used to search over all the neutron star parameters $h_0, \iota, \psi, \phi_0, f, \dot{f}, \alpha, \delta$. It would not be feasible to use the techniques described in Sec. 2.3.1 for an all sky search as to sufficiently cover the entire parameter space, it would require large computational cost. Instead semi-coherent searches were developed. These offered a solution to searching over the large parameter space and data size. The general idea of a semi-coherent search is to break the dataset into smaller segments of length T_{coh}, which can each be analysed coherently. The results from each segment can the be combined incoherently using various methods which will be summarised below. There are also searches such as [**messenger2007FastSearch**], which breaks the dataset into smaller frequency bands and combines them incoherently. Whilst these methods will be less sensitive than a fully coherent search, they are much faster and at a fixed computing cost are more sensitive.

There are many different types of semi-coherent search which use various methods to incoherently combine the coherently analysed time segments. Some of these methods are summarised and compared in [**walsh2016ComparisonMethods**] and I will summarise these and others below.

Stack-slide This method uses a set of Fourier transforms of the data known as short Fourier transforms (SFTs), more specifically it uses their power spectrum, i.e. $|S|^2$ where S is the SFT. Each of the separate SFTs (segments) is shifted up or down in frequency relative to the others based on the sky position α and δ to account for the Doppler modulation of the source. The SFT power from each frequency bin can then be summed (stacked). More explanation of this can be found in [**brady2000SearchingPeriodic**, **cutler2005ImprovedStackslide**]

Hough The Hough transform is similar to the stack-slide algorithm. The main difference is that the detection statistic for each segment is assigned a weight of 0 or 1 depending if it crossed a detection threshold. This weighted set of SFTs are then used as input to the Hough transform. The Hough transform maps a pattern in an image such as a straight line ($y = mx+c$) to the parameters (m, c) which are consistent with that line. This approach is explained in greater detail in [**krishnan2004HoughTransform**, **antonucci2008DetectionPeriodic**]. This method has been applied in two main ways known as Sky Hough [**krishnan2004HoughTransform**], which generates Hough maps in sky position (α, δ) for fixed spin down, and Frequency Hough [**antonucci2008 astone2014MethodAllsky**] which generates hough maps in $(f, \dot{f})$ for fixed sky position.

Einstein@Home This uses the $\mathcal{F}$-statistic mentioned in Sec. 2.3.1 calculated over a length of T_{coh}, where in the initial stages of this search these segments are combined incoherently. This is is done using a Hough transform scheme [**theligoscientificcollaboratio** or by generating candidate events where the $\mathcal{F}$-statistic crosses some threshold and then finding events which are coincident in parameter space [**ligoscientificcollaboration200** After the first stage, potential signals are returned (candidates) where post processing methods as in [**theligoscientificcollaborationandthevirgocollaboration2013Einste** select the most significant candidates. In [**theligoscientificcollaborationandthevirgocoll** they use a three step procedure, which starts with the Hough transform with more finely sampled parameters around the candidate, and then runs a semi and then finally fully coherent $\mathcal{F}$-statistic analysis. Other methods for combining results and following up candidates can be found in [**singh2016ResultsAllsky**, **papa2016Hierarchica** **walsh2016ComparisonMethods**]. Einstein@Home is the most sensitive of the current all-sky CW searches, however, uses a large amount of computing power. This is possible due to the use of a distributed computing project, where more details can be found at [**EinsteinHome**].

Time domain $\mathcal{F}$-statistic The time domain $\mathcal{F}$-statistic splits the data into narrowband segments of length ~ 2 days [**walsh2016ComparisonMethods**]. Then a coherent search using the $\mathcal{F}$-statistic is applied to each of these segments. Values of this statistic above a threshold are stored. Coincidences are then found in each segment, where candidates are selected based on a given threshold. This is explained in greater detail in [**aasi2014ImplementationTextdollar**, **walsh2016ComparisonMethods**].

Powerflux Powerflux uses a standard set of 1800s SFTs. For each point in parameter space, the frequency of a signal with those parameters is found and the power in each SFT at that frequency is recorded. This power is then weighted depending on the antenna pattern and noise of the detector. In longer stretches of ~ 1 month, the weighted power is summed. Any point in parameter space which produces high power in each of these stretches is identified as a potential signal. This search can then be repeated around each candidate with a finer resolution in parameter space. This is explained in more detail and tested in [**abadie2012AllskySearch**, **walsh2016ComparisonMethods**, **ligoscientificcollaborationandvirgocollaboration2**

Viterbi The Viterbi algorithm [**viterbi1967ErrorBounds**] has been used in [**sun2018HiddenM** **suvorova2017HiddenMarkov**, **abbott2017SearchGravitational**, **abbott2018Search** **sun2018ApplicationHidden**] to search for CWs with unknown randomly wandering spin frequency. This algorithm was applied to specific sources, where the $\mathcal{F}$-statistic is used on short duration segments which are then incoherently combined using the Viterbi algorithm which will be described in Chapter 3.

Table 2.1: From [**walsh2016ComparisonMethods**], shows the expected computational cost for the first four months of the first observing run of advanced LIGO (O1) for each search. This is measured in million standard units (MSU), where one standard unit is equal to one core-hour on a standard core. The Einstein@Home searches uses the computing resources of the Einstein@Home project and is designed to run for 6 - 10 months in the Einstein@Home grid.

Pipeline	Expected runtime of O1 search
Powerflux	6.8 MSU
Time domain $\mathcal{F}$-statistic	1.6 MSU
Frequency Hough	0.9 MSU
Sky Hough	0.9 MSU
Einstein@Home	100-170 MSU

Each of these searches has a large computational cost. In [**walsh2016ComparisonMethods**] a mock data challenge (MDC) was conducted to compare the sensitivity of some of the all-sky searches, where an expected runtime was presented for a search through the first four months of the first observing run of advanced LIGO (O1), shown in Tab. 2.1. The results from O1 for some of these searches can be found in [**ligoscientificcollaborationandvirgocollabor**] Even the fastest of these searches takes close to 1 million core-hours to search through four months of data. This presents one of the larger issues when searching for sources of CWs as generating results from observing runs can be time consuming.

Chapter 3

SOAP: A generalised application of the Viterbi algorithm to searches for continuous gravitational-wave signals.

Searches for CWs are notoriously computationally expensive, and it is important to investigate the trade off between computing power and sensitivity. In addition, these searches are generally highly tuned and are based around template matching methods. The SOAP [**ellis2006SnakesPlanea**] algorithm described in this chapter aims to address both of these issues.

SOAP searches though narrow-banded time-frequency spectrograms of data and identifies the 'most probable track' in frequency through it. The 'most probable track' is the most probable continuous narrowband signal in what is otherwise noisy data. The motivation of the search is simple: if we looked at a frequency band in a spectrogram as in Fig. 3.1, we could find every possible track from a starting frequency bin to an end frequency bin. For each of these tracks the sum of the spectrogram power along the track can be found such that for each track there is a single value. Figure 3.1 shows a histogram of a subset of these values, where the main distribution is from tracks which are through noise. Signals which are in the upper tail of this distribution are then tracks which follow features which are not noise like. The track which gives the maximum sum of spectrogram power is the least noise-like and therefore, can be taken as most likely to be from some signal. In Fig. 3.1 the optimum track in red shows a statistic value of ~ 1780 which is far outside the main distribution of summed powers. The red track follows that of an injected monochromatic signal. This demonstrates that the sum of the spectrogram power along a track which follows a signal is outside the distribution of tracks which randomly walk through noise. Therefore, it can be assumed that if the frequency track with the highest

sum of spectrogram power is found, then the corresponding track is most likely to follow a signal. Given that in the example in Fig. 3.1, the spectrogram has 180 frequency bins M and 400 time segments N. After each segment the track has T possible options to jump to (in this case we only allowed 3 options, up, down and center). The total number of possible tracks is MT^N. For this spectrogram this value is $\sim 10^{904}$ tracks, this is an unreasonable number of tracks and statistics to possibly calculate. This is where the Viterbi algorithm [**viterbi1967ErrorBounds**] is useful as it can efficiently find the track which gives the maximum sum of power. For an equivalent search the Viterbi algorithm would have to do TMN calculations for find the optimum track. A description of this method is in the following sections.

The majority of this chapter that follows has been reviewed and published as in [**bayley2019GeneralizedApplication**]. The exceptions are work in Sec. 3.9, Sec. 3.11, Sec. 3.12 and Sec. 3.13 which is supplementary material. This was work done by the author under the supervision of Prof. Graham Woan and Dr Chris Messenger.

3.1 Introduction

One of the main targets for current ground based GW detectors, including LIGO [**abbott2009LIG**
aasi2015AdvancedLIGO] and Virgo [**acernese2008StatusVirgo**, **acernese2015AdvancedVi**
are sources of continuous gravitational waves. These are long-duration, quasi-monochromatic sinusoidal signals that are well-modelled by a Taylor series expansion in the signal phase. A likely source of such signals is rapidly spinning non axisymmetric neutron stars. A number of possible emission mechanisms are outlined in [**prix2009GravitationalWaves**, **owen2009ProbingNeutron**].

These types of GWs are expected to give strain amplitudes that are significantly below the detector's noise spectral density, and need sensitive search algorithms for detection. The most sensitive method is to use a coherent matched filter which requires knowledge of the waveform beforehand such that it can be coherently correlated with the data. This approach is used in searches for gravitational signals from known pulsars such as [**dupuis2005BayesianEstimation**, **astone2010MethodDetection**, **schutz1998DataAnal**
collaboration2017FirstSearch, **abbott2019SearchesGravitational**]. For broad parameter space searches, where the parameters of the signal are unknown, a large number of template waveforms must be used to sufficiently cover the parameter space. This approach rapidly becomes computationally impractical as the search space grows, so semi-coherent search methods have been developed to deliver the maximum overall sensitivity for a given computational cost. Semi-coherent searches break the data up into sections of either time or frequency and perform a coherent analysis on these sections separately. These intermediate results can then be recombined incoherently in a number of different

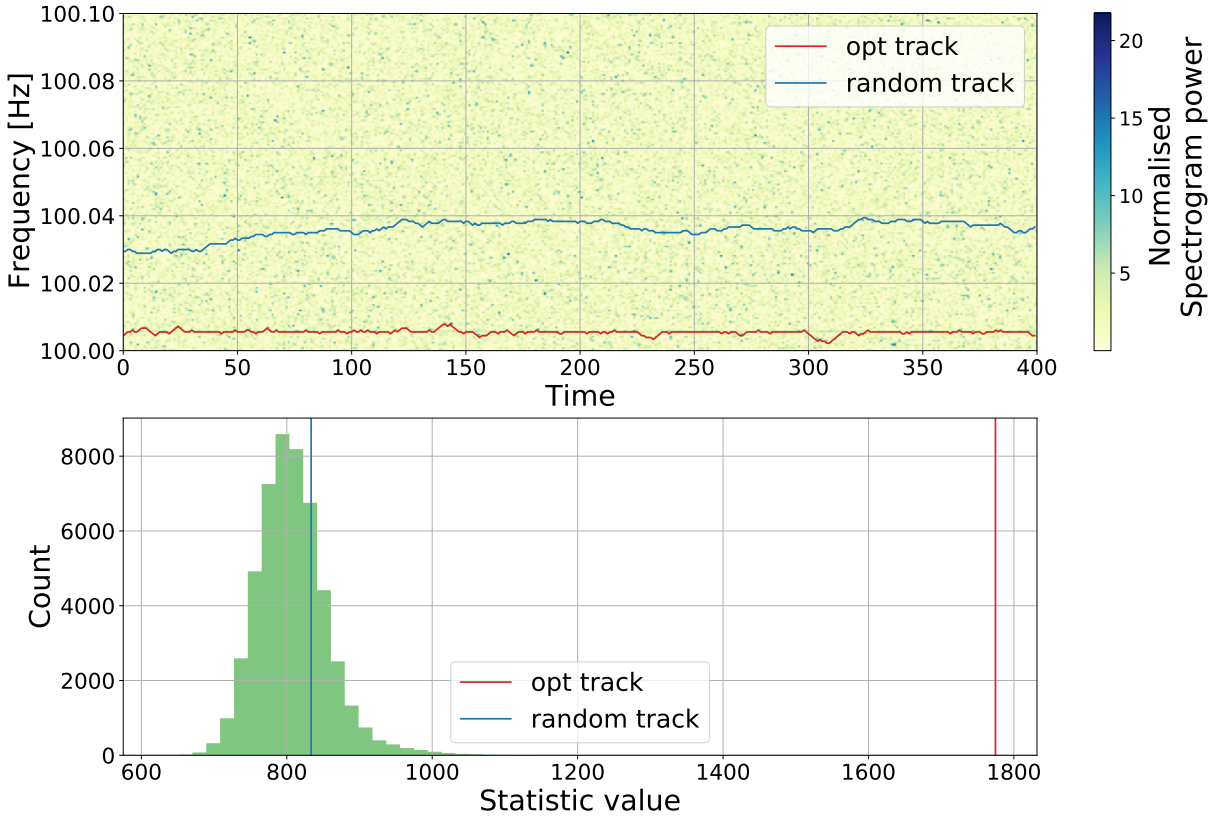

Figure 3.1: An example of a time-frequency spectrogram which is the typical LIGO data that SOAP searches through. Here a monochromatic signal has been injected at 100.006 Hz. The blue track shows a random walk track though this spectrogram whereas the red line shows the track which gives the highest sum of detector power. The second panel shows a histogram of the summed power of a subset of all tracks which can be found through the given spectrogram from start to finish. This is a randomly sampled subset as the total number of paths is too large to calculate. The value of the statistic which comes from the optimal path is ~ 1780. This is much larger than any of the random tracks in our subset and much larger than the mean statistic of all tracks.

ways to form the final search result outlined in [**creighton2000SearchingPeriodic**, **abbott2019AllskySearch**] and references therein.

The analysis that we present here is known as SOAP [**ellis2006SnakesPlanea**] and is based on the Viterbi algorithm [**viterbi1967ErrorBounds**]. The algorithm models a process that has a discrete number of states at discrete time steps, and computes the set of states which gives the highest probability (suitably defined) given the data. Our implementation of SOAP is intended as a stand-alone search which is naturally non-parametric and has broad applications to both searches for known signal types and signals which have an unknown frequency evolution. The algorithm works in the time-frequency plane, where our 'states' are represented by the time and frequency coordinates of a potential signal. We can then find the most probable set of frequencies a possible signal could have, i.e., we can find the most probable track in frequency as a function

of time. This is not the first application of the Viterbi algorithm to GW data. Another variant of the algorithm [**suvorova2016HiddenMarkova**] has recently been used, amongst other applications, as part of a CW search to track a pulsar with randomly wandering spin frequency [**sun2018HiddenMarkov**, **suvorova2017HiddenMarkov**, **abbott2017SearchGravitational**, **abbott2018SearchGravitational**, **sun2018ApplicationH** We develop an alternative version which is aimed to be applied more generally to search for any long duration signals using just SFTs.

In the next section we will describe the Viterbi algorithm and the basic SOAP implementation to GW time-frequency data. We then describe additional features to the algorithm, including the use of data from multiple detectors. As well as this we describe methods used to ignore instrumental effects in the data, such as incoherently summing data and a 'line aware' statistic. In the final section as well as a test of the computational cost of the search, we show results of a search performed on datasets of increasing complexity: Gaussian noise with no gaps (i.e., contiguous in time), Gaussian noise with gaps simulating real data more accurately, and finally real LIGO data taken during the sixth science run.

3.2 Viterbi algorithm

The Viterbi algorithm is an efficient method for determining the most probable set of states (a single 'track' of steps on the time-frequency plane) in a Markov model dependent on data, where the model has a discrete number of states at each step. Rather than computing the probability of every possible track and selecting the most probable, the algorithm maximises this probability after every discrete step. As a result, a partial track which cannot ultimately be the most probable is rejected before the next step is calculated, and only a fraction of all possible tracks need to be computed to find the one that is most probable.

In this work we apply the Viterbi algorithm to a GW strain time-series to find the most probable track of a single variable-frequency signal in the noisy data. We divide the time series into N equal-length and contiguous segments $\boldsymbol{x}_j$, defining the set $D \equiv \{\boldsymbol{x}_j\}$. The 'states' in the model correspond to the frequencies a signal could have in each segment. A 'track' is a list of such frequencies $\boldsymbol{\nu} \equiv \{\nu_j\}$, where ν_j is the frequency in the segment $\boldsymbol{x}_j$.

Our objective is to calculate the most probable track given the data, i.e., the track that maximises $p(\boldsymbol{\nu} \mid D)$. Using Bayes theorem, this posterior probability can be written as

$$p(\boldsymbol{\nu} \mid D) = \frac{p(\boldsymbol{\nu})p(D \mid \boldsymbol{\nu})}{p(D)}, \tag{3.1}$$

where $p(\boldsymbol{\nu})$ is the prior probability of the track, $p(D \mid \boldsymbol{\nu})$ is the likelihood of the track (i.e., the probability of the data given the track) and $p(D)$ is the model evidence (or

marginalised likelihood).

The Viterbi algorithm treats the track as the result of a Markovian process, such that the current state depends only on the previous state. It is therefore useful to split the track's prior into a set of transition probabilities such that

$$\begin{aligned} p(\boldsymbol{\nu}) &= p(\nu_{N-1}, \ldots, \nu_1, \nu_0) \\ &= p(\nu_{N-1} \mid \nu_{N-2}) p(\nu_{N-2} \mid \nu_{N-3}) \ldots p(\nu_1 \mid \nu_0) p(\nu_0) \\ &= p(\nu_0) \prod_{j=1}^{N-1} p(\nu_j \mid \nu_{j-1}), \end{aligned} \tag{3.2}$$

where $p(\nu_0)$ is the prior probability that the signal in the first time step has a frequency ν_0 and $p(\nu_j \mid \nu_{j-1})$ is the prior 'transition' probability for ν_j given the frequency at the last step was ν_{j-1}.

The noise in each of the segments can be treated as independent, so the likelihood component in Eq. 3.1 can be factorised as

$$p(D \mid \boldsymbol{\nu}) = \prod_{j=0}^{N-1} p(\boldsymbol{x}_j \mid \nu_j), \tag{3.3}$$

where $p(\boldsymbol{x}_j \mid \nu_j)$ is the likelihood of our signal having a frequency ν_j in the jth segment.

Using Eq. 3.1, 3.2 and 3.3, the posterior probability is then

$$p(\boldsymbol{\nu}|D) = \frac{p(\nu_0)p(\boldsymbol{x}_0|\nu_0) \prod_{j=1}^{N-1} p(\nu_j|\nu_{j-1})p(\boldsymbol{x}_j|\nu_j)}{\sum_S \left\{ p(\nu_0)p(\boldsymbol{x}_0|\nu_0) \prod_{j=1}^{N-1} p(\nu_j|\nu_{j-1})p(\boldsymbol{x}_j|\nu_j) \right\}}, \tag{3.4}$$

where in the denominator we must sum over all possible tracks S. We require the specific track, or set of frequencies, $\hat{\boldsymbol{\nu}}$ that maximises the posterior probability. Therefore, as the denominator in Eq. 3.4 is a sum over all possible tracks, the track which maximises the posterior is the same track which maximises the numerator on the right-hand side of Eq. 3.4, i.e.,

$$p(\hat{\boldsymbol{\nu}}|D) \propto \max_{\boldsymbol{\nu}} \left[p(\nu_0)p(\boldsymbol{x}_0|\nu_0) \prod_{j=1}^{N-1} p(\nu_j|\nu_{j-1})p(\boldsymbol{x}_j|\nu_j) \right]. \tag{3.5}$$

This track also maximises the log of the probability and can be written as,

$$\log p(\hat{\boldsymbol{\nu}}|D) = \max_{\boldsymbol{\nu}} \left\{ \log p(\nu_0) + \log p(\boldsymbol{x}_0|\nu_0) \right. \\ \left. \sum_{j=1}^{N-1} \left[\log p(\nu_j|\nu_{j-1}) + \log p(\boldsymbol{x}_j|\nu_j) \right] \right\} + \text{const.} \tag{3.6}$$

The Viterbi algorithm finds the most probable track $\hat{\boldsymbol{\nu}}$ by calculating the quantities in Eq. 3.6 for each frequency at each time step. In the following sections we explain how this is achieved in practice.

3.3 The transition matrix

An important concept when using the Viterbi algorithm is the 'transition matrix' T, which is defined as the matrix that stores the prior log-probabilities $\log p(\nu_j \mid \nu_{j-1})$. These transition probabilities depend only on the size and direction of the transition, and in our case correspond to a jump in frequency when moving from the $(j-1)$th to the jth state. It is within the transition matrix that we impose some loose model constraints. For example it is usual in the time-frequency plane for frequencies to only have discrete values (frequency bins) and a track might only be allowed to move by one bin in each time step, restricting it to a up, centre or down (UCD) transition or 'jump' or equivalently setting the size of the first dimension of the transition matrix $n_1 = 3$. We can also impose that the transition probabilities are independent of the current track location in frequency, i.e. $p(\nu_j \mid \nu_{j-1}) = p(\nu_{j+k} \mid \nu_{j+k-1})$. This leads to the transition matrix containing only three numbers, corresponding to the three prior log-probabilities that the track was in the corresponding UCD frequency bin at the previous time step. These numbers are chosen to reflect the prior probability of a frequency deviation in the track and depend on the class of signals that one wishes to detect. For the majority of examples that follow, a symmetric transition matrix is used, i.e. the probability of a transition up a frequency bin is equal to the probability of a transition down a frequency bin. This allows us to parametrise the one dimensional transition matrix with a single value, this value is the ratio of the probability of a transition from the same frequency bin, to the probability of a transition from either up or down a frequency bin.

In later sections we will consider more complex situations in which the transition matrix describes the prior probability associated with sequences of even earlier transitions ('memory') and the case where there are multiple detectors. In these cases the number of dimensions of the transition matrix can grow substantially to account for the extra complexity of the problem.

3.4 Single detector

We will first consider the simple case of a single dataset D, generated by a single gravitational wave detector, and consider only a one-dimensional transition matrix. We will make use of discrete Fourier transforms so that frequencies, and hence the track frequencies, are also discrete. These frequencies will be indexed by k and therefore $\nu_j \to \nu_{j,k} = k(j)\Delta f$ where $\Delta f = 1/T_{\text{time}}$ is the frequency bin width for a segment of duration T_{time}.

The Viterbi algorithm determines the most probable track on the time-frequency plane by calculating the value of Eq. 3.6 for every discrete Fourier frequency, incrementally in time. In other words, at each time segment it finds the most probable earlier track which ends at each particular frequency. On reaching the final segment it can look back to identify the most probable track connecting segment 1 to segment N.

There are two main components to Eq. 3.6: the transition probabilities $p(\nu_j \mid \nu_{j-1})$ and the likelihoods $p(\boldsymbol{x}_j \mid \nu_j)$. The transition probabilities are pre-calculated and stored in a transition matrix according to Sec. 3.3 above. To calculate the likelihood we follow the approach of [**bretthorst1988BayesianSpectruma**] which gives, under the assumption of a single sinusoidal signal in additive Gaussian noise in data segment $\boldsymbol{x}_j$,

$$p(\boldsymbol{x}_j \mid \nu_{j,k}, \sigma_{j,k}, I) \propto \exp\left[C(\nu_{j,k})\right]. \tag{3.7}$$

where $C_{j,k}(\nu_{j,k})$ is the Schuster periodogram normalised to the noise variance at frequency $\nu_{j,k}$ of segment j. This is equivalent to the log-likelihood, and is defined as

$$C(\nu_{j,k}) \equiv C_{j,k} = \frac{1}{\sigma_{j,k}^2}\frac{1}{N_{\text{s}}}\left|\sum_{r=0}^{N_{\text{s}}-1} x_{j,r}\mathrm{e}^{i\nu_{j,k}t_r}\right|^2, \tag{3.8}$$

where N_{s} is the number of data points in each segment and t_r is the time corresponding to $x_{j,r}$, the rth sample in the jth data segment. The noise variance $\sigma_{j,k}^2$ is calculated as an estimate of the noise PSD in the kth sample and the jth data segment. It is worth noting at this point that it is also possible to write this as a likelihood ratio, and therefore write out detection statistic as a log-odds ratio, however, we will discuss this in more depth in Sec. 3.8. The log-likelihoods of each segment can be calculated at discrete frequencies before running the algorithm by computing the power spectra for each segment from discrete Fourier transforms of the data. In the GW field these standard data forms are known as SFTs.

The Viterbi algorithm records two quantities for each frequency and time bin: The first, $V_{j,k}$, contains the value defined by Eq. 3.6, which is the log-probability of the most probable path ending in position j, k. The second, $A_{j,k}$, is the transition, or 'jump', used to achieve the most probable path. The algorithm can be divided into three main sections: initialisation, iteration and identification. These three sections are described in pseudo-

code in Alg. 3.1 and a simple demonstration of the algorithm at work is shown in Fig. 3.2.

1: Input: C, T {log-likelihood,transition matrix}
2: Output: $\hat{\boldsymbol{\nu}}$, V, A {most probable track, track probabilities, jumps}
3:
4: *Initialisation*
5: **for** Frequency $(\nu_{0,k})$, $k = 0 \rightarrow M-1$ **do**
6: $V_{0,k} = C_{0k}$
7: $A_{0,k} = 0$
8: **end for**
9:
10: *Iteration*
11: **for** Segment, $j = 0 \rightarrow N-1$ **do**
12: **for** Frequency $(\nu_{j,k})$, $k = 0 \rightarrow M-1$ **do**
13: $V_{j,k} = \max_i(C_{j,k} + T_i + V_{j-1,j+i})$
14: $A_{j,k} = \operatorname{argmax}_i(C_{j,k} + T_i + V_{j-1,j+i})$
15: **end for**
16: **end for**
17:
18: *Identification*
19: $\hat{\nu}_{N-1} = \operatorname{argmax}_k(V_{N-1,k})$
20: **for** Segment, $j = N-1 \rightarrow 0$ **do**
21: $\hat{\nu}_j = \hat{\nu}_{j+1} + A_{j,\nu_{k+1}}$
22: **end for**

ALGORITHM 3.1: The Viterbi algorithm in pseudo-code. N is the number of segments, M is the number of frequency bins in each segment. Here the maximisations over i run between $\pm(n_1-1)/2$ where n_1 is the size of the transition matrix. The values from Eq. 3.6 are stored in V, and the jumps are stored in A. The most probable track is denoted by $\hat{\boldsymbol{\nu}}$.

Initialisation The two parts of Eq. 3.6, $\log p(\nu_0)$ and $\log p(\boldsymbol{x}_0 \mid \nu_0)$, must be computed before the main recursive part of the algorithm can start. Therefore, the initialisation section (lines 5–8) in Alg. 3.1 calculates the first column in the lower panel of Fig. 3.2. A priori, there is no preferred initial frequency, so we take the log-prior $\log p(\nu_{0,k})$ to be uniform over the complete frequency range. As a result, this is does not affect the maximisation for any jump, therefore, can be omitted from the calculation. We then use the pre-calculated log-likelihood values $C_{0,k}$ to fill the track probabilities $V_{0,k}$. There is no previous position to jump from in this case, so the transition probabilities are irrelevant and $A_{0,k}$ are set to zero.

Iteration The main part of the calculation is the sum in Eq. 3.6. Lines 11–16 in Alg. 3.1 calculate the most probable tracks that end at each frequency bin for each segment

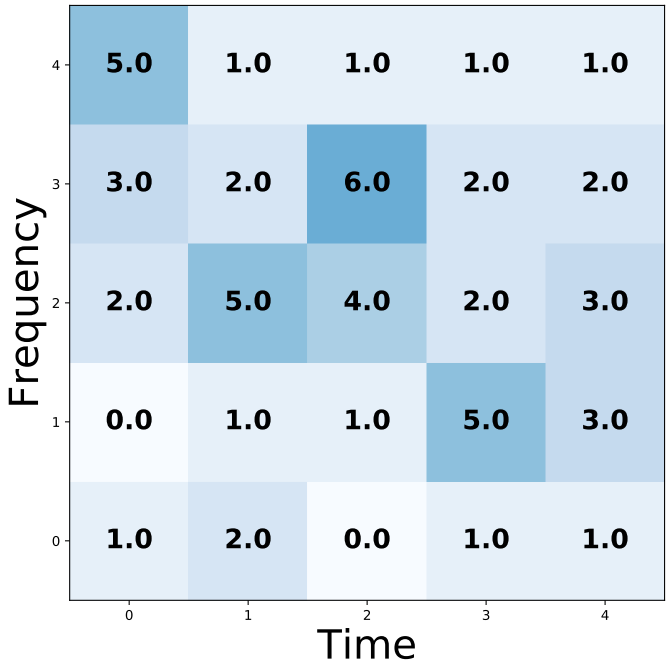

(a) The input data

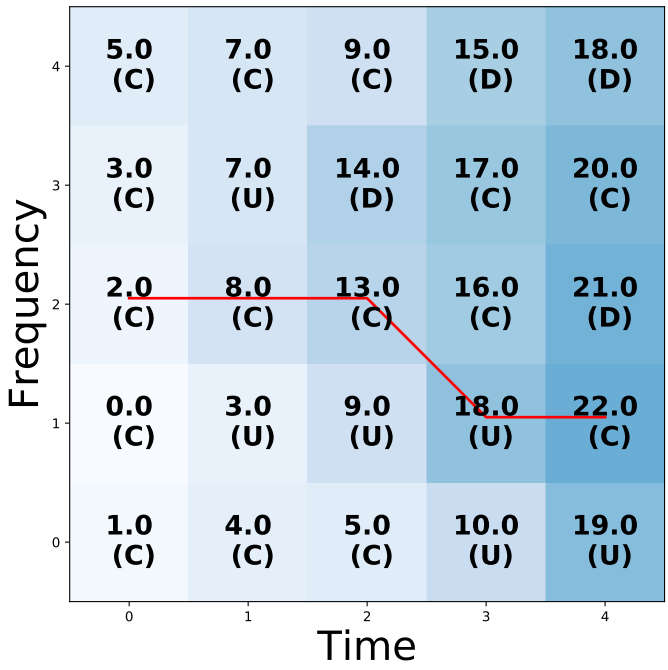

(b) The log-probabilities, jumps, and most probable path

Figure 3.2: Fig. 3.2a shows the observed data, i.e the log-likelihood values $C_{j,k}$. Fig. 3.2b shows the calculated log-probabilities $V_{j,k}$. $A_{j,k}$ is shown in parentheses, where the UCD components correspond to $i = [-1, 0, 1]$ respectively. The red line shows the path that gives the maximum probability. The transition matrix for the UCD jumps is $[0, 1, 0]$ and corresponds to the un-normalised prior log-probabilities of these jumps occurring, i.e. the track is more likely to stay at the same frequency. The jump in frequency of the track between times 2 and 3 is due to the likelihood $C_{3,2} = 5$, which gives a larger increase in the overall probability than continuing (straight) to $C_{3,2} = 2$ even with the extra value of 1 from the transition matrix, i.e. the extra likelihood one can accumulate by changing frequency overcomes the prior transition probability which prefers to go straight.

by using

$$V_{j,k} = \max_i (C_{j,k} + T_i + V_{j-1,k+i}), \tag{3.9}$$

where i is the size and direction of the jump. For example, in Fig. 3.2 columns 1–4 are calculated in order using Eq. 3.9, where it maximises over three possible previous positions in frequency. These positions are the frequency bins UCD of the current position. The size and direction of the jump, i, which gives the maximum probability is then saved to $A_{j,k}$. These are shown in parentheses below the log-probabilities in Fig. 3.2 where UCD correspond to values of $i = [-1, 0, 1]$ respectively.

Identification The final stage of the algorithm identifies the most probable track. This is done by initially finding the highest log-probability values in the final time segment, $\max_k(V_{N-1,k})$ (line 19 in Alg. 3.1). In the lower panel of Fig. 3.2 this is located at position $j, k = 4, 1$ with $V_{4,1} = 22$. To find the track which corresponds to this, the values in A_{jk} are followed backwards from this position (lines 20–21). For example, in Fig. 3.2 the final position is $j, k = 4, 1$ and $A_{j,k} = \text{Center} = 0$, this means that at the previous segment the most probable track was at position $j, k = 4-1, 1+0 = 3, 1$. At this time $A_{3,1} = R = 1$, therefore, the next track element is at $j, k = 3-1, 1+1 = 2, 2$. This then continues until $j = 0$ whereupon these retraced positions constitute the most probable track, highlighted in red in Fig. 3.2.

The most probable track is the one traced backwards from the highest probability final segment frequency position. However, tracks can also be traced back from any of the end-frequency positions, returning the most probable track conditional on a given final position. Such tracks should not be confused with the being equal to the second, third, fourth, etc. most probable tracks. Information regarding the rankings and properties of all possible tracks (excluding the most probable and conditionally most probable tracks) is lost during the maximisation procedures computed at each stage in the algorithm – a necessary consequence of the algorithm's speed and efficiency.

3.5 Multiple detectors

If there are Q detectors operating simultaneously we have Q sets of data which can be combined appropriately to provide input to the Viterbi search described above. We must also modify the allowed transitions encoded within the transition matrix to take account of the extra prior constraints that are now available.

The received instantaneous frequency of a given astrophysical signal will be nearly the same for all ground-based GW detectors, and our algorithm should be sensitive to tracks that show this consistency in frequency. However there *will* be small differences between the frequencies measured at detectors that are not co-located, due to differential Doppler

shifts caused by Earth rotation. As a result the signal could fall in different frequency bins at each detector.

To account for these small differences in signal tracks in each detector, we reference the observed tracks to a third (pseudo) detector located at the centre of the Earth which would be insensitive to Earth spin. The signal frequencies in each real detector are then allowed to vary within a certain number of frequency bins from the track in the reference detector. In the examples that follow, we only consider the possibilities that the track in each real detector is no more that one frequency bin away from the reference track. We can tune the length of the SFTs to ensure this is a valid assumption. As well as differences in signal frequency, due to antenna patterns and other effects, the measured signal amplitude may differ between the detectors. In the following example we assume that the signal has the same amplitude in each detector, however, in Sec. 3.8 we discuss the case where they differ.

We will now show how the algorithm in Sec. 3.4 can be modified to handle a two-detector network (i.e., $Q = 2$), however any number of detectors can easily be accommodated. In the two detector case the joint probability of two (real) tracks, $\nu^{(1)}$ and $\nu^{(2)}$, and the geocentric track ν, given the data, is

$$\begin{aligned} p(\nu, \nu^{(1)}, \nu^{(2)}|D^{(1)}, D^{(2)}) \propto p(\nu)p(\nu^{(1)}, \nu^{(2)}|\nu) \\ p(D^{(1)}|\nu^{(1)})p(D^{(2)}|\nu^{(2)}), \end{aligned} \tag{3.10}$$

where $D^{(1)}$ and $D^{(2)}$ represent the data from the two detectors. The main difference between this and that described in Sec. 3.4 is that the track probabilities $V_{j,k}$ are stored for the geocentric pseudo-detector. The main iterative calculation (defined for the single detector case in Eq. 3.9) now becomes

$$V_{j,k} = \max_{i,l,m}(C^{(1)}_{j,k+l} + C^{(2)}_{j,k+m} + T_{i,l,m} + V_{j-1,k+i}), \tag{3.11}$$

where $C^{(1)}$ and $C^{(2)}$ refer to the log-likelihoods in detectors 1 and 2 respectively and the transition matrix T is an $n_1 \times n_2 \times n_3$ matrix, where the n_1 dimension refers to the jump from the previous time step, and n_2 and n_3 refer to the relative frequency positions in each real detector. The transition matrix is now three-dimensional and holds the prior log-probabilities of $p(\nu)$ and $p(\nu^{(1)}, \nu^{(2)}|\nu)$. We now need to maximise over three indices: i, l and m. The index i refers to the size and direction of the jump at the geocentre (as before). The indices l and m refer to the number of frequency bins by which the two real tracks deviate from the geocentre track. For example, if the most probable track in the geocentred detector is in bin $j, k = 5, 12$ and the values of $i, l, m = 0, -1, 1$, then detector 1 is in position $j, k = 5, 11$ and detector 2 is in position $j, k = 5, 13$ and the geocentred track was in the position $j, k = 4, 12$ at the previous time step. As a result, the track at

the geocentre is only affected by Doppler modulations from the Earth's orbit whereas the tracks in the real detectors include Doppler modulations from the Earth's spin.

At every time step the frequency bin position for each real detector is forced to be within n_l or n_m bins of the track in the geocentred detector, where n_l and n_m depend on how much each detector could possibly be Doppler shifted. As mentioned previously, we only consider the case where $n_l = 1$ and $n_m = 1$, allowing the track from each real detector to be at most one frequency bin away from the geocentred track position. While we tune the SFT length to keep this condition for different frequencies, it is also possible to tune the values of n_l and n_m to get a similar effect. The implementation of the multi-detector algorithm is similar to the single detector case described in Sec. 3.4. However in the single detector case there is only a single variable to be maximised over for each time-frequency bin. This variable is the frequency jump from the position in the previous segment. For the multi-detector case there are at least three variables to be maximised over: the probability of the jump, i, at the geo-centre and the probability of the signal being in the surrounding positions in each of the Q real detectors, $l, m, \ldots$. The values of $i, l, m, \ldots$ are then saved to $A_{j,k}$ and are ultimately used to reconstruct the most probable consistent tracks in each real detector.

As in Sec. 3.4, there are three main sections: Initialisation, iteration, and the identification. For the multi-detector case each element is modified as follows.

Initialisation The first-row calculation (lines 5–8) in Alg. 3.1, are now modified to additionally maximise over the real detector track positions l and m. For each time-frequency bin the maximum sum of the log-likelihoods is saved together with the frequency locations of the corresponding tracks in the real detectors. The index $i = 0$ is kept constant as there is no previous position.

Iteration To process the subsequent time segments, lines 13–14 in Alg. 3.1 are modified to account for two (or more) detectors. Line 13 of Alg. 3.1 is changed to calculate Eq. 3.11, the log-probability of a track at the geocentre ending in bin j, k given that the signal is in the real detector positions of $j, k + l$ and $j, k + m$. Line 14 is then modified so that $A_{j,k}$ stores the jump values, i, and the real detector positions, l and m, which returned the highest probability.

Identification The most probable track is identified in the same way as for the single detector case, first by finding the maximum value in the final time step of $V_{j,k}$ (line 19 in Alg. 3.1). The track at the geocentre can then be found by iteratively following the jump values stored in $A_{j,k}$ back from this position. The track in each of the real detectors is determined by using the values of l and m indices also stored in $A_{j,k}$ to find the relative position of the track in each real detector compared to the geocentre.

This method can be extended to more than two detectors by including additional datasets and expanding the corresponding number dimensions of the maximisation procedures in the iterative steps.

3.6 Memory

In this section we extend the basic Viterbi algorithm to improve its sensitivity to non-stochastic signals where there is some knowledge of its frequency evolution. We do this by including a form of 'memory' and this extension applies to both the single and multiple-detector cases. Rather than considering only the previous step in our decision-making process, we now include the previous $m+1$ steps and expand the transition matrix to include these values. A memory of $m = 0$ therefore corresponds to the methods described in previous sections. With a non-zero memory the transition matrix can a-priori make certain sequences of jumps more probable and assign different prior probabilities for these jump sequences e.g., 'up then centre' may be less preferable to 'centre then centre'. As a result we can increase the chance of the most probable track matching an expected astrophysical signal. In a single detector search with a memory of $m = 1$, if we only allow UCD transitions, then for every frequency bin we save 3 values. These are proportional to the log-probabilities of a track coming from a UCD bin in the previous time step, where the maximisation is over the corresponding UCD bins two time steps back. Equation 3.11 then is then modified to,

$$V_{j,k,s} = \max_{h}(C_{j,k} + T_{s,h} + V_{j-1,k+s,k+s+h}), \tag{3.12}$$

where s and h refer to the UCD jumps at the time step $j-1$ and $j-2$ respectively. Similar to the previous two sections, the algorithm is split into three parts: initialisation, iteration, and the track identification:

Initialisation The initialisation process needs to populate the first $m+1$ steps before the main iteration can start. At the first time step, the elements $V_{0,k,s}$ are set to the log-likelihoods $C_{0,k}$ as in Sec. 3.4. There is no previous time step, so the element s is not relevant. At the second time step, $V_{1,k,s}$ is calculated using Eq. 3.12, where there is no maximisation over h, it is assumed to be 0, or a center jump. As there is no data before $j = 0$, the maximisation at this point will always return the jump which has the largest prior probability, which in this case is a center jump. Therefore, the maximisation returns the same value for all frequency bins and can be set to a center jump.

Iteration For all following time steps the values for each element of $V_{j,k,s}$ in Eq. 3.12 are calculated. This quantity is proportional to the log-probability of the track ending

in time-frequency bin j, k, which was in the previous position of $j-1, k+s$. The corresponding value of h that maximised the log-probability of the track is recorded in $A_{j,k,s}$.

Identification The most probable track is identified in a similar way to the non-memory cases, by finding the highest-valued last element, $V_{N-1,k,s}$. The values of s and h are then followed back to find the most probable track. As an example, let us assume the most probable track finishes in bin $j, k, s = 10, 5, 0$, where the value of m is $A_{10,5,0} = 1 =$ up. The previous position is then $j, k, s = 10-1, 5+s, m = 10-1, 5+0, 1 = 9, 5, 1$ with a value $A_{9,5,1} = 0 =$ Center, and the next track position is $j, k, s = 9-1, 5+1, 0 = 8, 6, 0$ etc. The values of j, k along this track describes most probable path.

The number of elements over which one must search increases rapidly with memory length, and has a strong impact on the computational cost of the analysis. For the single detector Viterbi approach the number of calculations made is $3 \times N \times M$ if we only allow UCD jumps, where N and M are the number of time are frequency bins respectively. When memory is included this increases to $3^{m+1} \times N \times M$.

3.7 Summed input data

In this section a method of incoherently-summing a set of SFTs to increase the SNR of a signal in a segment is outlined. To be more precise, it is actually the log-likelihoods which are summed, i.e. the quantity in Eq. 3.8. We can write the new summed set of data F_j as,

$$F_j = \sum_{i}^{N_s} C_{i,k} \tag{3.13}$$

where N_s is the number of SFTs to sum together and the log-likelihood $C_{i,k} = C(\nu_{i,k})$ is defined in Eq. 3.8. We can see this is possible by looking at Eq. 3.7, where we can use the product of likelihoods,

$$\begin{aligned} p(D \mid \nu) &\propto p(x_1, x_2 \ldots x_n \mid \nu) \\ &\propto p(x_1 \mid \nu) \ldots p(x_n \mid \nu) \\ &\propto \exp\left(\sum_i C_{j,k}\right). \end{aligned} \tag{3.14}$$

If the data contains gaps where the detector was not observing, then we fill the gaps in the power spectrum with a constant value which is the expectation value of the log-likelihood. The procedure of filling in the gaps of the data is completed before any summing. There-

fore, the data should have the same mean regardless of how much real data is in each sum. In the examples that follow, we sum the SFTs over the length of one day.

The main motivation for summing the data is to increase the SNR of a signal in the segments. The risk is that a signal can move between adjacent frequency bins during a day. To reduce this risk, we choose the frequency bin width such that it is more likely that a signal will be contained within a single frequency bin that cross a bin edge. In practice, to ensure that this is true, the segment or SFT length and the number of segments which are summed can be tuned for each search. As well as increasing the SNR, summing over one day should average out the antenna pattern. This means that the log-likelihood value in any bin should be more similar between detectors, however, there is still some variation due to the sky localisation and polarisation.

This also has two main effects on the transition matrix, the first is that as each segment of data is now one day long, a jump between frequency bins is far more likely, therefore, the transition matrix elements are modified to account for this. The second is that as the data is averaged over one day, the signal should remain is the same frequency bin between detectors, therefore, there is no longer a need for the multi-dimensional transition matrix described in Sec. 3.5.

The volume of the data is also reduced by a factor of $1/N_s$, therefore, the time taken for the algorithm to run is also reduced by the same factor.

3.8 Line-aware statistic

The single-detector algorithm described in Sec. 3.4 returns the most probable track of the loudest signal assumed to be in Gaussian noise. However, an astrophysical signal is not expected to have an amplitude which is orders of magnitude above the noise floor, but have an amplitude more similar to the noise. Therefore, a signal with a large amplitude is more likely to be of instrumental origin rather than astrophysical [**coughlin2010NoiseLine**, **aasi2015CharacterizationLIGO**, **covas2018IdentificationMitigation**].

We first consider the model of Gaussian noise with no signal present. Within a single summed segment, the likelihood of Gaussian noise at frequency ν is given by a χ^2 distribution,

$$p(F_j|\nu_j, M_{\mathrm{N}}, I) = \frac{1}{2^{d/2}\Gamma(d/2)} F_j^{d/2-1} \exp\left\{\frac{F_j}{2}\right\} \tag{3.15}$$

where F_j is the frequency domain power summed over sub-segments within a single day, as described in Sec. 3.7 and d is the number of degrees of freedom, equal to twice the total number of summed SFTs. M_{N} represents the model that the data is simply Gaussian noise. In the presence of a signal (model M_{S}), the power should follow a non central χ^2 distribution in which the non-centrality parameter λ is the square of the SNR, ($\lambda = \rho^2_{\mathrm{opt}}$),

i.e.,

$$p(F_j|\nu_j,\lambda,M_{\rm S},I) = \frac{1}{2}\exp\left\{-\frac{F_j+\lambda}{2}\right\}\left(\frac{F_j}{\lambda}\right)^{d/4-1/2} I_{d/2-1}\left(\sqrt{\lambda F_j}\right). \tag{3.16}$$

If a signal is present we therefore expect the SFT powers in the detector to follow Eq. 3.16. We can then determine the evidence for model $M_{\rm S}$ by marginalising over λ,

$$p(F_j^{(1)} \mid \nu_j, M_{\rm S}, I) = \int_0^\infty p(\lambda \mid M_{\rm S}) p(F_j^{(1)}|\nu_j,\lambda,M_{\rm S},I)d\lambda. \tag{3.17}$$

Here we set the prior on λ to be an exponential distribution of width w, this is done somewhat arbitrarily as we expect the majority of signals to have a low SNR. This distribution follows,

$$p(\lambda \mid M_{\rm S}) = \exp\left(\frac{-\lambda}{w_s}\right). \tag{3.18}$$

In this single-detector case, we expect an astrophysical signal to look very similar to that of a line other than its amplitude (or SNR). Therefore, we set the evidence for an astrophysical signal and an instrumental signal to follow Eq. 3.17, where the width w different between the two models.

We then have three models, one for an astrophysical signal, one for an instrumental line and one for Gaussian noise.

The posterior probability of model $M_{\rm GL}$, which contains the probability of Gaussian noise or Gaussian noise with a line (taken as mutually exclusive) is

$$\begin{aligned} p(M_{\rm GL} \mid F_j^{(1)}, \nu_j, I) = {} & p(M_{\rm G} \mid F_j^{(1)}, \nu_j, I) \\ & + p(M_{\rm L} \mid F_j^{(1)}, \nu_j, I). \end{aligned} \tag{3.19}$$

We can now find the posterior odds ratio for the presence of a signal over noise or a line,

$$\begin{aligned} O^{(1)}_{\rm S/GL}(F_j^{(1)} \mid \nu_j) &= \frac{p(M_{\rm S} \mid F_j^{(1)}, \nu_j)}{p(M_{\rm GL} \mid F_j^{(1)}, \nu_j)} = \frac{p(M_{\rm S} \mid F_j^{(1)}, \nu_j)}{p(M_{\rm G} \mid F_j^{(1)}, \nu_j) + p(M_{\rm L} \mid F_j^{(1)}, \nu_j)} \\ &= \frac{p(M_{\rm S})p(F_j^{(1)} \mid M_{\rm S}, \nu_j)}{p(M_{\rm G})p(F_j^{(1)} \mid M_{\rm G}, \nu_j) + p(M_{\rm L})p(F_j^{(1)} \mid M_{\rm L}, \nu_j)} \\ &= \frac{p(F_j^{(1)} \mid M_{\rm S}, \nu_j)p(M_{\rm S})/p(M_{\rm G})}{p(F_j^{(1)} \mid M_{\rm G}, \nu_j) + p(F_j^{(1)} \mid M_{\rm L}, \nu_j)p(M_{\rm L})/p(M_{\rm G})} \end{aligned} \tag{3.20}$$

In practice it is convenient to use the log odds ratio,

$$\begin{aligned}\log\left[O^{(1)}_{\mathrm{S/GL}}(F_j^{(1)})\right] &= \log\left[p(F_j^{(1)} \mid M_{\mathrm{S}})\right] \\ &\quad - \Big[\log\Big(p(F_j^{(1)} \mid M_{\mathrm{G}}) \\ &\quad + p(F_j^{(1)} \mid M_{\mathrm{L}})p(M_{\mathrm{L}})/p(M_{\mathrm{G}})\Big)\Big]\end{aligned} \tag{3.21}$$

As we are only interested in the maximum of $\log\left[O^{(1)}_{\mathrm{S/GL}}(F_j^{(1)})\right]$, the factor $\log\left[p(M_{\mathrm{S}})/p(M_{\mathrm{G}})\right]$ can be dropped from the expression.

In this version of the Viterbi algorithm, rather than storing a value proportional to the log-probabilities as in Sec. 3.5, here we store a value proportional to the log-odds ratio. Here we take the log-odds ratio defined in Eq. 3.21 and add the log-prior odds $p(\boldsymbol{\nu} \mid M_S)/(p(\boldsymbol{\nu} \mid M_N) + p(\boldsymbol{\nu} \mid M_L))$ which is the log-prior or any particular track. By assuming that the track transitions for the line and noise model are equally probable for any jump, we set the denominator of the prior-odds is a constant b. This then means Eq. 3.9 is modified to,

$$\begin{aligned}\hat{V}_{i,j} = \max_{k,l,m}\big(&T_{k,l,m} + b + V_{i-1,j+k} \\ &+ \log\left[O^{(1)}_{\mathrm{S/GL}}\left(F_j^{(1)}\right)\right]\big),\end{aligned} \tag{3.22}$$

where $\hat{V}$ refers to a log-odds ratio. The maximised statistic now has three tuneable parameters: the width (w_S) in Eq. 3.18, on the prior for a signal SNR squared, $p_{\mathrm{S}}(\lambda)$, the width (w_L) of the prior in the case of a line, $p_{\mathrm{L}}(\lambda)$, and the ratio of the prior on the line and noise models, $p(M_{\mathrm{L}})/p(M_{\mathrm{G}})$. These parameters are optimised for each search, where we initially estimate the SNR of a signal we hope to be sensitive to in each time slice, then use this as a guide for the width of the signal prior. This is then repeated for an expected line SNR and this is used for the width of the line prior. The ratio of line and noise models runs in the range 0 to 1, we set this limit as we do not expect an instrumental line to be as likely as Gaussian noise in any particular frequency bin.

This line-aware statistic can be applied in a more powerful way when we use multiple detectors and is similar to the approach in [**keitel2014SearchContinuous**]. The multiple-detector algorithm described in Sec. 3.5 returns the most probable track of a common signal assumed to be in Gaussian noise. As a consequence the algorithm will return large values of the log-likelihood even if there are inconsistent values of SFT power between the detectors, either from non-Gaussian noise or because the signal is not equally strong in the two detectors. However a signal with unequal power in the two detectors is more likely to be a non-Gaussian instrumental line than an astrophysical signal. The line-

aware statistic described in this section is designed to make the search more robust to such instrumental artefacts within realistic non-Gaussian data whilst maintaining sensitivity to astrophysical signals.

For most of the analysis examples presented here we use data which is the incoherent sum of 30-minute normalised SFTs over a day (described in more detail in Sec. 3.7). As a result the effects of the detector antenna patterns and of differential Doppler shifts are significantly reduced, and any signal should have a broadly similar summed log-likelihood in the same frequency bin in each detector. The statistic can then be modified such that we expect a similar log-likelihood in each detector.

In a similar way to the single-detector case, we can write out the evidence for each of the three models as follows. If a signal is present we therefore expect the SFT powers in both detectors to follow Eq. 3.16. Assuming for the moment that the noise variance is the same in both, we can determine the evidence for model M_{S} by marginalising over λ,

$$\begin{aligned} p(F_j^{(1)}, F_j^{(2)} \mid \nu_j, M_{\mathrm{S}}, I) = \int_0^\infty p(\lambda \mid M_{\mathrm{S}}) \\ p(F_j^{(1)}|\nu_j, \lambda, M_{\mathrm{S}}, I) p(F_j^{(2)}|\nu_j, \lambda, M_{\mathrm{S}}, I) d\lambda. \end{aligned} \tag{3.23}$$

We set the prior on λ the same as in the single detector case in Eq. 3.18. In this case, if an instrumental line is present in one of the detectors we expect to see signal-like power in that detector and noise-like power in the other. The evidence for this 'line' model (M_{L}) is therefore

$$\begin{aligned} p(F_j^{(1)}, F_j^{(2)} \mid \nu_j, M_{\mathrm{L}}, I) = \int_0^\infty p(\lambda \mid M_{\mathrm{L}}) \\ \Big[p(F_j^{(1)}|\nu_j, M_{\mathrm{N}}, I) p(F_j^{(2)}|\nu_j, \lambda, M_{\mathrm{S}}, I) \\ + p(F_j^{(1)}|\nu_j, \lambda, M_{\mathrm{S}}, I) p(F_j^{(2)}|\nu_j, M_{\mathrm{N}}, I) \Big] \, d\lambda, \end{aligned} \tag{3.24}$$

The third option is the simple case of approximately independent Gaussian noise in both of the detectors,

$$\begin{aligned} p(F_j^{(1)}, F_j^{(2)} \mid \nu_j, \lambda, M_{\mathrm{G}}, I) = p(F_j^{(1)} \mid \nu_j, M_{\mathrm{G}}, I) \\ p(F_j^{(2)} \mid \nu_j, M_{\mathrm{G}}, I). \end{aligned} \tag{3.25}$$

We can now find the posterior odds ratio for the presence of a signal over noise or a line by following the same steps as in Eq. 3.20. Once again we write this as a log-odds

ratio,

$$\begin{aligned}\log\left[O^{(2)}_{\mathrm{S/GL}}(F_j^{(1)}, F_j^{(2)})\right] &= \log\left[p(F_j^{(1)}, F_j^{(2)} \mid M_{\mathrm{S}})\right] \\ &- \Big[\log\Big(p(F_j^{(1)}, F_j^{(2)} \mid M_{\mathrm{G}}) \\ &+ p(F_j^{(1)}, F_j^{(2)} \mid M_{\mathrm{L}})p(M_{\mathrm{L}})/p(M_{\mathrm{G}})\Big)\Big]\end{aligned} \tag{3.26}$$

The factor $\log[p(M_{\mathrm{S}})/p(M_{\mathrm{G}})]$ can again be dropped from the expression.

For the multi-detector case we then modify Eq. 3.11 to,

$$\begin{aligned}\hat{V}_{i,j} = \max_{k,l,m}\big(&T_{k,l,m} + b + V_{i-1,j+k} \\ &+ \log\left[O^{(2)}_{\mathrm{S/GL}}\left(F_j^{(1)}, F_j^{(2)}\right)\right]\big),\end{aligned} \tag{3.27}$$

where $\hat{V}$ refers to a log-odds ratio. This is then optimised over the same three parameters as the single detector case.

Fig. 3.3 shows an example of the output of the statistic in Eq. 3.26 for different FFT powers F.

3.9 Line aware statistic for consistent amplitude

In Sec. 3.8 the 'line aware' statistic was designed to penalise high SFT powers in a single detector and reward powers which have a similar SNR. This is often a useful statistic to use when the detectors have similar sensitivities, however, this is not always the case. During an observing run of a GW detector, their sensitivity will vary with time due to fluctuating or new noise sources, or upgrades which increase the sensitivity. A change in the sensitivity, or noise floor, affects the SNR of a possible astrophysical signal in the data, i.e. a lower noise floor results in a higher SNR. In this section the above 'line aware' statistic is modified to account for the difference in sensitivities of the detectors. The statistic then highlights areas of consistent amplitude between detectors as opposed to consistent SNR.

There are two main factors which are taken into account when determining how sensitive a detector is in a particular time interval: the PSD of detector and the duty cycle. The PSD of the detector is a measure of how sensitive the detector is at that time and the duty cycle is the fraction of time in a given interval that the detector was collecting data. A decrease in the duty cycle and an increase in the PSD will decrease the SNR and vice-versa. To search for consistent amplitude Eq.3.27 is modified by weighting each detector by its PSD and duty cycle.

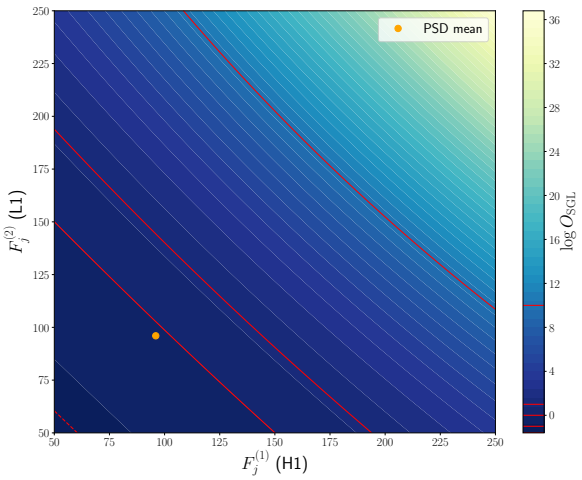

(a) The line-aware statistic is shown as a function of its input from each detector. This example is for parameters $p(\lambda, w_{\mathrm{S}}) = 4$, $p(\lambda, w_{\mathrm{L}}) = 0$ and $p(M_{\mathrm{L}})/p(M_{\mathrm{G}}) = 0$. So the line part of the statistic is not operating.

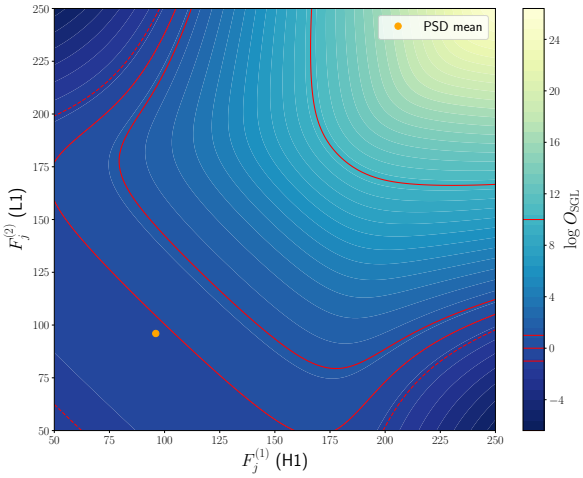

(b) The line-aware statistic is shown as a function of its input from each detector. This example is for parameters $p(\lambda, w_{\mathrm{S}}) = 4$, $p(\lambda, w_{\mathrm{L}}) = 5$ and $p(M_{\mathrm{L}})/p(M_{\mathrm{G}}) = 0.03$. Here we include the line part of the statistic.

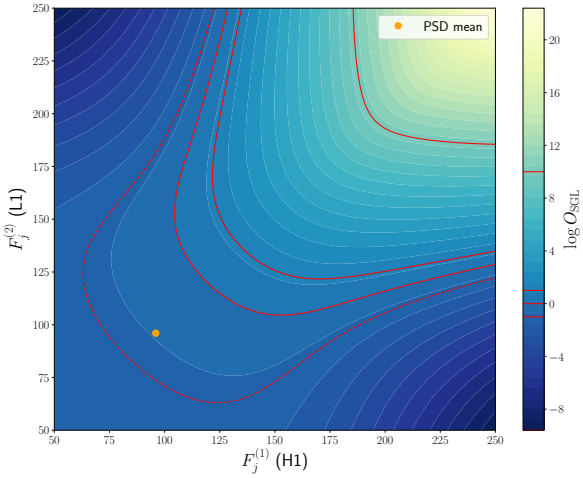

(c) The line-aware statistic is shown as a function of its input from each detector. This example is for parameters $p(\lambda, w_{\mathrm{S}}) = 4$, $p(\lambda, w_{\mathrm{L}}) = 5$ and $p(M_{\mathrm{L}})/p(M_{\mathrm{G}}) = 1$. Here the effect of lines is expected to be larger than the previous panel on the search. Therefore, the statistic forces the two detectors to have more similar power.

Figure 3.3: Lookup tables using the line aware statistic in Eq. 3.27. The PSD mean is the expected mean of a χ^2 distribution with 48 degrees of freedom, i.e. the expected power from our summed spectrograms F_j.

The definition of SNR is taken from [**prix2007SearchContinuous**] as

$$\rho_0^2 = \frac{h_0^2 T}{2S}(\alpha_1 A + \alpha_2 B + \alpha_3 C), \tag{3.28}$$

where ρ_0 is the optimal SNR, h_0 is the signal amplitude, T is the time of observation, S is the noise PSD and the terms in brackets include effects of the antenna pattern of the detector. The signal with amplitude h_0 will have the same amplitude at both detectors (H1 and L1), therefore we can relate the SNR in each detector by

$$\rho_L^2 = \frac{\rho_H^2 S_H T_L}{S_L T_H} \frac{(\alpha_1 A_L + \alpha_2 B_L + \alpha_3 C_L)}{(\alpha_1 A_H + \alpha_2 B_H + \alpha_3 C_H)}. \tag{3.29}$$

For the majority of the analysis that follows, the SFTs are summed over one day, this is explained in greater detail in Sec. 3.7. The components in the above equation which have the form $(\alpha_1 A + \alpha_2 B + \alpha_3 C)$, account for the antenna pattern of the detector as the earth rotates. These can be approximated to be the same for the two detectors H1 and L1 as we average out the daily modulation by summing SFTs. Therefore we can simplify the above Eq. 3.29 to

$$\rho_L^2 \approx \frac{\rho_H^2 S_H T_L}{S_L T_H} = l\rho_H^2. \tag{3.30}$$

This then gives a factor $l = S_H T_L / S_L T_H$ which relates the SNR of each detector, where S and T are the noise floor and duty cycle for a given data-set which is known prior to running the search.

This ratio of SNRs can be included in the integral over SNR for the signal model in Eq. 3.23 as follows

$$p(F_j^{(1)}, F_j^{(2)} \mid \nu_j, M_{\mathrm{S}}, I) = \int_0^\infty p(\lambda \mid M_{\mathrm{S}}) p(F_j^{(1)} | \nu_j, \lambda, M_{\mathrm{S}}, I) p(F_j^{(2)} | \nu_j, l\lambda, M_{\mathrm{S}}, I) d\lambda. \tag{3.31}$$

Similarly, the line model in Eq. 3.24 can be modified as

$$\begin{aligned} p(F_j^{(1)}, F_j^{(2)} \mid \nu_j, M_{\mathrm{L}}, I) = \int_0^\infty p(\lambda \mid M_{\mathrm{L}}) \Big[& p(F_j^{(1)} | \nu_j, M_{\mathrm{N}}, I) p(F_j^{(2)} | \nu_j, l\lambda, M_{\mathrm{S}}, I) \\ & + p(F_j^{(1)} | \nu_j, \lambda, M_{\mathrm{S}}, I) p(F_j^{(2)} | \nu_j, M_{\mathrm{N}}, I) \Big] d\lambda. \end{aligned} \tag{3.32}$$

Fig. 3.4 shows an example of the values of the statistic described in Eq. 3.32 plotted against a range of SFT powers from each detector. This demonstrates how the statistic accounts for a difference in sensitivity between detectors by allowing the SFT power, or effectively SNR, to vary more.

In Fig. 3.4 we show slices of the line-aware statistic with consistent amplitude for different values of l in Eq. 3.30. Figure 3.4a shows a slice where the SNR and duty cycle of the two detectors is the same, this is symmetric in the line-aware statistic as in Sec. 3.8.

The asymmetry in Fig. 3.4c demonstrates how as the sensitivity of one detector (L1) increases compared to (H1), the line-aware statistic allows for lower powers in H1 with corresponding higher powers in L1.

3.10 Testing the algorithm

The sensitivity of the algorithm was tested by searching for artificial signals from isolated neutron stars added to three types of noise-like data: continuous Gaussian noise, Gaussian noise but with periods of missing data, and real detector data (the S6 MDC [**walsh2016Comparisc**
The S6 MDC refers to a standardised set of simulated signals which are injected into real data, this set is also what is used for the injections into the two Gaussian noise cases. We describe each of the tests in more detail in Sec. 3.10.1, 3.10.2 and 3.10.3, but several common pre-processing steps are performed before running these datasets through the Viterbi algorithm:

1. We read SFTs generated from 1800 s stretches of data in 2 Hz bands between 100 and 200 Hz. The SFTs length is chosen to ensure that any signal is likely to be contained within the width of a single frequency bin during the length of one day, rather than being split across the bin edges (see below).

2. We estimate the noise PSD for each SFT by calculating a running median over frequency using LALSuite code `XLALSFTtoRnmed` [**ligoscientificcollaboration2018LIGOAlg**
this includes a bias factor to convert this to the mean and has a width of 100 bins. We then normalise the SFT by dividing it by its running median, giving the noise-like parts of the spectrum a mean power of approximately one.

3. The SFTs are then summed over one day, as described in Sec. 3.7. The signal parameters are chosen so that within the frequencies of the search, the signal will not fall in more than two frequency bins over this period.

   The differential Doppler shift of a signal seen at two detector sites due to the Earth's rotation $\Delta f_{\mathrm{rot}}^{(1,2)}$ is simply

   $$\Delta f_{\mathrm{rot}}^{(1,2)} = \frac{(\boldsymbol{v}^{(1)} - \boldsymbol{v}^{(2)}) \cdot \hat{\boldsymbol{s}}}{c} f_0, \tag{3.33}$$

   where $\boldsymbol{v}^{(1,2)}$ is the velocity of detector $1, 2$ in an inertial reference frame, f_0 is the instantaneous signal frequency in the frame, $\hat{\boldsymbol{s}}$ is the unit vector in the direction of the source and c is the speed of light. The maximum difference in frequency seen by the two LIGO detectors is

   $$\Delta f_{\mathrm{rot}} \approx 6.5 \times 10^{-7} f_0, \tag{3.34}$$

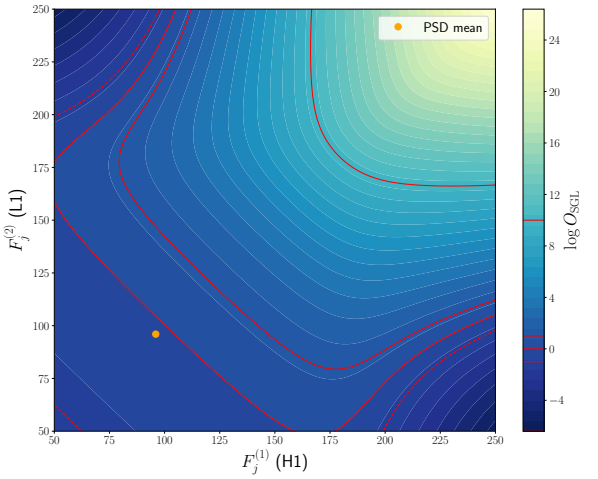

(a) The line-aware statistic with consistent amplitude is shown as a function of its input from each detector. This example is for an equal sensitivity and equal duty cycle for each of the detectors, i.e. $l = 1$.

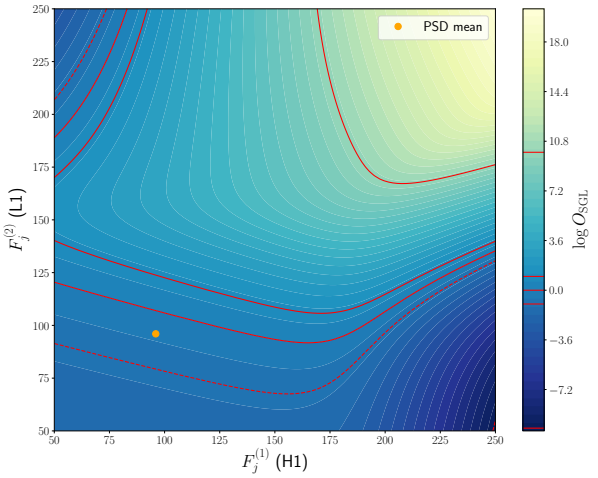

(b) The line-aware statistic with consistent amplitude is shown as a function of its input from each detector. This example has L1 with a greater sensitivity and/or duty cycle than H1 where $l = 0.55$.

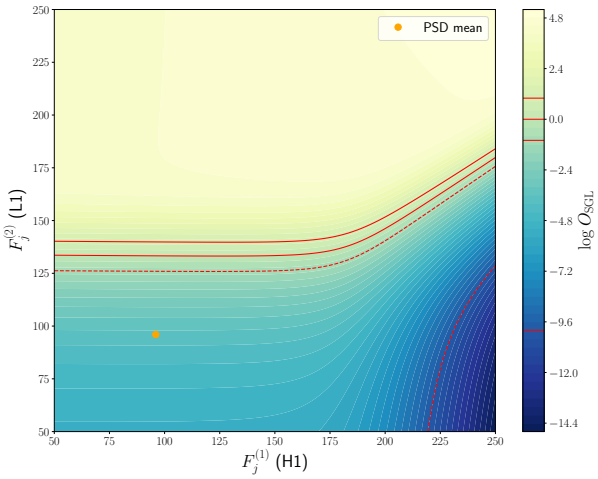

(c) The line-aware statistic with consistent amplitude is shown as a function of its input from each detector. This example has L1 with a greater sensitivity and/or duty cycle than H1 where $l = 0.1$.

Figure 3.4: Lookup tables using the line aware statistic for consistent amplitude as in Sec. 3.9. Each of these use the parameters $p_s(\lambda) = 4$,$p_l(\lambda) = 5$ and $p(M_L)/p(M_G) = 0.03$. The PSD mean is the expected mean of a χ^2 distribution with 48 degrees of freedom, i.e. the expected power from out summed spectrograms F_j.

so the frequency measured from a source in the equatorial plane with $f_0 = 200\,\mathrm{Hz}$ will differ by up to $1.3 \times 10^{-4}\,\mathrm{Hz}$ in the two detectors. This is ~ 4 times smaller than the frequency bin width of 1800 s SFTs ($5.6 \times 10^{-4}\,\mathrm{Hz}$), so signals at frequencies lower than this are likely to appear in the same frequency bin in the two detectors. Therefore, whilst at higher frequencies we still allow the signal to be in different frequency bins between the detectors, in the following searches, we do not allow this.

4. The data is then split into 0.1 Hz wide sub-bands which are overlapping by 0.05 Hz. These were chosen to ensure that signals are contained within a sub-band over the year. On these timescales the important contributions to the frequency evolution are the spin-down rate of the pulsar and the Doppler shift due to the earth orbit. To investigate the Doppler shift, we can look at a signal at 200 Hz, using Eq. 3.33 we can calculate the maximum shift in frequency due to the earth's orbit as,

$$\Delta f_{\mathrm{orbit}} = \frac{2\pi R_o}{T_o}\frac{1}{c} f_0 \approx 9.9 \times 10^{-5} f_0, \tag{3.35}$$

where T_o and R_o are the earth orbit time and radius. This gives a maximum Doppler shift of 0.019 Hz, this is a $\sim 1/5$ of the width of a sub-band, therefore, is more likely to be totally contained within a sub-band than crossing over the edge. To account for the cases where the signal frequency crosses over the edge of a sub-band, the sub-bands overlap by 0.05 Hz so that the majority of the signals should be completely contained within at least one of the sub-bands. To investigate the spin-down of the pulsar, we look at the length of data, $T = 4.05 \times 10^7\,\mathrm{s}$ and we choose a sub-band width of 0.1 Hz. For a signal to drift over the width of a whole sub-band we would need f-dot of,

$$\frac{df}{dt} > \left|\frac{-0.1}{4.05 \times 10^7}\right| = 2.4 \times 10^{-9}\mathrm{Hz/s}. \tag{3.36}$$

The majority of the injections that follow satisfy this condition, signals which are greater than this, and therefore drift over multiple bands, are vetoed from the search by excluding the frequency bands they cover.

5. The two detector Viterbi algorithm is then run using the line aware statistic (see Sec. 3.8). There are 4 parameters which we optimise in this search. The transition probabilities, where we have one parameter τ which is the ratio of the probability of going straight to the probability of going either up or down. Due to the averaging procedure, the signals received at each detector are forced to follow a common track which is equal to the 'imaginary' detectors track. The other three parameters, w_S, w_L and $\mathrm{p(M_L)/p(M_N)}$, are described in Sec. 3.8.

6. The algorithm then returns the most probable track though the data, and the value $\propto$ the log-odds in the final time step, i.e., the maximum final value, $\max_j(V_{N,j})$, in Eq. 3.27, which is then our detection statistic.

As an example of what the algorithm returns, Fig. 3.5 shows the tracks in the two detectors, H1 and L1. This also shows the log-odds ratio of ending in any frequency bin, i.e., all the elements in Eq. 3.27. In this figure, each time segment of the log-odds ratios have been normalised such that the sum of the odds ratios is 1.

In the following tests there are two main quantities which we use to determine the sensitivity. These are sensitivity depth $\mathcal{D}$ and the optimal SNR ρ. The sensitivity depth, $\mathcal{D}$, is defined in [**behnke2015PostprocessingMethods**] as,

$$\mathcal{D}(f) = \frac{\sqrt{S_h(f)}}{h_0}, \tag{3.37}$$

where $S_h(f)$ is the single-sided noise PSD and h_0 is the GW amplitude. The optimal SNR is defined as,

$$\rho^2 = \sum_X 4\Re \int_0^\infty \frac{\tilde{h}^X(f)\tilde{h}^{X*}(f)}{S^X(f)} df, \tag{3.38}$$

where X indexes the detectors and $\tilde{h}(f)$ is the Fourier transform of the time series of the signal $h(t)$. This expression is defined in [**prix2007SearchContinuous**] for a double-sided PSD and we have defined it for the more common single-sided case.

3.10.1 S6 injections into gapless Gaussian noise

The first test involves injecting signals into Gaussian noise. The power spectrum of a Gaussian noise time-series follows a χ^2 distribution with two degrees of freedom, therefore, as we search through the power spectrum, we generate spectrograms which follow a χ^2 distribution. These spectrograms are 0.1 Hz wide and are set at 0.05 Hz intervals between 100 Hz and 200 Hz. The bins are 1./1800 Hz wide and 1800s long, where the total length of data is the same as S6, i.e., $\sim$ 1.3 years. We then generate the signals, where the pulsars parameters are fixed to the same values as the injections in the S6 MDC in this band, these values are outlined in [**walsh2016ComparisonMethods**].

The values of f_0 for the injections were not always centred in a sub-band, therefore a number of sub-bands contained only part of the injected signal. These sub-bands were ignored as they contaminated the signal statistics and only the sub-band which contained the whole signal was accepted. This reduced the number of sub-bands from 2000 to 1762 with the removal of 238 sub-bands containing only part of a signal. This set also includes signals that drift across multiple sub-bands due to their high spin-down rate. Only two signals were removed due to their spin-down values, which were $> 5 \times 10^{-9}$ Hz/s, these

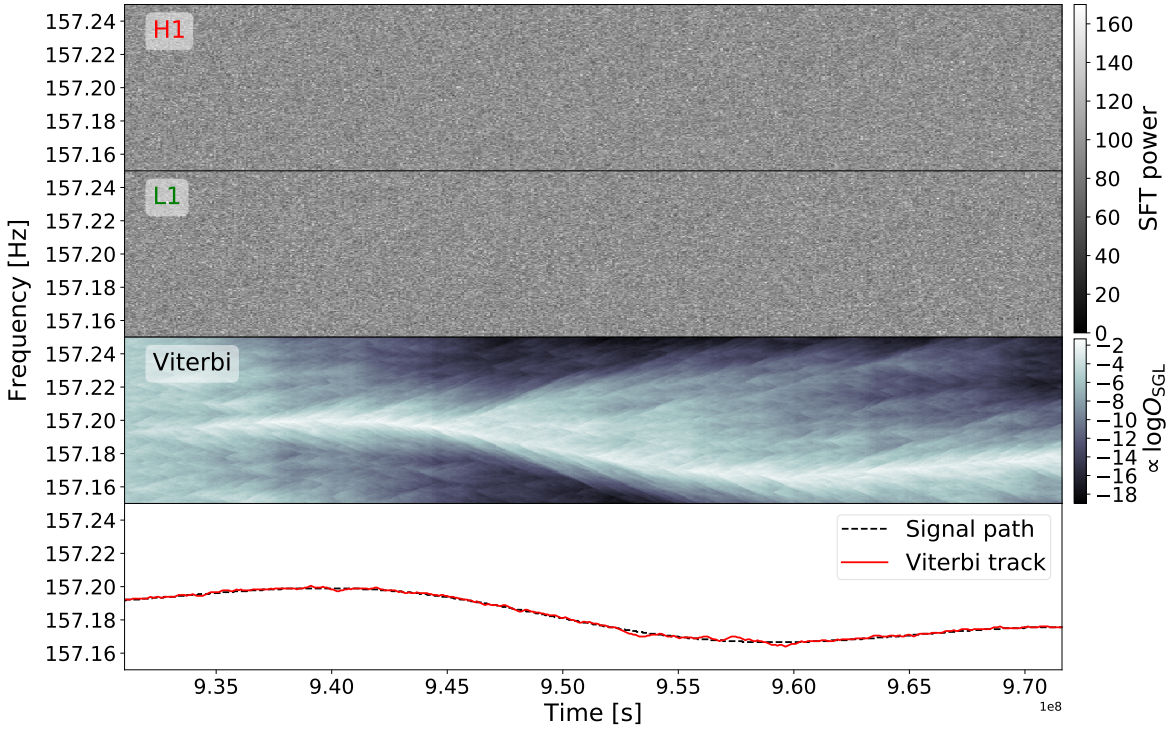

Figure 3.5: The results that the SOAP algorithm returns from an injection with an optimal SNR of 90, i.e., the SNR in H1 is 64 and the SNR in L1 is 62. The signal is injected into Gaussian noise, where the 1800 s SFTs have been summed over 1 day. The top panel shows a simulation of summed SFTs from H1, the second panel shows the same for L1, the third panel shows the values proportional to the log-odds ratios in Eq. 3.27. The log-odds have been normalised such that the sum of all the odds ratios in every time bin are equal to 1. The bottom panel shows the injected signal track (black dotted) and the track found in the 'imaginary' detector by the two-detector SOAP search with the line-aware statistic (red), both of these tracks are at the geo-centre. In this case the root median square (RMS) of the difference between the Viterbi track and injected signal track was ∼1 bin, where 1 bin is 0.00056 Hz wide.

were the two hardware injections in the 100-200 Hz band.

For each injection the SOAP algorithm returns the detection statistic described in Sec. 3.8 and 3.10. We calculate a false alarm rate, which is the fraction of bands that have no injection that do exceed a given threshold. This is set to 1% and is used as a detection threshold. We then take all of the bands and if they pass the threshold we set them as detected, i.e., 1, and if they do not they are set as not detected, i.e., 0. This then leaves us with a set of binomial data, where the efficiency curves later in this section are sigmoids which have been fitted to this. The sigmoid follows,

$$s(x; x_0, k) = \frac{1}{1 - \exp\left(-k(x - x_0)\right)}. \tag{3.39}$$

The fit is done by sampling the posterior, i.e.,

$$p(x_0, k \mid b) \propto p(x_0, k) p(x \mid x_0, k), \tag{3.40}$$

where $p(x_0, k)$ is the prior and we set to a flat prior and $p(x \mid x_0, k)$ is the likelihood function which is defined by,

$$p(\bar{x} \mid x_0, k) = \prod_{j=0} \frac{n!}{k!(n-k)!} s(x_j \mid x_0, k)^k \\ (1 - s(x_j \mid x_0, k))^{n-k}. \tag{3.41}$$

To plot the efficiency curves and lower and upper error bounds, we sample Eq. 3.40 using MCMC and then take the mean and the 5th and 95th percentiles respectively for each point in SNR or depth and plot these. Figures 3.6a and 3.6c then show the efficiency curves for the analyses plotted against the signals optimal SNR and depth respectively. The parameters of the search and their optimised values are shown in Tab. 3.1. Where we set the prior on the line model to 0 as this part is irrelevant to this search due to the lack of lines in the data.

From this we can determine that in Gaussian noise without gaps, the Viterbi algorithm can detect to an SNR of ~ 60 and a depth of $\sim 33\,\mathrm{Hz}^{-1/2}$ with 95% efficiency at a 1% false alarm.

Fig. 3.6b and 3.6d, show the RMS of the difference between the injected signal track and the track found by Viterbi for SNR and sensitivity depth respectively. This shows that at SNR of 60, where we are detecting signals with a 95% efficiency, the signals have a mean RMS of ~ 2 frequency bins. Here one bin width is 0.00056 Hz therefore, we have and RMS of ~ 0.0012 Hz.

Table 3.1: Table shows the ranges of the search parameters and their optimised values for injections into gapless Gaussian noise, Gaussian noise with gaps and the S6 MDC. For gapless Gaussian noise and Gaussian noise with gaps, there are 10 parameter values spaced linearly between the limits. For the S6 MDC the parameters, τ, w_{L} and w_{S} were distributed in log space between the limits and $p(M_L)/p(M_N)$ is distributed uniformly.

	τ	w_S	w_L	$p(M_L)/p(M_N)$
		Gapless Gaussian		
limits	[1.0,1.3]	[0.1,5.0]	None	0.0
optimised	1.1	2.06	None	0.0
		Gaussian with gaps		
limits	[1.0,1.3]	[0.1,5.0]	None	0.0
optimised	1.1	2.06	None	0.0
		S6 MDC		
limits	[1.0,1.1]	[0.1,5.0]	[0.1,6.0]	[0.0,1.0]
optimised	1.00000001	4.0	5.0	0.0387

3.10.2 S6 injections into Gaussian noise with gaps

In the second test, we attempt to more closely mirror the S6 MDC [**walsh2016ComparisonMetho**
in two stages. The first uses the same injection method as Sec. 3.10.1 however, removes the SFTs where there are gaps in S6. The second uses the same injection method again including gaps, however, uses a different value for the noise floor for each SFT, this is calculated for each band and SFT from S6 data.

Both detectors in S6 had a duty cycle of ∼50% [**aasi2015CharacterizationLIGO**], which means that there are sections of time where there is no data in either one or both detectors. In the sections where one detector is observing but the other is not, the multi detector statistic will not behave correctly as it only has access to data from a single detector. In these sections we switch from using the multi-detector statistic to the single-detector statistic using the same parameters, these are both defined in defined in Sec. 3.8.

The process of removing sub-bands and generating efficiency curves is the same as in Sec. 3.10.1.

We set a 1% false alarm rate and generate an efficiency curve for SNR and depth in Fig. 3.6a and Fig. 3.6c respectively. From these efficiency plots we can see to an SNR of ~ 72 or a depth of $\sim 13\,\mathrm{Hz}^{-1/2}$ at a 95% confidence with a false alarm of 1%.

The parameters of the search which were optimised and their optimised values are shown in Tab. 3.1.

In Fig. 3.6b and 3.6d show the RMS of the difference between the injected signal track

and the track found by Viterbi for SNR and sensitivity depth respectively. This shows that at SNR of 72, where we are detecting signals with a 95% efficiency, the signals have a mean RMS of ~ 10 frequency bins (0.0056 Hz).

3.10.3 Tests on the S6 MDC

For a more direct comparison to other CW searches and to see how the algorithm performs with real data, we test the two detector SOAP algorithm using the S6 MDC. We focus this search on the 100-200 Hz band, there are two main reasons for this, one being that this is LIGOs most sensitive band and the other is that for much higher frequencies the signal will drift over larger frequency ranges, therefore, our SFT length will have to be changed. Here the 1800 s SFTs are split as in Sec. 3.10, where after normalisation, the data is split into 0.1 Hz wide sub-bands overlapping by 0.05 Hz.

The two detector SOAP algorithm using the line-aware statistic in Sec. 3.8 is then run on each sub-band under the assumption that the detectors have the same sensitivity. For this search we have four parameters which we optimise, the ranges and optimised values are shown in Tab. 3.1.

As in Sec. 3.10.2, only the sub-bands which contained the entire frequency evolution of the signal were selected. Out of the 2000 sub-bands, 238 were removed due the sub-band only containing part of the signals frequency evolution. The main difference between the analysis for Gaussian noise and real data is that the real data is contaminated with instrumental lines. This means that whilst the techniques described in Sec. 3.8 reduce the number of contaminated bands with a high statistic value, there are still instrumental lines which are coincident between the detectors and which could not be removed with these techniques. Within the data there are large number of lines at integer Hertz, which are seen in coincidence between the two detectors, these are thought to originate from digital electronics [**coughlin2010NoiseLine**]. Therefore the frequency bins ± 1 bin of each integer frequency in Hertz were removed and filled with the expectation value of the noise. To remove instrumental effects at other frequencies, the sub-bands which gave values of our statistic above a chosen threshold were investigated by eye. In this case 344 sub-bands were investigated, and any which were contaminated were vetoed. From these 344 sub-bands, 193 were removed from the analysis. The predominant feature in the bands which were removed were broad spectral features which lasted the whole run. Therefore, out of the 2000 sub-bands which are searched over, a total number of 431 sub-bands were removed.

The process to calculate the efficiency curves is the same as in Sec. 3.10.2 and 3.10.1.

Fig. 3.6c and Fig. 3.6a show the efficiency curves for SNR and depth respectively. These show that we can detect and SNR of ~ 74 and a sensitivity depth of $\sim 13\,\mathrm{Hz}^{-1/2}$ with an efficiency of 95% at a false alarm of 1%. These results can then be compared to other searches

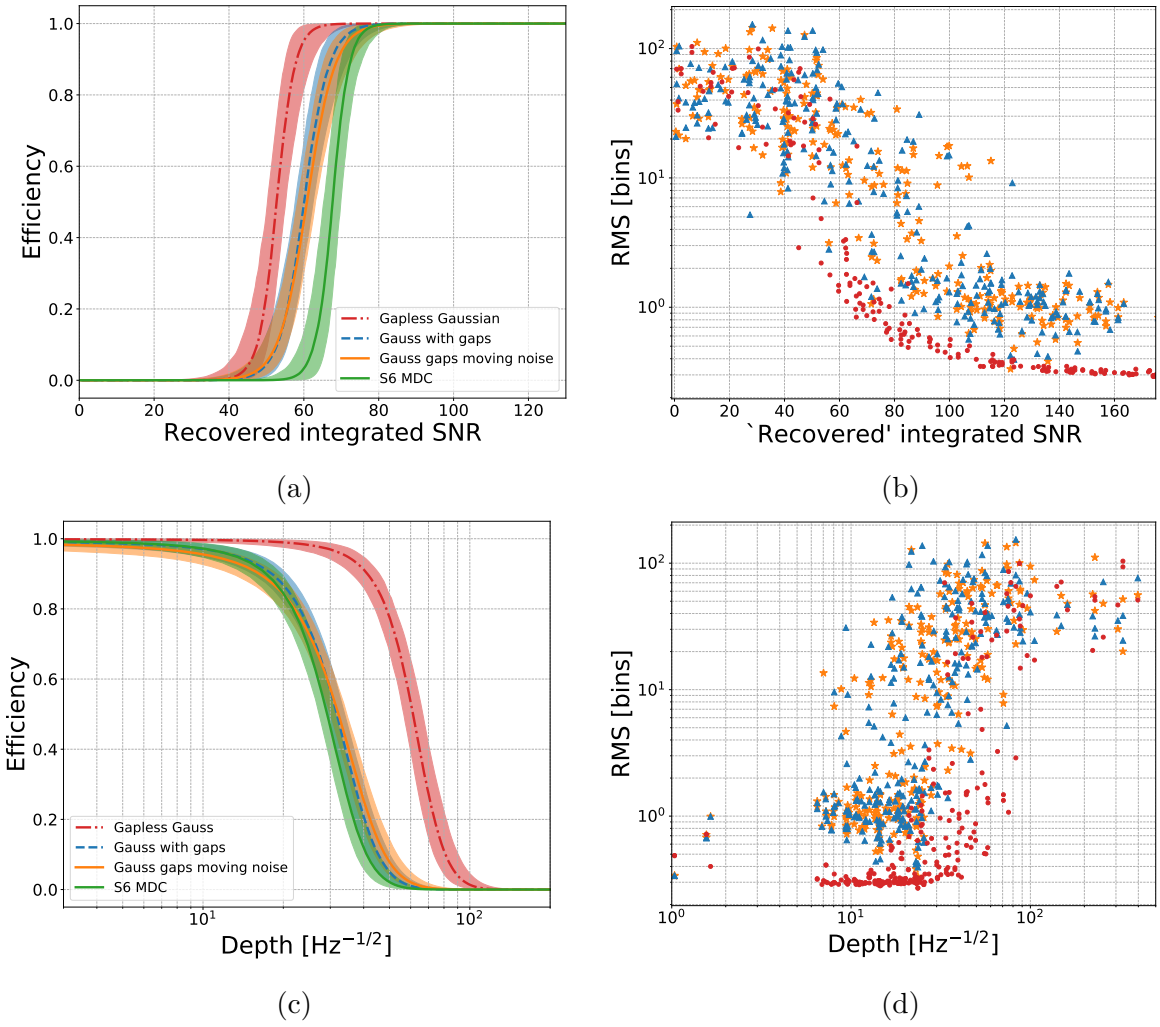

Figure 3.6: Panels 3.6a and 3.6c show the detection efficiency as a function of SNR and depth respectively. Here SNR is the the integrated SNR which we would expect to recover from the available data. The four curves refer to injections into gapless Gaussian noise (red), Gaussian noise with gaps in data, where the noise floor is either fixed (blue-dashed) or it is moving with time (orange) in the same way as the S6 MDC and injections into real data i.e., the S6 MDC. In the gapless Gaussian noise case, the recovered integrated SNR refers to the SNR the injection would have if it had the same amount of data as in the cases with gaps. The curves are made by fitting a sigmoid Eq. 3.37 to binomial detection data with a 1% false alarm rate, as explained in Sec. 3.10.1, the error bounds are the 5% and 95% intervals. At 95% efficiency and a 1% false alarm rate, this shows we can detect to an SNR of ~ 60 and a sensitivity depth of $\sim 34\,\mathrm{Hz}^{-1/2}$ for gapless Gaussian noise and an SNR of ~ 69 and 72 and a sensitivity depth of $\sim 13\,\mathrm{Hz}^{-1/2}$ and $\sim 10\,\mathrm{Hz}^{-1/2}$ for the Gaussian with gaps case with fixed noise floor and moving noise floor respectively. For the S6 MDC we can detect an SNR of ~ 74 and a sensitivity depth of $\sim 13\,\mathrm{Hz}^{-1/2}$. Panels 3.6b and 3.6d show the RMS of the difference between the injected signal track and the track found by SOAP as a function of SNR and sensitivity depth respectively. This is shown in units of bins where each bin is 0.00056 Hz wide.

in the S6 MDC comparison paper [**walsh2016ComparisonMethods**]. Whilst we only search in the 100 - 200 Hz range, the closest comparison in [**walsh2016ComparisonMethods**] is the test in the 40 - 500 Hz range, such as in Fig. 4 in [**walsh2016ComparisonMethods**]. Here our algorithm sits roughly in the middle of all other searches in terms of sensitivity.

3.11 Optimisation of Line-aware statistic.

For the above searches we used optimised versions on the line aware statistic, however, we have yet to explain how this was optimised. The aim is to find the best parameters for any given search; the four parameters are τ, w_{S}, w_{L} and $p(M_{\mathrm{L}})/p(M_{\mathrm{G}})$. We find the optimum values empirically by running the entire search for each parameter value that needs to be tested. This is possible as the search is relatively fast, this will be explained in Sec. 3.14. The line aware statistic is time consuming to calculate, therefore, to reduce the computational time, it is pre-calculated and placed into lookup tables such that it is calculated once and called many times. These lookup tables were calculated for values of the SFT power summed over one day F. The summed SFT power is in the range 1 to 400 in each of the detectors as shown in Fig. 3.3. The four parameters ranges were chosen based on what we expect to see. For example we expect a signal to have a small SNR therefore, the range of w_{S} is between 0.1-10 in the S6 case. We expect the instrumental lines to have a larger SNR therefore, w_{L} ranges between 0.1-20 in the S6 case. Each of the parameter ranges is shown in Tab. 3.2.

We can then measure of the sensitivity of that search and pick the lookup table associated with a set of parameters which gives the highest sensitivity. We measure the sensitivity by taking the value of SNR which is at 95% efficiency at 5% false alarm.

3.11.1 Gaussian noise simulations

For injections into Gaussian noise, we know that there are no instrumental lines, therefore, we do not need to optimise over the 'lines' part of the statistic and can set the parameter $p(M_{\mathrm{L}})/p(M_{\mathrm{G}})$ to zero which renders the parameter w_{L} ($p_L(\lambda)$) redundant. This then reduces the complexity of the problem by leaving us with only two parameters to optimise over, τ and w_{S} ($p_S(\lambda)$). Whilst this optimisation was partially done in Sec. 3.10, with the result in Tab. 3.1, this is repeated more completely here. The parameters were optimised in the range shown in Tab. 3.2.

For each point in Fig. 3.7, the entire SOAP search was run using the corresponding parameters as input. Efficiency curves are then generated for each of these runs and the values for the SNR at 95% efficiency are recorded. Figure 3.7 then shows the 95% efficiency for each parameter value. There appears not to be any single value which gives an optimum, however, the dark stripe in Fig. 3.7 running from the bottom left to the red

Table 3.2: Table shows the ranges of the search parameters and their optimised values for injections into Gaussian noise and the S6 MDC. For Gaussian noise there are 30 parameter values spaced linearly between the limits. For the S6 MDC the transition matrix parameters, τ, had three values space between the limits. This is because the search is relatively insensitive to this parameter. The parameters w_{L}, w_{S} and $p(M_{\mathrm{L}})/p(M_{\mathrm{G}})$ had 10 parameters distributed in linearly between the limits.

	τ	w_S	w_L	$p(M_{\mathrm{L}})/p(M_{\mathrm{G}})$
Gaussian noise				
limits	[1.0,1.1]	[0.1,7.0]	None	0.0
S6 MDC				
limits	[1.0,1.1]	[0.1,10.0]	[0.1,20.0]	[0.0,0.3]

cross is the combinations of parameters which give the best result. The point where the red lines cross is the parameters used in previous searched in Sec. 3.10.1 and 3.10.2. This falls on the line where the algorithm performs best. Venturing far from this 'optimum' line does not change the results a great deal as the SNR does not change much. The search is then not particularly sensitive to choice of parameters in Gaussian noise.

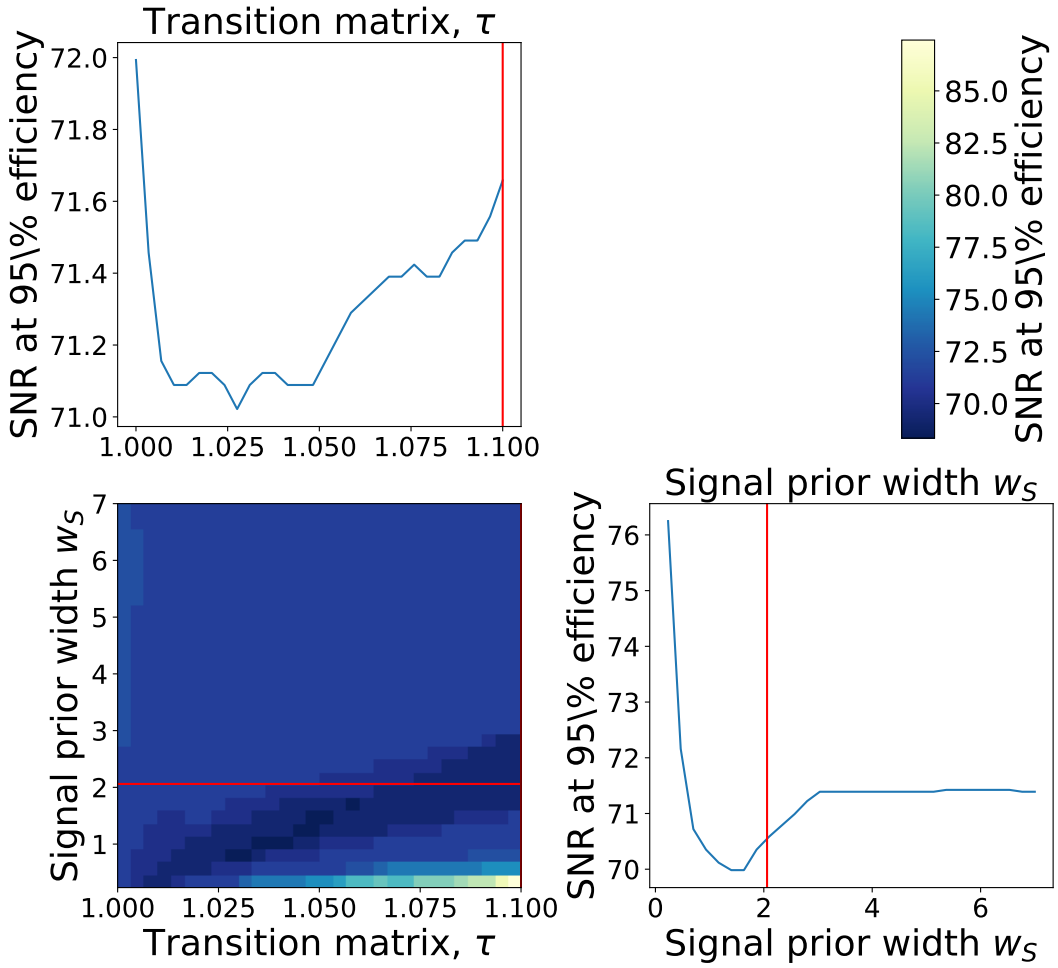

Figure 3.7: In Gaussian noise the transition matrix parameter τ and the width of the prior on the signal case w_S were optimised. The key part to remember when reading this plot is that the lower the value of SNR the better the search has performed. Therefore darker blue areas are when the search performed better. This map shows that there is an area parameter space where the search performed best, however the search is not that sensitive to the choice of parameter. The red lines on here shows the parameters used in the searches in this section.

3.11.2 S6 MDC injections

As the S6 MDC data-set is real detector data, there are many examples of instrumental lines. This is where we expect the line-aware statistic to have the greatest effect in improving the sensitivity. Here all four parameters are optimised over in the ranges described in Tab. 3.1. This greatly increases the number of lookup tables which need to be generated and therefore the number of times the search needs to be run. The tests were run for each set of parameters in the 100-200 Hz frequency band in the S6 MDC, where the testing process is the same as in Sec. 3.10. Figure 3.8 shows the projections in parameter space for each of the parameters, where the values are the SNRs at 95% efficiency. The projections are made by taking the mean across the other parameters.

In Fig. 3.8, the SNR does not change much at all for the transition matrix parameter τ. A small range was used for τ around lower values $(1.0-1.1)$ based on the test in Gaussian noise in Sec. 3.11.2. The parameter w_{S}, which is the width of the prior of a signal, also does not show much variation over the parameter range. The parameters which had the largest affect on the sensitivity of the search are the with of the prior of an instrumental line w_{L} and the ratio of the probabilities of a line and Gaussian noise $p(M_{\mathrm{L}})/p(M_{\mathrm{G}})$. Lower values of w_{L} are disfavoured in this range, this is to be expected as many instrumental lines have a large SNR. Also larger values of $p(M_{\mathrm{L}})/p(M_{\mathrm{G}})$ are preferred, which implies that there are a large fraction of instrumental lines within this dataset. There are then large areas of the parameter space which can give a reasonable sensitivity for the SOAP search.

To find the optimum set of parameters, the global minimum of this parameter space is taken. Using the SNR at 95% efficiency and 5% false alarm as the measure of sensitivity, there are seven different parameter sets which return the same minimum SNR, these are shown in Tab. 3.3. The exact set of parameters however, can vary depending on the choice of the sensitivity measure, i.e. using a 90% efficiency at 10% false alarm gives ~ 1000 possible parameter sets at the minimum. Whilst this leaves many choices for the correct set of parameters to use, it means that choosing a set of parameters which is in the area of low SNR, for example high w_{L}, will return a sensitivity comparable to the searches optimal sensitivity. A better estimate of the global minimum could be found by using a finer grid in parameter space and testing on a larger number of simulations to get smoother efficiency curves. This would cause a large increase in the computational cost and given that the sensitivity does not change much in the parameter range used, would result in a small gain in sensitivity. As one of the strengths of this search is its speed, it is not worth this computational cost given it performs well with many sets of parameters described above.

The parameters chosen for the search can then be any from the set in Tab 3.3, however, there are many others which can give a similar sensitivity. For the results in this chapter

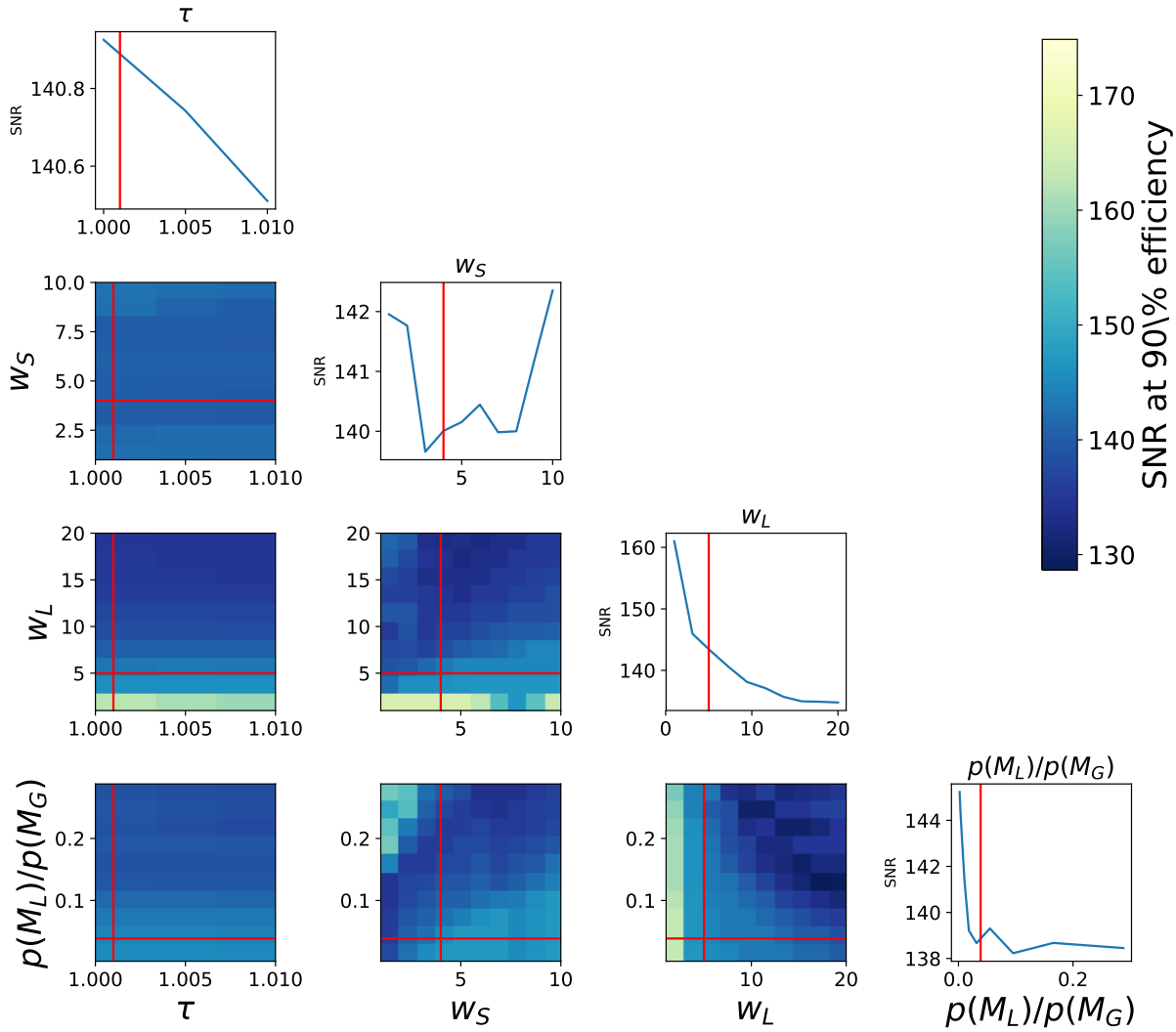

Figure 3.8: When using real S6 data, all four parameters of the search were optimised over on simulations in real data. The plot above shows the SNR at 90% efficiency for each of the parameters where the ranges are in Tab. 3.2. Lower values of SNR mean the search is performing better. The red lines show the parameters used in the searches in this section and the sections that follow. Whilst this does not seem optimal, the search does not underperform much using the current choice of parameters (red).

and the rest of this thesis, the parameters from Tab. 3.1 (red lines in Fig. 3.11.2) are used.

Table 3.3: A subset of the optimal parameters is shown, where there are ~ 1000 examples which fall at the minimum. The examples here shows the general structure where, $w_{\mathrm{S}} < w_{\mathrm{L}}$ and as w_{L} increased the ratio $p(M_{\mathrm{L}})/p(M_{\mathrm{G}})$ increases.

	τ	w_S	w_L	$p(M_{\mathrm{L}})/p(M_{\mathrm{G}})$
1	1.0	7.0	15.78	0.2879
2	1.005	8.0	20.0	0.2879
3	1.01	8.0	20.0	0.2879
4	1.0	6.0	13.67	0.2879
5	1.01	5.0	17.89	0.2879
6	1.0	8.0	20.0	0.2879
7	1.0	5.0	11.56	0.2879

Comparison of sensitivity

To visualise how the optimised parameters perform, we can test them on a simulated signal in a time-frequency spectrogram. In Fig. 3.9 one of the detectors contains a narrow instrumental line and both detectors contain a CW signal. In the case optimised in Gaussian noise, the search is looking for high power in both detectors. The strong instrumental line satisfies this when the astrophysical signal is weak. This is demonstrated in the Viterbi map in the fourth panel of Fig. 3.9, the log-odds becomes dominated by the instrumental line. Whilst the astrophysical signal is still visible for parts of the spectrogram, the line dominates the final statistic. The parameters optimised for S6, allow the search to look for more consistent SNR in each of the detectors. The lines in Fig. 3.9 labelled "Line-aware" refer to the set of parameters in row 1 of Tab. 3.3 and "Old Line-aware" refers to those in Tab. 3.1. Figure 3.9 demonstrates how using the line-aware part of the statistic improves the robustness of the algorithm against non-astrophysical signals compared to the Gaussian noise case. Figure 3.9 shows how the two statistics optimised for the S6 MDC perform similarly on this specific example. However, one can also see how each set of parameters performs when tested on many examples.

To see how each parameter performs on many examples, one can look at the efficiency curves from each parameter set. The parameter sets in Fig. 3.9 are tested alongside a simple statistic from Sec. 3.4 which uses the sum of the SFT power along the Viterbi track. These four parameter sets are tested on S6 MDC simulations between 100 and 200 Hz. The process of testing on the S6 MDC and generating the efficiency curves is the same as in Sec. 3.10. Figure 3.10 shows the efficiency curves at a 5% false alarm rate.

One can see that the parameters optimised for Gaussian noise do not perform well when instrumental lines are introduced. In fact this performs worse than using just the summed SFT power as a statistic. Improvements are then made when using the line-aware statistic parameters optimised in the S6 MDC. The parameters optimised in Sec. 3.11.2 outperform the ones in Tab. 3.1. However, given that the majority of the gain in sensitivity for this search is from manually removing contaminated bands as in Sec. 3.10, the parameters in Tab. 3.1 are used throughout this thesis.

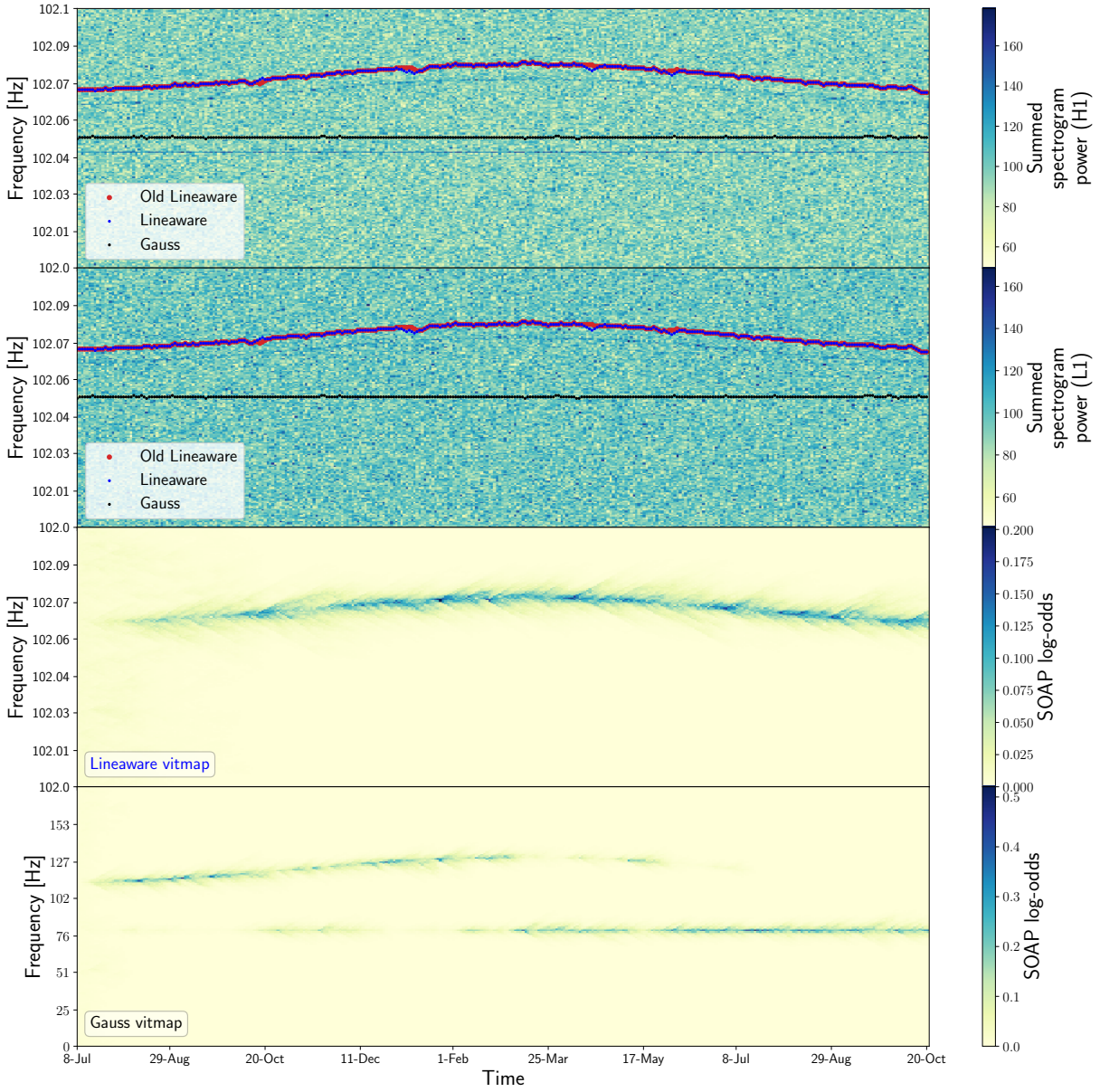

Figure 3.9: The spectrograms of H1 and L1 which contain a CW simulation are shown in the first and second panel respectively. The top panel (H1) also contains a narrow spectral line at $\sim$ 102.5 Hz. The Viterbi tracks from the SOAP search with Line-aware statistic optimised for S6 and Gaussian noise are shown in blue and black respectively. These are shifted up by 10 frequency bins to allow the underlying feature to be identified in the spectrogram. The third and fourth panel show the Viterbi map for the statistic values optimised in the S6 MDC and Gaussian noise respectively. The Viterbi map for the S6 MDC statistic shows areas of high log-odds around the signal track. The Viterbi map for the Gaussian noise optimised statistic shows high log-odds around the signal and the instrumental line and identified the track along the instrumental line to be the most significant.

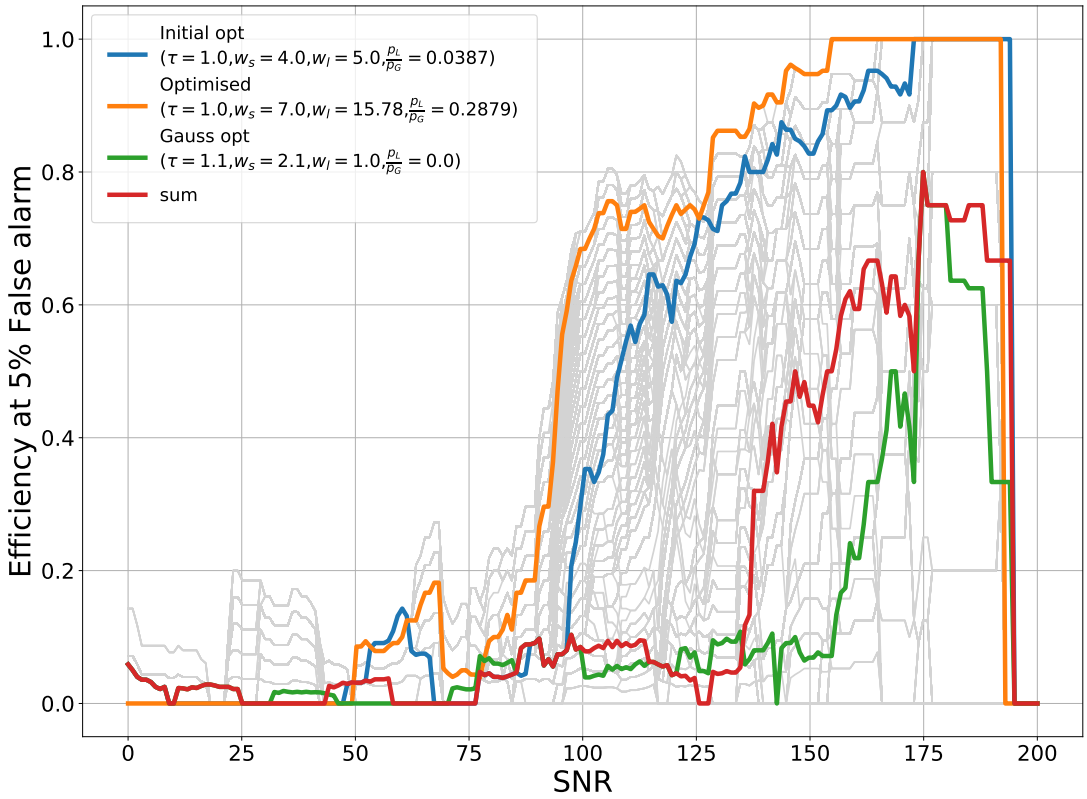

Figure 3.10: The sensitivity can be compared for three sets of parameters of the line aware statistic. These are the sets optimised for Gaussian noise and the S6 MDC in Sec. 3.11 above (Optimised and Gauss opt) and the values used in Tab. 3.1 (Initial opt). One other set uses the normalised SFT power as the statistic instead of the line-aware statistic, this is the red curve (sum). Each of these tests are results from being tested on the S6 MDC between 40-500 Hz. The grey curves show the results from the optimisations run using all line-aware statistic parameters, this used the S6 MDC data between 100-200 Hz.

3.12 Sensitivity with frequency

The tests in Sec. 3.10 on Gaussian noise and S6 data were conducted in the range from 100-200 Hz. This was chosen to be within the most sensitive band of LIGO as this is where a signal is most likely to be discovered. However, signals can appear at much higher frequencies also. Therefore, it is important to see how the sensitivity of the search varies with the frequency.

For this test we simulated CW signals in Gaussian noise with no gaps in data. The injections used the same source parameters as in the S6 MDC [**walsh2016ComparisonMethods**] and the tests above. This has the exception that the integrated recovered SNR of the signal is sampled uniformly between 50 and 500. These injections were then made at frequencies of 100, 250, 500, 750, 1000, 1500 and 2000 Hz, where the band width is 2 Hz. i.e. the simulations were in frequency bands 100-102 Hz, 250-252 Hz etc. The setup of the search was the same as in the above sections. Here each sub-band is 0.1 Hz wide, and the parameters of the SOAP search were as in Tab. 3.1.

Figure 3.11 shows the resulting efficiency curves from each of these tests. This is for a 1% false alarm rate, which means that 1% of sub-bands which contained no injection crossed the detection threshold. This plot shows how the sensitivity of the search drops as the frequency increases. This is perhaps unfair to the algorithm as we used the setup of the search which has been optimised for the range 100-200 Hz. Optimising the search means choosing the parameters of SOAP, the key parameter which will affect this is the transition matrix. As the simulated signals frequency is increased, the scale of the Doppler modulation will also increase. This means that at higher frequencies the signal is likely to jump greater than a single frequency bin. The current setup of the search does not allow this size of jump and therefore would struggle to identify this type of track. The other main factor which will decrease this sensitivity is the sub-band width of 0.1 Hz. As the signal frequency increases the scale of the Doppler modulation will increase as shown in Eq. 3.35. For example at 1000 Hz, the Doppler shift is $\sim$ 0.1 Hz, the signal is then more likely to not be fully contained within a frequency band. Therefore, the search can not accumulate all of the injected SNR The search in its current state however, does lose sensitivity as the signal frequency increases.

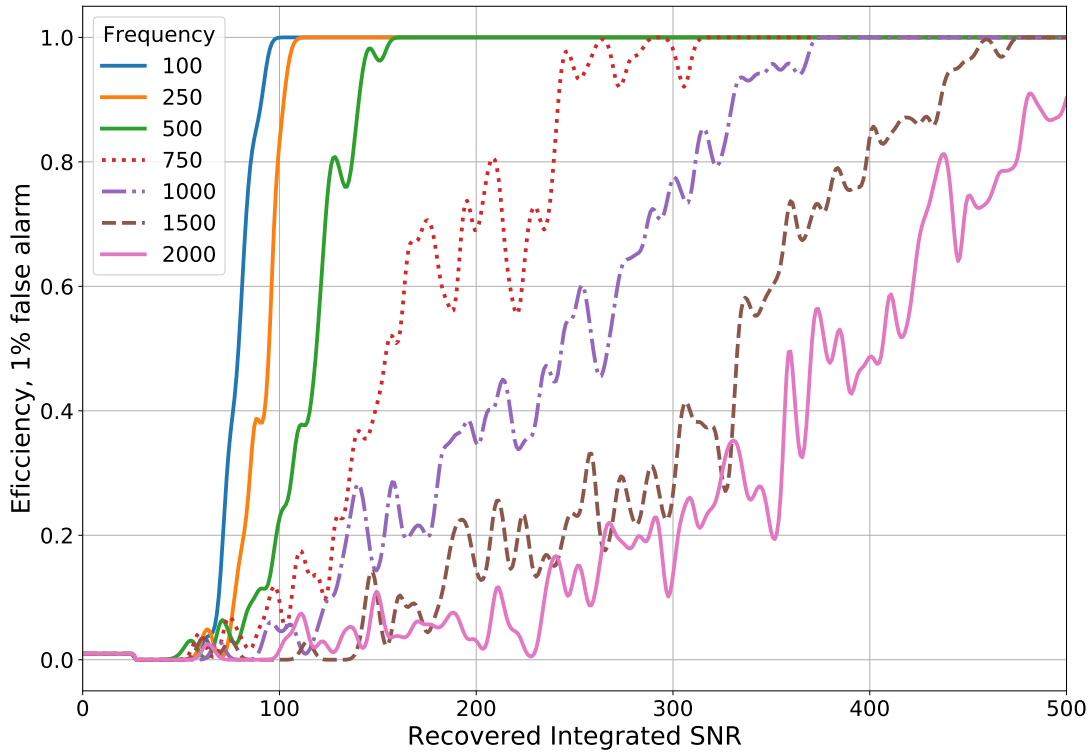

(a)

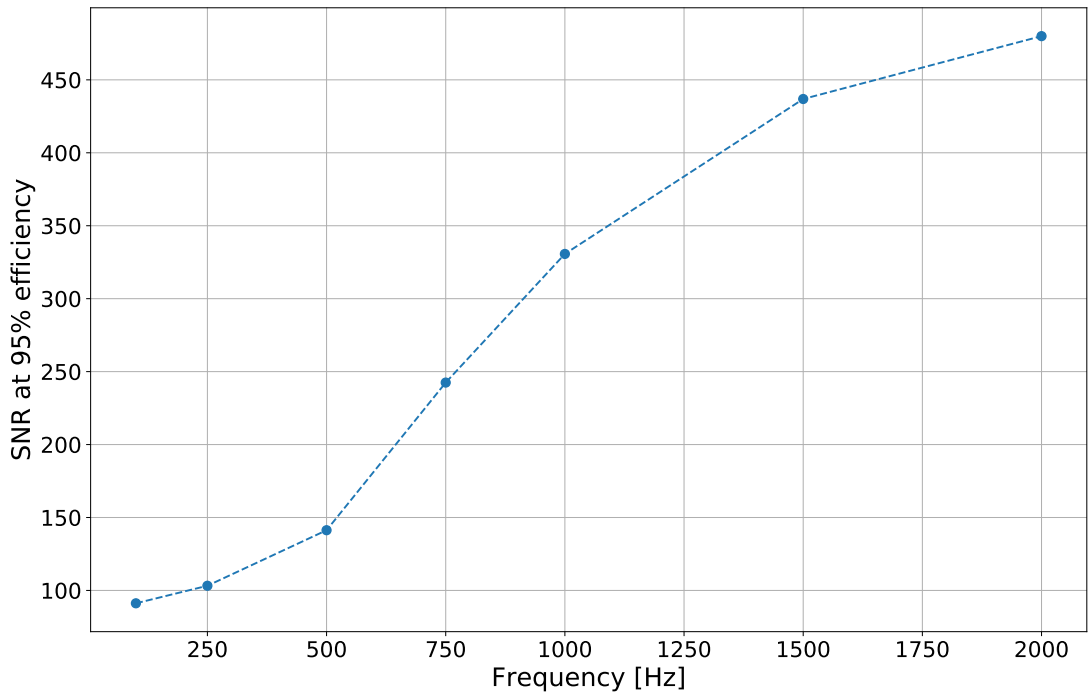

(b)

Figure 3.11: The sensitivity of the SOAP search in this configuration decreases as the frequency of the pulsar increases. This setup of data for the search however, was optimised for the 100-200 frequency band and can be changed for different frequencies. 3.11a shows the efficiency curves with 1% false alarm rate for each frequency. 3.11b shows the values from the efficiency curves at 95% efficiency.

3.13 Searching for non-CW sources

Whilst SOAP was designed to search for sources of CWs, when set up correctly, it can be applied to searching for other signal types. This is because the search is essentially un-modelled, and in its simplest form looks for tracks of high power in a time-frequency spectrogram. Therefore, if the signal can be represented in a spectrogram, then it can be searched for using SOAP. Ideally the signal will also live on a single track and span the time length of the spectrogram.

CBC signals cover a wide frequency range and are very short signals in LIGO detectors compared to CWs. The longest of these are BNS signals which are generally detectable by LIGO for $\mathcal{O}(10)$ s. In previous SOAP searches the default length of SFT has been 1800 s, however, this is not suitable when searching for CBC signals. We then need a shorter time base for each of the SFTs. In the following examples the SFTs are overlapping in time, this allows us to achieve the desired time and frequency resolution. However, this means that the SFTs are no longer independent and our Bayesian formalism is not technically correct.

Fig. 3.12 shows an example of the two detector SOAP search running on data +2s and -5 s of the GW170817 merger time [**abbott2017GW170817Observation**]. The spectrograms show the SFTs power spectra divided by their running median. The SFTs are 0.2 s long and are overlapping by 90% (0.189 s), this gives a frequency resolution of 5 Hz. Figure 3.12 shows how SOAP identifies a track which follows that of the BNS and the Viterbi map shows a clear excess of log probability where the signal lies. Whilst this may not be an optimal setup for this particular search, it demonstrates that SOAP can identify a BNS signal within the data. The example in Fig. 3.12 show the result between 20 and 520 Hz, however the SOAP search returns the same track for a wider band-width up to 2000 Hz. It should be noted here that some work has been done on another variant of the Viterbi algorithm to search for a post-merger remnant of the GW170817 merger [**abbott2019SearchGravitational**].

Searching for BBH systems becomes more difficult as they are in the LIGO band for a short period of time ($< 1s$). To see the evolution of the signal in a spectrogram, the time resolution required means that the frequency bins are too large to see the signals evolution. There are other time-frequency representations such as the Q-transform which allow us to visualise and search for these signals. However, the bins in a Q-transform are not independent, therefore again the Bayesian formalism described in this chapter is no longer technically correct. Despite this, the SOAP search can still be run on the Q-transform and return useful results. Figure 3.13 shows the Q-transforms of GW150914 [**abbott2016ObservationGravitational**] and the outputs of the SOAP search run on these transforms. The Viterbi map in Fig. 3.13 shows how the SOAP search highlights the GW signal, i.e. there are large values of the Viterbi statistic around the GW frequency

track. This representation could then be used with other algorithms to identify the CBC signal.

In both Fig. 3.13 and 3.12, the signal does not last for the entire length of the time-frequency band. SOAP is designed to search for long duration signals where the SNR can be built up over time. Regardless of the signal, SOAP will always return an optimal track for the entire length of the time-frequency representation. Therefore, although short CBC signals are not an ideal source for SOAP, what it can do is highlight areas which are more likely to contain a signal. This is shown in both the Viterbi maps in Fig. 3.13 and 3.12. This section serves as a demonstration that it is possible to use SOAP for other types of search, it has more flexibility than the majority of examples in this thesis show. This is an area of work which would benefit from further investigation.

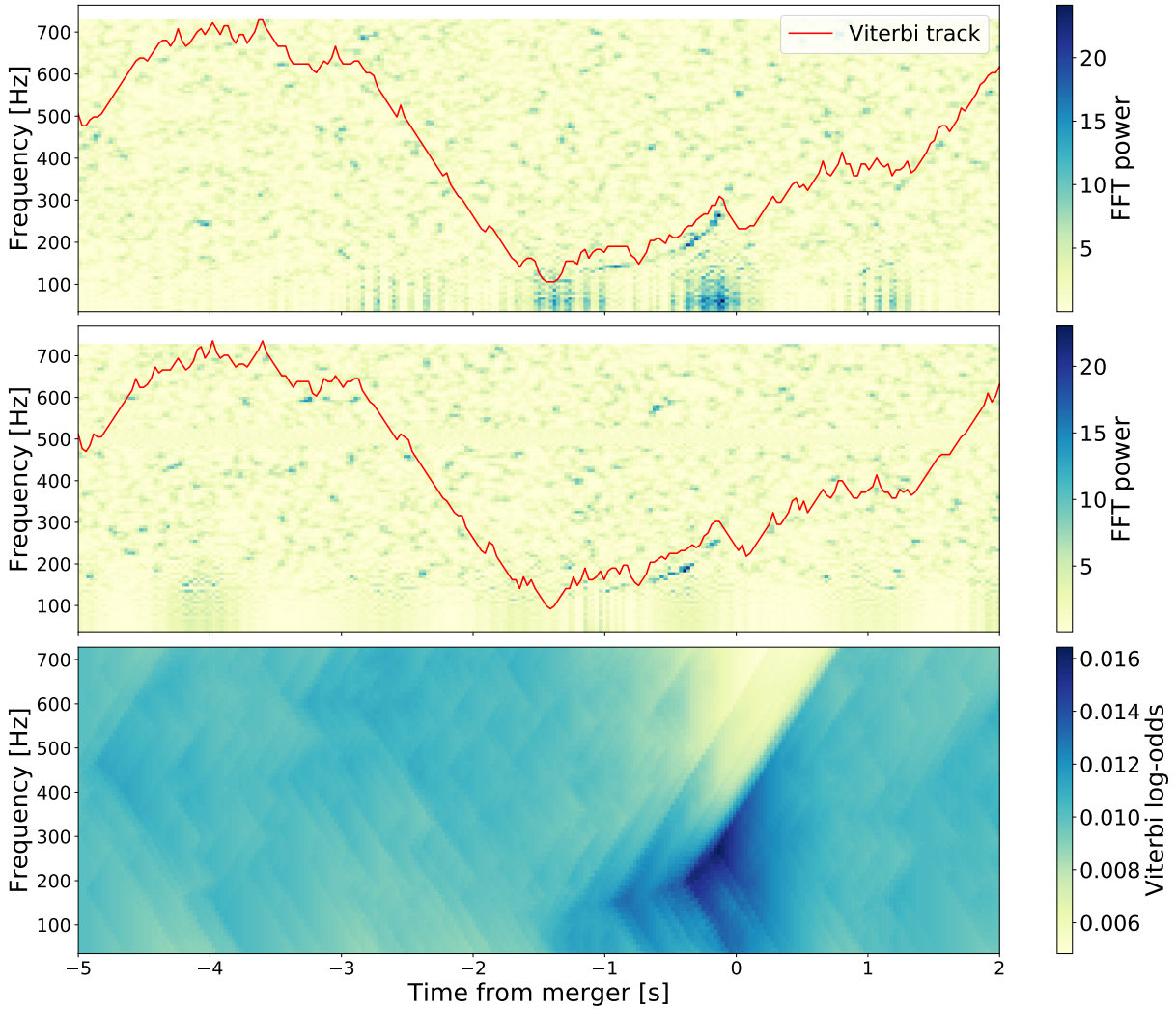

Figure 3.12: The SOAP search was run on a spectrogram of LIGO data +2 and -5 seconds around the merger of GW170817 [**abbott2017GW170817Observation**]. The top two panels show the spectrograms from LIGOs H1 and L1 detectors respectively. Each FFT in the spectrograms are 0.2 s long and are overlapping by 0.189 s (95%). The red track shows the output Viterbi track shifted up by 50 Hz so that the signal can bee seen in the spectrogram. The final panel shows the Viterbi map output. The BNS signal here is GW170817 [**abbott2017GW170817Observation**], where the coalescence is at a time of 0. The Viterbi map shows a area of higher log-odds along the path of the BNS signal.

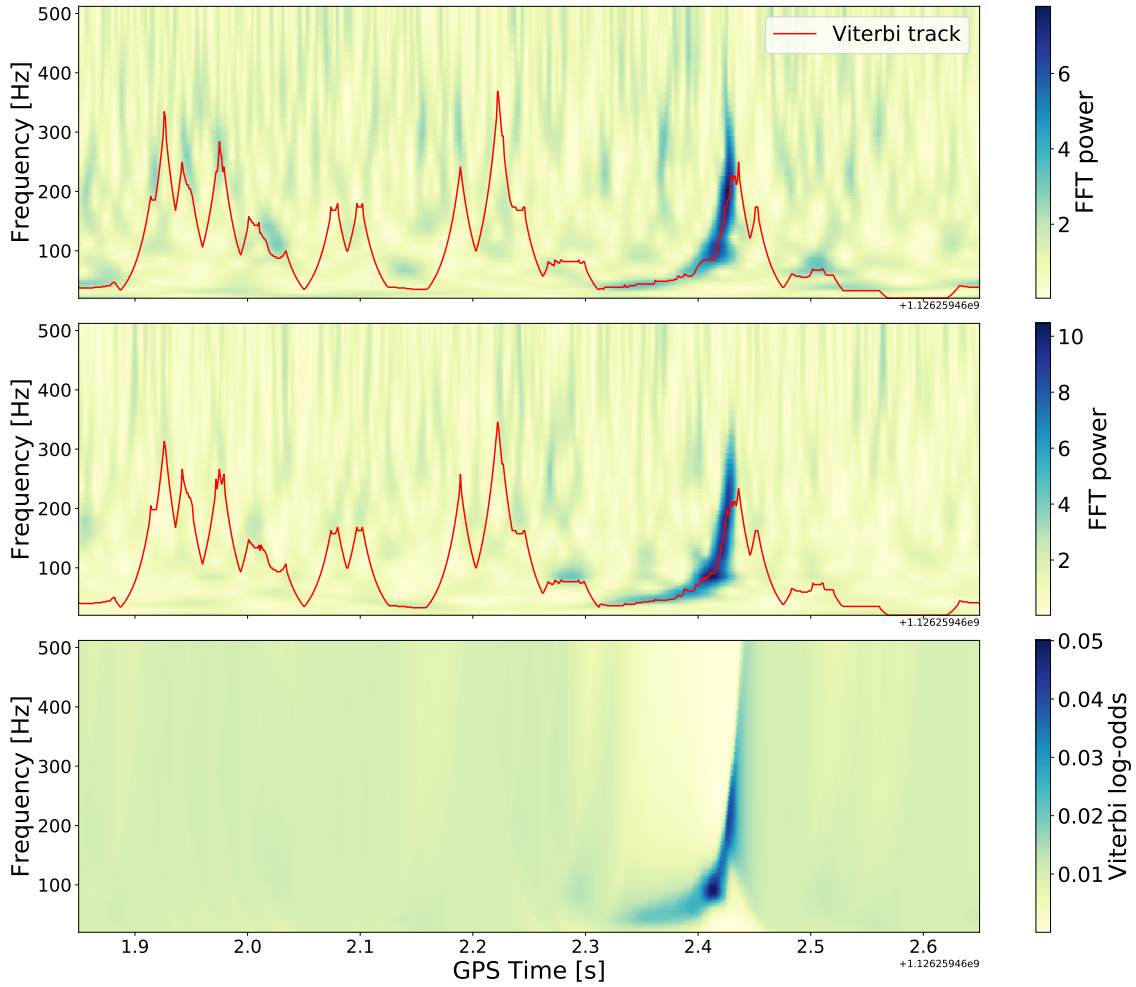

Figure 3.13: The Q-transform is taken around GW150914 [**abbott2016ObservationGravitational**]. The top two panels show the Q-transform for H1 and L1 respectively, where the red track is the Viterbi track identified in each of the transforms. The final panel then shows the output Viterbi map for this data. The two tracks follow the frequency evolution of the BBH signal as is sweeps through the band and the Vitebri map shows areas of large log-odds where the BBH signal has high Q-transform power.

3.14 Computational cost

One of the main strengths of this search is the drastically reduced computational cost when compared to other current CW searches. The scaling of the computing cost can be estimated for a single detector by looking at the number of calculations that need to be made. The number of calculations for a single detector search, $N^{(1)}_{\text{calcs}}$ is,

$$N^{(1)}_{\text{calcs}} = n_1^m NM, \tag{3.42}$$

where n_1 is the size of the transition matrix, N is the number of SFTs, M is the number of frequency bins and m is the amount of memory described in Sec. 3.6. Where the computing cost scales linearly with the number of frequency bins and SFTs. In the following test we ignore 'memory' and look at the time taken for the single detector search where the time taken to read and save data is ignored. Here the data is the same size as the S6 MDC for a single detector search and the search is over a 0.1 Hz band, where we set $n_1 = 3$. This test, and the following test, was run locally on a MacBook Air with a 1.3 GHz Intel Core i5 processor .We can then write the time taken ,T, as,

$$T = 0.56\,\text{sec}\left(\frac{\text{N}}{22538}\right)\left(\frac{\text{M}}{180}\right)\left(\frac{\text{N}_{\text{bands}}}{1}\right), \tag{3.43}$$

where N_{bands} is the number of different frequency bands. For the multiple, Q, detector case, we can then generalise Eq. 3.42 and write the number of calculations $N^{(Q)}_{\text{calcs}}$ as,

$$N^{(Q)}_{\text{calcs}} = NMn_1^m \prod_{q=1}^{Q} n_{q+1}, \tag{3.44}$$

where n_1 is the first dimension of the transition matrix, Q is the number of detectors and n_{q+1} is the size of the transition matrix element which refers to detector q. For our tests we set $n_1 = n_{q+1} = 3$ and use 2 detectors i.e., $Q = 2$ which each have the same size data as the previous test. The actual time taken to run however, depends on the version of the algorithm which is run. For example, including the line aware statistic slows the search slightly. For the two detector case where two SFT powers are summed,

$$T_{\text{sum-power}} = 1.35\text{s}\left(\frac{\text{N}}{22538}\right)\left(\frac{\text{M}}{180}\right)\left(\frac{\text{N}_{\text{bands}}}{1}\right). \tag{3.45}$$

The same search now including the line aware statistic, which is implemented using a lookup table, changes this to,

$$T_{\text{line-aware}} = 25.7\text{s}\left(\frac{\text{N}}{22538}\right)\left(\frac{\text{M}}{180}\right)\left(\frac{\text{N}_{\text{bands}}}{1}\right). \tag{3.46}$$

Other searches, excluding Einstein@home which takes on the order of months to run (> 100 million core-hours [**walsh2016ComparisonMethods**]), take $1 - 10$ million core-hours [**walsh2016ComparisonMethods**] when run on the first four months of LIGOs O1 data run. Running the line-aware statistic search should take ~ 14 core-hours to run between 100 and 200 Hz, not including any generation of data.

3.15 Discussion

In this chapter we describe an application of the Viterbi algorithm, called SOAP, to search for continuous sources of gravitational waves. This chapter outlines the method and derives the statistics behind the method in a consistent Bayesian formalism. It then presents the results from the first set of tests of sensitivity for the SOAP algorithm on three separate datasets.

In this chapter a statistic is derived to limit the effect of instrumental lines on SOAP by searching for consistent SNR between multiple detectors. This is then extended to search for consistent GW amplitude in Sec. 3.9. Searching for consistent amplitude mean that the each detector's sensitivity can differ with minimal impact on the search.

We tested SOAP on a set of fake isolated pulsar signals in the $100 - 200\,\mathrm{Hz}$ range, based on 1800s SFTs summed over one day. The three datasets that included these signals consisted of continuous Gaussian noise, Gaussian noise but with temporal gaps corresponding to LIGO dead times in the S6 data run, and real data, i.e., the S6 MDC. Although a major attraction of SOAP is its sensitivity to a wide range of signal types, in the tests above it was optimised to detect isolated pulsar signals below $200\,\mathrm{Hz}$ with low spin-down to offer a comparison with other CW searches. From these tests, by setting a 95% efficiency and a false alarm of 1%, we found that in the case of continuous Gaussian data we could detect a signal with an optimal SNR of ~ 60 and a depth of $\sim 33\,\mathrm{Hz}^{-1/2}$ with an RMS of the difference between the injected and Viterbi track being ~ 2 frequency bins (0.0012 Hz). When gaps were introduced into the data to simulate S6 we could detect a signal with an SNR ~ 72 and a depth of $\sim 10\,\mathrm{Hz}^{-1/2}$, with an RMS of ~ 10 bins (0.0056 Hz). The drop in sensitivity here is simply because there is $\sim 50\%$ less data compared to the previous case. Finally, in the S6 MDC we could detect a signal with an SNR ~ 74 and a depth of $\sim 13\,\mathrm{Hz}^{-1/2}$. The real data contains non-Gaussian artefacts such as instrumental lines and this causes a further drop in sensitivity. Whilst not a full comparison to other searches in the S6 MDC [**walsh2016ComparisonMethods**], as we only tested on a subset of the bands, this search has a sensitivity which is comparable to some other CW searches, however offers a massive increase in speed.

We chose the specific frequency band to search over as the data which we used, i.e., the summed data, becomes less effective at frequencies much higher than $200\,\mathrm{Hz}$, and

using the parameters of our simulations, signals can spread over many frequency bins in a day, reducing sensitivity further, however this can be mitigated by using shorter SFTs or performing their summation over 12 (rather than 24) hours. How the sensitivity changes with frequency is shown in Sec. 3.12.

The line aware statistic derived in Sec. 3.8 has 4 parameters which can be varied. These parameters were optimised by testing SOAP on the S6 MDC for each parameter set. This showed that the SOAP search performs well with many different sets of parameters, therefore, is insensitive to the choice of the parameters within a given range.

The flexibility of the SOAP search allows signal types other than CWs to be searched for. We show how this method can be used to highlight areas of a time-frequency spectrum which contain a CBC signal. Further algorithms can be used in addition to this to identify the signal, however, this requires a deeper investigation.

The methods described in this chapter present a basic approach for gravitational-wave signal searches using SOAP. However there are several further developments that could increase its sensitivity. Some of these are outlined below.

One variation of this method which has been described in this chapter is 'memory', which is where the tracks jump in frequency is determined by the previous n jumps. This has yet to be fully tested, however, we expect that this will increase our sensitivity to signals where we have a better idea of their frequency evolution. This however, comes at a cost in computational time which we can estimate given Eq. 3.44 in Sec. 3.14.

Further additions to the search include using the Fourier transform of the SFT power along the Viterbi track as a detection statistic. If the Viterbi track follows that from an astrophysical signal, then we should see the effects of the antenna pattern in this Fourier transform as a peak at half a sidereal day. If the track follows something which is not astrophysical then this peak should not be seen in the Fourier transform. This only applies to the search directly on the SFTs and not the summed data, as the antenna pattern variations will have been averaged out in the summing.

As well as searching for astrophysical signals, SOAP can also be used to search for and identify instrumental lines. Here we use single detector data, or multiple channels from a single detector, to identify quasi-monochromatic features on the data for further study. This is investigated further in Chapter 6.

Whilst this chapter presents initial tests on sensitivity, further tests will be needed for a full comparison to other CW search methods. This search, however, aims to look for signals which may not follow the standard frequency evolution and is intended to return potentially interesting candidates for a more sensitive follow up.

Chapter 4

Machine learning for continuous wave searches

'Machine learning' is a term which has been around since the 1950s, and is a subset of what is known as 'artificial intelligence'. This is a field which aims to use computers to learn information without being given explicit instructions. With the increase in available computing power in recent years, along with the easier access to large data-sets, machine learning has become a much more accessible technique. One of the techniques in particular is a method known as deep learning which uses deep neural networks. These have been used extensively in classification problems as well as many others. Neural networks have a large range of applications, and have gained increasing popularity for use in GW data analysis problems.

This chapter aims to give an overview of neural networks, specifically convolutional neural networks (CNNs) and their application to a CW search. The majority of this section is written in a paper which is yet to be published, however, is aimed to be submitted soon. The differences are, Sec. 4.3, 4.4 and 4.5 which describe the operation of neural networks. These have more detail in this thesis than in the paper draft. Sec.4.10 is additional material which is currently not included in the paper draft. This was work done by the author under the supervision of Prof. Graham Woan and Dr Chris Messenger.

4.1 Introduction

Gravitational wave detectors such as LIGO [**abbott2009LIGOLaser**, **aasi2015AdvancedLIGO**] and VIRGO [**acernese2015AdvancedVirgo**, **acernese2008StatusVirgo**] search for a number of different targets. Some targets such as CBCs have been observed [**abbott2017GW1708**, **abbott2017GW170814ThreeDetector**, **abbott2016ObservationGravitational**], however, other primary sources such as CWs are yet to be observed. CWs are well modelled quasi-sinusoidal signals with a duration much longer than observing times of detectors.

The source of these signals is thought to be rapidly rotating neutron stars which can emit GWs if there is some asymmetry around its rotation axis. This can be caused by various mechanisms as described in [**prix2009GravitationalWaves**]. These signals have a small amplitude, which if detected will be below the noise PSD of the detector. Therefore, sensitive search algorithms are needed to find the signals. These algorithms generally fall into three categories: Targeted, directed, and all-sky searches, listed in order of how much is known a priori about the source from electromagnetic (EM) observations.

In targeted searches the sky position, frequency, and its derivatives are assumed to be well known, in directed searches only the sky position is known and in all-sky searches the sky position and frequency of the source is unknown. The most sensitive of these are targeted searches which use coherent matched filtering [**dupuis2005BayesianEstimation**, **schutz1998DataAnalysis**]. These use template waveforms which are generated using the information already known about the source, then correlated this with the data. Directed and all-sky searches have a much broader parameter space to search, therefore, many templates are needed to sufficiently cover the parameter space. Using the coherent matched filter for broader parameter space searches becomes unfeasible due to the amount of computing time that is needed. This led to the development of semi-coherent searches where the data is divided up into smaller segments which can be coherently analysed separately and then the results can be recombined incoherently using various methods [**abbott2019AllskySearch**, **creighton2000SearchingPeriodic**]. Semi-coherent searches result in a trade off between sensitivity and computing time.

The analysis here is presented mainly as an addition to an existing semi-coherent search algorithm titled SOAP [**bayley2019SOAPGeneralised**]. This is a fast and largely unmodelled search which finds tracks of high FFT power in time-frequency spectrograms. When applied to multiple detectors using a 'line-aware' statistic, SOAP looks for frequency bins which have both a high power and are similar in each detector. This means that at a given frequency at a given time, SOAP will penalise frequencies where the FFT power is largely different in each detector. The algorithmic details summarised in Chapter 3.

One effect which limits the sensitivity of SOAP and many other GW searches is noise artefacts known as 'instrumental lines'. These can be anything from long duration fixed frequency or wandering lines to shorter duration fixed frequency transients. There are certain types of instrumental line which the SOAP search can struggle to distinguish from an astrophysical signal even with the development of a 'line aware' statistic in [**bayley2019SOAPGeneralised**]. Currently the method used to reduce the effect of these lines is to manually look at the SOAP output and the spectrograms for each sub-band to determine whether the sub-band is contaminated by instrumental effects. This process is slow, requires a lot of human input and is subject to human error. When the search runs over a larger bandwidth, it will no longer be practical to look through all

bands.

We aim to automate how the search deals with instrumental lines by using CNNs. These have been used extensively in image classification and we explain this in more detail in Sec. 4.4. CNNs have already been shown to detect gravitational wave signals from CBCs in [**gabbard2018MatchingMatched**, **george2018DeepLearning**, **gebhard2019Convolution** and other deep learning techniques have been used in searching for CW signals in [**dreissigacker201**

In Sec.4.2 we will summarise the basics of how the SOAP search works. In Sec. 4.3, 4.4 and 4.5 we explain how CNNs operate and how they are trained. Sec. 4.6 will describe how this is applied to an CW search. This includes the structure of the CNN in Sec. 4.6.1 and the entire search from raw data to results in Sec. 4.8. Finally in Sec. 4.9 we show the results from this search and compare to similar analyses.

4.2 SOAP

In Chapter 3 we introduced the SOAP algorithm. To recap SOAP [**bayley2019SOAPGeneralise** is an un-modelled search for long duration signals which is based on the Viterbi algorithm [**viterbi1967ErrorBounds**]. In its most simple form SOAP analyses a spectrogram to find the time-frequency track which gives the highest sum of FFT power. If a signal is present and sufficiently loud then this is the track which is most likely to come from some signal. In [**bayley2019SOAPGeneralised**] the algorithm has been expanded to search through multiple detectors as well as including a statistic to penalise artefacts in the data from the instrument as opposed to from an astrophysical source.

Fig. 4.1 shows an example of the spectrogram data which is searched through and the outputs of SOAP; the three main output components are the frequency track, the Viterbi statistic and the Viterbi map.

Viterbi track The Viterbi track is the most probable track through time-frequency data given a choice of statistic.

Viterbi statistic The Viterbi statistic is the sum of the individual statistics along the Viterbi track. In the analysis that follows, the 'line-aware' Viterbi statistic is used. This is the sum of the log-odds ratios, $p_{\text{signal}}/(p_{\text{line}} + p_{\text{noise}})$ along the track. This is defined in more detail in [**bayley2019SOAPGeneralised**]

Viterbi map The Viterbi map contains values of the Viterbi statistic for every time-frequency bin in the spectrogram. This represents the most probable track which ends in any time-frequency bin. In the Viterbi maps, each time slice is normalised individually, i.e., each vertical slice has been normalised such that the sum of their exponentiated values is equal to 1. This way each pixel in the image can be inter-

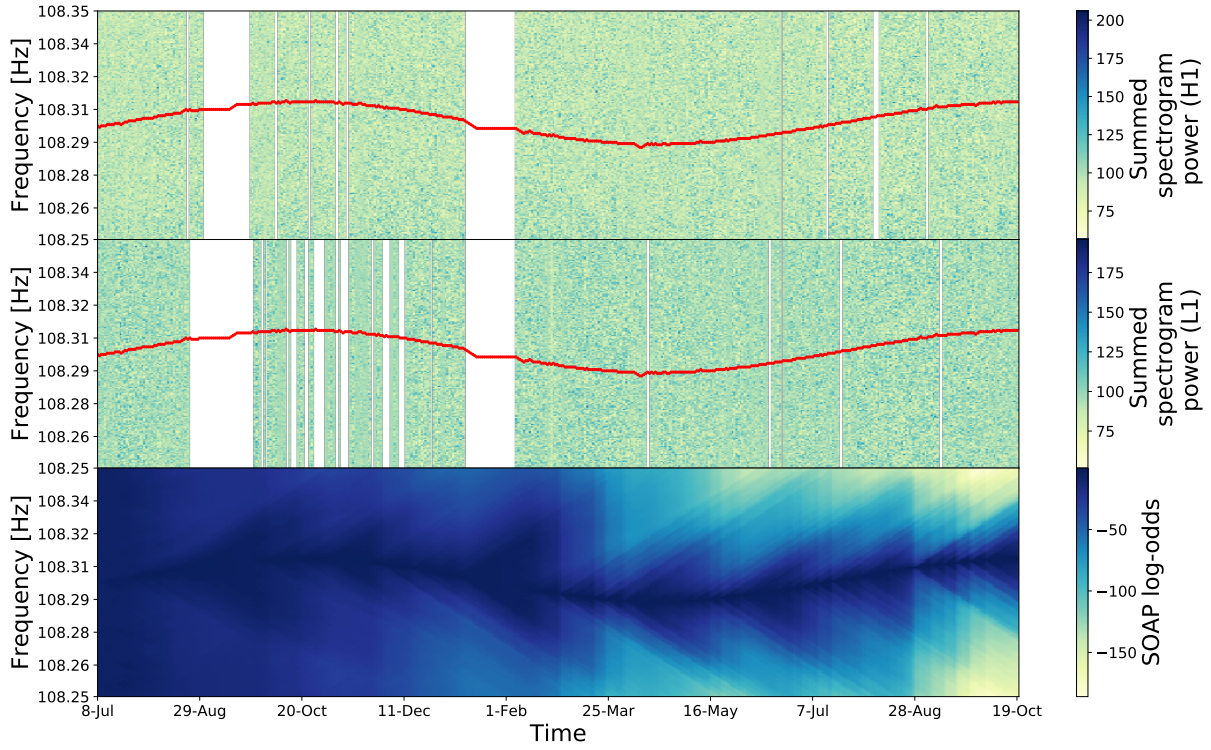

Figure 4.1: This plot shows the inputs and outputs of the SOAP search. The top two panels are time-frequency spectrograms which have been pre-processed as described in Sec. 4.8. This data is a 0.1 Hz wide frequency band from the LIGO S6 observing run which includes a strong simulated CW signal. The white areas in the spectrograms are gaps in data when the detector was not operating. These both have the optimal track found by SOAP overlaid. The bottom panel shows the normalised Viterbi map, the intensity of a pixel in this image relates to the log-probability that a track ends in and particular frequency bin at a given time.

preted as a value related to the log-probability that there is a signal in the bin at that time.

To determine whether an simulated astrophysical signal has been detected, in [**bayley2019SOA** we used the Viterbi 'line aware' statistic alone described above. The 'line-aware' statistic reduced the affect of instrumental lines on the analysis, however is still contaminated by certain types of line. For example, the statistic is affected by broad wandering lines as they offer high power tracks in both detectors. To reduce the effect of these instrumental lines, we looked through the spectrograms and Viterbi maps of individual bands by eye as in Fig. 4.1. Bands which appeared to be contaminated were then removed from the search.

In this search the spectrograms and the Viterbi map contained extra information over the Viterbi statistic. We aim to utilise this in addition to the Viterbi statistic to replace the process of removing contaminated bands 'by eye' and therefore automating the search. A useful tool which can be used to classify this extra information is convolutional neural

networks.

4.3 Neural networks

Throughout this section I will summarise one machine learning technique known as a neural network, for more information see [**emmert-streib2020IntroductoryReview**] for a recent review of machine learning techniques. Neural networks, as the name may suggest, were developed as a way for a computer to mimic neurons in the brain. To understand why this would be useful, one can try to design an algorithm to identify hand written digits. This seems like a simple task as a brain can complete with ease. However, writing a traditional algorithm to perform this same task is very difficult. The algorithm would have to identify a particular shape which has a huge amount of variation. Neural networks offer a way to deal with this problem as they can be trained on large datasets, similar to how a human brain is 'trained'. In the lifetime of a brain, many examples of different hand written digits are seen. For each new example the brain 'updates' itself based on the new version of the observed digit. This process is replicated in a neural network where the algorithm can be updated for each example, with the goal of correctly identifying a digit. A neural network has many parameters which can be modified or 'trained', it is these parameters which are updated after each new example of a digit. These parameters are grouped into objects called neurons, many combinations of neurons can then be used to build a neural network.

4.3.1 Neurons

Neurons are the building blocks of any neural network. They perform simple operations on any number of input values and then output a single value. The output o of a neuron is defined by the equation

$$o = f\left(b + \sum_{i=1}^{N} w_i x_i\right), \tag{4.1}$$

where b is the bias, x_i is an input value with a corresponding weight w_i, f is the activation function, o is the output and N is the number of inputs. Here the inputs $\boldsymbol{x}$ represent either the data which is input, in the example above this is the pixels in the digits image, or the output of another neuron. The weights $\boldsymbol{w}$ then represent the importance of each data point to this neuron. The bias b is then just an extra factor which can shift the data by a fixed value. The activation function f is a function which can have many forms, in the simplest case in a neuron known as a 'perceptron', it provides a cut where any value above a given threshold is 1 and any below is 0, this will be explained in more detail in Sec. 4.3.3.

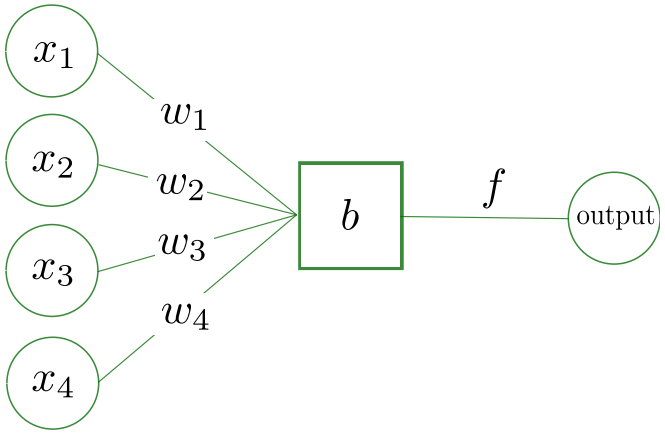

Figure 4.2: Basic neuron showing the four input parameters x_n and their corresponding weights w_n. These are multiplied and summed as in Eq. 4.1. A bias b is added and this value is passed through an activation function f to the output.

In the example in Fig. 4.2 I have shown a neuron which has 4 input variables, or 4 input data points. When a network is trained the weights and the bias are updated to better represent the input data. This training procedure is explained in more detail in Sec. 4.5. Many neurons are then used in combination with each other to develop a neural network which can be applied to more complex problems.

4.3.2 Network structure

The structure of a neural network is defined by the user and there is no set way to design a network. However, the general layout of a neural network is defined by structures called layers, sometimes known as fully connected layers. These are rows of N neurons which all take the same input such that there is N output values. An example of a simple neural network is shown in Fig. 4.3. The first layer is the input layer, this is just the data points from an input example. In the example of hand drawn digits, this would be the pixels from the image of the digit. The final layer represents the information that you intend the network to extract from the input data. In the hand drawn digit example, this could have 10 output neurons corresponding to each digit 0-9. Each of these outputs is then a value which is related to the probability of that digit being present in the image.

When designing a network, the user will have a defined input layer size from the data and a desired number of output neurons which represents, for a classification example, the number of output classes. The number of hidden layers and the number of neurons in those hidden layers can be arbitrarily changed. In general if the data contains more complex information the size or complexity of the network will need to be increased for it to be able to extract the information.

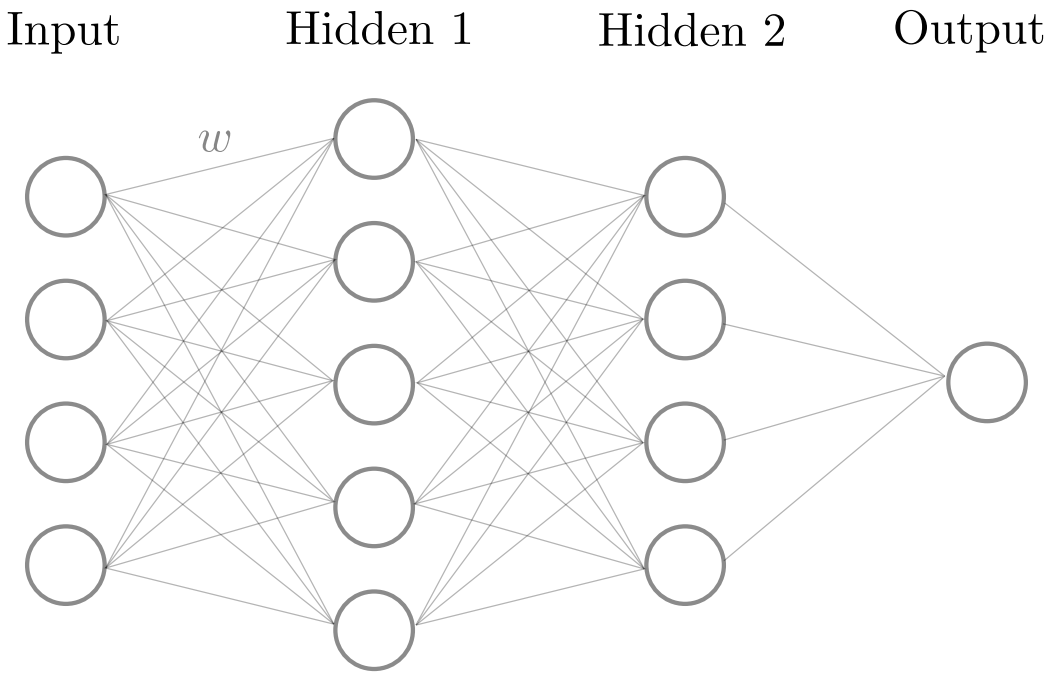

Figure 4.3: A neural network is structured with layers. Each of the circles in these layers are neurons as described in Sec. 4.3.1 and Fig. 4.2. The networks contain an input layer which is usually the data which you would like to analyse. Then this passes to a number of 'hidden' layers, in the above diagram there are two. Hidden layers are just layers which exist between the input and the output. The output layer is then the desired output, above I have chosen a single neuron as output. This is such that the network could classify the input to a value between 0 and 1. Every neuron in a layer is connected to the output of all neurons in the previous layer.

4.3.3 Activation functions

The activation function transforms the sum of the data and weights as in Eq. 4.1. The most simple activation function is to set a threshold where for any number above this the output is 1 otherwise the output is zero. However, this type of activation known as a perceptron does not always perform well in neural networks. Activation functions are generally non-linear, this reflects the non-linearity of real world problems and allows networks to learn that. A linear activation function means that any number of layers in a network is equivalent to a single layer network. Another property which is desired in an activation function is that it is continuously differentiable. This is to allow algorithms such as gradient descent to optimise the network [**nwankpa2018ActivationFunctions**]. There are many choices when defining an activation function, some of the common options are shown in Fig. 4.4 [**nwankpa2018ActivationFunctions**]. One of the more commonly

used activation function is the LeakyRELU function, this is explained in more detail in [**maas2013RectifierNonlinearities**]. In the work that follows we use the LeakyRELU function and the sigmoid function. The sigmoid function is used on the output such that values are constrained between 0 and 1, the LeakyRELU is used everywhere else.

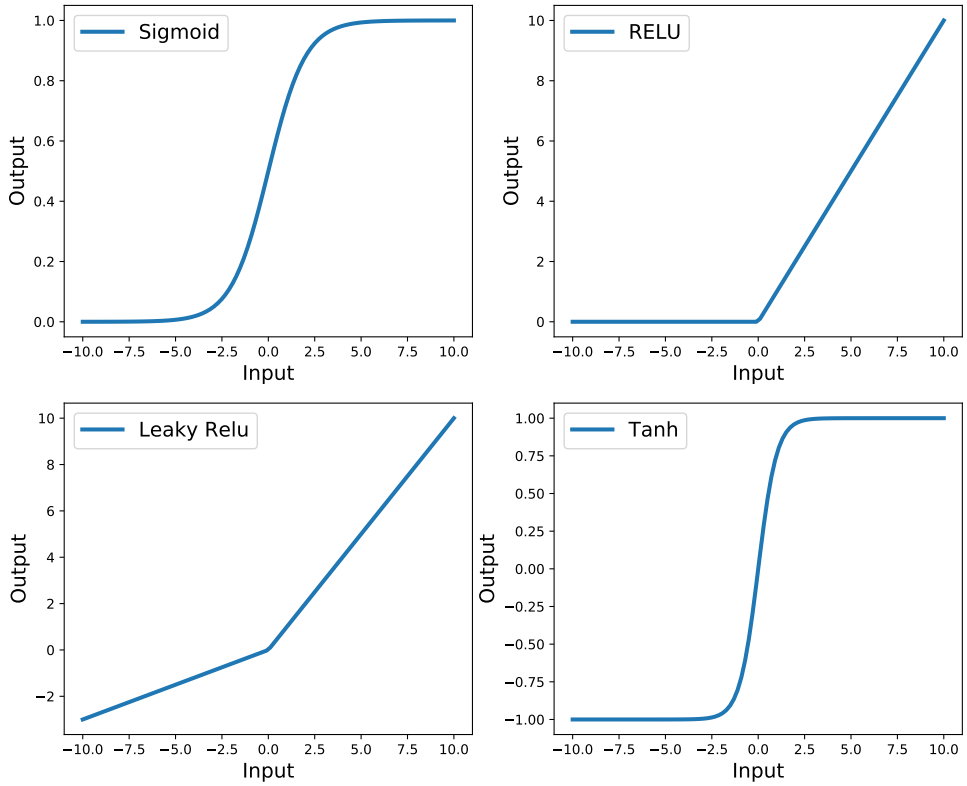

Figure 4.4: There are many different activation functions which are used, any function can be defined for this however, a subset of the more commonly used functions is shown here.

4.4 Convolutional Neural Networks

CNNs are a different type of deep neural network than in Sec. 4.3, they are primarily used in image processing and recognition [**lecun2015DeepLearning**, **lecun1998GradientbasedLearni**
waibel1989PhonemeRecognition, **krizhevsky2012ImageNetClassificationa**]. A CNN has a similar goal to a full connected neural network; it is designed to take in data, identify different features within that data and classify what those features or combinations of those features mean. In the context of this work the input data is a time-frequency spectrogram which may contain a simulated CW signal. The output is then a single number which gives a probability that a signal is present. A CNN can learn how to identify features by being trained on many examples of the input data which has a label. For example, an input spectrogram with a simulated CW signal would be labelled to have

a signal. Given the set of training examples, the many parameters of the CNN can be updated such that it gives the best result for any new image. This process is the same as neural networks in Sec. 4.3 and will be described in greater detail in Sec. 4.5.

The key features of CNNs which distinguish them from ordinary neural networks are some additional types of layers including: Convolutional layers and max pooling layers.

4.4.1 Convolutional layers

Convolutional layers have some similarities to fully connected layers as described in Sec. 4.3.2. The main difference being how the weights are applied to the inputs. If we assume that the input to the network is some image, then a fully connected neural network would flatten this image and apply Eq. 4.1 to the input pixels. This involves having a separate weight for each of the input pixels in an image. A convolutional layer however, filters the image and outputs a filtered image of the same size (the image can be a different size it depends how the layer was set up). This convolution is defined by

$$O_{i,j} = f\left(\sum_m \sum_n F_{m,n} x_{i-m,j-n}\right), \tag{4.2}$$

where O is the output image, x is the input image, F is the convolutional filter and f is the activation function. The weights of the filter $F_{m,n}$ are what are updated when the network is trained. Figure 4.5 shows an example of a 6x6 image and the results of filtering the image using Eq. 4.2 with two different filters F. In this case the network has 4 parameters for each filtered image which can be updated as opposed to the 36 which a full connected network would have for a single neuron.

Figure 4.5 demonstrates how a filter which matches a feature in an image can highlight that particular feature, i.e. the diagonal line in the bottom left of the input is enhanced by Filter 1, which matches that feature. When this type of layer is trained, the weights of the filter are updated. After training the filter weights should then ideally match the feature which is intended to be extracted from the image.

A convolutional layer has a number of different hyper-parameters which can be varied when setting up a CNN. Below I list each of the adaptable parameters and what they do.

Filter size The filter size is the size and shape of the convolutional filter. In Fig. 4.5 we use a filter size of 2×2. The filter does not have to be square, however must be less than the dimensions of the image.

Number of filters The number of filters can be any value. The convolutional layer will output the same number of filtered images as there are filters. In Fig. 4.5 we use two filters and therefore, the output of the layer is two images.

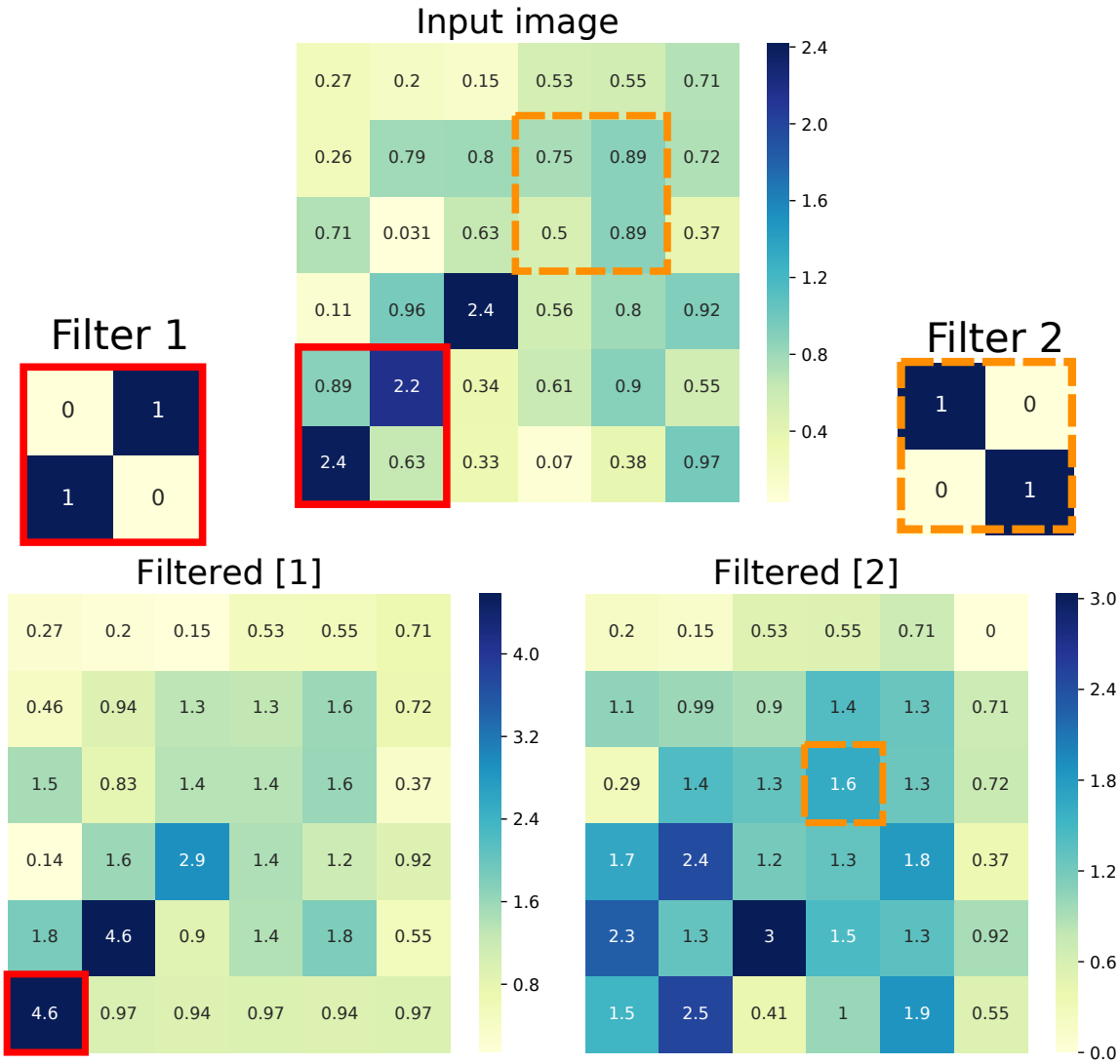

Figure 4.5: Convolutional filters can be designed to identify certain features within an image. In this simple example above, the first filter (filter 1) matches the diagonal line in the bottom left of the input better than filter 2. The output filtered image then exaggerates this filter. The coefficients of the filter i.e. $F_{m,n}$ in Eq. 4.2, in this are set to ones and zeros. These are the weights which are trained by the network. In this and cases that follow, to get the same size image in the output as the input, the image is padded with zeros. In this image it was necessary to pad above and to the right of the image, however this is not shown. The output of a convolutional layer is then the filtered images above after a bias and activation function have been applied.

Activation function The activation function is generally kept the same for each of the layers, however this can be set here. The different types have been explained in Sec. 4.3.3 and are applied as in Eq. 4.2.

Stride A normal convolutional layer applies a filter by multiplying by a filter, then shifting over by one pixel and repeating. Applying a stride mean rather than shifting by one pixel, one shifts by a number greater than one. This reduces the size of the output by the same factor of stride. i.e. if you skip one pixel (a stride of 2) then the image will be half the size on output. This has a similar affect to max-pooling which we describe in Sec. 4.4.2.

The convolutional layers can reduce the number of updatable parameters used in each network compared to an equivalent fully connected network. However, the output of a convolutional layer is a number of images which are potential the same size as the input. This has potentially increased the size of the parameter space for the next layer. To decrease this a type of layer known as max-pooling is used.

4.4.2 Max pooling layers

Max pooling layers are designed to reduce the size of the problem whilst holding on to as much important information as possible. These do not contain any trainable parameters. The idea of this layer is relatively simple, it reduces the image size by taking the maximum value in a region of a given size. Fig. 4.6 shows the output of the first filtered image in Fig. 4.5. The image is then reduced by a 2×2 max pooling layer. The output of max-pooling Then shows a large value in the bottom left, this is where the input image matched the filter in Fig. 4.5. This demonstrates how the max-pooling layer can hold on to important information whilst reducing the image size.

4.4.3 CNN structure

CNNs are usually structured such that they can extract larger features from an input image, then the outputs from this are passed on to be classified. The 'feature extraction' part of the network consists of the convolutional layers and the max-pooling described in Sec. 4.4. The outputs of the final max-pooling layer are then flattened and used as the input to a fully connected network. This fully connected network classifies these outputs into a number of classes. Figure 4.7 shows an example of the layout. Here an input image which is the same as in previous examples is passed onto a single convolutional layer with two different filters. The output of two filtered images is passed to a max-pooling layer. The two max-pooled images are flattened into 18 input neurons, this then passes through a fully connected network to a single output neuron. This shows a simple example, however,

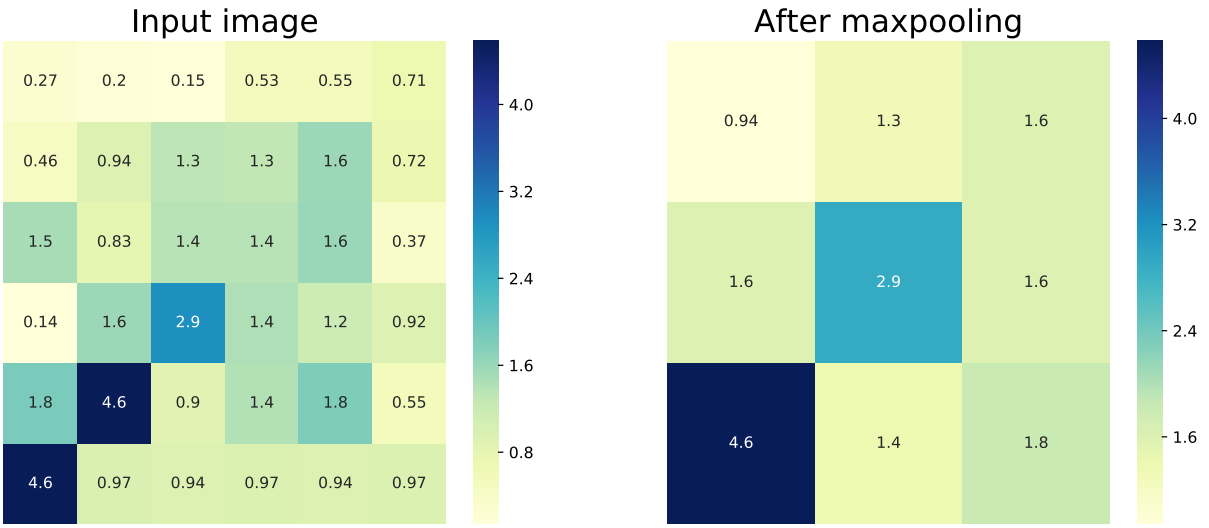

Figure 4.6: Max pooling layers aim to reduce the size of am image whilst retaining important information within the original image. Above shows an example where a 2×2 max-pooling layer is used on the output of Filter 1 in Fig. 4.5. This retains the information that the input image matches the filter in the bottom left.

n

there are many hyper-parameters of the network which can be changed. These include: the number of filters in a convolutional layer, the number of convolutional layers and max-pooling layers, the number of hidden layers in the fully connected section and the number of neurons in the hidden layers. This example also shows the network being classified to a single output as this is how we use CNNs for the following work. The hyper-parameters of the network are generally chosen to reflect the complexity of the problem, for example if there are many different features which are possible to appear in an image, one might use a larger number of convolutional filters to account for them. However, there is no set way to design a network, and often one tests a variety of structures to asses which performs best.

4.5 Training

Once the structure of the network is decided, the network needs to be trained. This means that the weights and bias' for every neuron and filter need to be updated such that the neural network gives a useful output. For this work we will classify input time-frequency spectrograms into a signal or noise class using a single output neuron. This neuron outputs a value in the range [0,1] by using a sigmoid activation function. In our case the CNN is trained using a process called supervised learning. In supervised learning, the class of each input example is known. For example, we assign a label of 1 when the input is a time-frequency spectrogram which includes a simulated CW signal. Similarly a time-frequency

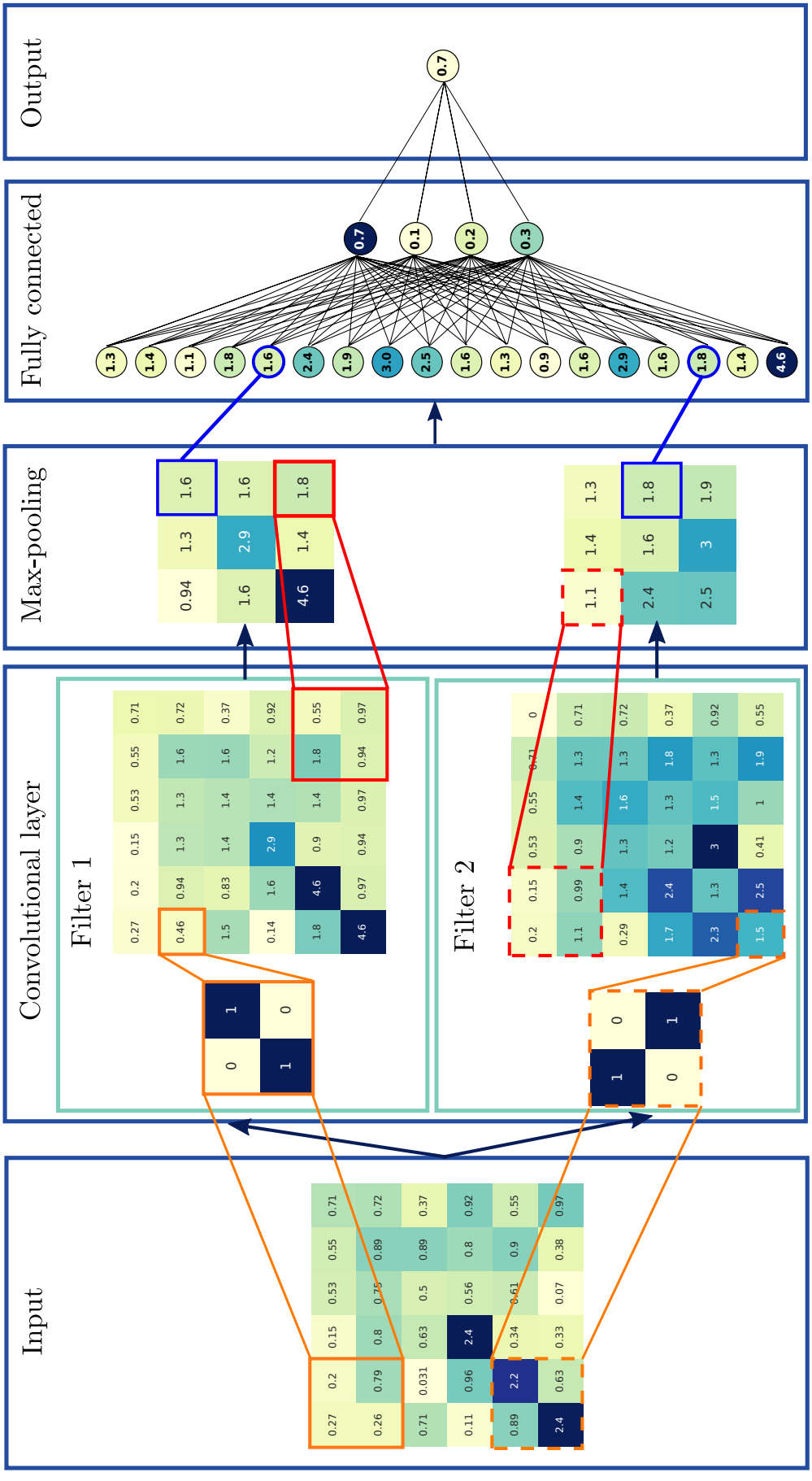

Figure 4.7: Convolutional neural networks consist of two broad sections, the 'feature extraction' part which is the convolutional and max-pooling layers, and the classification part which is the fully connected part of the network. This diagram shows a simple example of an image passing through a single convolutional layer with two filters, a single max-pooling layer and a simple fully connected network with a single hidden layer consisting of 4 neurons. The values in this diagram omit the use of any activation function such that the values are easier to follow. In a real network the activation functions are important.

spectrogram with no simulated signal is assigned a label of 0. In general when training neural networks this way, the performance of the network can be improved by increasing the number of input examples which are shown to the network. This stops the network from over-fitting to specific examples. Instead it should generalise to the full input and learn the underlying features within the data.

4.5.1 Loss function

Initially each of the training examples is propagated though the network to its single output value which lies between 0 and 1. Using a loss function, this output is then compared to the label of the input data which in this case is either 0 or 1. There are many types of loss function which can be used, this depends on the type of problem which one wants to solve. As we are classifying between two classes in our networks, the loss function, L, is the binary crossentropy defined as

$$L = -\frac{1}{N}\sum_{i}^{N} y_i \log\left(p_i\right) + \left(1 - y_i\right) \log\left(1 - p_i\right), \tag{4.3}$$

where p is the network's predicted output which has any value in the range $[0, 1]$ and y is the data label which has binary values of 0 or 1. This is calculated as the sum over all N training examples. The loss function is minimised when the output matches the 'truth' (the label). This tells the neural network how close to the truth this output is. The weights and bias' of the neural network can be updated based on the value of this loss function. The process of updating the weights and other parameters is called back-propagation, and typically uses a form of gradient descent [**kingma2015AdamMethod**]. Back-propagation uses the derivative of the loss function with respect to a weight to update that weight. If changing that weight in a particular direction decreases the loss function, then the weight will be updated in that direction. The size of the change of the weight value is related to the change in the size loss function. This means that the weights can be updated to minimise the loss function and therefore improve the performance of the network.

4.5.2 Training procedure

The training procedure entails passing a set of training examples through the network a number of times. Once the entire training data set has been passed through the network (forward pass) and the weights have been updated accordingly (back propagation), the training has completed one epoch. If the data was passed and the weights were updated a single time, the loss may decrease by is likely not at a minimum. Passing the data through again may move the weights to a lower loss. This process is repeated a number of times

to try and find the minimum loss. When training, the value of the loss at each epoch is monitored, where the trend of the loss of the training set should always decrease. In general a subset of the training data is set aside and not used in the training procedure, this is known as validation data. After each epoch the value of the loss for this validation set can be measured, i.e. all the validation data is passed though the network. This can be used to monitor the training of the network. If the validation loss begins to increase then this is a sign that the network is over-fitting to the training data-set.

4.6 Application to CW search

The aim for this work is to use a CNN to classify LIGO data into one of two classes: signal or noise. Here the signal class refers to a CW signal from an isolated neutron star as described in Sec. 2.1. Noise then refers to anything else which appears in the data, from Gaussian noise to instrumental artefacts. In Sec. 3.10 to reduce the effect of instrumental artefacts, each of the search sub-bands was analysed by eye to determine if a sub-band was contaminated. Sub-bands which contained an artefact were then removed from the search. This is a time consuming process. The main goal of the CNN approach is to automate this part of the search. This section will describe how we design the network to extract features and distinguish signals from instrumental artefacts. We will then present results from searches in a range of LIGO observing runs which include: S6, O1 and O2.

4.6.1 Network structure

In this section the structure of the networks which are used in this analysis are described. There are three main inputs of data for each CNN: spectrograms, Viterbi maps and the Viterbi statistic. Each of these are different representations of the raw detector data. In this analysis we train a separate CNN for each of these inputs and then a further three which use these combinations of inputs: Viterbi map + spectrogram, Viterbi map + Viterbi statistic and Viterbi map + Viterbi statistic + spectrogram. In all of the layers excluding the output layer of each CNN, the activation functions in Eq. 4.2 and 4.1 are defined by a function titled 'leakyRELU' [**maas2013RectifierNonlinearities**]. Our output neuron uses a sigmoid activation function as is often the case in classification problems as it constrains the output between 0 or 1 and is efficient when calculating the loss function. For a given input a CNN can then output a value between 0 and 1. When the output value is closer to 1, the input is more likely to contain a signal. The output value can then be treated as a detection statistic. The structure of the network is shown in Fig. 4.8 and is explained below.

Viterbi statistic This is the simplest of the networks and will give the exact same result

as the Viterbi statistic on its own. This is a single neuron which takes in the Viterbi statistic applies a weight and bias and then passes through a sigmoid function.

Viterbi map The Viterbi map CNN takes in a down-sampled Viterbi map of size (156,89), this is described more in Sec. 4.7.3. This CNN consists of two convolutional layers and 3 fully connected layers. The first layer has 8 filters which have a size of 5×5 pixels, the second layer has 8 filters with a size of 3×3 pixels. After each of these layers we use a max-pooling layer with a size of 8×8 pixels. This is then passed into three fully connected layers which all have 8 neurons and use a leakyRELU activation function. Finally these lead to an output neuron which uses a sigmoid function.

Spectrogram The spectrogram CNN takes in down-sampled spectrograms of size (156,89), this is described more in Sec. 4.7.3. This CNN has an identical structure as the Viterbi map CNN, however, takes two channels as input. The two channels are the spectrograms of two different detectors.

The next three networks are constructed from combinations of the previous described CNNs.

Viterbi map and spectrogram To combine the spectrogram and Viterbi map network, we remove the final output neuron and its 8 weights from each of the networks. The outputs from each network is then 8 neurons. These can be combined to a single sigmoid neuron which has 16 new weights.

Viterbi map and Viterbi statistic In this network we combine the Viterbi statistic with the Viterbi map. As before, this uses the pre-trained Viterbi map and Viterbi statistic CNNs. The output sigmoid neuron and corresponding weights are removed from each network. The 8 neurons from the Viterbi map network and the single neuron from the Viterbi statistic network are then combined to a single neuron with 9 new weights.

Viterbi map, Viterbi statistic and spectrogram This combination takes all component CNNs from above. As before the final sigmoid output and the corresponding weights from each network are removed. The 8 neurons from the Viterbi map and spectrograms CNNs and the single neuron from the Viterbi statistic are then joined into a single output neuron with 17 new weights.

When combining CNNs we use a process called transfer learning [**prattDiscriminabilityBased**
This uses the pre-trained weights of the networks as a starting point to continue training. In our examples we found that we could fix the weights inside the pre-trained networks

and just train the final 16 output weights from the neurons as in Fig. 4.8. These combinations of networks were chosen as the different representations of the data should contain slightly different information on the input. For example, the Viterbi statistic contains no information on the structure of the track in the data and the Viterbi maps lost some information about lines in the band. The addition of the spectrograms aimed to include even more information about this piece of data. Where each of these are combined, the CNN should be able to pick to important information from each of these representations.

4.7 Data generation

To train the CNNs we need to generate many examples of data, this includes the three data products above: Time-frequency spectrograms, Viterbi maps and the Viterbi statistic. When a CNN is trained it needs to see examples of all possible features which could appear in the data. These include, Gaussian noise, non-Gaussian artefacts and CW signals. As non-Gaussian artefacts are difficult to simulate, it is possible to use the non-Gaussian artefacts in real data as part of the training set. Therefore, for the majority of the analysis that follows, the time-frequency spectrograms which are used to generate the Viterbi data are from real detector data. The exact observing runs used will be explained in Sec. 4.9.

For the analysis that follows there are three main sets of data: training data, test data and search data. Training data uses a set of augmented (see Sec. 4.7.2) time-frequency spectrograms containing simulated signals and is used to train each of the networks. Test data is a separate set of simulations in time-frequency spectrograms which are not augmented. These are used to generate efficiency curves and test the network. Search data does not contain any simulated signal injections and is used to search for real signals within the data.

When training and testing a network it is important that the networks are not trained and tested on the same data. Otherwise the CNNs can learn specific features of the training data and not the underlying distribution of features. To avoid this, the spectrograms are split into 0.1 Hz wide sub-bands where alternating bands are designated as 'odd' or 'even'. This means that bands starting with 100.1,100.3 are odd and 100.2,100.4 are even etc. The networks can then be trained on the odd bands and tested on the even bands and vice versa. This then means that each time we want to search over data, we will have two final networks. One which will be run on odd bands and a separately trained network which is run on even bands.

4.7.1 Signal simulations

To inject the simulated signals into real data we generate a random set of signal parameters which are drawn from prior distributions defined in Table 4.1. The SNR of each simulation

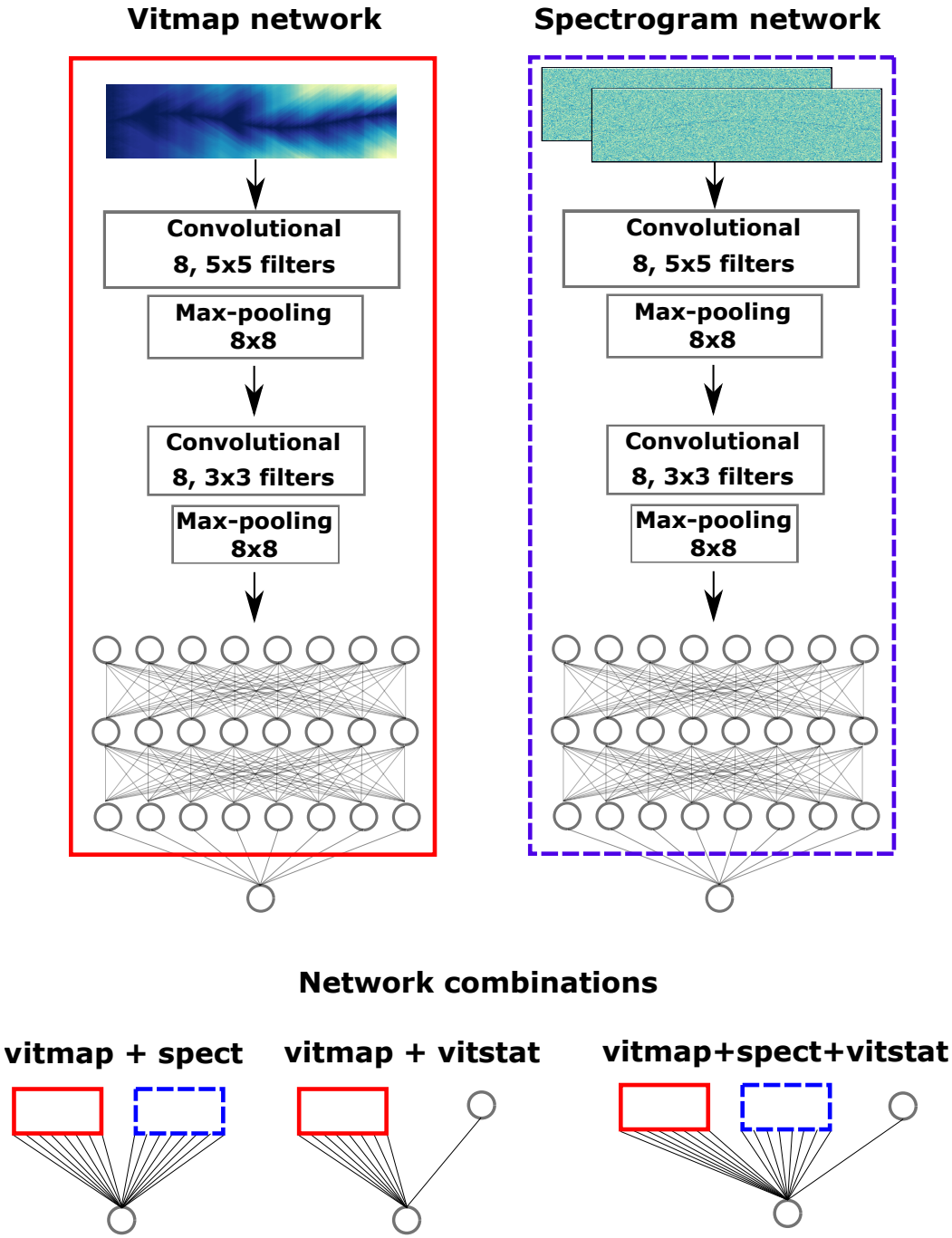

Figure 4.8: The structure of the Viterbi map and spectrogram CNNs used in this analysis are the same, with the difference that the spectrogram takes two images as input. They each use two convolutional layers and 3 fully connected layers before they're output to a single neuron which represents the probability of belonging to the signal class. The Viterbi statistic network is a single neuron that transforms the statistic into a number between 0 and 1 representing the probability of belonging to the signal class. For the combinations of networks, we remove the final output neuron and its 8 weights, i.e. we take the part inside the red or blue box. The 8 outputs from each network are then combined to a single neuron with 16 new weights.

Table 4.1: Table shows the upper and lower limits over which each signal parameter was randomized. The parameters $\alpha, \sin(\delta), f, \log\left(\dot{f}\right), \cos(\iota), \phi_0, \psi$ were sampled uniformly in the ranges specified in the table. The frequencies f_l and f_u refer to the lower and upper frequency of the band that each signal is injected into. Excluding the distribution of frequencies f, all the injection parameters are sampled from the same distributions as the S6 MDC [**walsh2016ComparisonMethods**].

	α [rad]	$\sin(\delta)$ [rad]	f [Hz]	$\log_{10}\left(\dot{f}[\mathrm{Hz/s}]\right)$	$\cos\iota$ [rad]	ϕ [rad]	ψ [rad]
lower bound	0	-1	$f_\mathrm{l} + 0.25$	-9	-1	0	0
upper bound	2π	1	$f_\mathrm{u} - 0.25$	-16	1	2π	$\pi/2$

is then uniformly distributed between 50 and 150. Where the SNR is the integrated 'recovered' SNR. This is calculated for each time segment using the definition of optimal SNR in [**prix2007SearchContinuous**], the total SNR is then the sum of the squares of these. The GW amplitude h_0 is scaled based on the noise PSD to achieve this SNR. The power spectrum of the signal can then be simulated in each time segment of a time-frequency spectrogram. This is done by assuming that the spectrogram is χ^2 distributed. The the antenna pattern functions are taken into account for the given source parameters and detector such that the SNR for each time segment is calculated. This SNR is spread over neighbouring frequency bins dependent on its location in frequency. See Appendix A for more details on the injection procedure. The power spectrum values can then be drawn from a non-central χ^2 distribution with the non centrality parameter equal to the square of the SNR. Each signal is simulated in two detectors: LIGOs H1 and L1. The SNRs reported below are then the sum of the squares of the SNRs from each detector.

4.7.2 Augmentation

To train a neural network, many examples of data from each class are needed to avoid over-fitting as described in Sec. 4.5. The number of training examples which are necessary varies greatly depending on the complexity of the problem, however it often exceeds $10^4 - 10^6$. In our case when we use data between 40-500 Hz, splitting the data into 0.1 Hz wide sub-bands does not give enough data for the networks to be trained effectively. Therefore, using a technique called data augmentation [**patrice1991TangentProp**, **baird1992DocumentImage**] we can artificially increase the number of training examples. Augmentation is when data is transformed such that, to the network, it appears to be 'new' data. For example, by shifting a time-frequency band up and down in frequency, this appears to be a new realisation of noise which we can then inject a simulated signal into. This would increase the size of the training data-set and reduce the likelihood of over-fitting to the training data.

The augmentations are applied to the spectrograms from each of the detectors. The

augmentations that are used on each sub-band are: reversing the data in time, flipping the data in frequency, rolling the data in time by a small number of segments and shifting the data in frequency by a small number of bins. As we use real data, there are gaps in time where the detectors were not operating. We preserve the location of these gaps when augmenting the data. When shifting the data in frequency, we shift each band up and down by 30 frequency bins (0.016 Hz) and up and down by 60 frequency bins (0.032 Hz). When rolling the data in time, we roll each sub-band by 100 time segments (100 days). Fig. 4.9 shows examples of the original data, a flip in frequency, a roll in time and a flip in time. For each frequency shift, we flip the sub-band in time and frequency and roll the sub-band in time. This then gives us 3 transformations for each of the 4 frequency shifts, which including the original data gives 20 times the number of training examples.

4.7.3 Downsampling

One further issue for our data sets is their size. The spectrograms we use have a large number of pixels within them ($\sim 4 \times 10^6$). This means that as the spectrograms are passed through the network, there are a large number of computations. Both this number of computations and the memory requirements of the GPU mean that training a network with a large number of data points takes longer. We implement a few methods to reduce the size of the data: summing time segments of spectrograms and down-sampling these summed spectrograms.

The spectrograms are summed over one day, i.e., every 48 time segments, as in [**bayley2019SOA**] This should increase the SNR for a given signal within a given time-frequency bin assuming that the signal remains within the frequency bin for the majority of the time segment. To reduce the size of the data further, the package 'resize' from scikit-image [**vanderwalt2014ScikitimageImage**] is used, this uses interpolation to resize the summed spectrograms to a size of (156,89) [time segments,frequency bins] ($\sim 1.3 \times 10^4$ pixels). This size was defined based on the summed spectrograms of the S6 data-set. This is 1/3 the number of summed segments in time, 1/2 the number of segments in frequency. The down-sampling is applied to the spectrograms and Vitmap. In [**bayley2019SOAPGeneralised**] we demonstrated that summing spectrograms can increase the speed and sensitivity of our search. When down-sampling the image, we found that reducing the amount of data had a small effect on the sensitivity of the CNNs used.

4.8 Search pipeline

In previous sections each component of the search pipeline has been described, however, described below is how each component fits together. Figure 4.10 shows a flow diagram

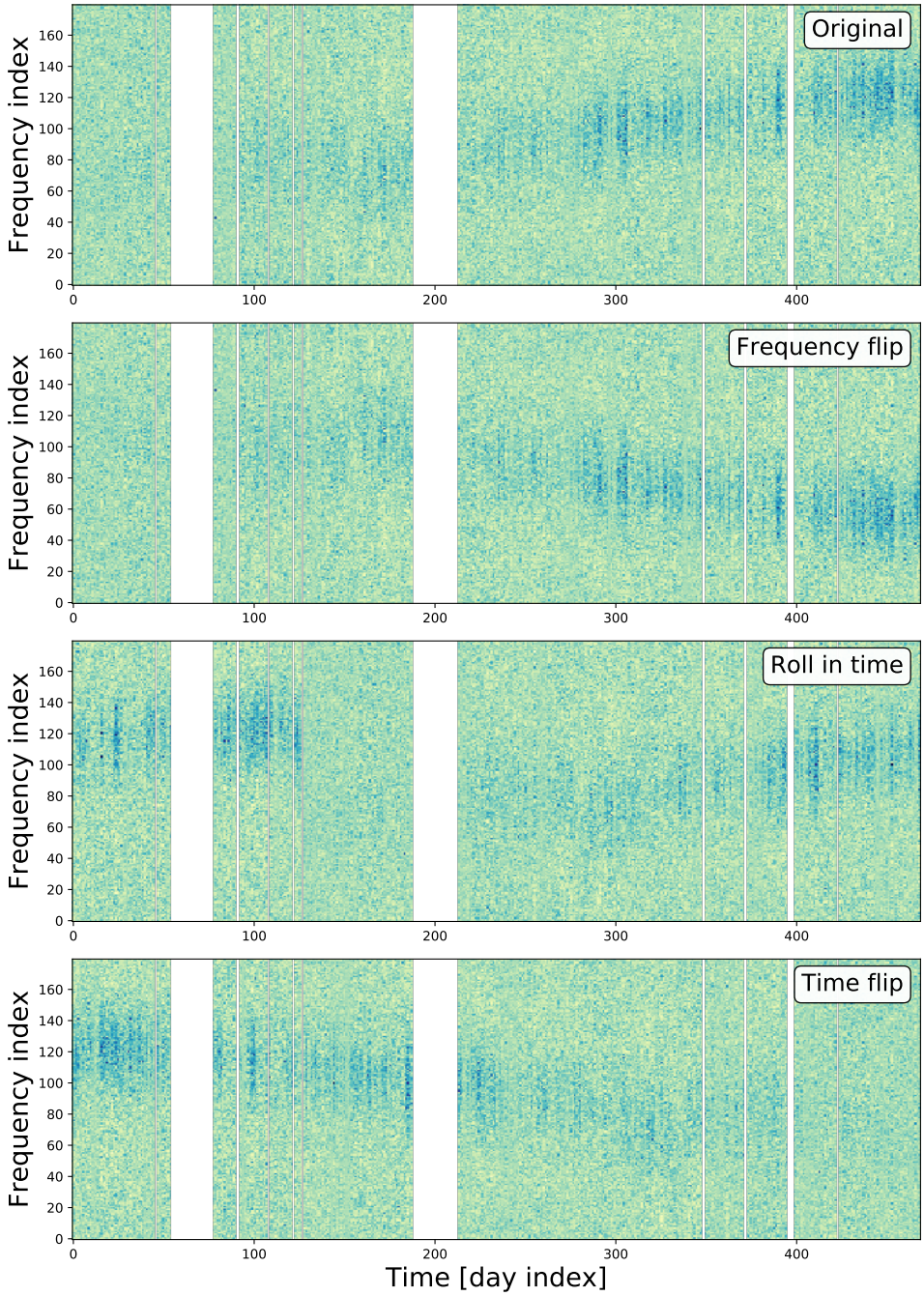

Figure 4.9: The data is transformed by flipping the data in frequency (panel 2), rolling the data in time by 100 bins (panel 3) and flipping the data in time (panel 4). The original summed spectrogram is show in panel 1. Simulated signals can then be injected using this data as noise. The plots above show a broad wandering line to demonstrate the changes to the data when it is augmented, however, the majority of sub-bands contain almost Gaussian noise.

of the pipeline. The pipeline is run in three different ways: training the CNN, testing the search and running a search on real data.

1. **SFTs** Generate 1800s long SFTs from detector time-series data. SFTs of this length are a standard set for CW searches which are continuously generated during observing runs by members of the LIGO collaboration.

2. **Normalising** The SFTs are then divided by their running median with a window width of 100 frequency bins. If we assume the resulting SFTs to be χ^2 distributed, we can apply a correction factor using LALSuite code `XLALSFTtoRngmed` [**ligoscientificcollabor** such that their power spectrum has a mean of ~ 1. By then multiplying this by 2, the noise like parts of the spectrum are χ^2 distribution with two degrees of freedom.

3. **Narrowbanding** The computational efficiency can be improved if the data is split into narrow bands. This is because the analysis can be completed on each band in parallel on separate CPU nodes. In this search the spectrograms are split into 2.1 Hz wide bands every 2 Hz, i.e. 100.0-102.1, 102.0-104.1 etc. The bands are 2.1 Hz wide as the analysis on each node will further split the data into 0.1 Hz wide sub-bands. The overlap then allows the sub-band from 1.95-2.05 to be calculated on a node. This band size was chosen based on the available computational memory at the time.

4. **Band splitting** A CNN should not be trained on the same data that it will be tested on. For this reason, each of the 0.1 Hz wide sub-bands are split into 'odd' or 'even' bands. A CNN can then be trained on even bands and tested on odd bands and vice versa.

5a. **Training data generation** To generate training data the process is the same as described in Sec. 4.7. Each of the 0.1 Hz sub-bands is 'augmented' as in Sec. 4.7.2. For each of the augmented bands, the data is duplicated such that there is a second copy of every augmented band. In the copied set of bands, signals are injected into them with SNRs in the range 50-150. This gives us and example for a noise class and a signal class. There are two of these sets, one for 'even' bands and one for 'odd'.

5b. **Test data generation** For test data, signals following the parameters in Tab. 4.1 are injected in to 50% of the 0.1 Hz sub-bands. These signal have and SNR in the range 20-200. The SNR range here is wider than the training set as a method to test how the trained networks perform s on a wider range od SNRs. Here we again have a set for 'odd' and a set for 'even'.

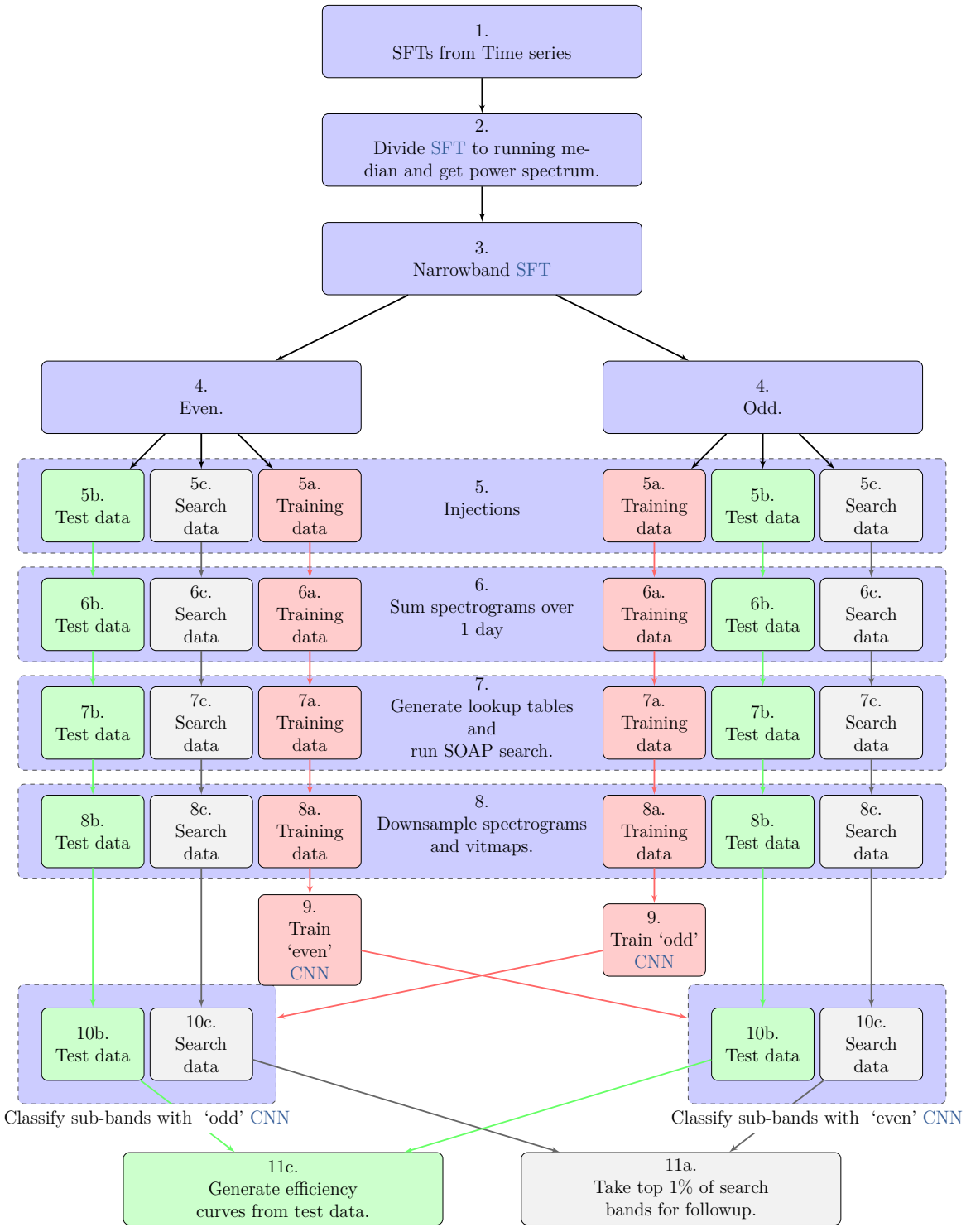

Figure 4.10: This diagram shows the SOAP pipeline from start to finish. There are three main sections: Training (red), Testing (green) and Searching (grey) for both the odd and even bands. The blue sections mean that the same operations is done in all cases.

5c. Search data This data is generated such that we can search for a real signal. The sub-bands described in part 4 are now overlapping by 0.05 Hz. This means that if there is an astrophysical signal present, it should be fully contained within at least one sub-band. We do assume that a signals frequency does not drift by more than 0.1 Hz, which is assumed to be true for isolated neutrons stars < 500 Hz. There are both 'odd' and 'even' versions of this search data.

6. Summing spectrogram As in [**bayley2019SOAPGeneralised**] the spectrograms are summed over one day, i.e., every 48 time segments (1 day) of the spectrogram are summed. This is done separately for each of the 6 data-sets (3 for 'odd', 3 for 'even').

7. Generate lookup tables and run SOAP search Before the SOAP search is run, the line-aware statistic lookup tables need to be generated as in [**bayley2019SOAPGenerali** Then for each of the 6 data-sets (3 for 'odd', 3 for 'even') the SOAP search is run separately.

8. Down-sample data At this stage there are four elements which are saved for each of the 6 data-sets. The two spectrograms, the Viterbi maps and the Viterbi statistic. The spectrograms and the Viterbi maps are down-sampled to a size of (156×89) using interpolation from scikit-image's resize [**vanderwalt2014ScikitimageImage**]. This size was chosen based on the S6 MDC data-set, where this is 1/3 the length in time and 1/2 the width in frequency of the summed spectrograms. This was chosen such that the CNNs trained efficiently and still achieved a reasonable sensitivity.

9. Train Networks The down-sampled training data is then used to train a CNNs. One CNN is trained on 'odd' bands and a different CNN with the same structure is trained on 'even' bands.

10b. Run search on test data The trained CNNs from part 9 are then used to classify each sub-band in the test data with injections, this returns a statistic in the range $[0, 1]$. The closer the value is to 1 the more likely it is from an astrophysical signal, therefore, the statistic can be interpreted as an estimate of the probability of a signal being present. Here the CNN trained on the 'odd' bands is tested using the 'even' bands and vice versa. The algorithms are run on this test data to asses the sensitivity of the analysis.

10c. Run search on real data The trained CNNs from part 9 are then used to classify each sub-band in the search data, this returns a statistic in the range $[0, 1]$. This statistic is the same as in part 10b. Once again the CNN trained on the 'odd' bands is tested using the 'even' bands and vice versa.

11a. Signal candidates The signals which have a statistic in the top 1% can be taken as potential candidates. This can then potentially be followed up with other CW search methods.

11c. Efficiency curves The output statistics from the test data-set (11b.) can be plotted against SNR to see how the network classified signals with the SNR of the injection. This can potentially be extended to other signal parameters also. Then the efficiency curves can be generated, this is described in further detail in Sec. 4.9.1.

4.9 Results

The networks described in Sec. 4.6.1 were trained and tested on four different data-sets: the S6 MDC as in [**bayley2019SOAPGeneralised**, **walsh2016ComparisonMethods**], our own injections into O1 and O2 data, Gaussian noise which had the same gaps and noise floor as the S6 data-set, and our own injections into real S6 data. Each of the searches use training and testing data in the frequency range of 100-400 Hz, except the S6 MDC which uses data in the range 40-500 Hz for testing and training.

4.9.1 Sensitivity

To investigate the sensitivity of the pipeline we use two measures: the sensitivity depth $\mathcal{D}$ [**prix2007SearchContinuous**] and optimal SNR ρ [**behnke2015PostprocessingMethods**] which are both defined in [**bayley2019SOAPGeneralised**]. The sensitivity depth is defined as

$$\mathcal{D}(f) = \frac{\sqrt{S_h(f)}}{h_0}, \tag{4.4}$$

where $S_h(f)$ is the single-sided noise PSD and h_0 is the GW amplitude. The optimal SNR is defined as,

$$\rho^2 = \sum_X 4\Re \int_0^\infty \frac{\tilde{h}^X(f)\tilde{h}^{X*}(f)}{S^X(f)} df, \tag{4.5}$$

where X indexes the detectors and $\tilde{h}(f)$ is the Fourier transform of the time series of the signal $h(t)$. This expression is defined in [**prix2007SearchContinuous**] for a double-sided PSD and we have defined it for the more common single-sided case.

The sensitivity curves shown in Fig. 4.12, 4.13 and 4.14 were generated using a 1% false alarm rate, where the false alarm threshold is the value of our statistic where 1% of sub-bands which do not contain an injection exceed that value. This is then used as a detection threshold. The efficiency is defined as the fraction of events which exceed the false alarm rate for any given SNR. The SNR is sampled uniformly between the range 20-200 as described in Sec. 4.8. Therefore, we do not have multiple simulations for a discrete

SNR but adopt a different approach. Instead, one can define some window around a point in SNR and count the fraction of statistics which exceed the false alarm threshold within that window. We define the window as a Gaussian with a standard deviation of 2, this is wide enough to contain enough injections at a given SNR to achieve a reliable value. The efficiency curves y are then calculated using,

$$y(\rho) = \frac{\sum_i H(O_i - O^{1\%})\mathcal{G}(\rho_i; \mu = \rho, \sigma = 2)}{\sum_i \mathcal{G}(\rho_i; \mu = \rho, \sigma = 2)}, \tag{4.6}$$

where O_i is the output statistic from the CNN, $O^{1\%}$ is the statistic value corresponding to a 1% false alarm rate, H is the Heaviside step function which has a value of 1 for positive input arguments and 0 for negative arguments. The SNR of a simulation with output O_i is defined in Eq. 4.6 using ρ_i. The current location in SNR is then ρ. The window is a Gaussian with a mean of the current SNR and a standard deviation of 2, $\mathcal{G}(\rho_i, \mu = \rho, \sigma = 2)$. The sensitivity curves for each of the described data-sets are shown in Figs. 4.12, 4.13 and 4.14.

O1

For the first test, injections were made into the O1 data-set as in Sec. 4.7 between 100 Hz and 400 Hz. Then each of the 6 networks described in Sec. 4.6.1 were trained and tested on this data. Figure 4.11 shows the sensitivity curves for this test for both SNR and sensitivity depth for each of the 6 networks. Focusing on Fig. 4.11a, the least sensitive, i.e. furthest to the right, of the CNNs is the Viterbi statistic (vitstat), this is expected as we know that the Viterbi statistic is sensitive to instrumental lines. The spectrogram CNN has an improved sensitivity over the Viterbi statistic, this importantly does not involve the SOAP search but is run entirely on down-sampled and summed spectrograms. Whilst this network is approaching the most sensitive of the examples in Fig. 4.11, and with further efforts may reach it, this network takes ~ 10 times the amount of training time. This will be explained in more detail in Sec. 4.9.2. The remaining networks achieved almost the same sensitivity. The vitmap network however, is the fastest of these to train and is used as an input for all of these remaining networks. For the O1 data-set we show that with a false alarm of 1% the Viterbi map CNN achieves a sensitivity of SNR ~ 73 and sensitivity depth of ~ 12 Hz$^{-1/2}$ with 95% efficiency. The SNR here should not be compared between different runs as this is the integrated 'recovered' SNR. Therefore, observing runs, such as O1, which were shorter will appear to have a greater sensitivity when they in fact do not.

O2

For the first test, injections were made into the O2 data-set as described in Sec. 4.7 between 100 Hz and 400 Hz. Each of the 6 networks described in Sec. 4.6.1 were then trained and

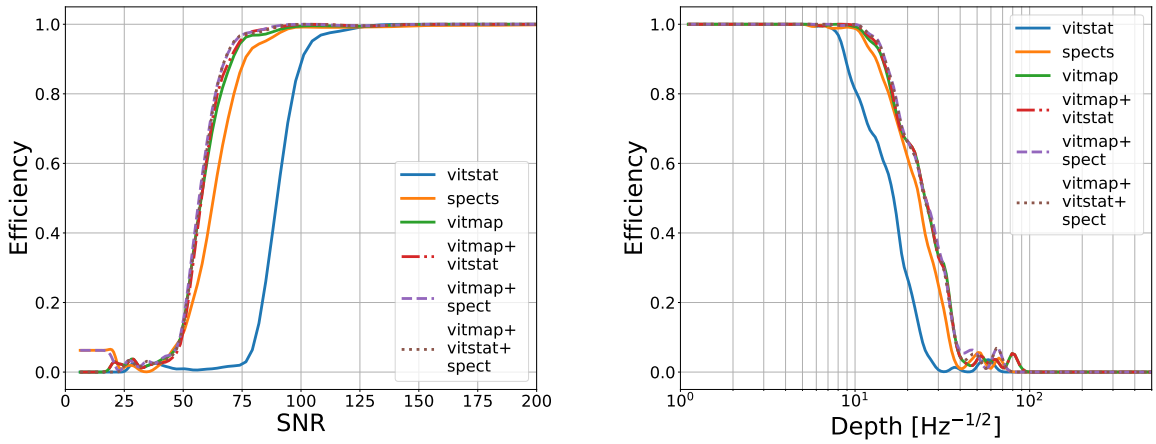

(a) (b)

Figure 4.11: In the O1 data-set, each of the six CNNs were tested. The efficiency plots above are for a 1% false alarm rate. Fig. 4.11a shows the efficiency of the search as a function of SNR and Fig.4.11b shows the efficiency as a function of sensitivity depth. The efficiency here is a measure of the fraction of events which exceed the 1% false alarm probability for any given SNR.

tested on this data. Figure 4.12 shows the sensitivity curves for this test for both SNR and sensitivity depth for each of the 6 networks. Focusing on Fig. 4.12a, the least sensitive of the CNNs is the Viterbi statistic (vitstat). This is expected as we know that the despite the line-aware aspect of the Viterbi statistic, it can still confuse some instrumental lines with an astrophysical signal. Similarly to O1, the spectrogram CNN has an improved sensitivity over the Viterbi statistic. The remaining four networks all achieve a similar sensitivity, each of these networks contain the Viterbi map (vitmap) as one of their inputs or their only input. Therefore, it is assumed that the dominating effect on the sensitivity originated from the Viterbi maps. In the following tests the focus will be on the Viterbi map CNN as in all cases this is among the most sensitive. For the O2 data-set we show that with a false alarm probability of 1% the Viterbi map CNN achieves a sensitivity of SNR $\sim$ 95 and sensitivity depth of $\sim$ 12 Hz$^{-1/2}$ with 95% efficiency. In Fig. 4.12a the sensitivity of the spectrogram CNN drops after an SNR of 150. This is most likely due to the training set containing simulations between and SNR of 50 and 150, therefore, has not seen signal simulations of higher SNR. The dip in sensitivity in Fig. 4.12b at lower depths is from the same origin as Fig. 4.12a.

Gaussian noise and S6

The second test involves using simulations in Gaussian noise and comparing this to simulations in S6 data. For this test we replicate the S6 data-set without including instrumental artefacts such as lines. We included the same gaps in data as S6 and the noise floor of

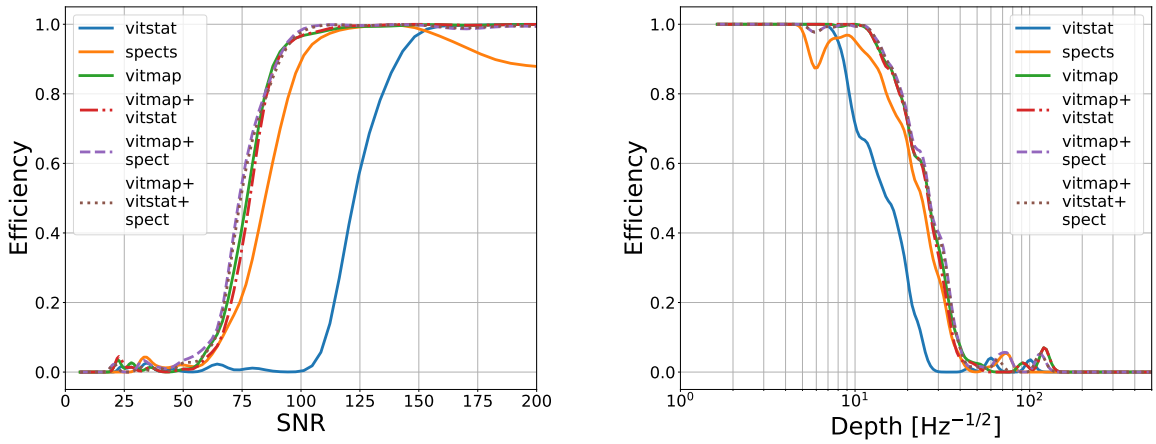

(a) (b)

Figure 4.12: In the O2 data-set, each of the six CNNs were tested. The efficiency plots above are for a 1% false alarm rates. Fig. 4.12a shows the efficiency of the search as a function of SNR and Fig.4.12b shows the efficiency as a function of sensitivity depth. The efficiency here is a measure of the fraction of events which exceed the 1% false alarm probability for any given SNR. These plots both show the sensitivity of the Viterbi statistic is far below that of the different CNNs. The others are grouped with a similar sensitivity.

S6 was replicated by scaling the SNR of an injection in any given SFT by an estimate of its PSD. Figure 4.13 shows the SNR and depth sensitivity curves for the Viterbi statistic and Viterbi map CNN for both the Gaussian noise run with S6 gaps and for injections into the S6 data-set. In the Gaussian noise data-set the curves for both statistics, Viterbi map CNN and the Viterbi statistic, show very similar results, this is to be expected as the main use of the CNN was to reduce the effect of instrumental lines, for which there are none in this data set. The advantage of using the Viterbi maps in a CNN becomes clear when it is tested on simulations into real S6 data with many instrumental lines. The two curves corresponding to simulations real S6 data in Fig. 4.13a show the sensitivity as a function of SNR in these tests. It becomes clear here that the Viterbi map CNN reduces the effect of instrumental lines and therefore increases the searches sensitivity to SNR. A similar feature can be seen in Fig.4.13b where the use of an CNN greatly increases the sensitivity.

These tests on S6 data also show that the effect of instrumental lines was far greater in this run than in O2. This is shown in Fig. 4.12a where the separation between the Viterbi statistic curves and the Viterbi map curves is much smaller than the S6 curves in Fig. 4.13a. For simulations into Gaussian noise following S6 gaps we show that with a false alarm of 1% the Viterbi map CNN achieves a sensitivity of SNR 85 and sensitivity depth of ~ 20 Hz$^{-1/2}$ with 95% efficiency. For injections into real S6 data the search achieves a sensitivity of SNR ~ 115 and sensitivity depth of ~ 11 Hz$^{-1/2}$ with 95% efficiency and

1% false alarm. We can also see from Fig. 4.13a that the sensitivity of the vitmap CNN in Gaussian noise with S6 gaps is better than in real S6 data. There are then still some artefacts in real data which reduce the sensitivity, these could potentially be non Gaussian artefacts such as weak instrumental lines.

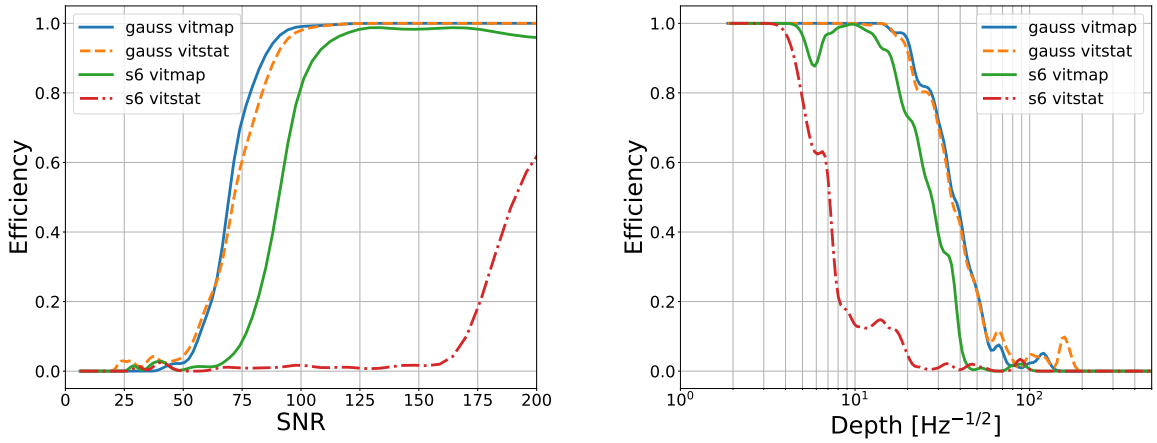

(a) (b)

Figure 4.13: We compared the sensitivity of this search on simulations on real S6 data (s6) to simulations in Gaussian noise (gauss). Figure 4.13a shows the efficiency of the search as a function of SNR and Fig. 4.13b shows the efficiency as a function of sensitivity depth. The efficiency is the fraction of events which exceed the 1% false alarm threshold for a given SNR or depth. The Gaussian noise injections included the same gaps in data as the S6 data set. The SNR of the simulated signal in Gaussian noise was adjusted based on the noise floor of S6. In the Gaussian noise simulations the searches achieve an efficiency of 90% with 1% false alarm at an SNR $\sim$ 85 and $\sim$ 90 for the Viterbi map and Viterbi statistic respectively. In the real S6 noise simulations the searches achieve an efficiency of 90% with 1% false alarm at an SNR $\sim$ 108 and $>$ 200 for the Viterbi map and Viterbi statistic respectively.

S6 MDC

The final test was set up to again use the S6 data-set, however, in this case we use a standard set of injections in the S6 MDC [**walsh2016ComparisonMethods**] to compare directly to other CW search pipelines. In Fig. 4.14 we show the results of the sensitivity curves from these injections. In both Fig. 4.14a and 4.14b the sensitivity curves are substantially more noisy than in Fig. 4.12 or 4.13, this is mainly due to the size of the testing set. The standard set of simulations in Fig. 4.14 contained $\sim$ 900 signal simulations between 100 and 400 Hz where the majority of these signals are distributed between an SNR of 0 and 150. Figures 4.12 and 4.13 are generated using 2300 simulations between 40 and 500 Hz and SNRs of 20 and 200 as described in Sec. 4.8. Figure 4.14b shows the direct comparison in depth of the results in [**walsh2016ComparisonMethods**] with the

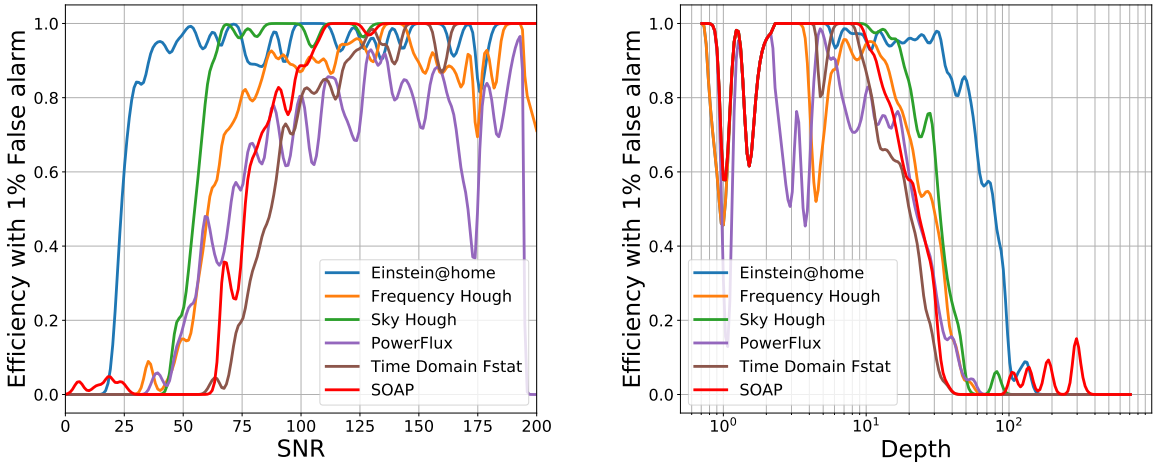

(a) (b)

Figure 4.14: To compare the SOAP and CNN search to other existing CW searches, we used a standard set of injections used in the S6 MDC [**walsh2016ComparisonMethods**]. We have taken the list of detected pulsars for each search from this paper [**walsh2016ComparisonMethods**] and replotted using the method in Sec. 4.9.1 to compare the sensitivities to the SOAP + CNN search. This includes results for all pulsar simulations between 40 and 500 Hz. The efficiency curves are generated with a 1% false alarm probability.

results from the SOAP search with the Viterbi map CNN. This shows that we achieve a sensitivity consistent with that of other semi-coherent searches with the exception of the Einstein@home search [**abbott2016ResultsDeepest**]. Whilst we are not at the most sensitive end of these searches, the SOAP and CNN search offers a greatly reduced computational cost. This will be explained in more detail in Sec. 4.9.2. This particular test was limited to searching for isolated neutron stars, however, unlike some other semi-coherent searches such as Einstein@Home [**singh2016ResultsAllsky**] or the time domain $\mathcal{F}$-statistic [**aasi2014ImplementationTextdollar**], SOAP has a lot of flexibility in the type of signal which it can search for. The inclusion of the CNN does introduce some dependency of the search on the model as the training set for the CNN contained simulations of isolated pulsars. However, this is not a limitation of the method but of the training set as, for example, a new training set using a different signal model could be generated. There may be some more computational cost to the CNN for a different signal model, for example, a more complex frequency evolution may require more training. However, this is not expected to make large differences to the computational cost, and is still expected to be orders of magnitude faster than other semi-coherent searches. For tests in the S6 MDC we show that with a false alarm of 1% the Viterbi map CNN achieves a sensitivity in SNR of ~ 90 and sensitivity depth of ~ 16 Hz$^{-1/2}$ with 95% efficiency.

4.9.2 Computational time

A key property of any CW search is the computational time taken for the search to run. Table 4.2 shows the timings for different sections of the search when run on the S6 dataset. This can be split into three main sections: data generation, CNN training and CNN testing. To get from raw SFTs to results with this search, the majority of the computational time taken is in the data generation step. The timings shown Tab. 4.2 are for the S6 observing run where each section is run on a single central processing unit (CPU) or graphics processing unit (GPU), however, in practice the generation of the data is generally run on multiple CPUs on a computing cluster. The training and testing of a CNN is done on a single GPU, this substantially decreases the training time compared to a CPU due to the parallel nature of neural networks.

One can start from raw SFTs from the S6 dataset without any trained networks, where this dataset has 22538, 1800 s long SFTs and we search between 40-500 Hz, i.e. 828000 frequency bins. This search would have a total computing time of ~ 366 hours on a single CPU and GPU. However, the majority of this time is taken generating the appropriate data. The generation of training, testing and search data can be easily parallelised, where in practice this is split over 200 CPUs so that it takes ~ 2 hours instead of ~ 364 hours. After this parallelisation, if one was given S6 data without any trained networks, the search would then take approximately 13 hours to get an efficiency curve and a list of candidates. In the cases above I assume that only the Viterbi map network is trained and tested based on the conclusions from Sec. 4.9.

The computational cost could be reduced further if a network had been trained on a previous observing run. This would mean that the generating of the training data and the training of the network may not be needed. This would reduce the total run time on S6 to ~ 9.5 hours. However, this does not drastically reduce the run time as the majority of the time is spent narrow-banding the SFTs which is not run in parallel.

To reduce the time taken to generate results at the end of an observing run, one could narrowband the SFTs periodically as the data is taken during an observing run. This would allow the results to be generated within ~ 3.5 hours of the end of the run. SFTs generated on a regular basis would allow results to be generated during an observing run. This could be done, for example, on a weekly basis by adding 7 days of pixels to a spectrogram, then retraining a CNN and generating results.

The computational cost of this search is small when compared to other existing CW searches. In [**walsh2016ComparisonMethods**] the expected computational cost for the first 4 months of O1 for each search is shown, where the fastest search takes 0.9 million core-hours (Hough searches) and the slowest is $100-170$ million core-hours (Einstein@Home). The equivalent cost of the SOAP + CNN search is $\sim 100-200$ core-hours which is $\sim 5-10$ thousand times faster.

Table 4.2: The approximate timings were measured for each part of the search. This table shows the timings for training and testing starting from raw SFTs. This is the results from S6 which is the longest run we tested. We used S6 data in the frequency range between 40-500 Hz and it had a length 22538 SFTs with time base of 1800 s. In the training,testing and search data sections we averaged the SFTs over one day such that we had 469 time segments as input to the CNNs. The data generation times here are for a single CPU however, in reality this will be split across many separate CPUs. The training and testing is completed on a single GPU.

Generating data on single CPU

	Time [hrs]
Narrow-banding	~ 9
Training data	~ 240
Testing data	~ 75
Search data	~ 40

Training CNNs on single GPU

	Training time [hrs]	Loading time [hrs]
Viterbi statistic	0.03	0.2
Viterbi map	0.8	0.7
spectrogram	9	1
Viterbi map + Viterbi statistic	1	0.7
Viterbi map + spectrogram	1.4	1.6
Viterbi map + Viterbi statistic + spectrogram	1.5	2

Testing CNNs on real data on GPU

	Testing [s]	Loading [s]
All CNNs	5	$60 - 160$

4.10 Sensitivity with the size of dataset

When training a CNN, the general rule is that the more data the better. More data can limit effects such as over-training mentioned in Sec. 4.5, and can increase the CNNs sensitivity. To investigate how the sensitivity of the search changes with the number of training examples, the Viterbi map (vitmap) network in Sec.4.9 was trained using a range of sizes of the training set. These networks are then tested on a separate dataset of a fixed size to see how they perform. This was repeated for two data-sets: CW simulations in Gaussian noise and simulations in LIGOs O1 data-set. For both of these cases six different networks were trained, these used: 100, 500, 1000, 5000, 10000 and 15000 Viterbi maps as their training datasets. Each of these different sizes of training data is a randomly selected subset of the training data used in Sec. 4.9.1. The test data for each was the same entire test sets as in Sec. 4.9.1.

Figure 4.15a shows that in the Gaussian noise case, the majority of the networks performed with approximately the same sensitivity. This is with the exception of the network which was trained with 100 input Viterbi maps. As expected, Fig. 4.15b shows that the SNR decreases (sensitivity improves) as the number of training examples increases, the point at 10000 images appears to increase in SNR, however this is expected to be within the noise. The range over which the SNR decreases however, is only by an SNR of ~ 5. The implication of this is that the information in the Viterbi maps is relatively easy to extract when simulations are in Gaussian noise. In this case the network is trying to distinguish Gaussian noise from a simulated CW signal. Therefore, one would expect this to be an easier problem for the network to solve compared to trying to distinguish an CW signal from instrumental lines and Gaussian noise.

When simulating signals in real O1 data, many of the sub-bands will contain instrumental lines. The noise class for the CNN then contains many variations compared to the Gaussian noise case. This is a harder challenge for the CNN as it increases the size of the parameter space. Because of this, one would expect the network to need many more training examples to be able to achieve a similar sensitivity to Gaussian noise. In Fig. 4.16a, one can see that using 100 training examples is not enough for the CNN to achieve any sensitivity at any SNR. This means that the CNN cannot classify any injection as detected using this number of training examples. Figure 4.16b seems to agree that real data poses a harder problem as the sensitivity drastically increases as the number of training examples is increased. Therefore, more training examples are needed for the network to perform well on real data.

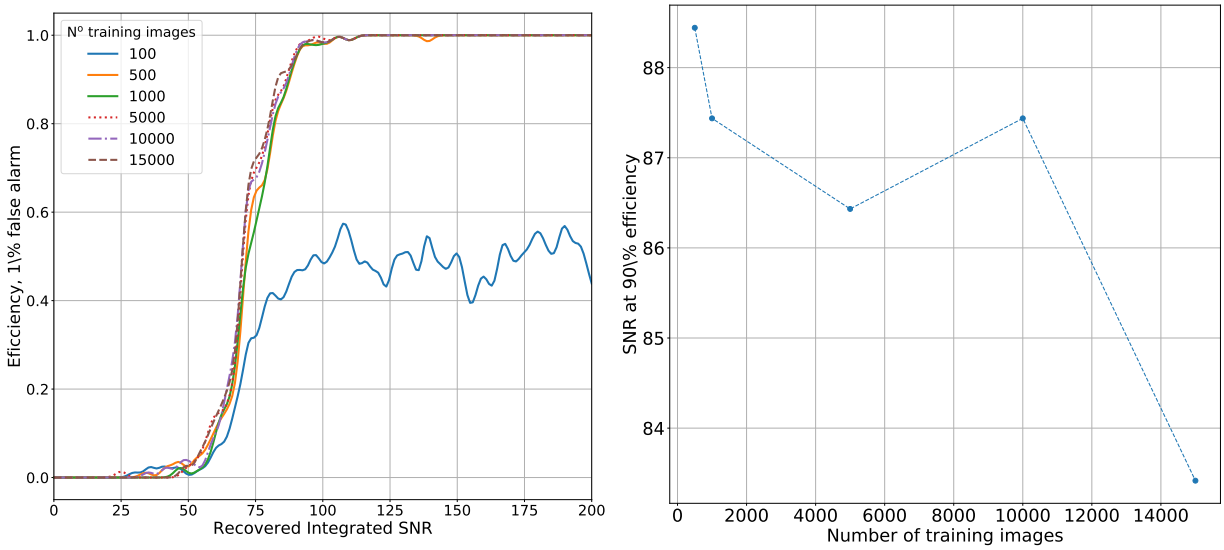

(a) (b)

Figure 4.15: The amount of training data needed for an CNN to perform well depends on the problem. Here we show how the sensitivity changes as a function of the number of training examples for simulations in Gaussian noise. Figure 4.15a shows the efficiency curves for each of the different data-set sizes and Fig. 4.15b shows the values of SNR at 90% efficiency as the data size increases. This shows that the increase in data size causes a slight increase in the sensitivity of the search. The efficiency curve for 100 training examples is not shows in Fig. 4.15b as it does not reach the 90% efficiency mark.

4.11 Network Visualisation

Neural networks are generally hard to visualise due to the large number of parameters in the network that have to be varied. However, there are methods which can be used to see how input data is affected by the network. This can be useful to see how the network performs when given certain types of data and gives some insight into how the networks work.

One way to visualise the network is to pass a piece of data through the network and see how each of the layers transforms the input. Figs. 4.17, 4.18 and 4.19 show examples of this. The layout is equivalent to that in Fig. 4.8. In these figures, the outputs from each of the layers in the CNN are shown. The first being the convolutional layers, followed by their max-pooling layers. The final fully connected layers are illustrated with connecting lines. The final neuron is then the value of the statistic which we use for the above analysis. Fig. 4.17 shows an input of a Viterbi map where the corresponding time-frequency spectrograms contained a strong CW signal. In this figure the next layer is the first convolutional layer, where 8 filtered Viterbi maps can be seen. This is then reduced in size by a max-pooling layer, followed by another convolutional and max-pooling layer. After this point, the figures can be compared and it becomes obvious that different neurons light up when the input is part of the signal class or when it in the noise class.

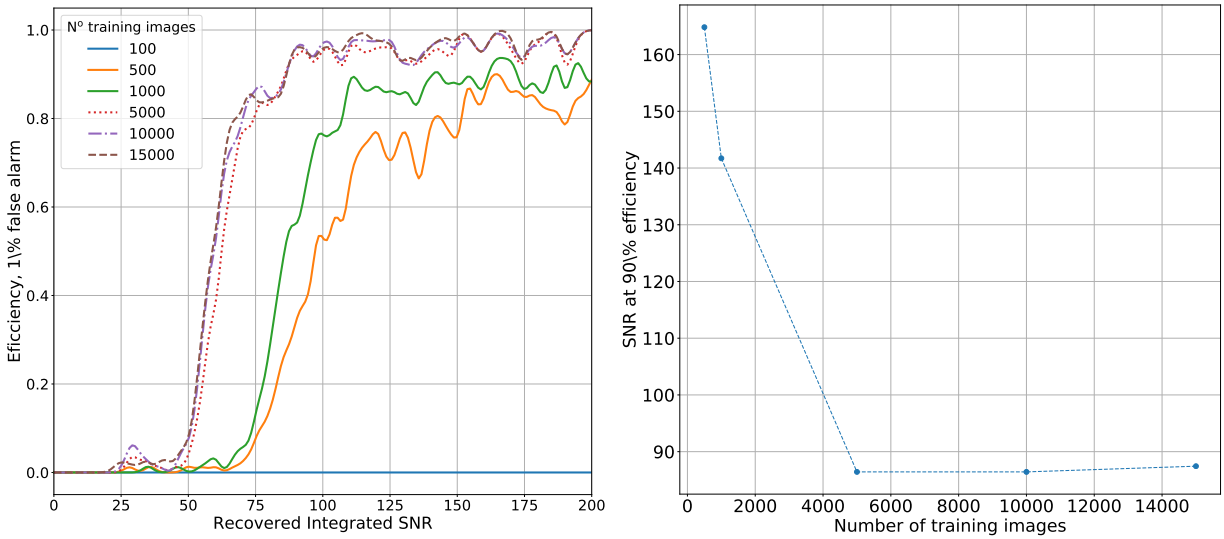

(a) (b)

Figure 4.16: Here I show how the sensitivity changes as a function of the number of training examples for simulations in O1 data. Figure 4.16a shows the efficiency curves for each of the different data-set sizes and Fig. 4.16b shows the values of SNR at 90% efficiency as the data size increases. This shows that the increase in data size causes a large increase in the sensitivity of the CNN. The efficiency curve for 100 training examples is not shows in Fig. 4.16b as it does not reach the 90% efficiency mark.

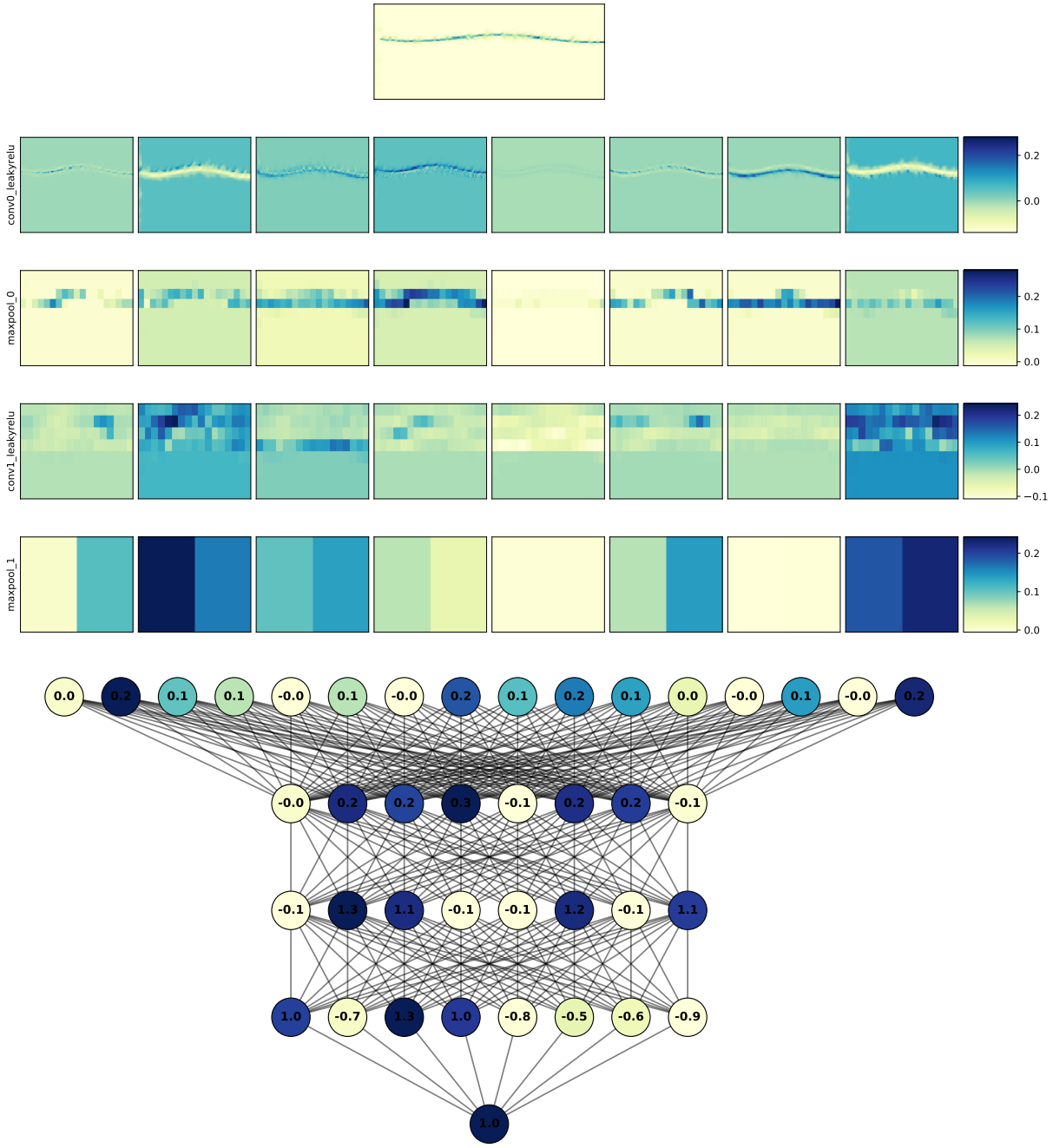

Figure 4.17: The CNN can be visualised by seeing how a piece of data is passed through the network. This figure shows how the image is processed in each layer of the network. The input here is a Viterbi map which results from the SOAP algorithm. The input to SOAP here is a time-frequency spectrogram which contains a strong CW signal. This then passes through 8 convolutional filters, then 8 max-pooling layers, then another set of 8 convolutional and max-pooling layers.the values are then flattened and it passes through 3 layers of 8 fully connected neurons.The final output neuron here is a 1 indicating that this is likely to contain a signal.

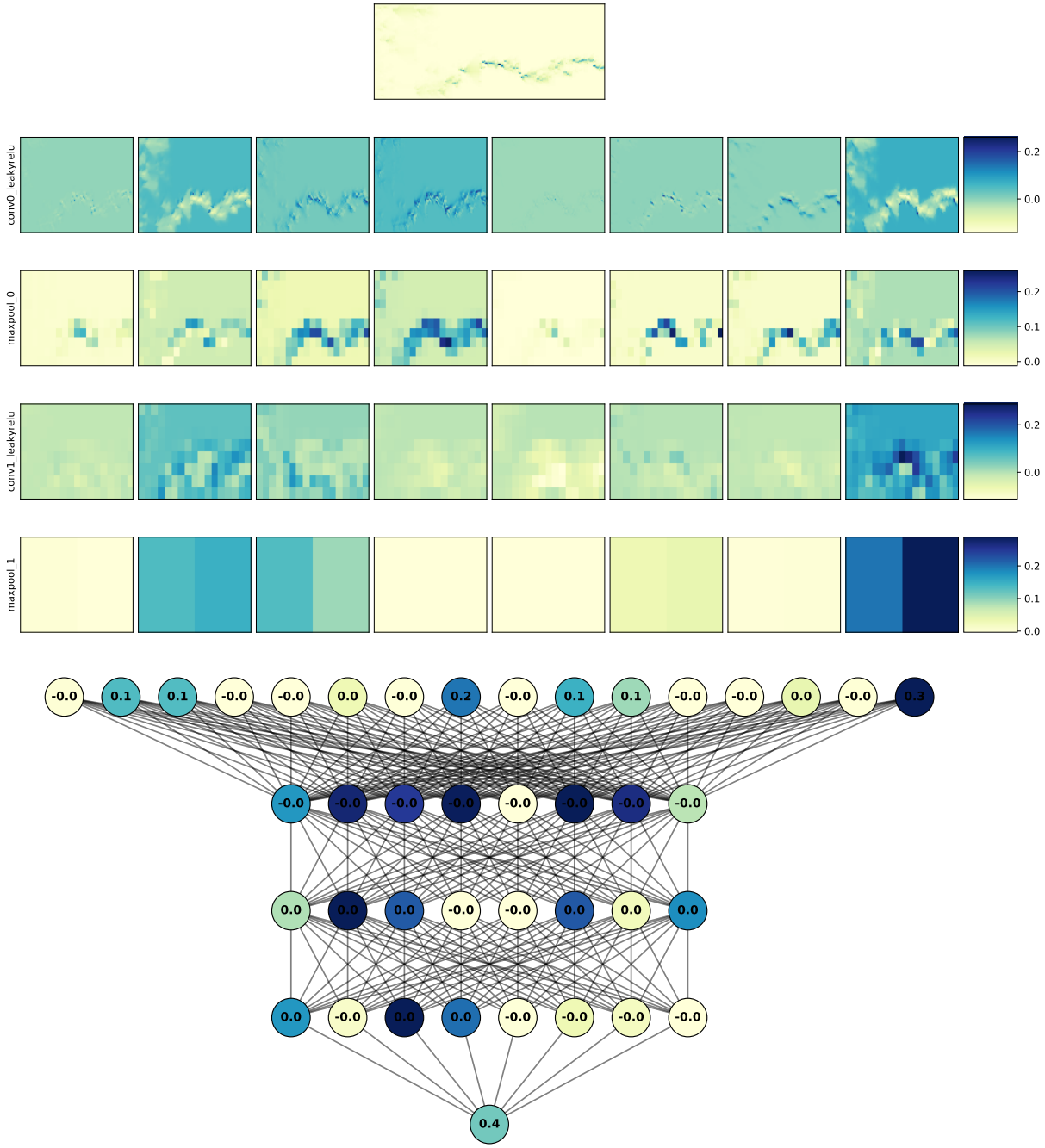

Figure 4.18: This visualisation of the Viterbi map CNN shows the input of a Viterbi map where the time-frequency spectrogram contains an instrumental line. Here the output neuron has a value of 0.4, far below that in Fig. 4.17.

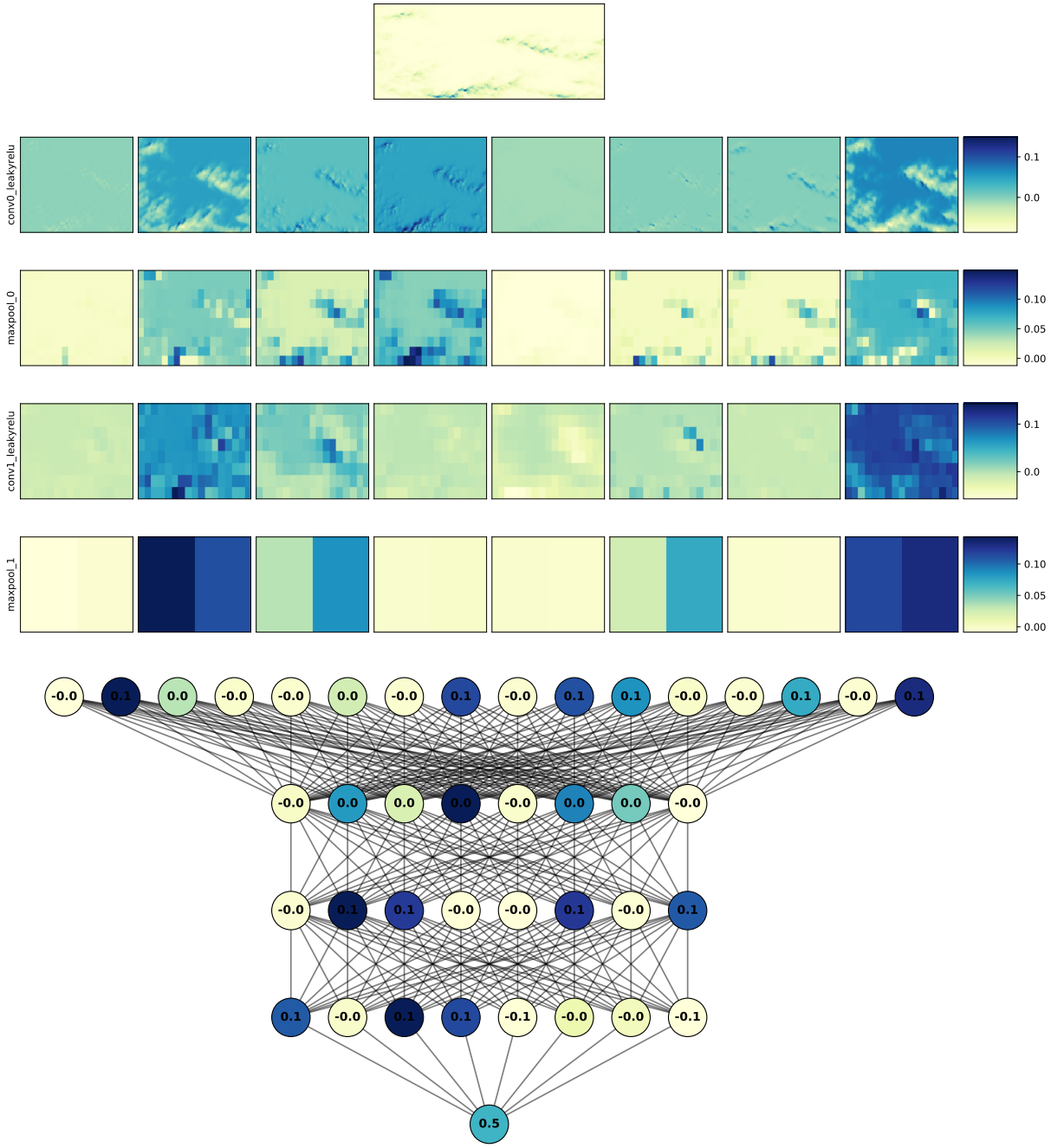

Figure 4.19: This visualisation of the Viterbi map CNN shows the input of a Viterbi map where the time-frequency spectrogram contains just Gaussian noise. The output here is similar to the case where an instrumental line is injected, i.e. the output is much less than 1.

4.12 Summary

In this Chapter we summarise an extension of the SOAP algorithm [**bayley2019SOAPGeneralise**
The extension makes use of a CNN to limit the effect of instrumental lines in a search for sources of CWs. The SOAP search has a number of outputs for a given input spectrogram, in this paper we focus on using two of the outputs: the Viterbi statistic and the Viterbi map. The Viterbi statistic has previously been used as a measure of whether there is an astrophysical signal in a given frequency band as in [**bayley2019SOAPGeneralised**]. The Viterbi maps are output maps with the same shape as the input spectrogram, these however give a value related to the probability that a signal is in any time-frequency bin. The aim of the CNN approach is to use both the Viterbi maps and spectrograms as input images to more effectively classify each frequency band to either having an astrophysical signal or not. This would then remove then need to manually look through frequency bands and remove those which are contaminated with non-astrophysical (instrumental) features.

We tested 6 separate CNNs which take in some combination of the three representations of the input data: the Viterbi statistic, the Viterbi map and normalised spectrograms. The aim of using different input data types is that each would provide a different representation of the same information, this had the potential to increase the sensitivity of the search. The tests found that the CNN which uses the Viterbi map alone as input was more sensitive than any other which used a single data type as input. Each of the CNNs that used a combination of input data types had a similar sensitivity to the Viterbi map CNN, therefore, we concluded that the Viterbi map provides the most useful information when detecting a signal. Given that the main aim of this paper was to reduce the effect of instrumental lines on the SOAP search, in Gaussian noise data (with no such lines), the CNN search should achieve a similar sensitivity to the Viterbi statistic alone. The tests in Gaussian noise with S6 gaps showed that at a 95 % efficiency and a 1% false alarm rate the Viterbi statistic and Viterbi map achieved a sensitivity of SNR 95 and 90 respectively. When the same test was run in real S6 data at a 95 % efficiency and a 1% false alarm rate the Viterbi statistic and Viterbi map achieved corresponding sensitivities of SNR 300 and 120 respectively. This demonstrates that the Viterbi map approach has a much larger effect when used on real data due to the presence of many instrumental lines.

These tests were once again repeated using a standard set of injections into S6 data such that a direct comparison can be made with other CW search pipelines. At a 95% efficiency and a 1% false alarm rate the Viterbi map CNN achieved a sensitivity of SNR ~ 90 and sensitivity depth ~ 14 Hz$^{-1/2}$. We have shown that the SOAP + CNN approach can achieve a similar sensitivity to other semi-coherent CW search algorithms but with a greatly reduced computational cost.

This search also offers a lot of flexibility in the signal type which can be searched, in

the above examples the focus is on isolated neutron stars such that a comparison can be made to other CW searches, however, this search is un-modelled. By changing the input parameters of the search, different signal types can be searched over, and in future work we aim to test its ability to identify other sources of GWs such as neutron stars in binary systems. Further to this, we aim to apply a more advances Bayesian analysis to enable parameter estimation of some parameters of the signal. These parameters would then provide crucial information for a deeper followup by fully coherent pipelines.

Chapter 5

Parameter estimation using SOAP

Throughout Chapters 3 and 4 we have developed techniques that could identify whether a potential CW signal is present within a small frequency band of width 0.1 Hz, and then return the frequency track that the signal is most likely to follow. This provides the frequency bands in which a signal could be present, which is useful for all-sky searches as it can limit the parameter space and therefore computational time for deeper searches such as those described in Sec. 2.3.1. However, this only limits the parameter space in frequency to a smaller frequency band, where there is still a large parameter space which needs to be searched. If the Viterbi track returned by SOAP in Chapter 3 follows the frequency evolution of a CW source, then this track contains information on the sky position and frequency evolution of the CW. If one could extract this information then the size of the parameter space could be reduced for more sensitive coherent searches, decreasing their computational cost.

In this Chapter we will outline a Bayesian method that uses the output Viterbi tracks of the SOAP search in Chapter 3 to return a subset of astrophysical parameters of a source. Section 5.1 will outline the model of the frequency evolution of a CW from a source with a slowly varying frequency, Sec. 5.2 will outline the Bayesian model for this analysis and Sec. 5.3 will show the results from testing on simulated signals.

5.1 CW source frequency evolution

The SOAP search, both single and multi detector, returns a frequency track known as the Viterbi track, if this track follows the frequency of a CW source, then the frequency evolution contains information of the sky position (α, δ), the frequency of the source f and its derivative $\dot{f}$, where we ignore higher order frequency derivatives. From the Viterbi track, we should then be able to extract this information as we have a model for the phase evolution (and therefore frequency evolution) of the source described in Eq. 2.4 in Sec. 2.1. To relate this phase evolution to the sky position parameters, we can look closer at Eq. 2.5,

where we describe the shift in arrival time due to the Earth's motion.

The second term in Eq. 2.5 describes the Doppler shift due to the earth's orbit and rotation. Where the $\boldsymbol{r}$ is the position of the detector and $\boldsymbol{n}$ is a unit vector in the direction of the source. As in [**schutz1998DataAnalysis**], we use the ecliptic coordinate frame in the SSB where the z axis is perpendicular to the ecliptic and the x axis points towards the first point of Aries. In this frame the unit vector pointing towards the source can be written as

$$\boldsymbol{n} = \begin{pmatrix} 1 & 0 & 0 \\ 0 & \cos\epsilon & \sin\epsilon \\ 0 & -\sin\epsilon & \cos\epsilon \end{pmatrix} \begin{pmatrix} \cos(\alpha)\cos(\delta) \\ \sin(\alpha)\cos(\delta) \\ \sin(\delta) \end{pmatrix}, \tag{5.1}$$

where α and δ are the right ascension and declination (sky position) of the source and ϵ is the obliquity of the ecliptic, which is the inclination angle of the earths equator with respect to the ecliptic. The first matrix in Eq. 5.1 describes a rotation from the celestial frame to the ecliptic frame an the second vector transforms the sky position parameters to their component x, y, z coordinates in the celestial frame.

The position vector of the detector, $\boldsymbol{r}$ in Eq. 2.5, at a time t can be split into two components, the position due to the orbit of the earth and position of the detector due to the rotation of the Earth. If we assume the orbit is circular, then the position of the earth in its orbit is described in Cartesian coordinates as

$$\boldsymbol{r}_{\text{orb}} = R_{\text{orb}} \begin{pmatrix} \cos\left(\Omega_{\text{orb}} t\right) \\ \sin\left(\Omega_{\text{orb}} t\right) \\ 0 \end{pmatrix}, \tag{5.2}$$

where R_{orb} is the radius of the earth's orbit (1 AU), Ω_{orb} is the angular frequency of the earth's orbit $2\pi/T_{\text{orb}}$, where T_{orb} is one year and the time $t = 0$ is when the earth is at the spring equinox. The position due to the rotation of the earth can then be described by

$$\boldsymbol{r}_{\text{rot}} = R_{\text{rot}} \begin{pmatrix} 1 & 0 & 0 \\ 0 & \cos\epsilon & \sin\epsilon \\ 0 & -\sin\epsilon & \cos\epsilon \end{pmatrix} \begin{pmatrix} \cos\left(\beta\right)\cos\left(\Omega_{\text{rot}} t + \phi_{\text{rot}}\right) \\ \cos\left(\beta\right)\sin\left(\Omega_{\text{rot}} t + \phi_{\text{rot}}\right) \\ \sin\left(\beta\right) \end{pmatrix}, \tag{5.3}$$

where R_{rot} is the radius of the earth, Ω_{rot} is the angular frequency of the earth's rotation $2\pi/T_{\text{R}}$, where T_{rot} is one day and β is the detectors latitude. The phase ϕ_{rot} defines the position of the earth in its rotation at $t = 0$ and is determined by $\phi_{\text{rot}} = \text{LST}_{\text{t=0}} = \text{GMST}_{\text{t=0}} - \lambda$, where λ is the longitude of the detectors site, the Greenwich mean sidereal time (GMST) is the angle between the first point of Aries and the Greenwich meridian and the LST is the local sidereal time. The sum of these two components then define the

location of the detector in the SSB frame

$$\boldsymbol{r} = \boldsymbol{r}_{\text{orb}} + \boldsymbol{r}_{\text{rot}}. \tag{5.4}$$

We can now describe the phase evolution of the signal at the detector sites (latitude β and longitude λ) starting at a time $t = 0$ from the source sky position (α, δ), frequency f and its derivative $\dot{f}$. We can write the phase evolution from Eq. 2.4 as

$$\begin{aligned}\Phi(t) = 2\pi\left(f_0 t + \frac{\dot{f}t^2}{2}\right) + \frac{2\pi}{c}\left(f_0 + \dot{f}t\right)\{R_{\text{orb}}\left[\cos\alpha\cos\delta\cos\left(\Omega_{\text{orb}}t\right)\right. \\ + \left(\cos\epsilon\cos\alpha\cos\delta + \sin\epsilon\sin\delta\right)\sin\left(\Omega_{\text{orb}}t\right)] \\ \left. + R_{\text{rot}}\left[\sin\beta\sin\delta + \cos\beta\cos\delta\cos\left(\alpha - \Omega_{\text{rot}}t - \phi_{rot}\right)\right]\right\},\end{aligned} \tag{5.5}$$

where we ignore frequency derivatives higher than first order. The frequency of a CW signal at any point on the frequency track is then defined by the derivative of the phase with respect to time

$$f(t) = \frac{1}{2\pi}\frac{d\Phi(t)}{dt}. \tag{5.6}$$

5.2 Bayesian Model

As described in Sec. 5.1 we have a model of the frequency evolution of a CW and we have a Viterbi track which is our observation of a frequency track. We would now like to estimate the parameters $\boldsymbol{\theta} = \left\{\alpha, \delta, f, \dot{f}\right\}$ of a CW given that we have observed the frequency track $\boldsymbol{V}$. To do this we use a Bayesian model

$$p(\boldsymbol{\theta} \mid \boldsymbol{V}, I) = \frac{p(\boldsymbol{\theta} \mid I)p(\boldsymbol{V} \mid \boldsymbol{\theta}, I)}{p(\boldsymbol{V} \mid I)} \tag{5.7}$$

where $p(\boldsymbol{\theta} \mid \boldsymbol{V}, I)$ is the posterior which we are interested in, $p(\boldsymbol{\theta} \mid I)$ is the prior, $p(\boldsymbol{V} \mid \boldsymbol{\theta}, I)$ is the likelihood and $p(\boldsymbol{V} \mid I)$ is the Bayesian Evidence. The following sections will describe how we define the prior and likelihood for this problem.

5.2.1 Likelihood

The likelihood describes the probability of measuring the data given a signal, where in this case our data is the Viterbi track $\boldsymbol{V}$ and our signal is the model frequency track $\boldsymbol{M}(\boldsymbol{\theta})$. The aim is to find this probability distribution such that we can evaluate it for any model parameters $\boldsymbol{\theta}$ and any data $\boldsymbol{V}$.

We define our likelihood from the deviation in frequency bins of the Viterbi track from a model frequency track given some parameters $\boldsymbol{\theta}$, i.e. $\boldsymbol{M}(\boldsymbol{\theta}) - \boldsymbol{V}$. If the simulated CW

signal has an infinitely large SNR then the Viterbi track would follow the CW frequency track exactly, giving a delta function with 0 variance for the deviation of the Viterbi and CW frequency tracks. If conversely, the SNR was zero then the Viterbi track would wander randomly through the frequency band independently of the CWs frequency track, meaning that the deviation of the two frequency tracks would have a variance $\mathcal{O}(\text{width})$ of the frequency band. The distribution of these deviations is then dependent on the SNR ρ of the signal.

We can also think about how the Viterbi track will deviate from the model frequency track for different values of the parameters $\boldsymbol{\theta}$. For a fixed SNR we assume that the deviation of the two tracks is independent of the parameters which define the frequency evolution of the signal. For simplicity, we also assume that the deviation of the tracks is independent of the track position. Given that the distribution of the deviations is difficult to find analytically, we calculate it empirically using the deviations of the two frequency tracks for many simulated of CW signals.

In Sec. 4.9 we generated $\mathcal{O}(10^4)$ simulated CW signals in Gaussian noise between 40 and 500 Hz, which had SNR ρ uniformly distributed between 40 and 200 and source parameters which follow those in Tab. 4.1. For each of these simulations, the SOAP search using the line-aware statistic with parameters from Sec. 3.10 returns a Viterbi track associated with the simulated parameters. As we have assumed the distribution of the deviations is independent of the position in the track, we can calculate the difference between the Viterbi track and simulated CW frequency track $M_i(\boldsymbol{\theta}^{\text{sim}}) - V_i$ for each element in the track and each simulation . At a fixed SNR, the density of these at a given deviation is the likelihood $\mathcal{L}$. We can model the likelihood distribution by finding the histogram of the track deviations. As the track deviations are integer frequency bin widths, the histogram bins centers are at $0, \pm 1, \pm 2 .... \pm W$, where W is the width of the frequency band in bins.

In this case our likelihood is also dependent on SNR, therefore, we split our simulations into bins of width SNR 2 between 40 and 200. Within each SNR bin, this gives us ~ 300 simulated tracks each with ~ 400 elements. In Fig. 5.1, rather than using a histogram we use a kernel density estimate (KDE), which is a different method to estimate the probability density, this is the same result but makes the likelihood easier to interpret in a plot. Figure 5.1 shows an example of the KDEs for a subset of the SNR bins. The sharp peaks in the center of each KDE in Fig. 5.1 represent simulations where the Viterbi track is close to the simulated CW track, and the broader distributions represent areas where the Viterbi track has not identified the CW track but is wandering randomly. Figure 5.1 shows that as the SNR increases, the distribution is more closely centred around 0, i.e. the Viterbi and CW tracks are similar, which is expected.

The dependence of the likelihood on the SNR ρ introduces one more parameter to include in our Bayesian model. The likelihood is binned in SNR with widths of $\rho_w = 2$

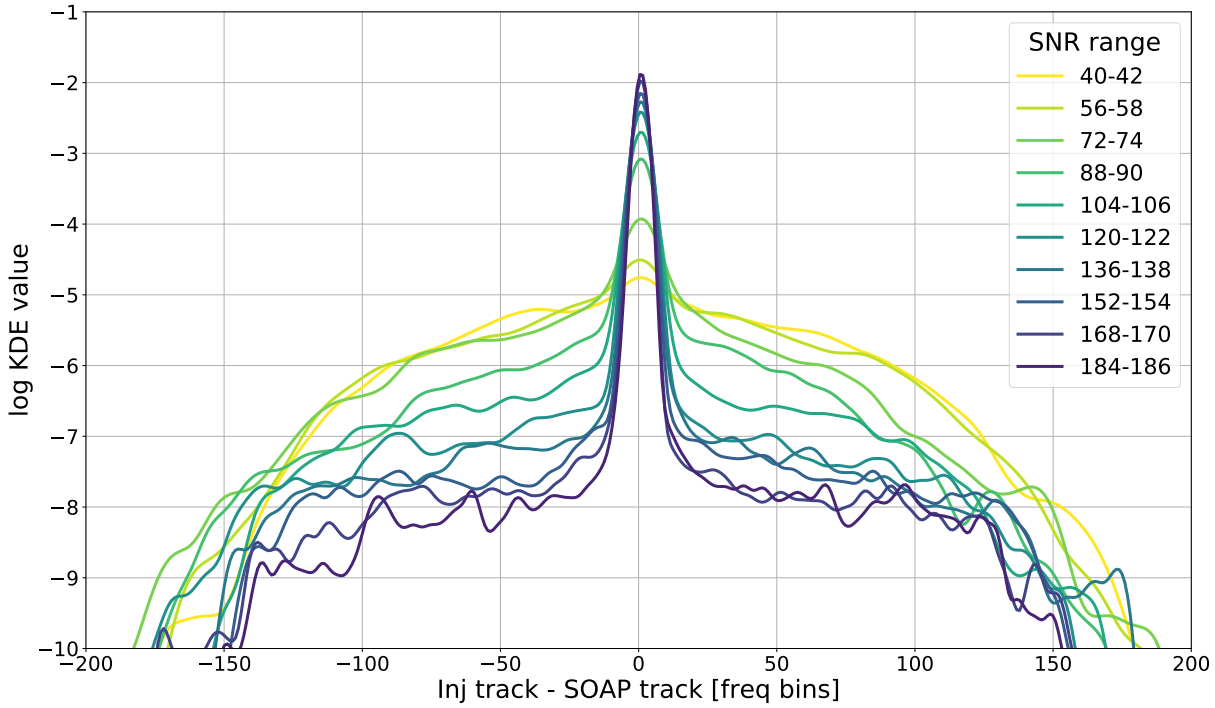

Figure 5.1: The likelihood can be modelled by using an KDE or a histogram. Here we show the KDE of the deviation of the recovered Viterbi track from the simulated (injected) CW frequency track for a number of SNR ranges. The deviation of the track is measured in discrete frequency bins. Each KDE is generated from ~ 300 simulations which each have ~ 400 elements in their frequency tracks. This shows a subset of the binned likelihoods between the range of SNR 40 and 200.

as described above, therefore any value of ρ which lies in the range $\rho_c \pm \rho_w/2$ uses the likelihood histogram $\mathcal{L}_{\rho_c}$, where ρ_c is the bin center. The histograms $\mathcal{L}_{\rho_c}$ are then used to define the likelihood function $p(\boldsymbol{V} \mid \boldsymbol{\theta}, \rho, I)$ in Eq. 5.7, where we now have five parameters in our model $\alpha, \delta, f, \dot{f}$ and ρ. As we assume independent track elements for a given Viterbi track, the likelihood is then the product of the likelihoods at each track element

$$p(\boldsymbol{V} \mid \boldsymbol{\theta}, \rho, I) = \prod_{i=1}^{N} \mathcal{L}_{\rho_c(\rho)}(M_i(\boldsymbol{\theta}) - V_i), \tag{5.8}$$

where N is the length of the Viterbi track $\boldsymbol{V}$.

5.2.2 Prior

For this analysis we choose to use a simple prior which is flat in parameter space in some range. We use a flat prior for α between $[0, 2\pi]$, a flat prior in $\sin\delta$ between [-1,1], a flat prior in f in the range of the 0.1 Hz wide sub-band which SOAP searches through, a flat prior in the frequency derivative in the range $[-10^{-9}, 10^{-9}]$ Hz/s and a flat prior for the SNR ρ in the range $[40, 200]$.

5.3 Results

The method described in Sec. 5.2 takes in a Viterbi track and uses this to estimate the five dimensional posterior distribution $p\left(\left\{\alpha, \delta, f, \dot{f}, \rho\right\} \mid \boldsymbol{V}, I\right)$. To calculate this posterior we use a technique known as nested sampling, specifically the package *Dynesty* [**speagle2019DynestyDynamic**], which is introduced in Sec. 2.2.2.

As an example of what the Bayesian analysis returns, we can first simulate a CW signal with parameters

$$\begin{aligned} \alpha &= 4.2 \text{ rad} \\ \delta &= -0.06 \text{ rad} \\ f &= 148.23 \text{ Hz} \\ \dot{f} &= -3.55 \times 10^{-15} \text{ Hz/s} \\ \rho &= 151, \end{aligned} \tag{5.9}$$

and generate the associated spectrograms for the LIGO detectors H1 and L1 shown in Fig. 5.2. The SOAP search from Chapter 3 is then run using the line-aware statistic with the same parameters as given in Tab. 3.1, where the multi detector search returns a single frequency track. The output Viterbi track is then plotted with the CW frequency track in Fig. 5.2. In this case the Viterbi track can be seen to closely follow the simulated CW frequency track.

The Bayesian analysis described in Sec. 5.2 is then run using this Viterbi track as input, where this returns the posterior distribution shown in Fig. 5.3. In this example, the injected parameter values (marked in orange) are contained within the marginal posterior distributions for all of the parameters excluding the SNR. The distribution in SNR appears to have hard edges at the edge of the binned likelihood function, which begins to demonstrate some problems with the definition of the likelihood, this will described more in Sec. 5.3.1.

The marginal posterior distribution of the sky parameters is easier to interpret when it is projected onto a sky map, therefore, in Fig. 5.4 the parameters α and δ are shown on a sky projection in the ecliptic frame. The sky position parameters α, δ of the CW signal are in the equatorial coordinate system, therefore these have been transformed into the ecliptic frame β, γ. The Viterbi tracks and CW frequency tracks used in this analysis are sampled once a day, therefore, we should only see the Doppler modulation from the orbit of the earth around the sun. In the ecliptic frame, i.e. where the z axis is perpendicular to the orbital plane of the earth, for any ecliptic longitude, there are two sky positions at opposite ecliptic latitudes which will return the same frequency track. This then means that we would expect the marginal posterior distribution to have two modes on the sky at these two locations, where this is seen in 5.4.

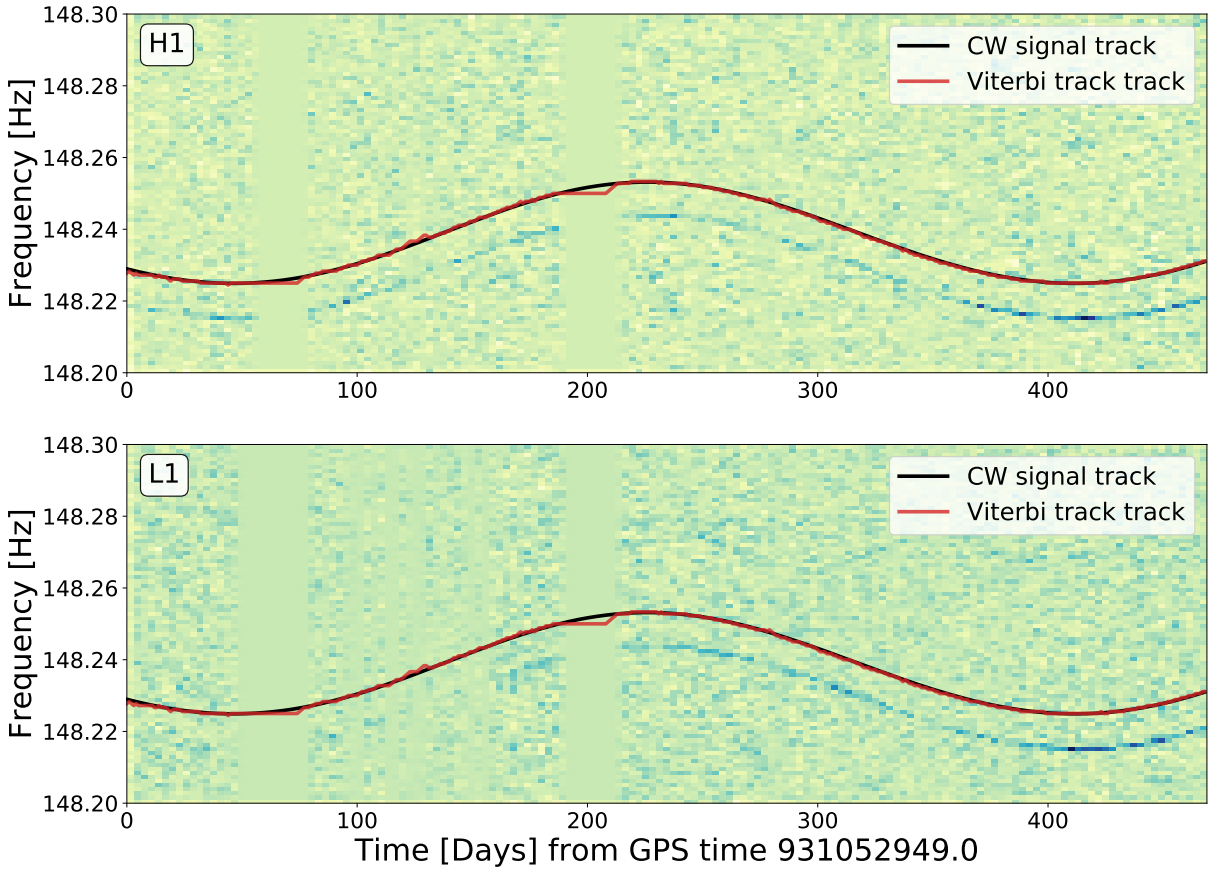

Figure 5.2: Example simulated CW simulation in LIGO detectors H1 and L1 using parameters in Eq. 5.9. The simulated frequency track of the signal is shown as the black line. The multi detector analysis returns a single frequency track (Viterbi track) which is the red line shown overlaid in both detectors. Both the Viterbi track and the simulated frequency track are shifted up in frequency bu 0.01 Hz to make the signal visible in the spectrogram. The track is sampled once per day, where the oscillation visible here is due to the Doppler modulation of the Earth's orbit.

5.3.1 Simulations

To test the Bayesian method described in Sec. 5.2, we generate a set of spectrograms which contain simulations of CW signals in Gaussian noise as in Sec. 3.10 and Sec. 4.9. This is the same simulated test set from Sec. 4.9, where CW signals were injected into 50% of the 0.1 Hz wide sub-bands between between 40 and 500 Hz, with the parameters as described in Tab. 4.1. The SOAP search using the line aware statistic with parameters in Tab. 3.1 is run on each sub-band, where the Viterbi track and CW signal parameters $\alpha, \delta, f, \dot{f}$ and ρ associated with each simulation are recorded. The Viterbi track can then be used to run the Bayesian analysis described in Sec. 5.2. In these simulations, we have 2300 simulated signals which have an SNR range between 40 and 200, where for this test we randomly select 200 of these simulations.

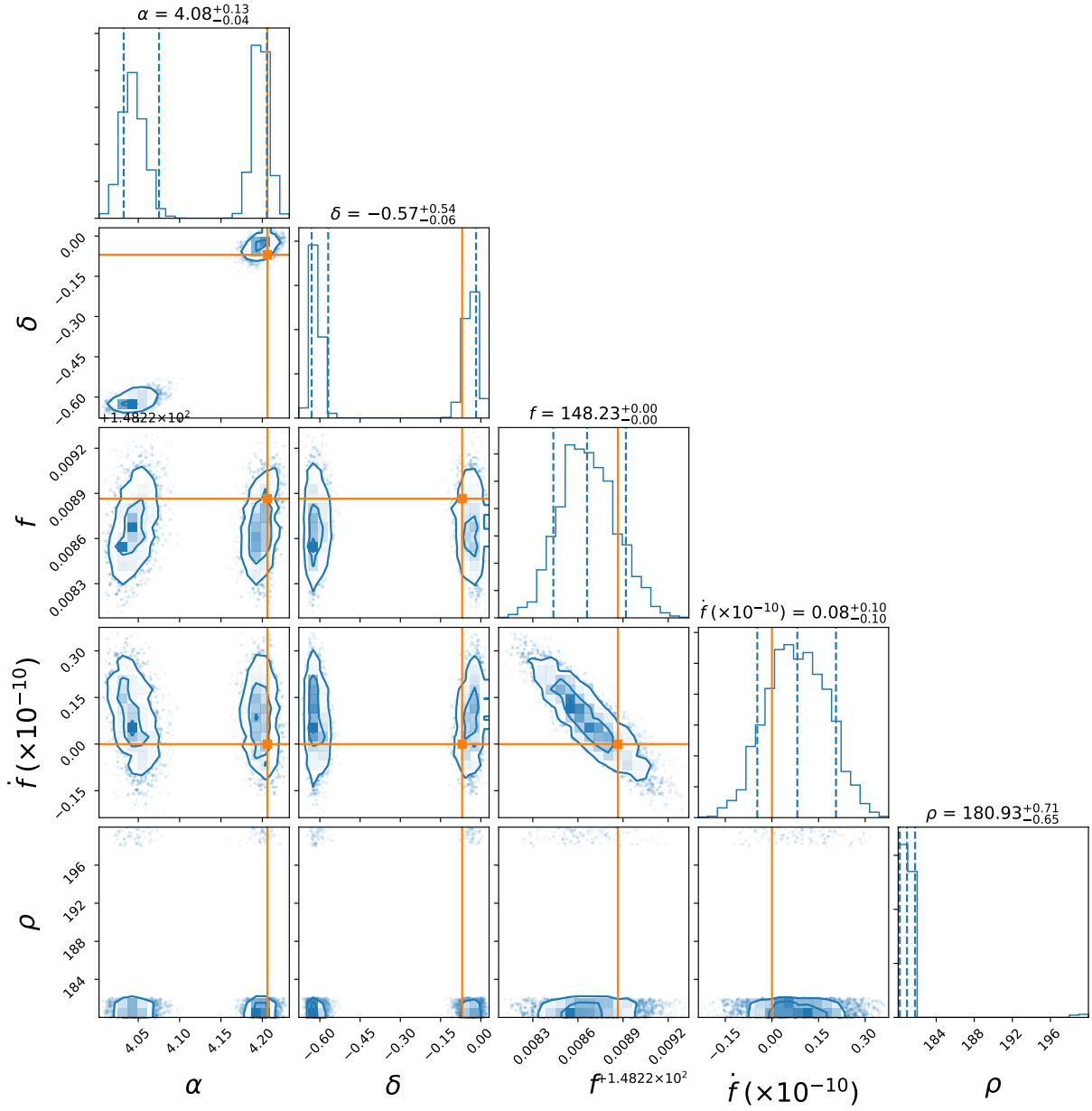

Figure 5.3: This figure shows an example of the posterior distribution of a signal with SNR 151. Each panel shows the marginal distributions for each parameter, where the parameters used for the simulation are marked in orange. In this example each of the posteriors match well with the injected parameters. The contours on each of the marginal distributions are at confidence levels of 10, 50 and 90 %.

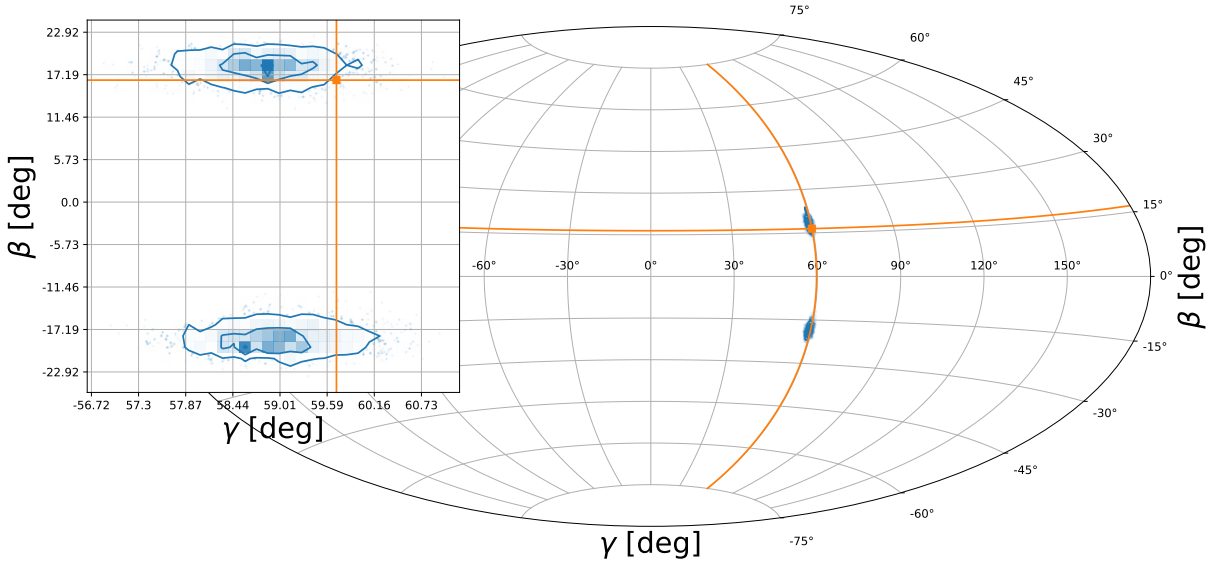

Figure 5.4: This figure shows an example of the marginal posterior distribution of the sky position in the ecliptic frame γ, β of a signal with SNR 151. The overlaid panel is a zoomed area around the posterior distribution, where the orange marker shows the injected parameters. The contours in are defined at 10, 50 and 90 % confidence.

p–p plot

The p–p plot is a mechanism to validate the effectiveness of the Bayesian model and computation using many simulations. From Sec. 5.3 we have the output posterior distribution $p(\boldsymbol{\theta} \mid \boldsymbol{V}, I)$, or more correctly we have N samples from this distribution $\boldsymbol{\theta}_i$, and we have the injected parameters $\boldsymbol{\theta}_{\text{inj}}$. For each simulation, we can calculate the posterior quantile $q(\theta_{\text{inj}})$ from the marginal posterior distribution

$$q(\theta_{\text{inj}}) = P(\theta_{\text{inj}} > \theta) = \frac{1}{N} \sum_{i=1}^{N} H(\theta_{\text{inj}} - \theta_i), \tag{5.10}$$

where $H(x)$ is the Heaviside step function. This calculates the fraction of the marginal posterior distribution which has a parameter θ less than the injected parameter θ_{inj} [**cook2006ValidationSoftware**]. If the Bayesian model and computation of the posterior is valid, then as the number of samples approaches infinity ($N \to \infty$), the posterior quantile $q(\theta_{\text{inj}})$ should follow a uniform distribution $[0, 1]$ [**cook2006ValidationSoftware**]. This then provides a method to check the validity of our analysis.

For each of our simulations we can calculate $q(\theta_{\text{inj}})$, such that we have values $\boldsymbol{q}_\theta$, where the fraction of simulations which fall within a given confidence interval (CI) C is the cumulative distribution of $\boldsymbol{q}_\theta$, i.e. $P(\boldsymbol{q}_\theta > C)$, where C ranges between $[0, 1]$. If $q(\theta_{\text{inj}})$ and therefore $\boldsymbol{q}_\theta$ follows a uniform distribution, then $P(\boldsymbol{q}_\theta > C) = C$ [**cook2006ValidationSoftware**]. Plotting $P(\boldsymbol{q}_\theta > C)$ against C for each parameter θ, then shows the fraction of simulations which have a $q(\theta_{\text{inj}})$ within some CI C, this is known as a p–p plot.

If the Bayesian posteriors can be trusted, then this plot should follow a straight diagonal line, indicated by the black line in Fig. 5.5. If the the majority of the marginal posterior distributions are shifted to right of the injected parameters, i.e. the true value lies in the lower tail of the posterior for the majority of the simulations, then the p–p plot will show a curve above the diagonal, this is shown in the top left panel of Fig. 5.5. Similarly, if the majority of the marginal posterior distributions are shifted to left of the injected parameters, i.e. the true value lies in the upper tail of the posterior for the majority of the simulations, then the p–p plot will show a curve below the diagonal, this is shown in the top right panel of Fig. 5.5. If the posterior is under-constrained, i.e. the injected parameters are scattered with a narrower distribution than the posterior suggests, then the curve will follow an S shape where the S is below the diagonal when $C < 0.5$ and above the diagonal when $C > 0.5$. This is shown in the third panel of Fig. 5.5. Similarly, if the posterior is over-constrained, i.e. the injected parameters are scattered with a larger width than the posterior suggests, then the curve will follow an S shape where the S is above the diagonal when $C < 0.5$ and below the diagonal when $C > 0.5$.

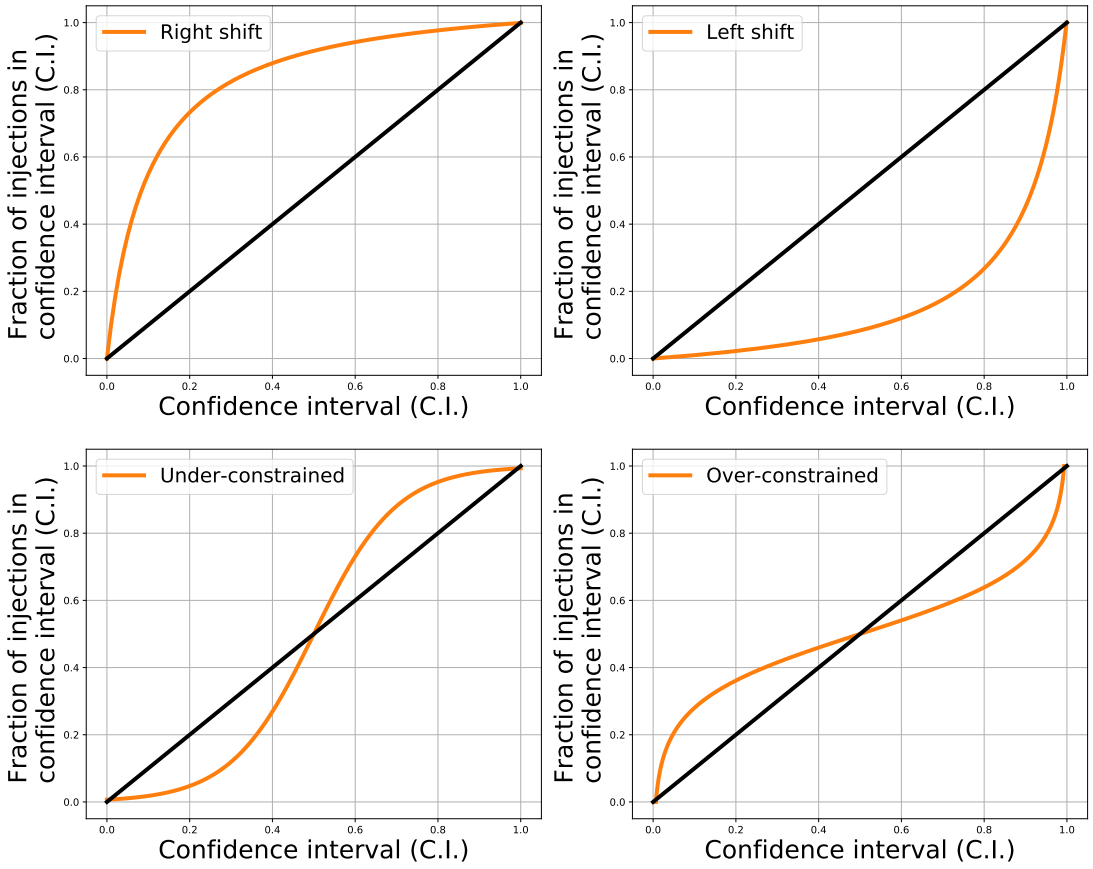

Figure 5.5: This figure shows examples of p-p plots for posterior distributions which are shifted to the right (larger values of the parameter), to the left (smaller values of the parameter) and over and under constrained posteriors. The black curve shows the p-p plot when the posterior distribution is perfectly recovered, i.e. the confidence intervals follow a uniform distribution.

We can then generate the p–p plot for the 200 simulations in the test described in Sec. 5.3.1, this shown in Fig. 5.6. Using the information from Fig. 5.5, we can see that for the parameters f and $\dot{f}$ we recover an over-constrained posterior distribution. For the SNR parameter ρ, the recovered posterior is both shifted to the right and is over constrained, i.e. we assume higher SNRs than perfectly recovered distribution. For both the right ascension parameter α and the declination parameter δ, we can see that we recover an over-constrained posterior distribution at 95% confidence.

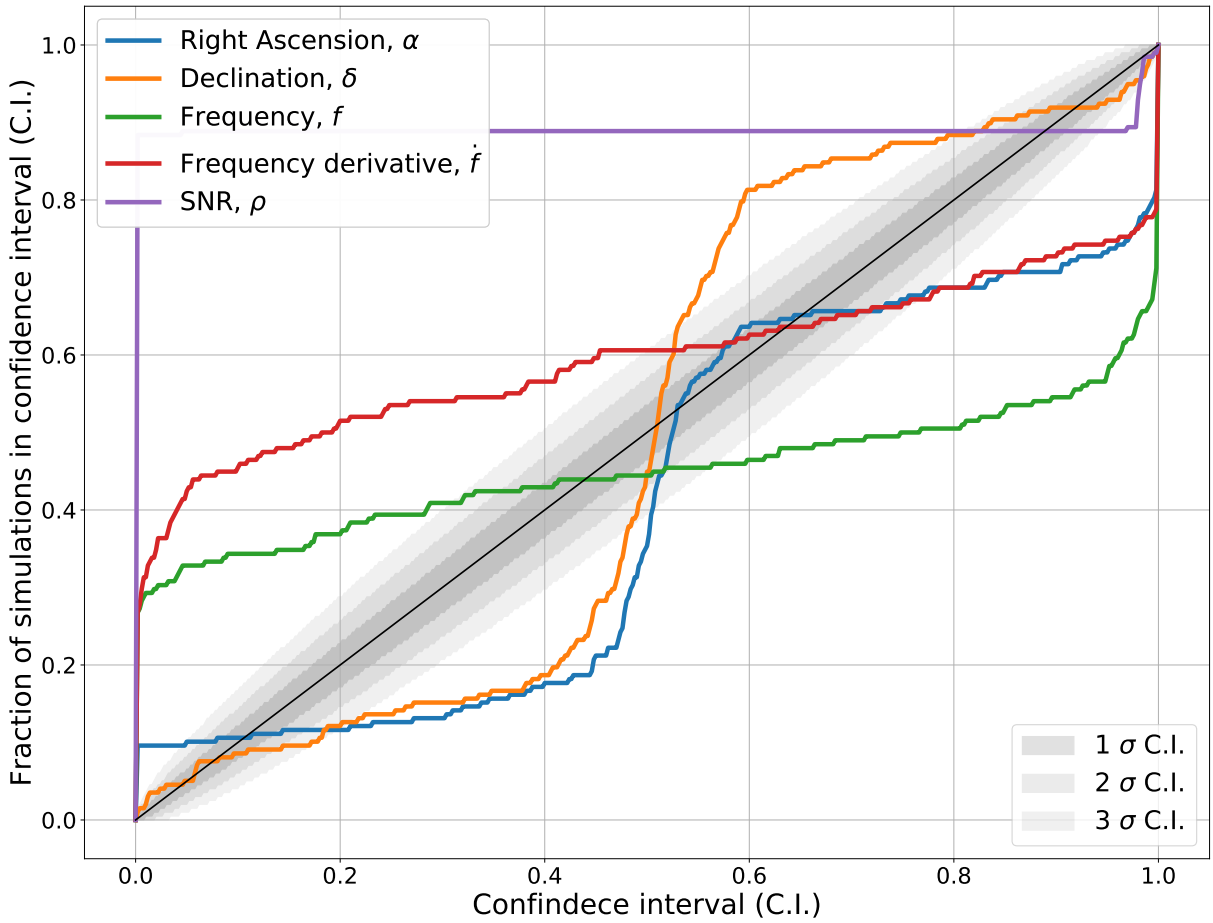

Figure 5.6: The p–p plot is shown for the 200 signals described in Sec. 5.3, which range between 40 and 200 in SNR. This describes how well the marginal posterior distributions for each parameter match the simulated parameter. The SNR, frequency and frequency derivative are over-constrained distributions and the sky position parameters α, δ are under-constrained.

Each of the curves in Fig. 5.6 indicate that the current analysis does not correctly reproduce the true posterior distribution. One likely reason for this could be due to an incorrect definition of the likelihood in Sec. 5.2.1, for example, to simplify the problem we assume that all track components are independent, this is not necessarily true and could contribute to the over constrained posterior distributions.

Sky area at given confidence interval

If we assume that the posterior contours are trustworthy, i.e. we do not under constrain or shift our posterior, then we can estimate the area of the sky which this method can localise the source to. To do this we can use our estimation of the marginal posterior distribution on the sky, and draw a contour on the posterior which contains 95% of the probability. The area contained within this contour is then the sky area which the source can be localised to at a 95% confidence, this can be seen as the green contour in Fig. 5.7. Similarly, a contour can be drawn at the values of the injected sky position parameters, this is shown as the red contour in Fig. 5.7. This contour defines the confidence at which the injected parameter in contained.

If the contour at the injected parameter is much larger than the contour at 95% confidence, then this implies that the posterior distribution is over-constrained. These two areas are another measure of the validity and ability of this method to extract the sky parameters.

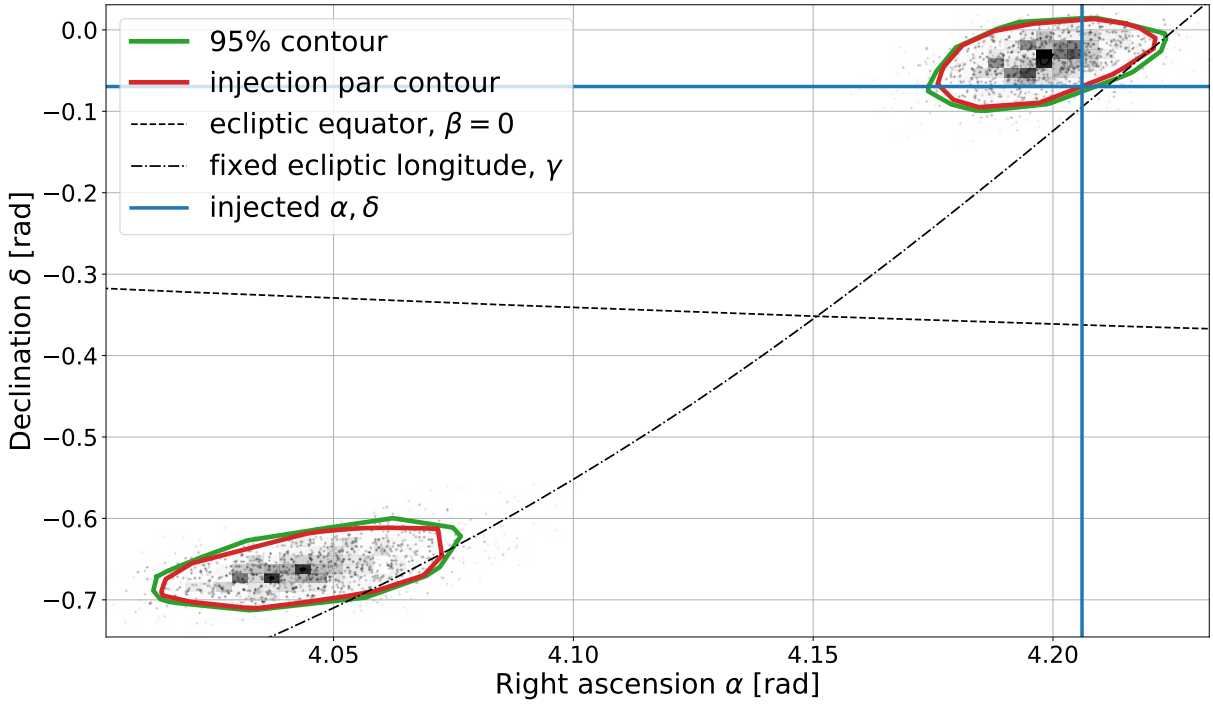

Figure 5.7: For the injection in Sec. 5.3, we plot the the contour in sky position posterior which contains 95% of the probability and the contour at which injected sky position parameter values fall. In this example the two contours are similar. The black lines refer to the ecliptic coordinates, showing that the posterior is symmetric around the ecliptic equator.

The contours and therefore their associated sky areas can be calculated for all of the simulations described in Sec. 5.3. The first panel of Fig. 5.8 shows the histograms of the areas contained within the contours at 95% confidence. The second panel shows the areas

contained within the contours which are drawn at the value of the injected parameters. From the distributions in Fig. 5.8 we can see that the sky areas which contain the injected

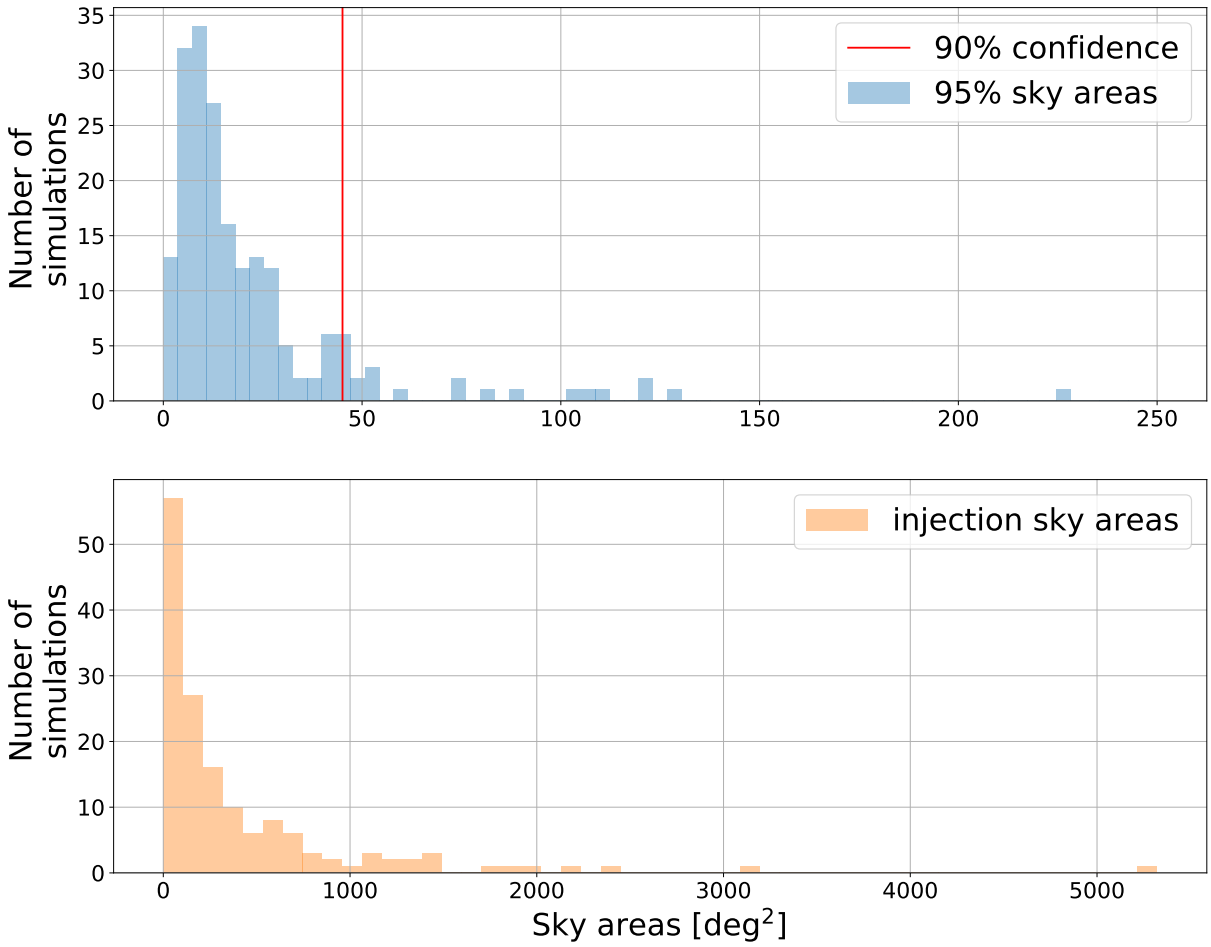

Figure 5.8: The top panel shows a histogram of the sky area which this method can localise a source to with 95% confidence. This is the area of a contour which contains 95% of the posterior distribution. The second panel shows the sky areas associated with a contour which is draw on the posterior through the injected parameter value. From the first panel, we can say that 90% of the time we can localise to a sky area less than 45 deg^2 with 95% confidence, this is shown as the red 90% confidence line in both panels. The true parameter however, is contained within the 95% contour only 42% of the time.

parameters are larger by a factor of $\sim$ 20 than those at 95% confidence. We can also determine from this that the injected parameters fall within the 95% confidence contour only 42% of the time. This implies that these posterior distributions are over-constrained, and that the sky areas at 95% confidence are overly optimistic.

However, if we assume that the 95% confidence sky areas are trustworthy, we can approximate the sky area which this method can localise to. From the first panel in Fig. 5.8, we can say that 90% of the time we can localise to a sky area less than 45 deg^2 with 95% confidence. In this case the sky area only contains the true parameter 42% of the time. However, if we did trust the value of 45 deg^2, given the full sky has $\sim$ 41253

square degrees, this is factor of $\sim 10^{-3}$ of the whole sky. For a fully coherent search for CWs, this reduction in sky area would drastically reduce the computational cost of the of the search.

5.4 Discussion

In this chapter we describe a Bayesian analysis to extract the Doppler parameters $\alpha, \delta, f\dot{f}$ and SNR ρ of a potential CW source from the Viterbi track which is described in the SOAP search in Chapter 3. The aim of this method is to provide estimates of the CW parameters, and then use these to reduce the size of the parameter space for a more sensitive fully coherent search.

In Sec. 5.2 we outline the setup of a Bayesian model, where the input is a Viterbi track which is described in Chapter 3, and the output is a posterior distribution of the Doppler parameters of a CW signal. In this model, the likelihood is empirically calculated by simulating $\mathcal{O}(10^4)$ CW signals and then recording the difference between the Viterbi track and CW frequency track for multiple SNR bands. The histogram of these values is then used to construct the likelihood of this method. For each of the parameters in the search, we assume a flat prior. In Sec. 5.3, the analysis is tested on 200 simulations which had parameters drawn from the same prior as the Bayesian model. In this section we generate p–p plots to asses the validity of this model and find that the SNR, frequency and frequency derivative all are over constrained distributions and the sky position parameters are a mixture of over and under-constrained depending on the confidence.

We investigated the area contained within contours on the marginal posterior for the sky position to gauge the ability of the search to localise a source, where we found that with a 95% confidence we can detect to a sky area within 45 deg^2 90% of the time. However, the true value of the parameter fell within this confidence contour only 42% of the time, implying that the posterior distributions are over-constrained. To contain the true value 95% of the time, this sky area would have to be expanded by a factor of ~ 30. Other methods could be used to reduce this sky area such as using the antenna response of the detector, this would locate the source to one hemisphere removing one mode from the bi modal sky distribution.

These results imply that in its current state, the search does not provide a valid way to estimate the parameters of the source from its Viterbi track. However, this is a toy case and with the development of a more appropriate likelihood function and further investigation, we aim to develop this such that it can correctly estimate CW parameters.

Chapter 6

Detector Characterisation with SOAP

When searching for GW signals, it is important to understand the origins of noise artefacts in the detector data which do not originate from an astrophysical source. A large fraction of GW search algorithms, including the basic SOAP search described in Chapter 3, assume that the detectors noise follows a Gaussian distribution (although Sec. 3.8 does account for non Gaussianities). However, the detectors contain artefacts which do not follow this distribution. These artefacts can negatively affect many searches for GWs as they can be easily mistaken for a real GW signal. Some of the potential sources of these artefacts have been mentioned in Sec. 1.3.1. There are many different classes of artefact, including: glitches [**aasi2015CharacterizationLIGO**, **abbott2016CharacterizationTransienta**], which are short duration broad band bursts in power, and instrumental lines [**covas2018IdentificationM** which are long duration narrow-band signals. To conduct a reliable search there are two main tasks which are necessary for detector characterisation. The first is identifying the artefact such that contaminated frequency bands and time segments can be passed on to a search. These segments can then be addressed, this could mean removing that section of data or using more sophisticated techniques to deal with the artefact [**pankow2018MitigationInstrumental**]. The second task is to find the instrumental or environmental source of the artefact. If the source of the artefact is found, it can potentially be removed or limited for future data runs.

The focus of this Chapter is on how to search for and identify instrumental lines, and how this can improve the sensitivity of CW searches. Sec. 6.1 will introduce different sub-classes of instrumental line and how each of them affects a CW search. Sec. 6.2 will outline how these artefacts are detected and monitored, and describe current tools used for this task. Sec. 6.3 will describe how the CW search algorithm introduced in Chapter 3 can be used to search for instrumental lines. Finally Sec. 6.4 will describe the user interface for investigating SOAP's output.

6.1 Instrumental lines

Instrumental lines can be generally described as persistent noise artefacts. There are many classes of instrumental line spanning a range from narrow, fixed frequency spectral artefacts to broader (< 0.1 Hz) features which have a time varying frequency known as wandering lines. For many of these lines, it is difficult to distinguish them from an astrophysical signal, making it difficult for astrophysical searches. They affect CW search methods in three main ways. They can cause the search to produce outliers which are then considered as GW candidates. Extra efforts then have to be made to analyse these outliers further. If the line is close to or overlapping with the GW frequency, then it can conceal the power of the GW. Lines can also affect searches for CWs by giving an incorrect estimate of the noise floor of the detector. In searches for the stochastic gravitational wave background (SGWB), channel data from multiple detectors is cross-correlated to identify a potential signal [**allen1999DetectingStochastic**]. If there is a noise source such as an instrumental line which is coherent between the detectors, this will show up as an excess in the cross-correlation statistic[**covas2018IdentificationMitigation**]. Any noise source which is local to both the detectors could then be visible in this cross-correlation. It is therefore crucial to understand the structure and origin of these lines when performing a search for GWs, specifically for CWs and stochastic searches.

Some instrumental lines are clearly visible when looking at an amplitude spectral density (ASD) or PSD of the LIGO detectors. Figure 6.1 shows the ASD for LIGOs Hanford and Livingston detectors during their first observing run (O1) [**GWOpen**]. This clearly shows peaks which are associated with strong lines, where some of these have been labelled. There are however, many more weaker lines which become visible when spectra are averaged over longer times. The ASD in Fig. 6.1 shows the time averaged spectra of the GW channel of the LIGO detectors. The lines seen in the spectrum are not from any GW and are usually from terrestrial sources. To see the lines in the GW channel, they must be transferred via some mechanism to this channel, known as coupling in. There are a number of ways in which this happens which are outlined in [**covas2018IdentificationMitigation**]. This includes coupling via shared power sources and shared grounds in the electrical circuits. When different components share the same power supplies, if a component draws power with a given period, then the voltage will decrease repeatedly at this frequency. Another component which shares this same power supply can then also see this drop in voltage and this can potentially become visible in a recorded output. Another mechanism is coupling through magnetic fields, this is common when cables are close to each other, the magnetic field in one can affect the other, therefore, coupling noise between different systems. Coupling can also occur though a physical connection, known as mechanical coupling, for example the resonances of the suspension fibers which couple directly into the mirrors and therefore the output error signal.

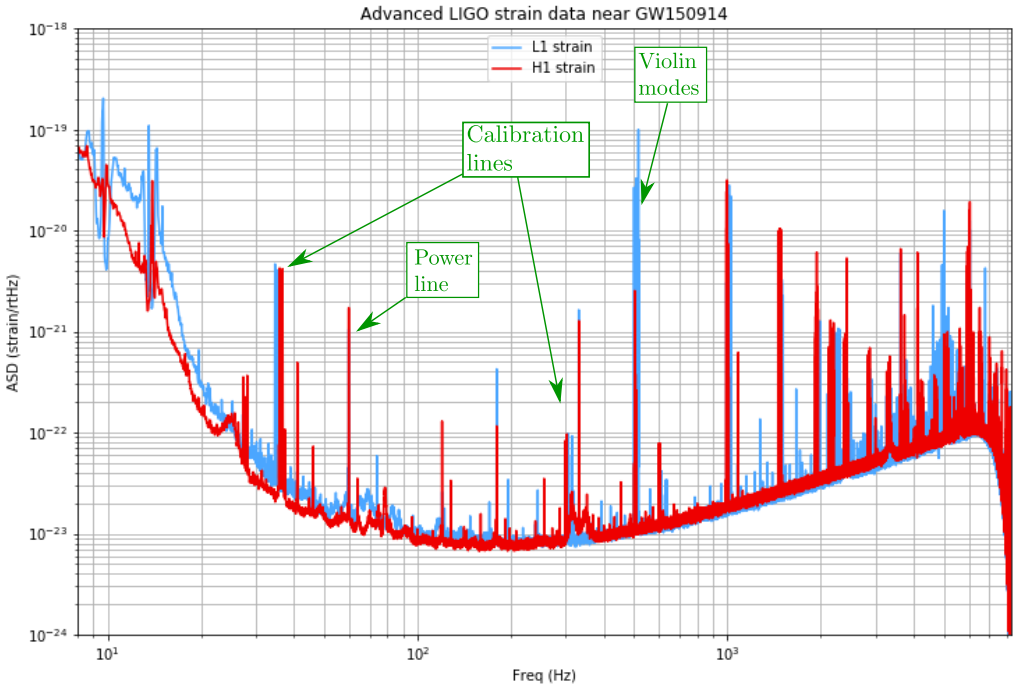

Figure 6.1: The LIGO detectors averaged ASD is shown around the GW150914 event in O1 [**abbott2016ObservationGravitational**]. This figure is from [**GWOpen**] where the Power lines, Calibration lines and Violin modes are annotated. The power line from the mains in the USA is at 60 Hz. Some of the calibration lines are around 30 Hz, 331 Hz and 1083 Hz. The various violin modes of the suspensions are at 300, 500, 600 and 900 Hz where I have only marked the 500 Hz mirror suspension modes [**GWOpen**].

Many of the spectral lines seen in the frequency spectrum in Fig. 6.1 are fundamental to the design of the detector. These are difficult to eliminate at their source, therefore need to be understood such that their effect on searches is minimised. Some of the strongest of these lines are listed below:

Power line The power line harmonics are fundamental to the detector and originate from the mains power supply in the United States of America (USA). These lines exist at 60 Hz which is the frequency of the mains alternating current [**aasi2015CharacterizationLI** The European detectors Virgo and GEO have a power line at 50 Hz instead of 60 Hz.

Violin modes The violin modes are associated with the suspensions fibers of the mirrors and the beam splitter in the detector. These are designed to have a narrow frequency spectrum such that they contaminate as small a part of the spectrum as possible. These are the lines around 500 Hz for the mirrors and 300, 600 and 900 Hz for the beam-splitter [**GWOpen**] in Fig. 6.1.

Calibration lines As described in Sec. 1.3 a GW passing the detector will cause a change in the arm lengths of the interferometer, causing a power fluctuation at the output of the detector. For stable operation of the interferometer, the power fluctuations are suppressed by using a feedback loop to control the detectors differential arm length. The error signal of this loop is then $h(t)$ [**ligoscientificcollaboration2017CalibrationAdva** However, this is not entirely true as the transfer function of this feedback loop will affect the measurement of $h(t)$. It is therefore important to understand and correct for this feedback loop. The primary method for calibrating this is known as a photon calibrator [**karki2016AdvancedLIGO**]. This applies a power modulated laser to the test mass, where the periodic force from radiation pressure appears as a calibration line in the detectors spectrum. This is then applied at a range of frequencies from a few Hz to several kHz [**karki2016AdvancedLIGO**]. This can then be used along with other methods to calibrate the feedback loop [**ligoscientificcollaboration2017CalibrationAdvanced**, **coughlin2010NoiseLine**, **tuyenbayev2016ImprovingLIGO**].

Together with the fundamental lines of the detector, which are difficult to remove at the source, there are a large number of other lines whose source has been found and can be removed. Many of these are from mechanisms described earlier such as shared power supplies or grounds. These can be removed by, for example, using a different power supply for different systems. See [**covas2018IdentificationMitigation**] for a full investigation into the mitigation of these lines.

Instrumental lines have a large effect on all searches for CWs, the lines can cause outliers in a search or can hide the CWs power if the frequencies overlap or are close

to the astrophysical frequency. Searches for long duration CWs are particularly sensitive to this type of artefact. As described in Sec. 2, CWs are long duration signals with a slowly varying frequency. In the case of an isolated neutron star, the signal which is searched for is a narrow-band sinusoid with a slowly varying frequency, where the frequency can be Doppler modulated by the earth's rotation and orbit, and the amplitude is modulated by the antenna pattern of the detector as the earth rotates. For certain areas of parameter space, such as a sky position close to the poles of the earth's orbit, the astrophysical signal of an isolated neutron star can appear very similar to a narrow band fixed frequency instrumental line. The affect of many of these lines can be mitigated by using multiple detectors data. If a signal appears in one detector and not the others, then it is likely that the signal is from an instrumental line and not an astrophysical source. These contaminated frequency bands can either be removed or a statistic similar to that described in Sec. 3.8 or [**keitel2014SearchContinuous**] can be used to limit their effect. However, there are many examples of instrumental lines which appear at the same or similar frequencies in multiple detectors. These pose a real challenge to some CW searches, and require a substantial investigation to limit their affect.

6.2 Identifying and monitoring instrumental lines

When a detector is running, it is very important to identify instrumental lines and monitor them. The source of the line can potentially be located and its cause mitigated, or the line can be flagged such that astrophysical searches can avoid outliers near that frequency. The astrophysical searches use data from the GW channel, therefore, the aim is to limit the affect of instrumental lines in this channel.

In addition to the GW channel, the detector records many others known as auxiliary channels. These channels monitor many components of the detector, and importantly are not sensitive to GWs. Many of the channels useful for line searches are the outputs of physical environment monitors (PEMs). PEMs include sensors such as seismometers, temperature sensors, magnetometers etc. These channels can be very useful in identifying the source of an instrumental line. The main goal is to reduce the number of artefacts in the GW such that it is as close to Gaussian noise as possible. If an artefact shows up in the GW channel in coincidence with one of the PEMs then this is an indicator that the artefact originates from something related to that PEM. For example, consider that a magnetometer identifies a periodically changing magnetic field in a rack of electronics (which contains oscillators, clocks etc). If a signal with the same frequency is observed in the main GW channel, this indicates that noise from this piece of electronics is somehow coupling into the detector. One can then investigate the electronics near that magnetometer further to identify how and if it couples in.

There are a number of tools which teams of scientists use to monitor these spectral lines. A summary of the results from these investigations for the first two observing runs of LIGO can be found in [**covas2018IdentificationMitigation**]. Some of the tools used to monitor these lines are described below.

Fscan FFTs are taken of the raw detector data, typically these are 1800s long, for all of the auxiliary channels as well as the GW channel. The power in each FFT frequency bin is then normalised to a running median and then averaged over the set of FFTs [**coughlin2010NoiseLine**]. After known lines such as Violin modes and power lines are subtracted, noise lines can be identified. A threshold can be set where spectrogram powers which exceed this threshold are flagged as a line. These can then be compared across multiple different channels. More detail on how the lines are identified can be found in [**coughlin2010NoiseLine**].

Coherence This tool searches for the coherence between different channels and different detectors. This is similar to searches for the stochastic gravitational wave background [**allen1999DetectingStochastic**]. This uses the cross correlation between two different channels, which can be different detectors GW channels or a GW channel and a PEM channel. Significant lines are then found by setting thresholds on the values of the coherence, where these can be flagged for further investigation. More detail of how this works can be found in [**covas2018IdentificationMitigation**, **coughlin2010NoiseLine**].

Finetooth If a line exhibits some periodic amplitude or frequency modulation, then it can appear as harmonics in the frequency spectrum, where the collection of regularly spaced harmonics make up a 'comb'. Many of the instrumental lines identified in the spectrum are then not from separate sources but are part of 'combs' which originate from a single source. These combs are characterised by their start frequency and the spacing of the harmonics (tooth spacing). Finetooth is a tool which identifies and monitors these combs [**neunzertGravitationalWaves**, **neunzertDailyComb**].

Noise frequency event miner (NoEMi) This tool uses various methods to identify peaks in an SFT, analyse these peaks, find coincidences between SFTs and track lines. The method initially runs a peak finding algorithm on each SFT, and for each peak stores the frequency, width, amplitude and critical ratio (CR), which is defined as the difference between the peak amplitude and the mean value of the spectrum divided by the spectrum's standard deviation. These peaks are then analysed by investigating the peaks found in $\mathcal{O}(10)$ SFTs. The distribution of the peaks in frequency can be used to identify stationary instrumental lines. Looking at the CR versus frequency, can help identify non-stationary lines. Coincidences can then be

found by comparing the peaks identified in the GW channel and some auxiliary channel. The time evolution of the line is then reconstructed such that it can be tracked. Each of the identified lines is then stored in a database. More details on this pipeline can be found in [**accadia2012NoEMiNoise**].

These tools offer different methods to identify and mitigate instrumental lines, and more generally understand the noise of the detector. A summary of these efforts for the advanced LIGO data can be found in [**covas2018IdentificationMitigation**], or specifically for O3 on the LIGO wiki page [**O3Lines**]. The following sections describe how the SOAP search described in Chapter 3 can be used as an extra tool to aid in the identification and monitoring of instrumental lines.

6.3 Identifying instrumental lines with SOAP

The SOAP search has been tested on a number of observing runs to search for CWs. One of the major factors that limits the sensitivity of the search, is the presence of instrumental lines within the data and many of the potential candidates which SOAP returned could be identified as an instrumental line. Figure 6.2 shows a broad and wandering line during the O2 observing run, where the line in H1 is causing the SOAP search to mistake the track for an astrophysical signal. This is because the SOAP line-aware statistic from Sec. 3.8 finds areas of higher power which are consistent between detectors. These types of line are difficult to mitigate in an astrophysical search as there is consistent high SFT power in both the broad line and the noise in the other detector. However, this has a side-effect of being useful to identify the instrumental lines themselves. In this section, I will explain the setup of the SOAP search to identify instrumental lines.

It is often useful to search through the auxiliary channels when trying to identify the source of a line. This would involve using the multiple detector search described in Sec. 3.5 to identify lines which are coincident between channels. The aim of this section however, is to flag potential lines within the GW channel in individual detectors. Whilst we have developed a statistic in Eq. 3.22 to penalise line-like signals, we revert to using the 'normalised' SFT power as the statistic in the SOAP search. The single detector search then has one parameter to vary, the transition matrix parameter τ. This governs how probable the frequency track is to transition up, straight or down a frequency bin. In this search we are aiming to find any line-like artefact. Therefore, we allow an equal probability for the track to jump in any direction, but limit it to change by one frequency bin after each time segment.

In the astrophysical search, the SFTs were summed over one day taking the average over the antenna pattern such that the SNR in each detector is similar and to increase the SNR in a given frequency bin. However, in the line search, there is no antenna pattern

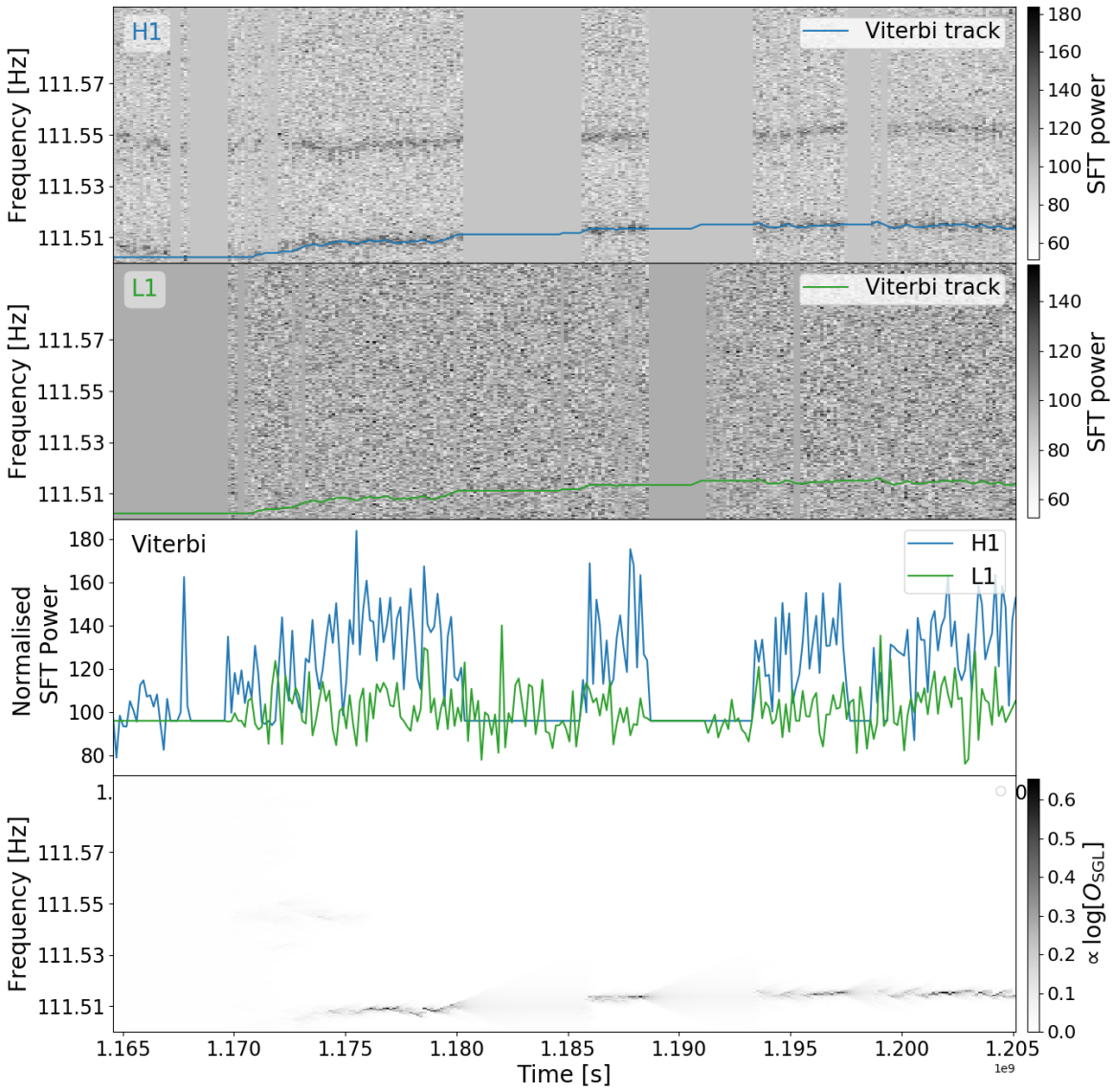

Figure 6.2: The spectrograms generated from 1800s long SFTs which are summed over one day are shown for H1 and L1 in the top two panels, where two broad wandering lines can be seen in H1. The Viterbi track returned by the SOAP astrophysical search described in Chapter 3 is overlaid on each of these spectrograms. The third panel shows the normalised spectrogram power along the Viterbi track for each of the detectors. The final panel shows the Viterbi map for this frequency band.

to average over and the majority of instrumental lines are expected to have a higher SNR than astrophysical signals. Therefore the search is run over normalised 1800s long SFTs, which also reduces the preprocessing time of the search. The 1800s SFTs are also generated as part of the Fscan search described in Sec. 6.2, therefore, this reduces the computational cost of generating SFTs as part of this search. For this line search, we split the 1800 s SFTs into 0.1 Hz wide sub-bands and run the single detector search on each sub-band. The search then returns the same outputs as described in Sec. 3 and Sec. 4: the frequency track (Viterbi track), a Viterbi map and a Viterbi statistic. Here the Viterbi statistic is just the maximum sum of the SFT power along a track through the spectrogram. This is defined in Sec. 3.4 as $\max_k(V_{N-1,k})$ where V is the un-normalised Viterbi map defined in Eq. 3.9.

These three outputs can then indicate whether an instrumental line is present within any given sub-band. Initially, one can look at the distribution of the Viterbi statistics for each sub-band, Fig. 6.3 shows a histogram of the Viterbi statistics from the H1 detector between 40-500 Hz for the O3 observing run. This shows that the distribution of Viterbi

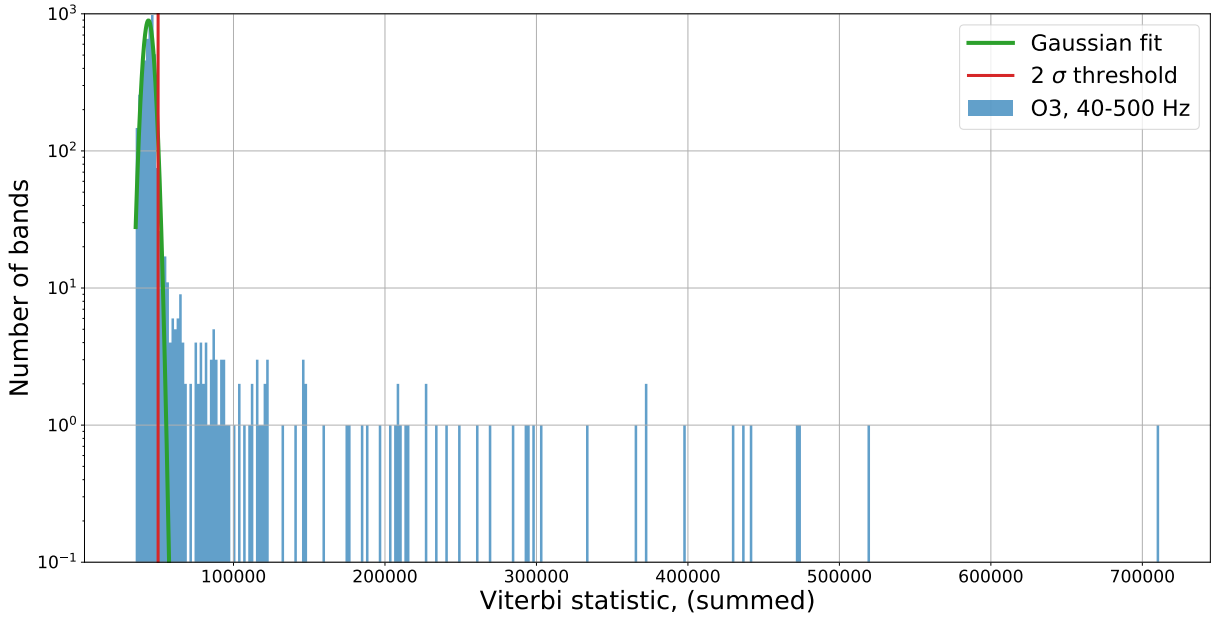

Figure 6.3: This shows a histogram of the Viterbi statistics from the SOAP search from Chapter 3, where the statistic is the summed SFT power along the Viterbi track. These results are between 40-500 Hz for the Hanford detector (H1) during the O3 observing run. The red line indicates the value of 2σ from the mean of a Gaussian fit, which is used as the detection threshold.

statistics has a long tail, where larger values of the Viterbi statistic in this tail are good indicators that there is an instrumental line present within the sub-band. We assume that the Viterbi statistics follow a Gaussian distribution if they are not contaminated with instrumental artefacts. We can therefore fit a Gaussian as in Fig. 6.3 and set the detection threshold as values of the statistic $> 2\sigma$ of the mean of this fit. Statistics which

cross this threshold can then be investigated further by looking into other outputs of the SOAP search, including the Viterbi map and the Viterbi track. Whilst the Gaussian fit will not be perfect due to the long tail in the distribution, each of the events that cross the threshold are investigated further, so this just serves as a method to reduce the number of sub-bands which need to be investigated.

The line search also outputs plots similar to those shown in Fig. 6.4, 6.5 and 6.6. There are three panels to each plot: the first shows the normalised SFT power searched through by SOAP with the Viterbi track overlaid, and the second panel shows the output Viterbi map. The final panel shows the SFT power along the Viterbi track and the mean noise floor of the detector as a function of time in the frequency band. The aim is to use the information contained within these plots and the equivalent ones for other sub-bands to classify each sub-band as containing an instrumental artefact or not.

There are certain features in each of the panels in, for example Fig. 6.4, which indicates whether SOAP has identified a potential line within a sub-band or not. The Viterbi track in Fig. 6.4 appears to be randomly wandering around the full width of the sub-band, implying that there is no strong signal within the band which SOAP can identify. The Viterbi statistic also falls within the main distribution of statistics in Fig. 6.3, whilst this does not cross the detection threshold, I describe it here to show the differences in the outputs compared to when there is a line. The second panel of Fig. 6.4 which shows the Viterbi map, contains no areas of high log probability and no clear long duration features. These features will become apparent in Fig. 6.5 and 6.6. The normalised SFT power along the Viterbi track shows values which are consistent with a χ^2 distribution with two degrees of freedom, which has a mean of two, implying that the SFT power along the track follows the expected noise distribution. Each of these indicate that there is no line present within this sub-band.

If we then look at the outputs of Fig. 6.5, we see a Viterbi track which is spread over a narrow frequency range ($\mathcal{O}(1)$ frequency bins) for the entire duration of the run. This indicates that there is an area of SFT power around this frequency which is higher than other areas in the sub-band. In the Viterbi map in the second panel of Fig. 6.5, the log-Viterbi probability is contained within a narrow frequency range around the Viterbi track. This again indicates that there is a narrow spectral line within this sub-band. Finally the third panel shows the SFT power along the Viterbi track, which no longer follows a χ^2 distribution but instead is variable with time and has a large excess of power. Each of these features are strong indicators that there is an instrumental line present within this sub-band.

Figure 6.6 shows the equivalent plots to Fig. 6.4 and 6.5 but now contains a wandering spectral artefact. This is a line which wanders in frequency as it moves though time. This can be seen in the frequency track, which here does not have much spread, however, the

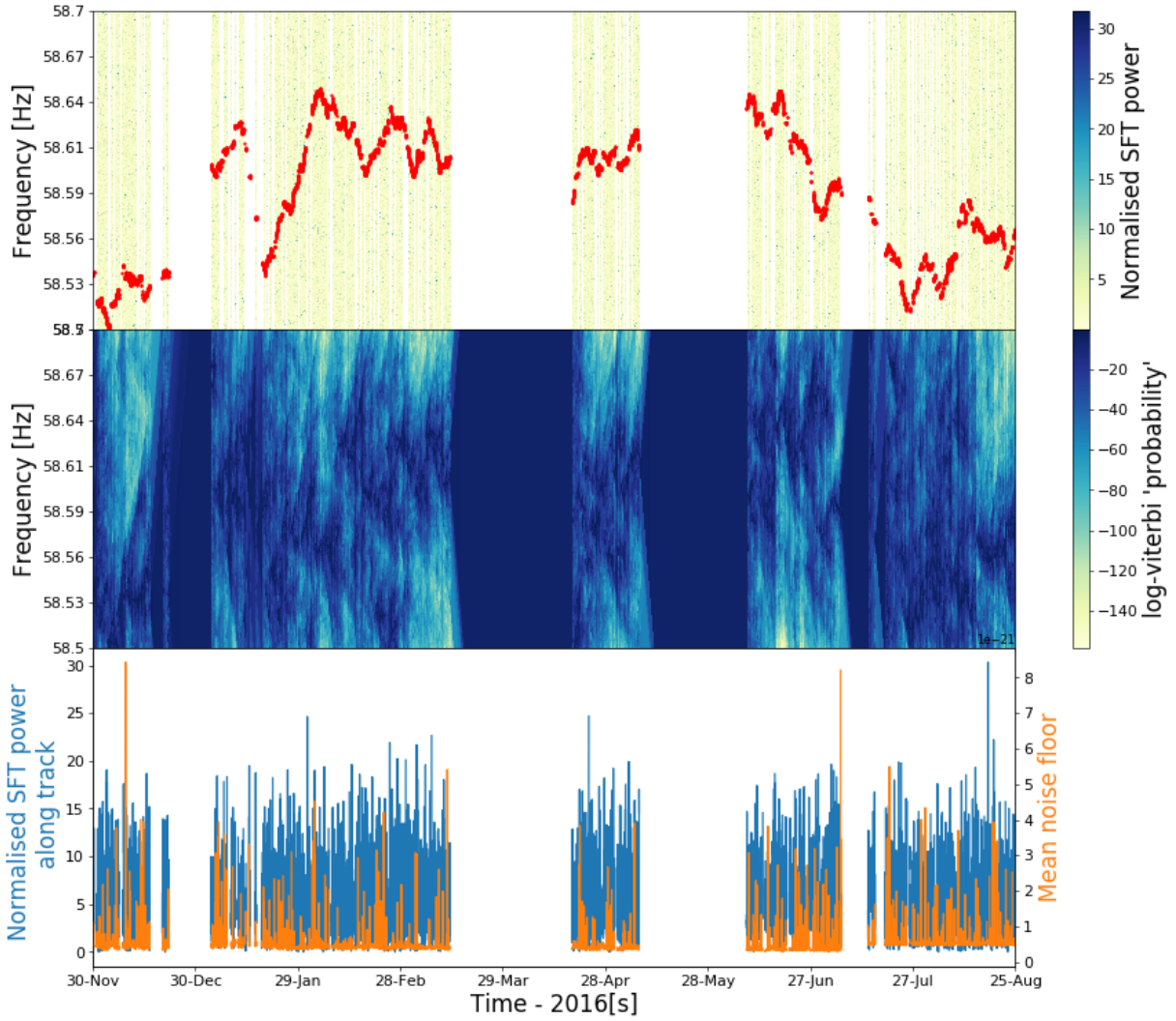

Figure 6.4: The SOAP search outputs three main quantities, the Viterbi maps, the Viterbi track and the Viterbi statistic. The Viterbi track is shown above overlaid onto the 1800s SFT power spectrum including the detector gaps for LIGOs Hanford detector (H1) in its third observing run (O3). This track is an indicator as to what the SOAP search has identified within the band, where this track indicates that SOAP has identified noise and no signal. The returned Viterbi statistic is also consistent with that of noise. The Viterbi map is another visualisation of the sub-band, how to interpret this has been explained in chapters 3 and 4. The final panel is a way to visualise how the SFT power changes along the Viterbi track. Also on this plot is an estimate of the mean noise floor for this band to visualise how the sensitivity of the detector changed over the course of the run.

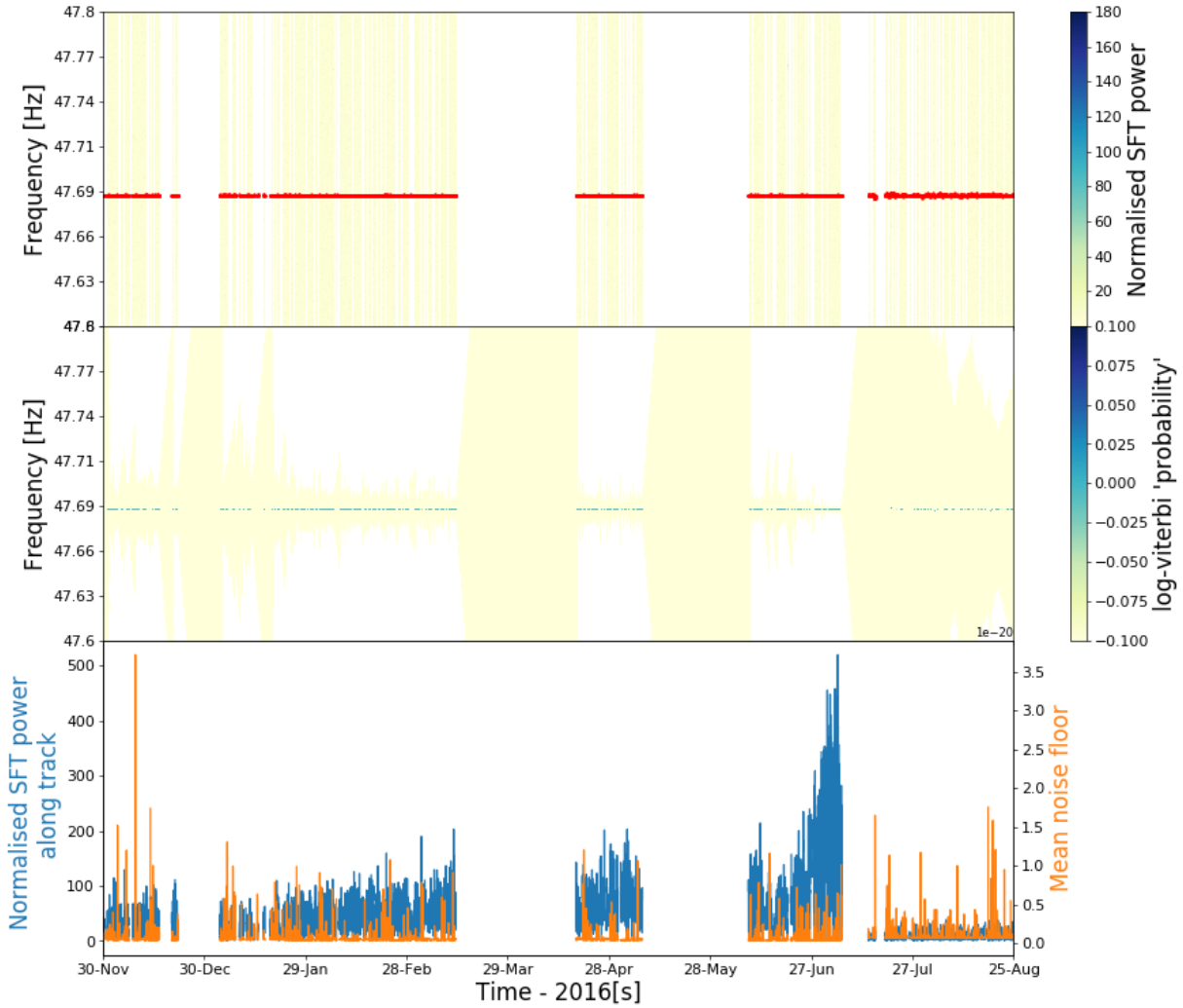

Figure 6.5: The equivalent plot as in Fig. 6.4 can be made when there is a narrow spectral artefact in the band. The above again shows results from the LIGOs Hanford detector (H1) in its third observing run (O3) using an 1800s SFT power spectrum. In this there is a narrow spectral line at ~ 47.69 Hz, where the Viterbi track follows this line of high power. The Viterbi map has much higher values for the log-probability in this line case compared to the noise case. This is an indicator some real instrumental signal. The probability in the Viterbi maps drops to zero in some areas due to the strength of the instrumental line, these are the white areas in the Viterbi map plot (second panel).

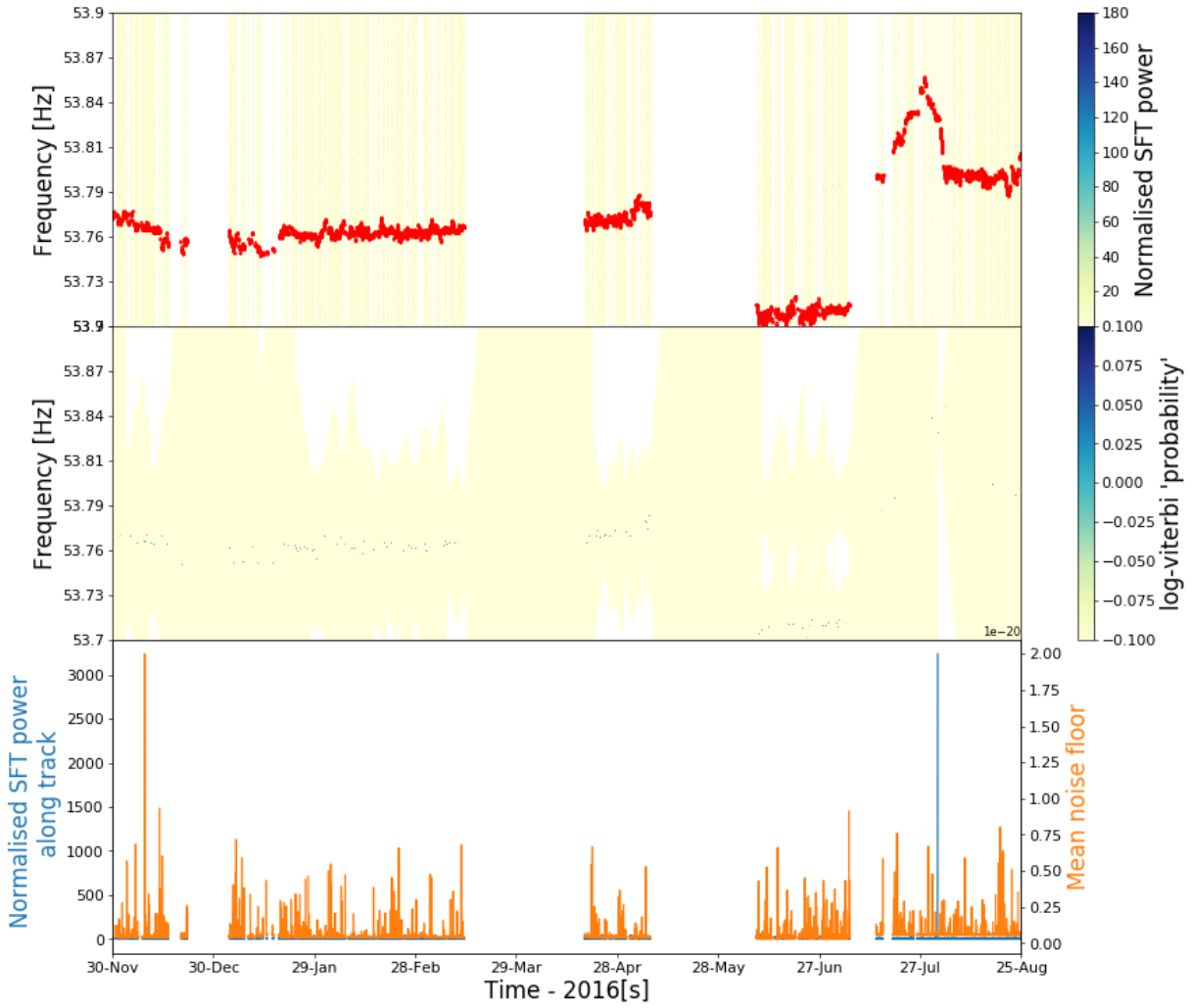

Figure 6.6: The equivalent plot as in Fig. 6.4 can be made when there is a wandering spectral line. The above again shows results from the LIGOs Hanford detector (H1) in its third observing run (O3) using an 1800s SFT power spectrum. This shows how some spectral lines do not have a fixed frequency and can wander through the band. These are especially hard to track and monitor. The Viterbi track here shows is clearly different from the noise case in Fig. 6.4 as the track is more tightly concentrated around some areas of power.

frequency of the track changes with time. There are also areas where the track switched to a separate spectral artefact within the same band. SOAP only returns a single track which follows that of the highest SFT power, if there are multiple spectral artefacts within a sub-band, then SOAP will identify the areas of high power in each which correspond to the highest sum of SFT power. This means that the track can, and does, switch between different spectral artefacts accumulating the highest SFT power from each. Fig. 6.6 shows this discrete jump around January.

The Viterbi statistic is used as an initial flag for a sub-band which could potentially contain an instrumental line. One can then use the equivalent plots as Fig. 6.4, 6.5 and 6.6 to investigate each sub-band and return a list of potential lines. This line-list can then be compared to existing O3 LIGO line-lists which are generated using the searches described in Sec. 6.2. There are currently two line-lists produced by LIGO scientists, one which contain lines where the source has been identified and one where the source is not known. Known lines can be accessed at [**goetzKnownO3**] and unknown lines at [**goetzUnknownO3**] or are both stored in a git repository [**goetzLinesGit**].

We measure the performance of the SOAP line search by comparing a list of potential lines generated with SOAP to the LIGO list generated with existing techniques. For the SOAP search we count the line as detected if the sub-band which contains the line has an associated Viterbi statistic which crosses the detection threshold from Fig. 6.3. SOAP then detected all of the lines of known origin with the exception of those from "Calibration line mixing" or "Calibration line non-linearity", which made up $\sim 45\%$ of lines in the 40-500 Hz band. Upon further investigation of the frequency bands around the location of the undetected lines, we found that in general they appear as short duration (< 1 week) signals in SOAP's output, where some examples of these can be seen in Fig. 6.7. SOAP struggles to find short duration signals if the signal is weak as it cannot build up enough SNR to pass the detection threshold. However, the line is still visible when investigating the Viterbi maps and Viterbi track.

We identified 30% of the lines in the unknown LIGO line-list, where we class a line as identified if the Viterbi statistic for a given sub-band crosses our detection threshold. However, Viterbi statistics from sub-bands which contained these unknown lines and fell below the detection threshold showed signs in the Viterbi maps and Viterbi tracks which indicate an instrumental line is present. An example of this can be seen in Fig. 6.8a where in the second half of the observing run, the width of the Viterbi track narrows indicating that a narrow signal could be present. In the Viterbi maps an increase in the concentration of the log-probability around this frequency can be seen, again indicating a signal is present. Similar features can be see in Fig. 6.8b and 6.8c. For some other lines in LIGOs unknown line-list, such as in Fig. 6.8d, there is no indication of an instrumental line in the SOAP outputs. However, for over 50% of the lines in the unknown line-list

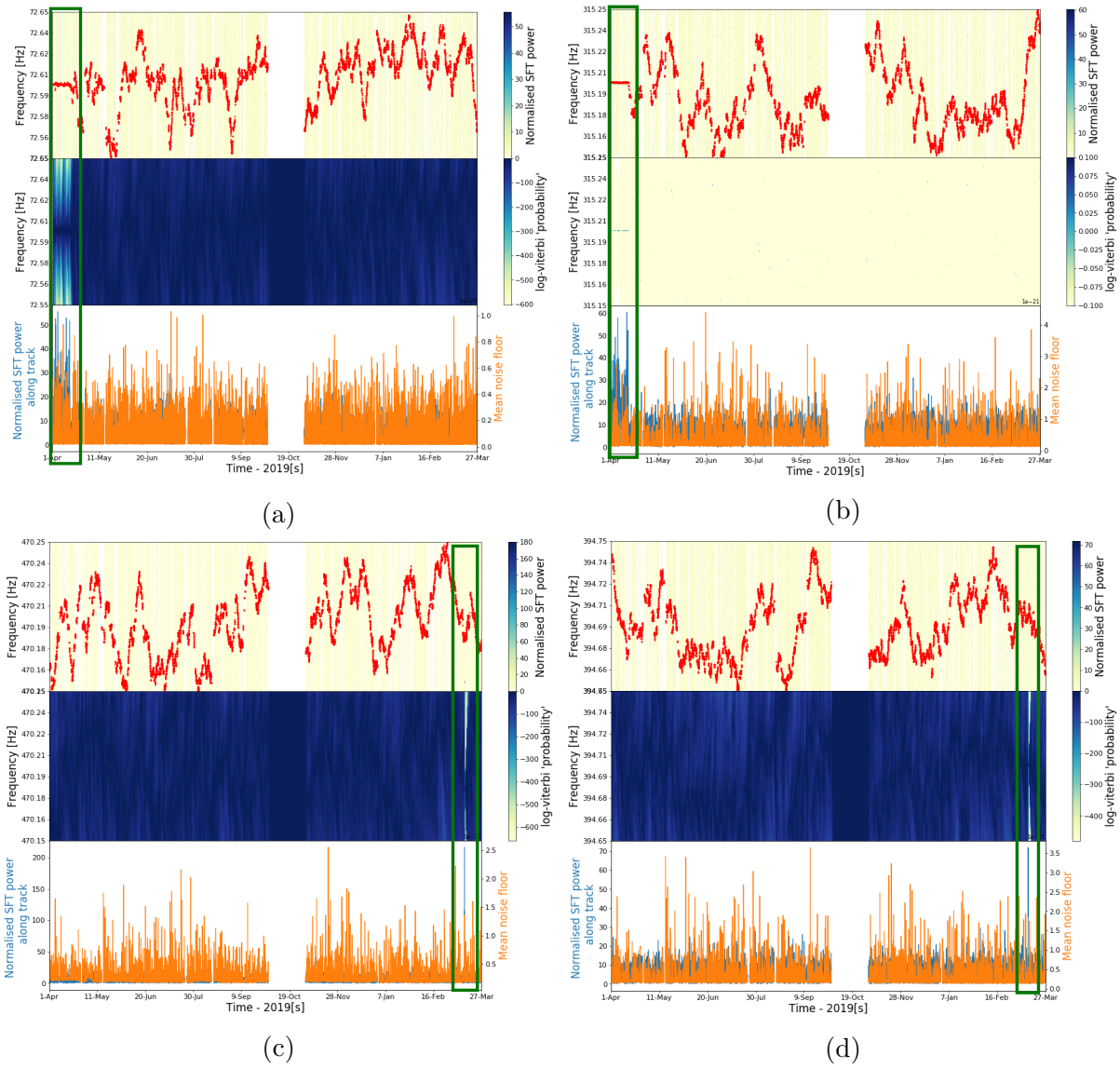

Figure 6.7: Example of lines from "calibration line mixing" and "calibration line non-linearity". Fig. 6.7c and 6.7d are examples of lines from "calibration line mixing", where these examples appear as short burst of SFT power towards the end of the observing run. Fig. 6.7a and 6.7b are examples of lines from " calibration line non-linearity", where these examples appear as short duration lines at the beginning of O3. In each of these images I have highlighted the areas of interest with green squares. These are both short durations lines, therefore, SOAP will struggle to identify them in the Viterbi statistic if they do not have enough SFT power, however is still visible in the Viterbi maps and Viterbi track.

which we did not detect and have investigated further, there is some evidence of a line in the other outputs of SOAP.

Therefore, one possible addition to the SOAP line search could be a method similar to that described in Chapter 4, where here the Viterbi maps and Viterbi tracks associated with instrumental lines would be used as training data for a neural network. The neural networks could then be used to classify sub-bands into containing an instrumental line or Gaussian noise. The difficulty with using these Viterbi maps as training examples is that we do not have a set of training data with known labels. We could generate these labels from each sub-band in real data which contains an instrumental line, but this would require a large effort investigating the many sub-bands. Another method could be simulating instrumental lines, however this can be difficult due to the large variation in the types of instrumental line. Each of these types would need some functional representation such that they be generated, which would also need investigation in to the many types of line. Methods such as in [**zevin2017GravitySpy**] have had success using machine learning to classify short duration noise artefacts (glitches). This project uses time-frequency representations of the glitches that have been classified by volunteers from the public as training data for machine learning algorithms. A similar approach could be used to classify the outputs of the SOAP search, where labels can be applied to sub-bands such that a machine learning algorithm can be trained. Alternatively this may be better suited to an un-supervised machine learning approach, which would group the data into line or noise categories without using labels.

Whilst SOAP did not identify all of the same lines as the methods in Sec. 6.2, it did identify $\sim$ 150 lines which did not appear in either the known of unknown line-list. For example, in Fig. 6.9a, SOAP identified a line at $\sim$ 64.0 Hz which does not currently appear in the LIGO line-list. Further examples are at $\sim$ 119.88 Hz in Fig. 6.9b and $\sim$ 150.055 Hz in Fig. 6.9c which show strong transient lines. Finally Fig. 6.9d shows that there may be multiple strong lines present within this sub-band, this is because the Viterbi track appears to have identified multiple features and 'jumps' between these during the observing run. In total, SOAP identified $\sim$ 150 sub-bands which potentially contain an instrumental line which did not appear on the LIGO line-list. Whilst many of these will require further investigation to determine if they are indeed a line and what their source is, it demonstrates the ability of this search to identify new instrumental lines.

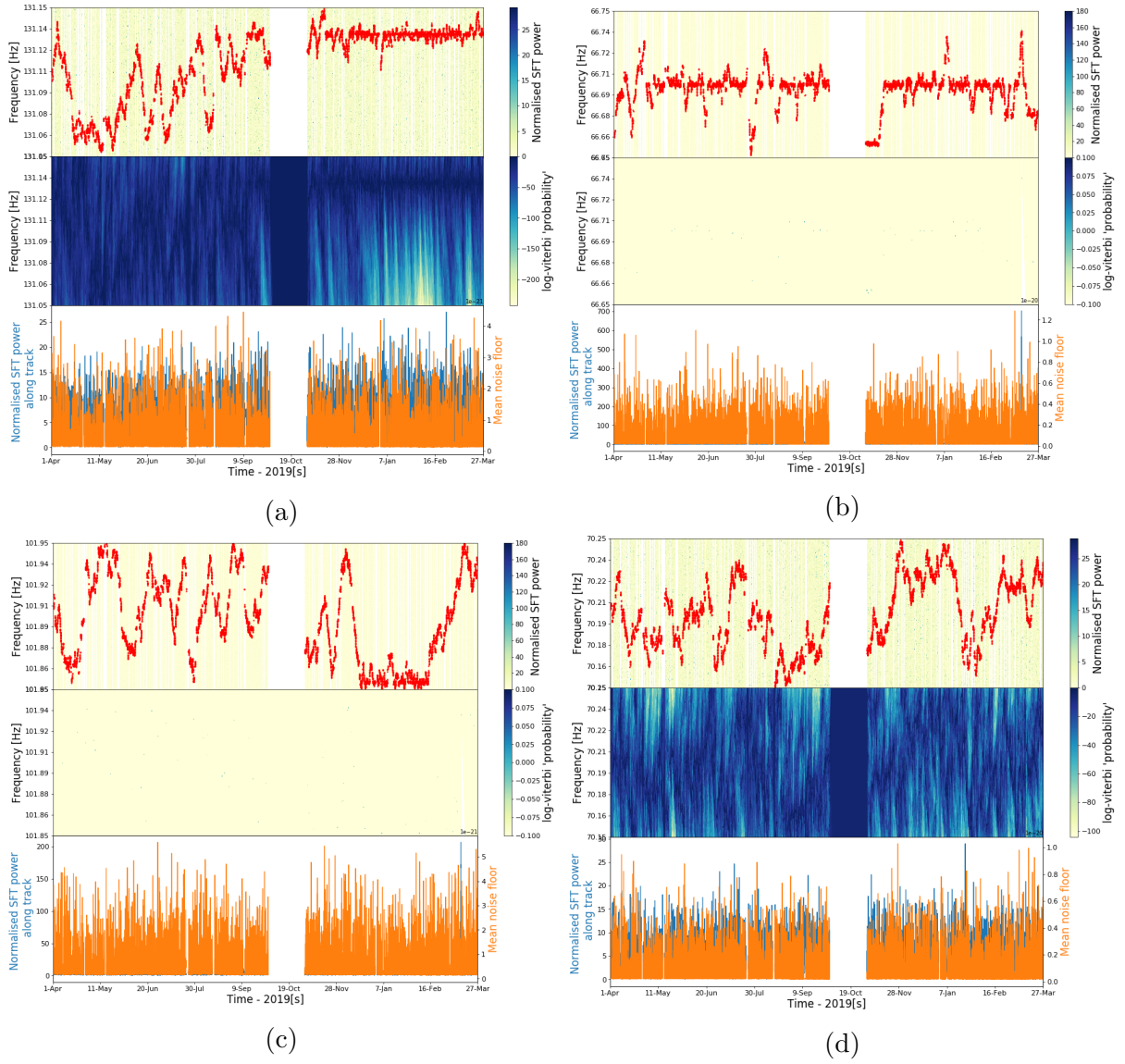

Figure 6.8: Examples of unknown instrumental lines in H1 during the O3 run which were not identified by SOAP using the Viterbi statistic. These show the 1800s spectrograms for H1 in the top panel and the Viterbi maps in the second panel. The final panel shows the SFT power along the Viterbi track and the mean noise floor in this band. Fig. 6.8a, 6.8a and 6.8a have areas of the Viterbi track which are narrow and are not spread over the entire band, indicating a non Gaussian signal is present. In Fig.6.8a and 6.8a the Viterbi maps show some areas of high log-probability which are difficult to see at this resolution, hence the uniform appearance.

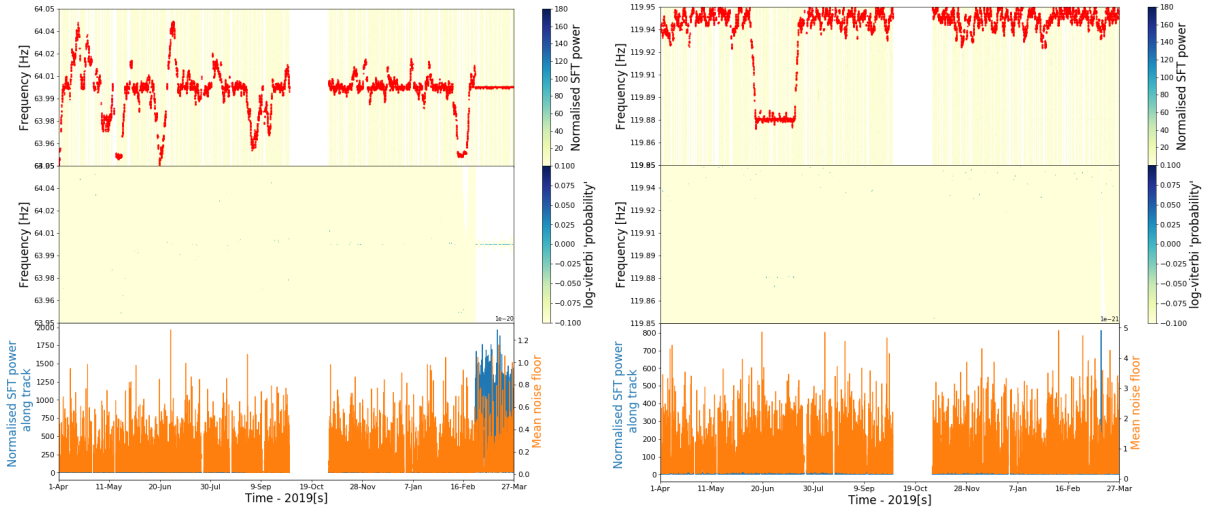

(a) (b)

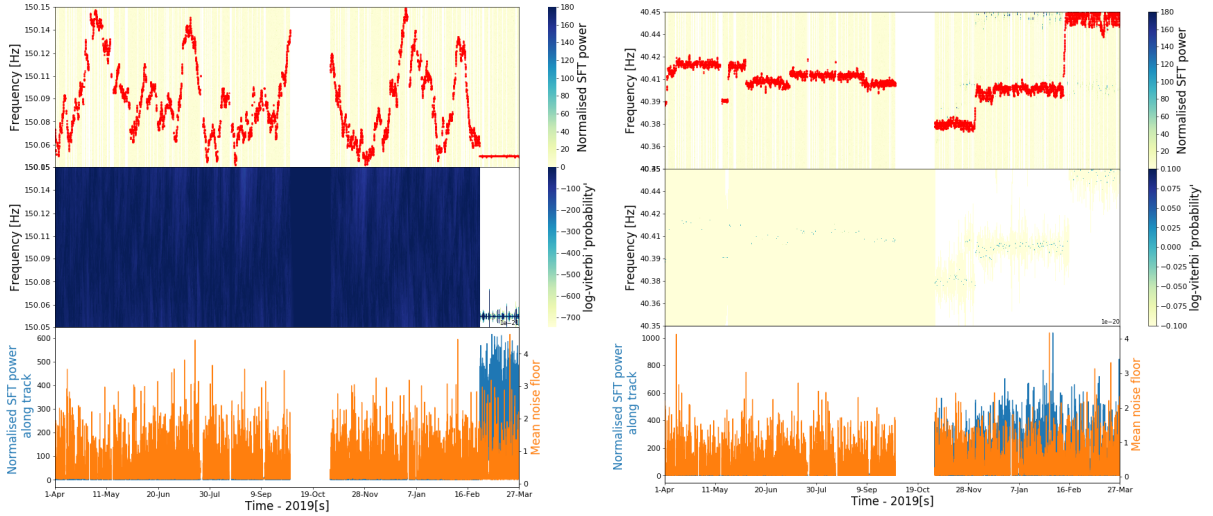

(c) (d)

Figure 6.9: Examples of instrumental lines identified by the SOAP line search in H1 during the O3 run which did not appear in LIGO line-lists are shown. Fig. 6.9b and 6.9c show transient lines which had a large enough SNR to be identified. Fig.6.9a shows a narrow band line which increases in SNR in the final month of this O3. Finally Fig. 6.9d shows multiple features within the sub band, where the Viterbi track 'jumps' between the different features during the run.

6.4 Summary pages

Summary pages are an important tool when searching for both instrumental lines and astrophysical signals as there is a large amount of data in both frequency and time to search through, where for line searches there are also a large number of different channels. Summary pages distil this data such that only the important information is shown. This enables signals to be identified easily when looking through sub-bands. The criteria when designing summary pages is that they are easy to navigate and the important information is shown in a clear and concise way. These summary pages exist for the line searches in this chapter and the astrophysical searches from chapters 3 and 4 in [**bayleyHome**] where this is only accessible by LIGO, Virgo and KAGRA members. In this section I will explain the line summary pages, however, the astrophysical pages have a similar design.

Summary pages have currently been generated from the results of the SOAP search for observing runs O2 and O3 for the two LIGO detectors, where pages for other detectors and observing runs are planned. This was done for various timescales: for the entire observing run and separately for each month. This allows the variation of a line to be observed for both the entire length of the run and shorter timescales. Once the detector, observing run, and timescale is set, we currently split the 40-500 Hz band into 0.1 Hz wide sub-bands. The SOAP search is then run on each sub-band using a flat transition matrix and the sum of SFT powers along the Viterbi track as the detection statistic. A flow diagram of how the SOAP search works for instrumental line searches can be found in Fig. 6.10. These stages are as follows:

1. **SFTs from time series** The SFTs are generated for the GW output channel. This is done as part of the Fscan search, therefore we do not repeat this process. Currently the search only runs on the GW channel, however, in the future could be made to run on others.

2. **Divide SFT by running median** In this stage each SFT power spectrum is divided by its running median, where a correction factor is applied such that the data has a mean of 1. The running median has a window of width 100 bins, this was chosen such that broad features wider than this window are removed whilst outliers should remain. The output of this stage is then a high pass filtered SFT power spectrum.

3. **Narrow-band SFT** The SFT is then split into 0.1 Hz wide sub-bands for the SOAP search to run on. These smaller bands are chosen as the SOAP search only returns information on the most likely track in a sub-band, therefore, smaller bands are not contaminated by areas of high power in neighbouring frequency bands.

4. **Run SOAP and generate plots** This stage runs the SOAP search with a flat transition matrix probability and generates plots as shown in Fig. 6.4.

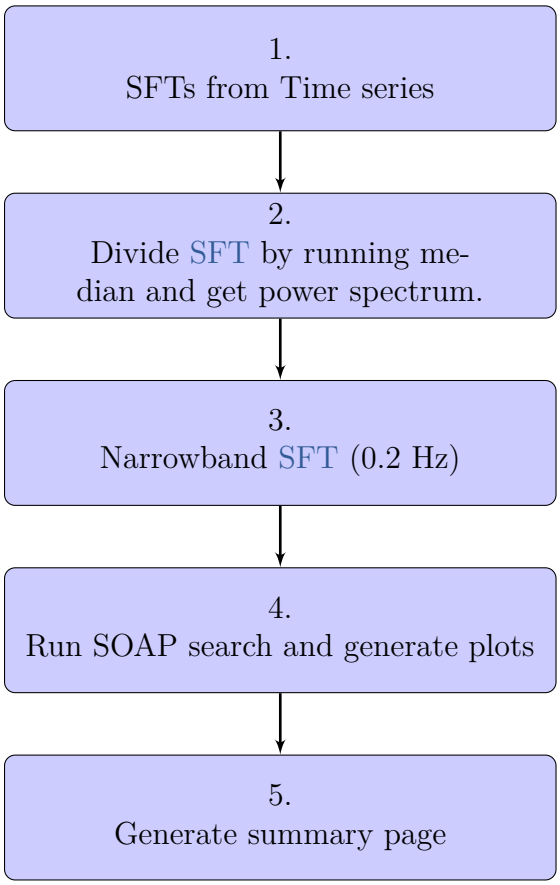

Figure 6.10: The SOAP search for instrumental lines is simpler than other searches. A simple version of the search is run separately for each detector, where the raw SFTs are divided by their running median, narrow-banded and then the search is run.

5. **Generate summary page** Finally web pages known as 'summary pages' are generated which summarise the SOAP outputs from each sub-band. This puts all sub-bands into a table where it can be ordered by the value of the Viterbi statistic, or can be searched for particular frequency bands. Where selecting a frequency band will display the output plots shown throughout this chapter.

An example of a summary page is shown in Fig. 6.11. This has been annotated showing how to navigate the page. There are generally two separate parts to the page: selecting the observing run and frequencies, and viewing the outputs. The observing run is selected at the top of the page, where currently this has been run on O2 and O3. From this menu the detector can be selected, currently LIGOs H1 and L1 detectors are present. On this page the desired frequency bands can be selected, where the output plots can be displayed. The key information of each page is the plots shown in Figs. 6.4 - 6.9. They show the time frequency spectrograms of the data, the output Viterbi tracks which identify the most probable frequency track, the Viterbi maps which allow the probability of a signal as a function of the time and frequency bin to be viewed. Finally they show the spectrogram power along the Viterbi track with the mean noise floor of the detector during the observing run. Each of these should provide useful information to asses whether an instrumental line in present within a given sub-band.

To navigate each page, the left panel contains a calendar where the start and end times of a result can be selected. Currently there are pre-defined times which can be selected from. This allows a line to be investigated for a shorter or longer time period. This can be useful when a new instrumental line appears and it needs to be investigated only from when the line appears. Below this in the left panel of the page there is a table where each cell is one of the sub-bands which was searched through. This allows individual frequency bands of interest to be searched for as well as the table to be limited between different frequencies. The table contains four columns: the frequency of the sub-bands, the Viterbi statistic, the σ from the mean of all the sub-band Viterbi statistics and extra information. The first two columns are self explanatory, the frequency range of the sub-band and the resulting Viterbi statistic from that sub-band. The table can be ordered by the Viterbi statistic such that only the highest values are investigated. The σ from the mean is found by approximating the distribution of the Viterbi statistics as a Gaussian. A Gaussian is then fit to the distribution using a simple least squares, each statistic then has a multiple of σ away from the mean of this distribution. This is an approximate calculation to give a scale of how significant the statistic in that sub-band is. The final column contains any extra information which exists for that particular frequency range. For example, this is filled with other line-list information which has been collected from other search methods. The loud features such as Violin modes can then be marked. This means that these particular bands are likely to have been investigated already allowing this search to focus

on any extra instrumental lines.

The summary pages offer a way to easily view the outputs of the SOAP line search, where sub-bands which are identified by SOAP as containing a potential signal can be investigated further. The aim of this tool is to be used alongside existing methods described in Sec. 6.2 to aid in the identification of potential instrumental lines.

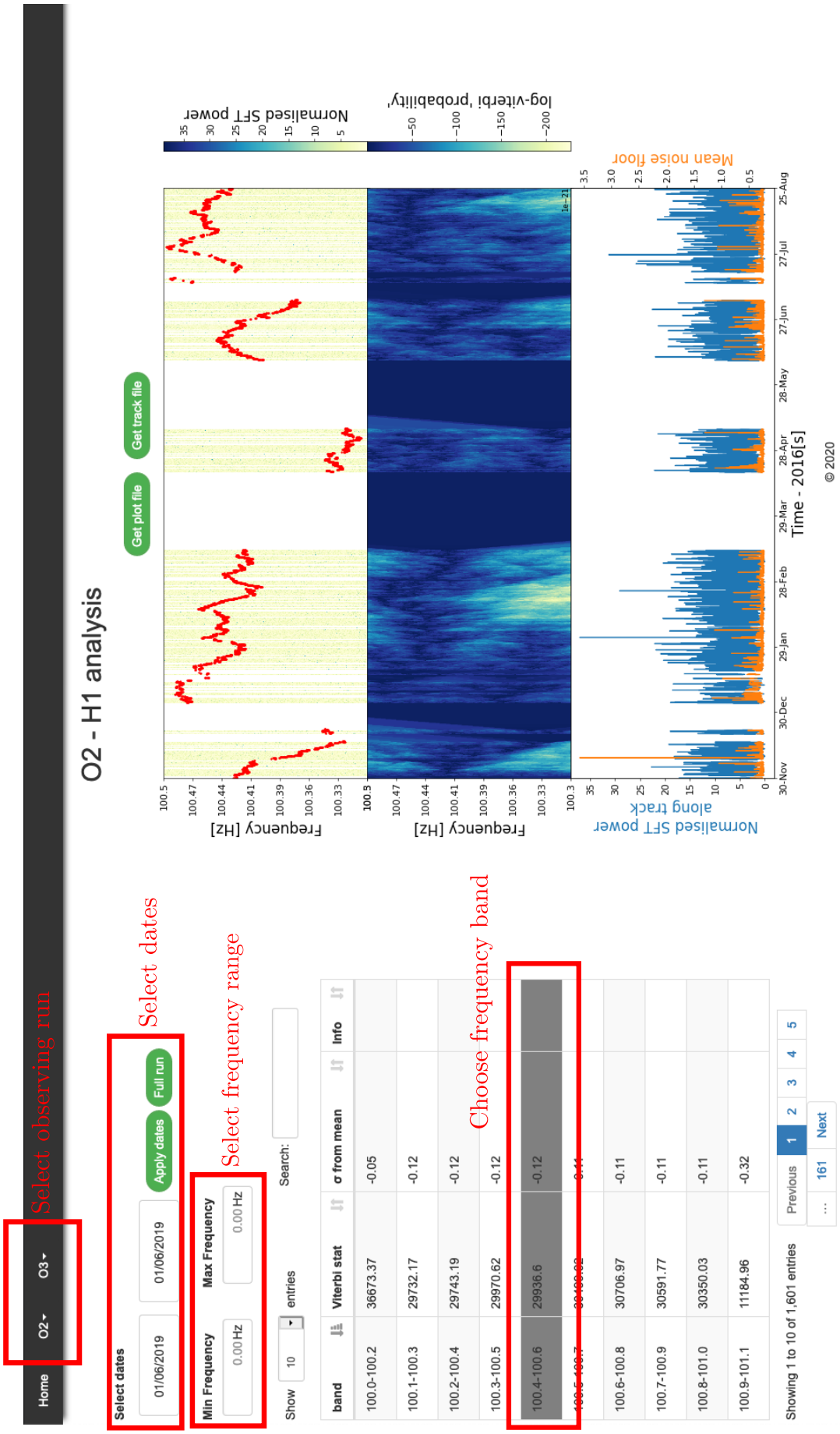

Figure 6.11: The summary pages are made for each observing run (in this case just O2 and O3). The range of times can then be selected from a set of start and end times. This is in general the entire observing run and monthly runs of this search. These pages can be accessed at [**bayleyHome**]

Chapter 7

Summary

This thesis outlines the current state of searches for CWs, and describes new techniques which have been developed to address some of the challenges in this type of search. Whilst CWs have not yet been detected, they are expected to originate from rapidly rotating neutron stars which are not symmetric around their rotation axis and are expected to have a long duration quasi-sinusoidal signal. For many CW searches the large observation times and parameter space, mean that there is a substantial computational cost associated with each search. Chapter 2 outlines some existing CW search methods and highlights the large computing cost. The methods described in this thesis address the challenge of balancing the computational cost against the sensitivity when searching for CWs, and also provide a non-parametric way to search for long duration signals.

In Chapter 3 we described a search algorithm entitled SOAP which is a mostly unmodelled CW search. This is based on the Viterbi algorithm which was designed to find the most likely set of states through a discrete Markov process. We used this algorithm to search through time-frequency spectrograms of LIGO data to identify frequency tracks which may be associated with a CW signal. Some constraints can be placed on the 'model' of the frequency track, where the track can be limited to change by a given number of frequency bins at each time segment. This is governed by a 'transition matrix' described in Sec. 3.3 and can help focus the search on particular frequency evolutions. The search then returns the frequency track which gives the highest value of a statistic. There are a number of statistics which were developed, the simplest being the sum of the FFT power along the frequency track and more complex Bayesian statistics were developed to be robust against instrumental artefacts.

Initially this was a search though a single time-frequency spectrogram, in Sec. 3.5 this was extended to search through multiple detectors, i.e. multiple time-frequency spectrograms. This simple statistic which used just the sum of the FFT power encountered problems in both the single and multi-detector approach when frequency tracks of high FFT power originated from instrumental artefacts as opposed to astrophysical ones. Specifi-

cally, the data is contaminated with instrumental lines which are long duration narrow band spectral artefacts. The multi-detector approach allowed us to mitigate the effect of these instrumental lines with the development of a Bayesian statistic in Sec. 3.8. This effectively down-weights normalised FFT powers which appear to be from instrumental lines, i.e. when there is a large difference in normalised FFT power between the detectors. As we normalise the LIGO time-frequency spectrograms to their running median, SOAP then searches for consistent SNR between multiple detectors. However, these multiple detectors can have different sensitivities, therefore, the SNR of the same astrophysical signal can be different in each detector. In Sec. 3.9, the Bayesian statistic was modified to search for consistent signal amplitudes, i.e. consistent values of h_0, by incorporating the detector noise floor and the fraction of the observation data in each segment. For each of these statistics there is a set of hyper-parameters which were optimised based on CW signals simulated in noise.

SOAP was then tested on three main data-sets containing simulations of CW signals from isolated neutron stars. The data-sets include: Gaussian noise, Gaussian noise with temporal gaps corresponding to times when the detector was off in LIGOs S6 data run, and in real LIGO S6 data, which was from a standard set of simulations generated to compare CW searches sensitivity to isolated neutron stars [**walsh2016ComparisonMethods**]. In this test we achieved a sensitivity which is comparable to other CW searches, achieving a depth of $\sim 13\,\mathrm{Hz}^{-1/2}$ at 95% efficiency and 1% false alarm. However, the computational cost of this search is orders of magnitude less than those described in the S6 MDC [**walsh2016ComparisonMethods**]. SOAP is also not limited to searching for isolated neutron stars but can search for many signal types as it identifies un-modelled frequency tracks of high power. Section 3.13 shows an example of this, where SOAP was tested by searching for GW170817 which was the first detected BNS signal and GW150914 which was the first detected BBH signal. This test returned high values of the Viterbi statistic in areas of the time-frequency spectrum around the BNS or BBH signal, this would however require more investigation to develop a reliable detection statistic. SOAP however , still has limitations. The line-aware statistic in Sec. 3.8 reduced the effect of instrumental lines but many contaminated frequency bands were missed and had to be manually removed in the analysis. In Chapter 4 we aim to address this problem using CNNs.

There are a number of additions which we aim to add to this search in the future. For example, there are additional statistics, such as using the Fourier transform of the detector power along the track in the SFTs. If an astrophysical signal is present then the effects of the antenna pattern should be seen at a sidereal day. Future work on this also includes using the output of the SOAP search to estimate parameters of the source which is discussed in Chapter 5.

The aim of Chapter 4 was to follow on from the SOAP algorithm in Chapter 3 using

machine learning algorithms. One of the main challenges in the SOAP search was the contamination of frequency bands with instrumental lines. In Chapter 3, we described how many bands had to be investigated and potentially removed from the analysis if they were deemed to be contaminated. This is a time consuming process and becomes impractical when searching over larger bandwidths. Therefore, we aimed to replace the manual removal of bands with a CNN which would classify each sub-band into containing a signal or not.

Section 4.3 contains an introduction to how neural networks are structured and how they operate on a given input, and is then followed by an explanation of how a CNN operates in Sec. 4.4. CNNs are well suited to the classification task described above as they were originally designed to identify features within an image, where the time-frequency spectrograms in our problem can be thought of as images. A CNN can identify features within these images and extract useful information from them, for example it could classify whether an astrophysical signal is present in the data.

In Sec. 4.5 we describe a key part of using neural networks, which is training their many parameters. Training a network involves showing it many examples of data which are labelled based on the classes associated with the problem. This means that in our examples, a time-frequency spectrogram which contains an astrophysical signal is labelled to contain a signal and a spectrogram with noise or an instrumental line is labelled as noise. The many parameters of the network can then be updated such that given the set of training data, it should give the best result when any new example is shown to the network. The 'best result' in our problem is higher values of the output (close to 1) if an astrophysical signal is present and lower values (close to 0) if not. Training data-sets are generally very large which allows the weights to be updated without over fitting to a particular data-set.

We then designed CNNs in Sec. 4.6.1 which took in three main types of data: down-sampled time-frequency spectrograms of LIGO data, down-sampled output Viterbi maps and the output Viterbi statistic. The Viterbi maps and Viterbi statistic are the SOAP outputs which are different representations of the time-frequency spectrograms. The time-frequency spectrograms and Viterbi maps were downsampled to reduce the amount of data passed through the CNN and to speed up the training time. There were then 6 main networks which took these data types and combinations of them as inputs. The networks return a statistic which ranges between 0 and 1, and is used as a detection statistic. Each of the 6 networks were tested on CW simulations divided into four data-sets: Gaussian noise and real LIGO data from the observing runs O1, O2 ,and S6. In each of these tests the CNN which contributed most to the sensitivity was the network which took the Viterbi map as input, therefore for most results in Chapter 4 we use the Viterbi map CNN.

The results of Chapter 4 showed that applying a CNN to the output Viterbi maps of

the SOAP search eliminates the need to manually remove the contaminated bands. This method achieved a similar sensitivity to the SOAP search alone in Chapter 3, whilst fully automating the search and reducing the time needed to generate results. In this Chapter a complete comparison to other all-sky CW searches was conducted by comparing their sensitivities on a standard set of simulations of isolated neutron stars in LIGOs S6 data. A comparison was made of the sensitivity to signals with frequencies in the range of 40-500 Hz, where we found that SOAP + CNN has a sensitivity which is comparable to that of other all-sky searches. This search however, can run with a computational time orders of magnitude faster than the others. In Sec. 4.9.2 we compare the computational cost of the searches for the first four months of LIGO O1 data, where the SOAP + CNN search is $\sim 5-10$ thousand times faster than the next fastest all sky CW search.

The two methods described in Chapters 3 and 4 will identify with some probability whether a signal is present within a small frequency band. To understand astrophysical properties of the source, one needs to return more parameters other that just its frequency band. In Chapter 5 we aimed to return the Doppler parameters, i.e. the sky position α, δ, the frequency f and its derivative $\dot{f}$, of the source using the outputs of the SOAP search in Chapter 3. The SOAP search returns a Viterbi track from any frequency band, which is a track in frequency where assuming SOAP has correctly identified the signal, will describe the frequency evolution of the source. This frequency evolution then contains information on the Doppler parameters mentioned above. Therefore, in Chapter 5 we described a Bayesian method to extract the Doppler parameter from the Viterbi track.

The Viterbi track does not have an easily predicable noise distribution, therefore we simulated this distribution using many CW signals and their associated Viterbi tracks. This distribution is dependent on the SNR ρ, therefore, our Bayesian model estimated the parameters $\alpha, \delta, f, \dot{f}$ and ρ associated with a given Viterbi track. This analysis was then tested on 200 simulations of CW signals in the frequency range of 40-500 Hz, where we found that this Bayesian model returns a posterior distribution which at 95% confidence is over-constrained in the parameters $\alpha, \delta, f, \dot{f}$ and ρ. These results implied that the current model does not provide a valid method to estimate the source parameters, however, this was a toy case to demonstrate how one would extract source parameters from the SOAP search. With the development of a more appropriate likelihood and further investigation, we aim to develop this such that the parameters of a CW source can be estimated reliably.

In Chapters 3 and 4, we found that instrumental artefacts, particularly instrumental lines contaminated the SOAP search. However, the fact that SOAP is contaminated by these lines means that SOAP can identify them. In Chapter 6 we describe how the SOAP search can be used for detector characterisation particularly to identify instrumental lines within the data.

Section 6.1 introduces instrumental lines and how, due to their long duration and narrowband nature, they contaminate many searches for GWs. This is followed by and overview of the current methods used to detect and monitor lines within the data in Sec. 6.2. In Sec. 6.3 we describe how the SOAP algorithm can be used to identify these lines where we use a single detector search, which uses the sum of the SFT power along the Viterbi track as a simple statistic. We have searched between 40 and 500 Hz for instrumental lines in LIGOs O3 observing run in the Hanford detector (H1), generating a list of potential lines to be investigated further. This list was compared to the list generated by LIGO scientists using the methods described in Sec. 6.2. We found that SOAP detects ~ 37 % of the lines present on this list, where upon further investigation many of the lines which were not detected contained more information in the Viterbi maps and Viterbi tracks which indicate that they do originate from an instrumental line. Often these un detected lines were transient and therefore not a priori expected to be detected by SOAP. Therefore, using an approach as in Chapter 4 one could incorporate the Viterbi map and Viterbi track into the statistic improving its sensitivity to instrumental lines. Whilst the SOAP line search did not detect all of the lines on the LIGO line list according to the Viterbi statistic, it did identify ~ 150 which were not present in this list. These however, would require further investigation to determine their source.

In Sec. 6.4, we describe the SOAP summary pages, which are web pages that summarise the information in both the SOAP line and astrophysical searches. The line pages provide a method to easily identify contaminated frequency bands and view the SOAP soap outputs, where we aim for this tool to be used alongside the current line detection methods to aid in the discovery and mitigation of instrumental lines.

This thesis gives an overview of the current state of searches for GWs, with a focus on the methods used to search for CWs. We presented a new non-parametric search method for CWs entitled SOAP, which is orders of magnitude faster than other existing searches with a comparable sensitivity. We then describe developments to this algorithm which include: using machine learning to make the search more robust against instrumental artefacts, using the outputs of SOAP to extract astrophysical parameters of the source, and applying the search to detector characterisation where it can be used to identify instrumental lines. SOAP then provides a rapid method to search for long duration signals, where the flexibility of the search allows an investigation into signal types which do not follow the standard frequency evolution in the search for CWs.

Appendix A

Continuous gravitational wave injections

In this section I outline how we inject a CW signal into data. This can generally be done in two different ways: simulating a signal in the time domain and injecting into time domain noise or simulating the signal in the frequency domain. The searches described in Sec. 3 and Sec. 4 only use output power spectra] Generating the time series and performing a Fourier transform or generating the signal in the frequency domain is time consuming. In this section I will outline how I simulate the power spectrum of CW signals and inject them into a PSD. This should greatly improve the speed of data generation.

A.1 Signal SNR

To inject into a spectrogram the power spectrum of the signal will need to be simulated. In our injection we do not have access to a time-series, therefore, we do not simulate the signal in in the time series or complex frequency domain. Instead, the SNR of the signal can be estimated in given frequency bins and injected straight into the power spectrum.

It can be shown that the PSD of Gaussian noise with zero mean and unit variance is a χ^2 distribution with 2 degrees of freedom. Therefore, if we want to generate a spectrogram for Gaussian noise, we just generate a two dimensional array of values distributed as χ^2 with two degrees of freedom. Assuming that there is some sinusoidal signal with a given SNR within a Gaussian noise time-series with zero mean and unit variance, the FFT power in a particular frequency bin can be estimated using a non-central χ^2 distribution with 2 degrees of freedom, where the non centrality parameter is the square of the SNR. To calculate the SNR in a given frequency bin the equation in [**prix2007SearchContinuous**] for optimal SNR was used

$$\rho(0)^2 = \frac{1}{2} h_0^2 T S^{-1} \left[\alpha_1 A + \alpha_2 B + \alpha_3 C\right], \tag{A.1}$$

where h_0 is the GW amplitude, T is the total observing time is seconds, S^{-1} is the mean PSD noise floor. The values of α are then defined in [**prix2007SearchContinuous**] by

$$\begin{aligned}
\alpha_1 &= \frac{1}{4}\left(1+\cos^2(\iota)\right)^2\cos^2(2\psi)+\cos^2(\iota)\sin^2(2\psi)\\
\alpha_2 &= \frac{1}{4}\left(1+\cos^2(\iota)\right)^2\sin^2(2\psi)+\cos^2(\iota)\cos^2(2\psi)\\
\alpha_3 &= \frac{1}{4}\left(1-\cos^2(\iota)\right)^2\sin(2\psi)\sin^2(2\psi)
\end{aligned} \tag{A.2}$$

where ψ is the gravitational wave phase and ι is the inclination angle of the source. The values of A, B and C in Eq. A.1 are functions which represent the time averages antenna patterns, they are defined by

$$\begin{aligned}
A &\equiv \langle a^2\rangle\\
B &\equiv \langle b^2\rangle\\
C &\equiv \langle ab\rangle,
\end{aligned} \tag{A.3}$$

where a and b are the antenna pattern functions defined in [**schutz1998DataAnalysis**] as

$$\begin{aligned}
a(t) = &\frac{1}{16}\sin 2\gamma(3-\cos 2\lambda)(3-\cos 2\delta)\cos[2(\alpha-\phi_r-\Omega t)]\\
&-\frac{1}{4}\cos 2\gamma\sin\lambda(3-\cos 2\delta)\sin[2(\alpha-\phi_r-\Omega t)]\\
&+\frac{1}{4}\sin 2\gamma\sin 2\lambda\sin 2\delta\cos[\alpha-\phi_r-\Omega t]\\
&-\frac{1}{2}\cos 2\gamma\cos\lambda\sin 2\delta\sin[\alpha-\phi_r-\Omega t]\\
&+\frac{3}{4}\sin 2\gamma\cos^2\lambda\cos^2\delta,
\end{aligned} \tag{A.4}$$

$$\begin{aligned}
b(t) = &\cos 2\gamma\sin\lambda\sin\delta\cos[2(\alpha-\phi_r-\Omega t)]\\
&+\frac{1}{4}\sin 2\gamma(3-\cos 2\lambda)\sin\delta\sin[\alpha-\phi_r-\Omega t]\\
&+\cos 2\gamma\cos\lambda\cos\delta\cos[\alpha-\phi_r-\Omega t]\\
&+\frac{1}{4}\sin 2\gamma\sin 2\lambda\cos\delta\sin[\alpha-\phi_r-\Omega t].
\end{aligned}$$

Hereγ is the orientation of the detectors arms, λ is the latitude of the detectors site, α and δ are the right ascension and declination of the GW, ϕ_r is a deterministic phase defining the position of the earth and Ω is the rotational angular velocity of the earth. This takes into account the antenna pattern modulation of the signal as the earth rotates the sun and orbits the earth. We then have a description of the SNR of a signal with a set of

parameters for any given time and duration. This however does not describe how the SNR of a signal varies with frequency which we need for spectrogram injections.

A.2 SNR with frequency

If one takes a sinusoidal signal and the takes the Fourier transform of that, then this should be a delta function at the frequency of the sinusoid. However, in the real world this sinusoid has a limited length and one will instead take the FFT of that signal, the signal will then be broken into discrete frequency bins. If the sinusoids frequency falls at the center of a frequency bin then the entire power of the signal will be contained within that frequency bin. However, if it is not perfectly centered on a frequency bin, then the power of the signal will begin to be spread over surrounding frequency bins. The aim is then to simulate how the signal is spread over surrounding frequency bins. If one has a sinusoid with a finite length, this is equivalent to taking an infinitely long sinusoid and convolving it rectangular window (box). The frequency response is then the Fourier transform of the sinusoid convolved with the Fourier transform of the box window. The Fourier transform of a box window is a sinc and of an infinitely long sinusoid is a delta function. The resulting Fourier transform is then a sinc function. One can write this down mathematically by writing the signal as

$$n(t) = \exp\{i2\pi f_0 t\}, \tag{A.5}$$

where f_0 is the signals frequency. The Fourier transform for this for a finite length of time which ranges between $-T/2 < t < T/2$ can be written as

$$\begin{aligned}\tilde{n}(f) &= \int_{-T/2}^{T/2} \exp\{-i2\pi(f-f_0)t\}dt \\ &= \frac{1}{-i\pi(f-f_0)}\left(\exp\{-i\pi(f-f_0)T\} + \exp\{-i\pi(f-f_0)T\}\right) \\ &= \frac{2\sin\left(\pi(f-f_0)T\right)}{\pi(f-f_0)} \\ &= T\mathrm{sinc}\left(\pi(f-f_0)T\right)\end{aligned} \tag{A.6}$$

One can verify this by taking the power spectrum of a finite length sinusoid, and plotting the square of a sinc function on top as shown in Fig. A.1.

For a sinusoid which has some frequency derivative the Fourier transform changes slightly. Similarly to above one can start with the definition of a signal with a constant frequency derivative such that

$$f = f_0 + \dot{f}t, \tag{A.7}$$

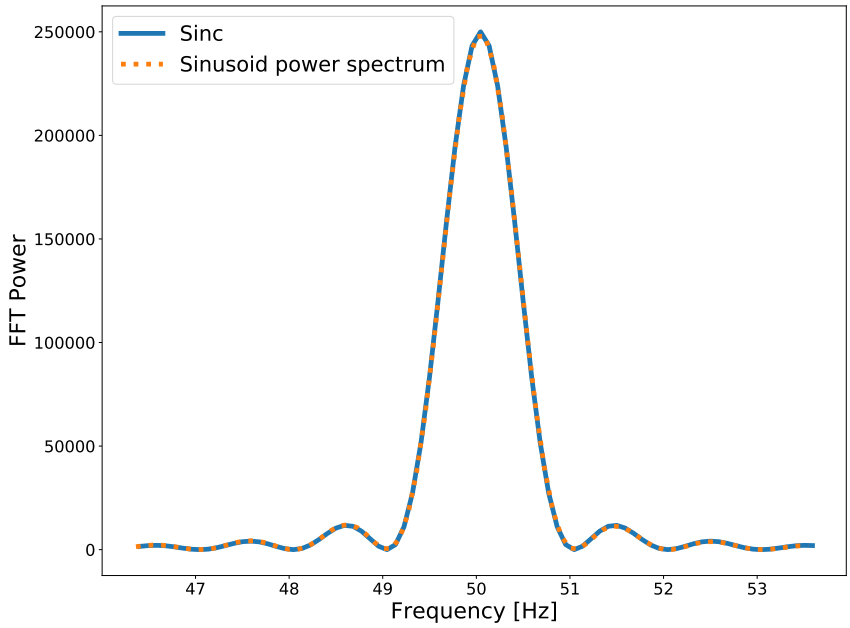

Figure A.1: If one takes the power spectrum of a sinusoid with finite length, this returns the same distribution as the square of a sinc function.

where f is its frequency, f_0 is the center frequency, $\dot{f}$ is its frequent derivative and t is time. The signal can then be written as

$$\begin{aligned} n(t) &= a \exp\left[2\pi \int_0^t f(t)dt + \phi\right], \\ &= a \exp\left[2\pi(f_0 t + \frac{\dot{f}}{2}t^2) + \phi\right], \end{aligned} \tag{A.8}$$

where ϕ is some extra phase. In cases that follow we will have a finite length of data, we can center this around a time of zero; this is equivalent to applying a box window the signal. If we define the length of our signal as T we can say that the signal $n(t) = 0$ outside of $-T/2 \leq t \leq T/2$ [**misaridis2005UseModulated**]. The Fourier transform can then be written as

$$\begin{aligned} \tilde{n}(f) &= \frac{a}{2}\int_{-T/2}^{T/2} n(t) \exp\left\{-i2\pi t f\right\} dt \\ &= \frac{a}{2} e^{i\phi} \int_{-T/2}^{T/2} e^{i2\pi\left(\frac{\dot{f}}{2}t^2 + f_0 t - ft\right)} dt \\ &= \frac{a}{2} e^{i\phi} \left[I\right]. \end{aligned} \tag{A.9}$$

The integral can then be written as

$$\begin{aligned} I &= \int_{-T/2}^{T/2} \exp\left\{ i2\pi \left(\frac{\dot{f}}{2}t^2 + f_0 t - f \right) \right\} dt \\ &= \int_{-T/2}^{T/2} \exp\left\{ i2\pi \left(\frac{\dot{f}}{2}t^2 + (f - f_0)t \right) \right\} dt \\ &= \int_{-T/2}^{T/2} \exp\left\{ i\frac{\pi}{2}2\dot{f} \left(t^2 + 2\frac{(f - f_0)}{\dot{f}}t \right) \right\} dt \\ &= \int_{-T/2}^{T/2} \exp\left\{ i\frac{\pi}{2}2\dot{f} \left[\left(t + \frac{(f - f_0)}{\dot{f}} \right)^2 - \left(\frac{(f - f_0)}{\dot{f}} \right)^2 \right] \right\} dt \\ &= \exp\left\{ -i\frac{\pi}{2}2\dot{f} \left(\frac{(f - f_0)}{\dot{f}} \right)^2 \right\} \int_{-T/2}^{T/2} \exp\left\{ i\frac{\pi}{2}2\dot{f} \left[\left(t + \frac{(f - f_0)}{\dot{f}} \right)^2 \right] \right\} dt \end{aligned} \tag{A.10}$$

We can then substitute using

$$v = \sqrt{2\dot{f}} \left(t - \frac{(f - f_0)}{\dot{f}} \right) \tag{A.11}$$

where

$$dv = \sqrt{2\dot{f}} dt. \tag{A.12}$$

The integral then becomes

$$I = \exp\left\{ -i\frac{\pi}{2}2\dot{f} \left(\frac{(f - f_0)}{\dot{f}} \right)^2 \right\} \int_{-V_l}^{V_u} \exp\left\{ i\frac{\pi}{2}v^2 \right\} dv \tag{A.13}$$

When $t = -T/2$ and $t = T/2$ we can define the limits of the integral V_l and V_u respectively as

$$\begin{aligned} V_l &= \sqrt{2\dot{f}} \left(\frac{T}{2} + \frac{(f - f_0)}{\dot{f}} \right) \\ V_u &= \sqrt{2\dot{f}} \left(\frac{T}{2} - \frac{(f - f_0)}{\dot{f}} \right). \end{aligned} \tag{A.14}$$

As the $\sin(v^2)$ function is symmetric, this integral can be split up further such that

$$\begin{aligned} I = \exp\left\{ -i\frac{\pi}{2}2\dot{f} \left(\frac{(f - f_0)}{\dot{f}} \right)^2 \right\} \frac{1}{\sqrt{2\dot{f}}} \\ \cdot \left[\int_0^{V_u} \exp\left\{ i\frac{\pi}{2}v^2 \right\} dv + \int_0^{V_l} \exp\left\{ i\frac{\pi}{2}v^2 \right\} dv \right]. \end{aligned} \tag{A.15}$$

One can then use the Fresnel $S(x)$ and $C(x)$ defined by

$$\begin{aligned} C(x) &= \int_0^x \cos\frac{\pi}{2}t^2 dt \\ S(x) &= \int_0^x \sin\frac{\pi}{2}t^2 dt \end{aligned} \tag{A.16}$$

The Fourier transform is then

$$\tilde{n}(f) = \frac{a}{2\sqrt{2\dot{f}}} \exp\left\{ i(\phi - \pi\frac{f-f_0}{\dot{f}}) \right\} \left[C(V_l) + C(V_u) + i(S(V_l) + S(V_u)) \right], \tag{A.17}$$

where the power spectrum is then

$$|\tilde{n}(f)|^2 = \frac{a^2}{4|\dot{f}|} \left[(C(V_l) + C(V_u))^2 + (S(V_l) + S(V_u))^2 \right] \tag{A.18}$$

By taking a simple signal, we can verify that this is correct. Figure A.2 demonstrates the FFT of a simple signal and the power spectrum estimation using Eq. A.18.

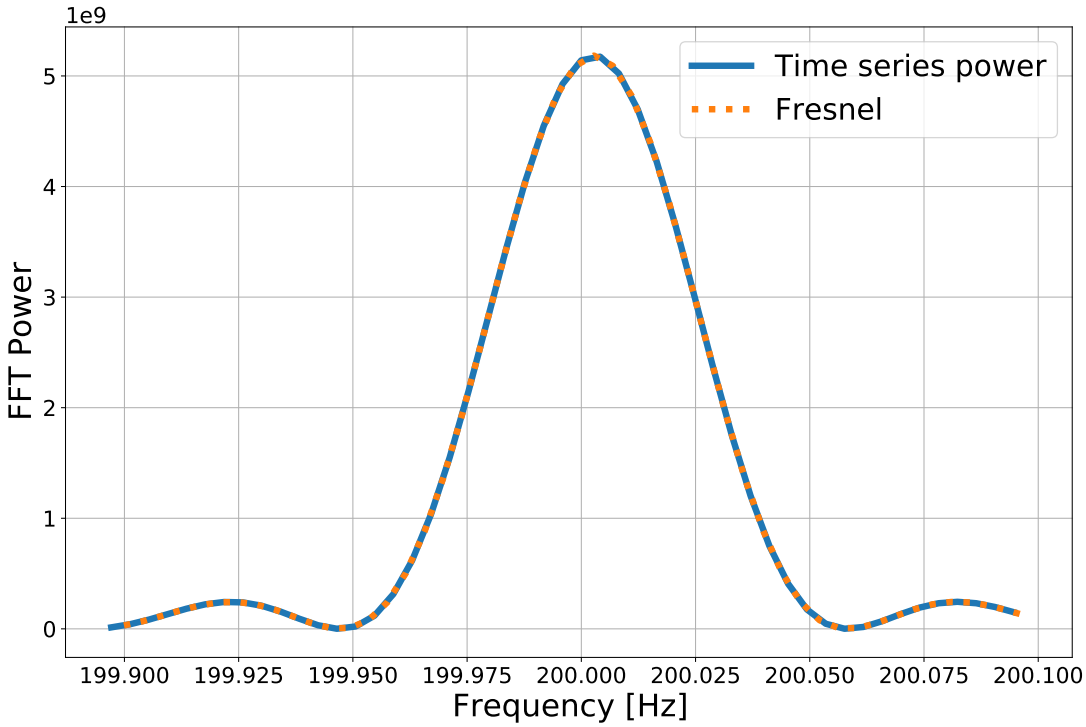

Figure A.2: The Fresnel integral form of the power spectrum above can then be compared to a numerically calculated power spectrum from Eq. A.8. This looks very similar to the sinc form in Fig. A.1, this is because the frequency derivative that are common for CW sources are very small $\sim 1e^{-9}$.

The values of this for the center location of each frequency bin surrounding the signal frequency can then be calculated for each time segment. A full spectrogram of a loud

signal ($\sim$ 1000 SNR) can be seen in Fig. A.3, A.4, A.5 and A.6 to demonstrate the signal simulations. The signal frequency for each time segment can be found using the model described in Sec. 2.1. Figure A.3 shows an example of a signal of fixed frequency which is simulated at the center of a frequency bin. When the signals frequency is then moved

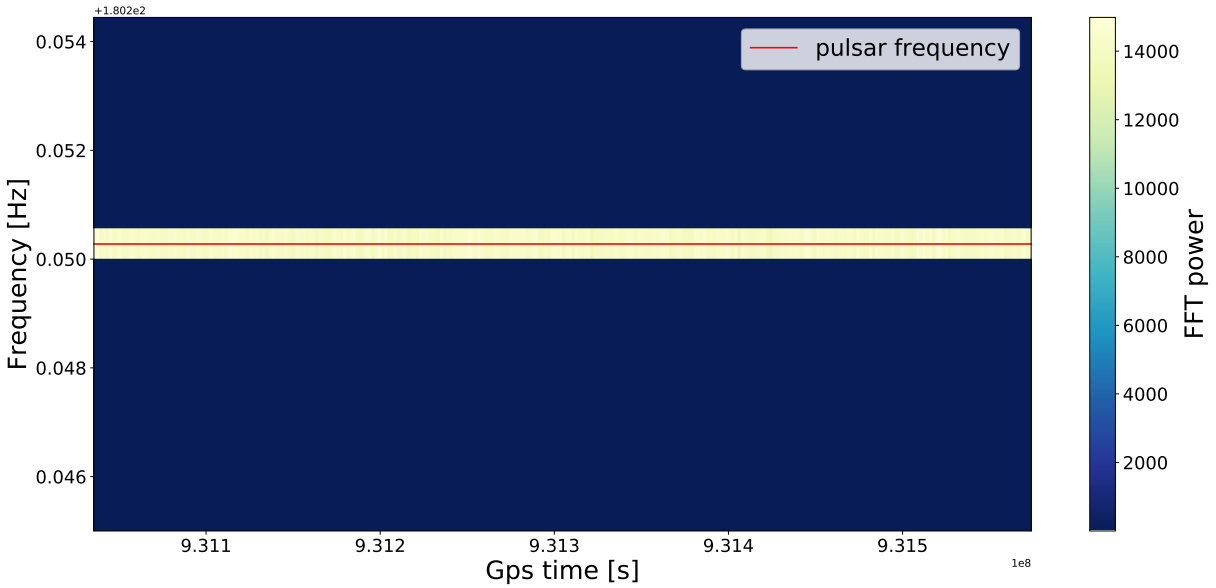

Figure A.3: By simulating a signal with a frequency in the center of a band, all of the signals power is contained within a single frequency bin. This shows an example of this kind of simulation in a spectrogram. The red line is the signals frequency evolution.

to the edge of a bin, the power can be seen to be distributed evenly between the two surrounding frequency bins. This can be seen in Fig. A.4. The doppler shift of a signal can then be added such that the frequency changes with time. This is shown in Fig. A.5. Finally Fig. A.6 shows the Doppler modulation and the antenna pattern modulation of a CW signal.

These simulations in the power spectrum greatly increased the speed of data generation when compared to simulating the signal in the time-series and taking their Fourier transform.

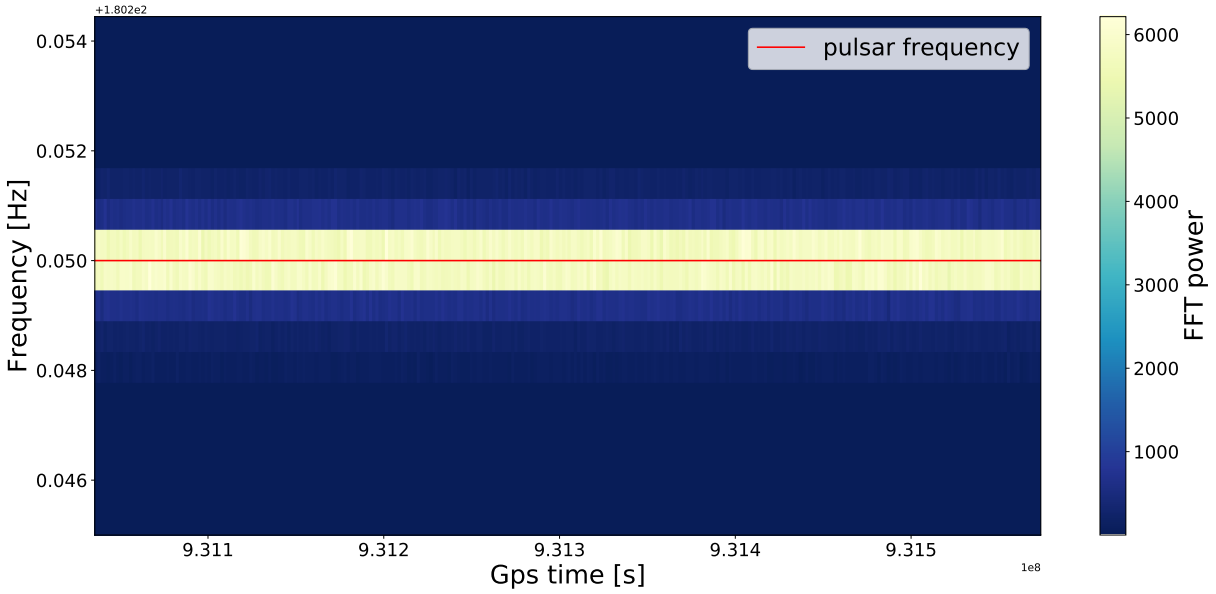

Figure A.4: By placing the signal at the edge of a frequency bin, the power is distributed around surrounding frequency bin, this can be seen above. The red line is the signals frequency evolution.

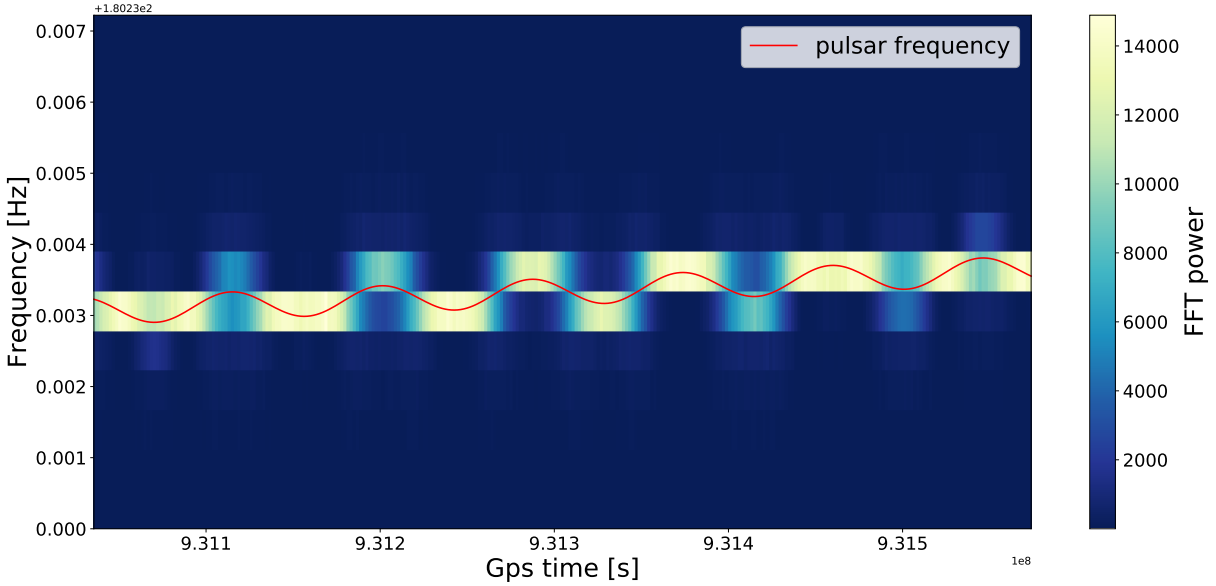

Figure A.5: Including the Doppler shift of a signal due to the earths rotation and orbit cause the signal to be modulated in frequency. This also causes a modulation in the SNR of the signal in and single frequency bin as it moves between bins. The red line is the signals frequency evolution.

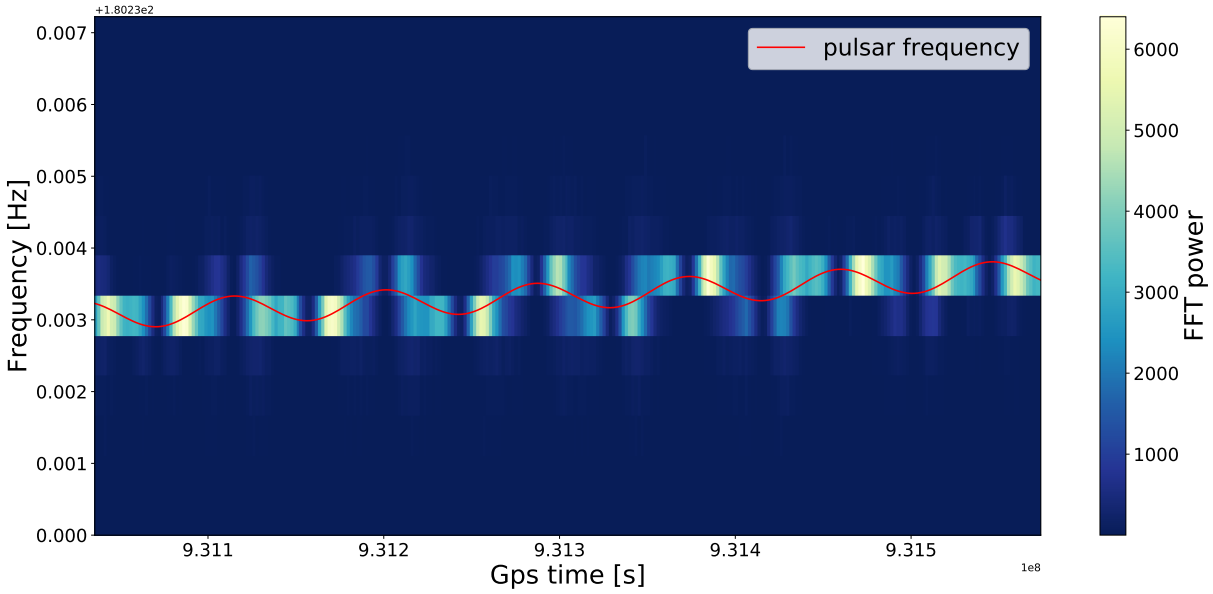

Figure A.6: The antenna pattern modulation can also be included to completely simulate a potential CW signal in a spectrogram. The red line is the signals frequency evolution.

Appendix B

Nested sampling

B.1 Evidence integral

Nested sampling is a method to estimate the Bayesian evidence defined by,

$$Z = p(\boldsymbol{d} \mid I) = \int \mathcal{L}(\theta)\pi(\theta)d\theta. \tag{B.1}$$

This integral can be transformed such that one integrated only over one dimension and not over all dimensions of θ, this is described below. From the definition of the expectation value of a function $g(X)$ we have

$$E[g(X)] = \int g(x)f_X(x)dx, \tag{B.2}$$

where $f_X(x)$ is the probability distribution of a random variable X. From this we can see that the Bayesian Evidence can be defined as

$$Z = \int \mathcal{L}(\theta)\pi(\theta)d\theta = E[\mathcal{L}(\theta)], \tag{B.3}$$

where the prior $p(\theta \mid I) = \pi(\theta)$ is the probability distribution of θ and the likelihood is $p(\boldsymbol{d} \mid \theta, I) = \mathcal{L}(\theta)$. From the definition of the expectation value of random variable X we can write

$$E[X] = \int_0^\infty P(X > \lambda)d\lambda = \int_0^\infty \int_\lambda^\infty f_X(x)dxd\lambda, \tag{B.4}$$

This can then be applied to Eq. B.3 such that the Evidence can be written as

$$Z = E[\mathcal{L}(\theta)] = \int_0^\infty P(\mathcal{L}(\theta) > \lambda)d\lambda = \int_0^\infty X(\lambda)d\lambda, \tag{B.5}$$

where we can define $X = P(\mathcal{L}(\theta) > \lambda)$ as the prior mass

$$X(\lambda) = \int_{\mathcal{L}(\theta)>\lambda} \pi(\theta) d\theta, \tag{B.6}$$

which is the amount of the prior where $\mathcal{L}(\theta) > \lambda$. As the prior mass is an integral of a probability distribution, we know that it has a minimum value of zero and a maximum value of 1, therefore, we can rewrite Eq. B.5 as

$$Z = p(\boldsymbol{d} \mid I) = \int \mathcal{L}(\theta)\pi(\theta) d\theta = \int_0^1 \mathcal{L}(X) dX, \tag{B.7}$$

where the function $\mathcal{L}(X)$ is the value of the likelihood such that $P(\mathcal{L}(X) > \lambda) = X$. This then mean that we have a one dimensional integral over the prior mass X which has a range between zero and one.